Dissertation
submitted to the
Combined Faculties of the Natural Sciences and Mathematics
of the Ruperto-Carola-University of Heidelberg, Germany
for the degree of
Doctor of Natural Sciences

put forward by

Bastian Sikora

born in Munich, Germany

Oral examination: April 18th, 2018

Quantum field theory of the g-factor of bound systems

Referees: **Honorarprof. Dr. Christoph H. Keitel**
Prof. Dr. Maurits Haverkort

Abstract

In this thesis, the theory of the g-factor of bound electrons and muons is presented. For light muonic ions, we include one-loop self-energy as well as one- and two-loop vacuum polarization corrections with the interaction with the strong nuclear potential taken into account to all orders. Furthermore, we include effects due to nuclear structure and mass. We show that our theory for the bound-muon g-factor, combined with possible future bound-muon experiments, can be used to improve the accuracy of the muon mass by one order of magnitude. Alternatively, our approach constitutes an independent access to the controversial anomalous magnetic moment of the free muon. Furthermore, two-loop self-energy corrections to the bound-electron g-factor are investigated theoretically to all orders in the nuclear coupling strength parameter $Z\alpha$. Formulas are derived in the framework of the two-time Green's function method, and the separation of divergences is performed by dimensional regularization. Our numerical evaluation by treating the nuclear Coulomb interaction in the intermediate-state propagators to zero and first order show that such two-loop terms are mandatory to take into account in stringent tests of quantum electrodynamics with the bound-electron g-factor, and in projected near-future determinations of fundamental constants.

Zusammenfassung

In dieser Arbeit wird die Theorie des g -Faktors von gebundenen Elektronen und Myonen präsentiert. Für leichte myonische Ionen betrachten wir die Ein-Schleifen-Selbstenergie- sowie Ein-und Zwei-Schleifen-Vakuumpolarisationskorrekturen, wobei die Wechselwirkung mit dem starken Kernpotential zu allen Ordnungen berücksichtigt wird. Darüber hinaus berücksichtigen wir die Effekte aufgrund von Kernstruktur und Masse. Wir zeigen, dass unsere Theorie für den g -Faktor des gebundenen Myons, kombiniert mit möglichen zukünftigen Experimenten mit gebundenen Myonen, genutzt werden kann, um die Genauigkeit der Myon-Masse um eine Größenordnung zu verbessern. Alternativ stellt unser Ansatz einen unabhängigen Zugang zu dem umstrittenen anomalen magnetischen Moment des freien Myons dar. Desweiteren werden Zwei-Schleifen-Selbstenergiekorrekturen für den g-Faktor von gebundenen Elektronen zu allen Ordnungen im Atomkern-Kopplungsstärke-Parameter $Z\alpha$ theoretisch untersucht. Formeln werden im Rahmen der *two-time Green's function*-Methode hergeleitet, und die Separation von Divergenzen erfolgt durch dimensionale Regularisierung. Unsere numerische Berechnung, bei der die Coulomb-Wechselwirkung in internen Propagatoren zu nullter und erster Ordnung berücksichtigt wird, zeigt, dass solche Zwei-Schleifen-Beiträge für strenge Tests der Quantenelektrodynamik mittels des g-Faktors des gebundenen Elektrons berücksichtigt werden müssen, sowie in naher Zukunft für die geplante Bestimmung von Naturkonstanten.

Within the framework of this thesis, the following article has been published in peer-reviewed journals:

- "Extraction of the electron mass from g factor measurements on light hydrogenlike ions" [1],
  J. Zatorski, B. Sikora, S. G. Karshenboim, S. Sturm, F. Köhler-Langes, K. Blaum, C. H. Keitel, and Z. Harman , *Phys. Rev. A,* 96, 012502, (2017).

The following articles have been submitted or are in preparation:

- "Access to improve the muon mass and magnetic moment anomaly via the bound-muon g factor" [2],
  B. Sikora, H. Cakir, N. Michel, V. Debierre, N. S. Oreshkina, N. A. Belov, V. A. Yerokhin, C. H. Keitel, and Z. Harman, submitted (2017); arXiv:1801.02501v1.

- "Theory of the two-loop self-energy correction to the g-factor in non-perturbative Coulomb fields" [3],
  B. Sikora, N. S. Oreshkina, H. Cakir, Z. Harman, V. A. Yerokhin, and C. H. Keitel, in preparation

- "Muonic vacuum polarization correction to the bound-electron g-factor" [4],
  N. A. Belov, B. Sikora, R. Weis, V. A. Yerokhin, S. Sturm, K. Blaum, C. H. Keitel, and Z. Harman, submitted (2016); arXiv:1610.01340v1.

- "Light-by-light scattering-modified self-energy correction to the bound electron g factor" [5],
  V. Debierre, B. Sikora, H. Cakir, N. Oreshkina, Z. Harman, and C. H. Keitel, in preparation

Contents

1 Introduction

The g-factor of the electron and the muon

Quantum field theory (QFT) describes the fundamental quantum interactions between elementary particles. The Standard Model of particle physics which is based on QFT provides accurate descriptions of the electromagnetic, the strong and weak interactions [6–11]. Quantum electrodynamics (QED), which is the quantum theory of the electromagnetic interaction, is a part of the Standard Model. It is, as of now, the most successful physical theory [6, 12, 13]. Among the most precisely determined quantities are the magnetic dipole moments (or, the associated g-factors) of the free electron and muon [6, 14–20].

An excellent 11-digit agreement between the theoretical and experimental g-factors of the free electron has been found (e.g. Ref. [19]). In fact, experimental measurements and theoretical calculations for the free electron have reached a level of precision that the g-factor measurement is used to determine the fine-structure constant α, assuming the correctness of QED [21]. The value of α extracted from the comparison of theory and experiment of the electron g-factor [22] was found to be in good agreement with α determined in independent methods such as atom recoil measurements [17]. Nowadays, the most precise value of α stems from a comparison between the experimental and theoretical g-factors of the free electron [19, 22].

For the g-factor of the free muon, however, a significant disagreement between the theoretical and experimental values has been found. This could be due to uncertainties of the hadronic vacuum polarization contribution, but the origin of this discrepancy is not known [19]. Another muon-related mystery is the proton radius puzzle [23–25]. Due to a larger overlap between the muon's wavefunction and the proton, a Lamb shift measurement on muonic hydrogen, i.e. the bound system formed by a proton and a negatively charged muon, allowed the determination of the proton radius with a better accuracy compared to the value accepted by the Committee on Data for Science and Technology (CODATA) [23]. The proton radius determined this way was found to be smaller by 5 standard deviations than the accepted CODATA value [23] which is determined from electron-proton scattering experiments and precision spectroscopy of the hydrogen atom [23]. A similar deviation was observed for the deuteron radius [26, 27]. However, a recent measurement using hydrogen atoms found a proton radius which is consistent with the proton radius from the muonic experiment [28].

Another discrepancy involving bound particles is the recently observed deviation between the theoretical and experimental hyperfine splittings in hydrogenlike and lithiumlike bismuth [29]. A weighted difference of hyperfine splittings of these two charge states of bismuth was determined experimentally and was found to be in significant

disagreement (7 standard deviations) with the theoretical prediction [29]. The question arises whether it is our understanding of nuclear structure or the QED theory of magnetic interactions which caused this deviation, motivating studies in the latter field. The magnetic sector of QED can be especially well tested by employing an external magnetic field, as it is the case for g-factor experiments.

In this work, we investigate the g-factor of electrons and muons bound in a nuclear potential. Measurements of the bound-electron and bound-muon g-factors allow tests of QED in the presence of strong electric background fields which are not present in the free-electron and free-muon g-factor determinations [30]. Also, in the case of bound particles, the atomic number Z of the nucleus provides an additional parameter which can be varied experimentally in a wide range.

The g-factor of the bound electron is typically measured in Penning-trap experiments. In such an experiment, the Larmor frequency ω_L of the bound electron and the cyclotron frequency ω_c of the ion are determined. The Larmor frequency depends on the bound fermion's g-factor as follows [1]:

$$\omega_\mathrm{L} = \frac{g}{2}\frac{|e|}{m_e}B\,. \tag{1.1}$$

The cyclotron frequency of the ion is [1]

$$\omega_\mathrm{c} = \frac{Q}{M}B\,. \tag{1.2}$$

Here, e is the (negative) elementary charge and Q is the ion's charge, m_e and M are the electron's and ion's mass, respectively, and g is the bound-electron g-factor [1]. There have been measurements of the bound-electron g-factor in hydrogenlike $^{12}C^{5+}$ [30, 31], $^{16}O^{7+}$ [32], and, more recently, $^{28}Si^{13+}$ [33]. An excellent agreement between the experimental and the theoretical value according to state-of-the-art calculations was found in these measurements. The experiment with hydrogenlike $^{28}Si^{13+}$ has since been repeated, improving the experimental accuracy of the bound-electron g-factor by one order of magnitude [34]. With this, the experimental accuracy for the $^{28}Si^{13+}$ ion is one order of magnitude better than the theoretical prediction [33, 34]. The ALPHATRAP setup at the Max Planck Institute for Nuclear Physics is anticipated to increase the experimental accuracy even further and also to extend the range of ions to be investigated to elements as heavy as lead ($Z = 82$) [35]. g-factor measurements with very heavy highly charged ions are also planned at the FAIR facility in Darmstadt [35, 36]. As for experimental techniques, we refer to the detailed discussions in Ref. [37–40].

There are several applications for bound-electron g-factor measurements. One prominent example is the determination of the electron mass [41]. Equations (1.1) and (1.2) can be solved for the electron mass [1]:

$$m_e = \frac{g}{2}\frac{e}{Q}\frac{\omega_\mathrm{c}}{\omega_\mathrm{L}}M\,. \tag{1.3}$$

For the determination of m_e, the frequency ratio needs to be measured and, assuming the correctness of QED, one uses the theoretical value of the g-factor. Recently, the

accuracy of the electron mass was improved this way by one order of magnitude [31, 42], employing a $^{12}C^{5+}$ ion. Subsequent investigations lead to small corrections (less than one standard deviation) of the value of the electron mass [1, 43]. A further application of the bound-electron g-factor is the determination of the electron-proton mass ratio, provided the ion-proton mass ratio is known with sufficient accuracy [44].

The g-factor of bound electrons is also sensitive to the nuclear structure, especially in heavy ions. A measurement of the bound-electron g-factor could be used as a probe for the nuclear structure, assuming the correctness of QED [45]. This was demonstrated in Ref. [33], where the radius of the ^{28}Si nucleus was determined, albeit with an accuracy which is not as good as the accuracy of the current literature value. Bound-electron g-factor measurements can in principle be used as well to determine nuclear magnetic moments by a measurement involving hyperfine-split atomic levels [45, 46].

Another system of interest are lithiumlike ions. Apart from binding corrections to QED effects, electron-electron interactions and QED corrections to electron-electron interactions are also relevant in lithiumlike ions. Theoretical investigations on lithiumlike ions have been performed e.g. in Ref. [47–50]. A measurement of the g-factor of the lithiumlike silicon ion $^{28}Si^{11+}$ showed an excellent agreement between theory and experiment [51]. Two different isotopes of lithiumlike Ca were investigated experimentally and theoretically in Ref. [52], allowing the study of nuclear recoil effects.

Finally, schemes have been proposed to determine the fine-structure constant α from the bound-electron g-factor [45, 53–55]. While the g-factor of the free electron is mainly described by radiative QED corrections (apart from small contributions due to strong and weak interactions), the leading α dependence of the bound-electron g-factor is due to non-radiative binding corrections [56]. Therefore, an α determination by means of the bound-electron g-factor constitutes an independent measurement [54]. However, the uncertainties of the nuclear radius and further details of the nuclear structure constrain the accuracy of the theoretical g-factor predictions. The uncertainty due to the nuclear parameters is larger than the uncertainty due to the current accuracy of α in all hydrogenlike ions, except for the He^+ ion [1]. Therefore, in order to make a competitive α determination by means of the bound-electron g-factor feasible, weighted differences of g-factors of ions in different charge states are being considered. In Ref. [54, 55], a weighted difference of g-factors of hydrogenlike $g_{\rm hyd}$ and lithiumlike $g_{\rm lit}$ ions is considered: $\delta_\Xi g = g_{\rm lit} - \Xi g_{\rm hyd}$. The weight Ξ is optimized in such a way that nuclear effects are suppressed in $\delta_\Xi g$ by several orders of magnitude, such that the uncertainty of $\delta_\Xi g$ due to the uncertainty of the nuclear radius is rendered to be smaller than the uncertainty due to the uncertainty of α. This procedure allows a determination of α, using low- and medium-Z ions, with an accuracy of up to one or two orders of magnitude better than the current literature value, provided that the theoretical and experimental g-factors can be given with sufficient accuracy [54, 55]. A weighted difference between the g-factors of heavy hydrogenlike and boronlike ions for the determination of α has also been investigated [53].

To push forward the boundaries of theory, QED corrections at the one- and two-loop level need to be calculated with increasing accuracy. One-loop corrections have been evaluated both perturbatively as a power series in $Z\alpha$ and non-perturbatively

in $Z\alpha$ (see e.g. Ref. [56, 57]). Two-loop corrections were evaluated as an expansion in terms of the parameter $Z\alpha$ up to fourth order in Ref. [56]. Two-loop diagrams with two vacuum polarization (VP) loops and those with one VP and one self-energy (SE) loop were evaluated non-perturbatively in $Z\alpha$ [58]. A previously uncalculated two-loop light-by-light scattering contribution of the order $(Z\alpha)^4$ was determined [59]. Evaluations of two-loop $(Z\alpha)^5$ terms were also performed [60–62]. However, for large Z, the perturbative approach cannot be expected to give good approximations, since the expansion parameter of this approach, $Z\alpha$, is close to unity. The perturbative evaluation of the two-loop self-energy correction to the Lamb shift resulted in numerically large coefficients in the $Z\alpha$ expansion, showing a slow convergence of the $Z\alpha$ series even for small Z [63]. This slow convergence even for low Z cannot be ruled out for the two-loop corrections to the g-factor. Therefore, methods which include the interaction between fermion and nucleus exactly, i.e. without a perturbative expansion, are required.

The subject of this thesis

In this thesis, we investigate the g-factor of the bound muon [2]. The methods to compute one-loop radiative corrections to the bound-electron g-factor were applied to bound muons. As stated above, nuclear effects are enhanced in muonic ions. Therefore, in order to achieve a high theoretical accuracy for the bound-muon g-factor, we develop the theory of the bound-muon g-factor specifically for muonic ions without any remaining bound electrons and with low nuclear charge numbers. For the muonic $^4He^+$ ion, the accuracy of our bound-state QED calculations is comparable to the accuracy of the free-muon g-factor predictions [2, 19]. Therefore, our theory serves as an independent method to determine the controversial free-muon g-factor by subtracting the QED binding corrections we calculate [2]. Furthermore, we put forward a method to improve the muon mass via the bound-muon g-factor, similarly to the determination of the electron mass discussed above. As we shall see, the bound-muon g-factor allows the improvement of the accuracy of the muon mass by one order of magnitude, provided the required experimental accuracy can be achieved [2]. Such investigations can shed some light on the existing discrepancies between the theoretical description and experimental findings involving the muon mentioned above.

Furthermore, we investigate the previously uncalculated two-loop self-energy corrections to the bound-electron g-factor non-perturbatively in $Z\alpha$ [3]. For a broad range of ions, the two-loop self-energy corrections, which are by far the hardest to treat theoretically, are the largest source of uncertainty. This holds true even at $Z = 6$, after a recent high-precision evaluation of the one-loop SE corrections [1, 64]. Therefore, we see that higher-order terms in $Z\alpha$ are also necessary at low nuclear charges, if an ultimate precision is required. Furthermore, a very recent computation of the order $(Z\alpha)^5$ contribution to the two-loop SE correction does not seem to improve the theoretical uncertainty of the bound-electron g-factor [62]. Improving the theoretical accuracy of the bound-electron g-factor is crucial for the determination of α from the bound-electron g-factor [54, 55] as well as for stringent tests of bound-state QED since, even for $Z = 14$, the experimental

accuracy is one order of magnitude better than the theoretical accuracy [1, 34, 62]. This further shows the need of a non-perturbative evaluation of the two-loop SE correction.

These calculations are by no doubt challenging: the analogous evaluation of the simpler two-loop self-energy contribution to the Lamb shift took several years for a group of several authors [65–67]. We start them by developing the theoretical framework for the evaluation of two-loop SE corrections to the g factor of an atomic electron in a hydrogenlike ion in the Furry picture, i.e. to all orders in $Z\alpha$ [3]. As we shall see, many two-loop self-energy contributions contain ultraviolet and infrared divergences. We demonstrate that all ultraviolet and infrared divergences mutually cancel such that the complete two-loop self-energy correction is finite [3]. We then separate all contributions into different categories, analogously to the two-loop self-energy correction to the Lamb shift [63], namely the so-called loop-after-loop (LAL) contribution as well as the F, P and M terms which will be properly defined later. Each of these categories requires a different approach for numerical evaluation. We also compute the complete F term numerically and demonstrate that it converges to the two-loop self-energy correction of the free-electron g-factor for low Z [3]. This was an important consistency check of our results since the LAL contribution as well as the P and M terms can be expected to converge to zero in this limit, as will be discussed later.

Structure of the thesis

This work is organized as follows. In Chapter 2, we begin with an overview of the g-factor contributions for free electrons and muons computed so far, as well as binding corrections computed in the framework of non-relativistic QED, which treats binding corrections perturbatively. We will also illustrate how this approach is restricted to low nuclear charge numbers.

We then discuss the two-time Green's function method [68] which we will use to compute binding effects in QED non-perturbatively in Chapter 3. To illustrate the two-time Green's function method, we compute the leading contribution to the bound-fermion g-factor. In addition, we summarize the contributing nuclear effects.

In Chapter 4, we discuss the methods to compute one-loop Feynman diagrams for bound fermions. There are two different kinds of one-loop corrections to the bound-fermion g-factor, namely, the self-energy (interaction of the bound fermion with the quantum photon field) and the vacuum polarization (creation and annihilation of virtual fermion-antifermion pairs). We begin with the discussion of the self-energy correction by deriving all contributing terms using the two-time Green's function method. The cancellation of ultraviolet and infrared divergences will be explained, as well as methods to compute the individual self-energy contributions. We then briefly discuss the renormalization of vacuum polarization contributions. In this thesis, we consider two cases of vacuum polarization in which the virtual particles created have a different mass than the bound particle under consideration. Specifically, we investigate muonic vacuum polarization corrections (i.e. corrections due to the creation and annihilation of virtual muon-antimuon pairs) to the bound-electron g-factor [4] as well as electronic vacuum

polarization corrections (virtual electron-positron pairs) to the bound-muon g-factor [2]. The contributions to the bound-electron g-factor due to one-loop Feynman diagrams have been discussed in the literature in great detail, e.g. [57, 69–71].

In Chapter 5, we discuss applications of the bound-fermion g-factor. First, we review the recent high-precision determination of the electron mass [1]. Then, we present our theory of the bound-muon g-factor which also includes the computation of two-loop vacuum polarization contributions for the case of virtual electron-positron pairs. We will demonstrate, how this theory can be used to improve the accuracy of the muon mass by one order of magnitude [2].

In Chapters 6 and 7, we move on to the main part of this thesis, namely, the theory of two-loop self-energy corrections to the bound-electron g-factor [3]. In Chapter 6, we discuss the analytical theory of these previously uncalculated elaborate terms, namely, the cancellation of ultraviolet and infrared divergences and the separation of these diagrams into different groups suitable for numerical evaluation. In chapter 7, we describe our methods for the computation of the so-called F term in detail. We also present our numerical results for the F term and show the consistency of our results with the free-electron QED theory.

Units

Throughout this work, we will use relativistic units, i.e. the unit system with $\hbar = c = m_e = 1$ (see e.g. Ref. [72]). In these units, the fine-structure constant can be expressed as $\alpha = \frac{e^2}{4\pi}$, where e is the negative elementary charge [6].

2 Free-fermion g-factor and $Z\alpha$ expansion

The g-factor of an elementary fermionic particle is a dimensionless quantity which parametrizes its magnetic dipole moment according to the formula [69]

$$\boldsymbol{\mu}_\mathrm{f} = g_\mathrm{f} \frac{q_\mathrm{f} \boldsymbol{J}}{2m_\mathrm{f}}. \tag{2.1}$$

Here, $\boldsymbol{\mu}_\mathrm{f}$ is the particle's magnetic dipole moment, q_f and m_f are the fermion's charge and mass, respectively, g is the g-factor and J is the total angular momentum of the particle. For a free electron or muon and for a bound electron or muon in the ground state of the hydrogen atom or a hydrogenlike ion, J is equal to its spin. In this thesis, we specifically consider electrons and muons which are both spin-$\frac{1}{2}$ fermions. We sometimes use the term "fermion" when refering to electrons and muons if a statement is applicable to both.

Various physical theories make contradictory predictions for the g-factor of the electron and muon. Classical electrodynamics predicts a g-factor of precisely $g = 1$ [73]. In the derivation of this result, the electron or muon is assumed to be a rotating charge distribution with a spatially constant charge to mass ratio and with total angular momentum $\boldsymbol{J}$ [73]. Non-relativistic quantum mechanics does not predict the g-factor of elementary particles but contains the g-factor as a free parameter which has to be determined experimentally [74, 75]. Including special relativity into the quantum mechanical theory, which is equivalent to the Dirac theory, the g-factor is no longer a free parameter. The Dirac theory predicts a g-factor of precisely $g = 2$ [6].

Quantum field theory predicts a g-factor which can be parametrized as

$$g = 2 + \text{radiative corrections},$$

where the "radiative corrections" can be determined only perturbatively [6]. They correspond to Feynman diagrams with closed loops [6]. Pure QED effects can be parametrized as a perturbation series in powers of the fine structure constant α, where the number of closed loops in the diagram corresponds to the power of α [6, 17, 19, 20, 69]:

$$g_f = 2\left(C_\mathrm{f}^{(0)} + C_\mathrm{f}^{(2)}\left(\frac{\alpha}{\pi}\right) + C_\mathrm{f}^{(4)}\left(\frac{\alpha}{\pi}\right)^2 + C_\mathrm{f}^{(6)}\left(\frac{\alpha}{\pi}\right)^3 + C_\mathrm{f}^{(8)}\left(\frac{\alpha}{\pi}\right)^4 + C_\mathrm{f}^{(10)}\left(\frac{\alpha}{\pi}\right)^5 \cdots\right). \tag{2.2}$$

The coefficients $C^{(2n)}$ correspond to the sum of all n-loop diagrams (i.e. diagrams with $2n$ interaction vertices between the fermion and the quantum photon field) [69].

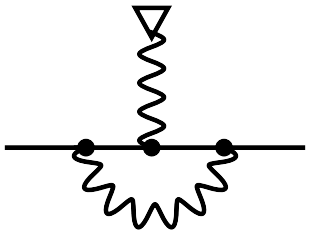

Figure 2.1: One-loop correction to the free-fermion g-factor [6]. The straight line represents the free fermion (electron or muon), the wave line represents a virtual photon and the wave line terminated by the triangle represents the interaction with the magnetic field [69].

As mentioned above, $C_{\mathrm{f}}^{(0)} = 1$. The lowest-order correction was first calculated by J. Schwinger in 1948 [76]. It corresponds to the one-loop vertex diagram shown in Fig. 2.1.

$$C_{\mathrm{f}}^{(2)} = \frac{1}{2} \tag{2.3}$$

The computation of $C_{\mathrm{f}}^{(2)}$ is described in detail in standard textbooks, e.g. [6, 77–81]. This prediction was in excellent agreement with the experimental value for the g-factor of the free electron [6] and greatly contributed to the development of quantum field theory [56].

In g-factor Feynman diagrams with at least two loops, there can be contributions due to vacuum polarization (VP), i.e. contributions due to the creation and subsequent annihilation of virtual fermion antifermion pairs. VP contributions depend on the mass ratio of the fermion whose g-factor is to be determined and the particle species in the loop [19]. E.g. VP due to virtual electron positron pairs gives different contributions to the electron's and the muon's g-factors [19]. Therefore, the coefficients $C_f^{(2n)}$ with $n \geq 2$ are different for electrons and muons [82].

By now, g-factor contributions to the free electron and muon which correspond to diagrams with up to five loops (i.e. $\left(\frac{\alpha}{\pi}\right)^5$) have been computed [19, 21, 83–87]. Contributions up to order $\left(\frac{\alpha}{\pi}\right)^3$ have been evaluated analytically [56, 85, 86]. Recently, the order $\left(\frac{\alpha}{\pi}\right)^4$ contribution to the free-electron g-factor was evaluated with extremely high accuracy [88]. Apart from QED corrections, there are also hadronic (e.g. [19, 89–91]) and electroweak (e.g. [19, 92]) contributions to the electron and muon g-factors.

The theoretical and experimental g-factor of the electron are in excellent agreement with each other [19]. The determination of the fine-structure constant α from a comparison of the theoretical and experimental g-factor of the electron gives the most accurate value of this fundamental constant [19, 93]. There is, however, a significant deviation between the theoretical and experimental g-factor of the free muon [19, 94, 95].

In this thesis, we do not consider free particles but bound electrons and muons in the ground state $|a\rangle$ of a hydrogenlike ion. The term hydrogenlike ion refers to a bound

system of one electron and a nucleus with nuclear charge number Z. With a hydrogenlike muonic ion, we refer to a bound system of one muon and an atomic nucleus with charge number Z, and no further electrons bound in this system.

If a hydrogenlike ion is exposed to a magnetic field $\boldsymbol{B} = B\boldsymbol{e}_z$, the energy levels of the bound particle are shifted (Zeeman effect) according to the equation [69]:

$$\Delta E = -\langle a|\boldsymbol{\mu}_f \cdot \boldsymbol{B}|a\rangle. \tag{2.4}$$

Replacing the magnetic dipole moment using equation (2.1), we obtain the following relation between the bound-fermion g-factor and the Zeeman energy shift [69]:

$$\Delta E = -m_j g \frac{q_\mathrm{f} B}{2m_\mathrm{f}}. \tag{2.5}$$

Here, m_j is the angular momentum projection quantum number of the atomic state of the bound particle. In this thesis, we only consider the case $m_j = \frac{1}{2}$.

To compute the bound-fermion g-factor, the interaction between the bound fermion and the atomic nucleus needs to be taken into account. This means that the coefficients $C^{(2n)}$ are modified by the interaction between fermion and nucleus. This interaction can be taken into account perturbatively, using the framework of non-relativistic quantum electrodynamics [96, 97], with the expansion parameter of this perturbation series being $Z\alpha$. This means that the coefficients $C_\mathrm{f}^{(2n)}$ can be expressed as a series in $Z\alpha$ (e.g. [98, 99]).

Various problems in atomic physics can be computed using the $Z\alpha$ expansion approach [100–108] apart from the g-factor, e.g. the Lamb shift (e.g. [78, 109, 110]) and the hyperfine structure (e.g. [111–113]).

In the framework of non-relativistic quantum electrodynamics, the bound-fermion g-factor is parametrized as a double perturbation series in two expansion parameters, namely α and $Z\alpha$.

The order $(Z\alpha)^0$ contributions to $C_\mathrm{f}^{(2n)}$ correspond to the free-fermion contributions [114]. By now, the first few correction terms in $Z\alpha$ have been computed. A simple formula was derived to compute the $(Z\alpha)^2$ from the $(Z\alpha)^0$ contribution in refs. [114, 115]. The order $(Z\alpha)^4$ contribution was computed for one-loop diagrams in Ref. [116] and for two-loop diagrams in Ref. [44, 56]. A recent investigation of a light-by-light scattering contribution resulted in an additional contribution of order $(Z\alpha)^4$ to two-loop diagrams [59] which had not been taken into account in the earlier investigation [56]. The lowest-order in $Z\alpha$ contribution $(Z\alpha)^5$ to the "magnetic loop" vacuum polarization diagram was determined in Ref. [117] for electronic VP, and in Ref. [59] for the case of muonic VP. The first step towards computing the order $(Z\alpha)^5$ contribution to two-loop diagrams was done in Ref. [60], where two-loop vacuum polarization diagrams were analyzed. We would like to point out that most $Z\alpha$ expansion formulas for VP contributions are developed for the case of the bound particle mass being equal to the mass of the virtual particles. The order $(Z\alpha)^5$ correction to one-loop self-energy diagrams was computed in Ref. [61], and the order $(Z\alpha)^5$ contribution to two-loop diagrams was computed in Ref. [62].

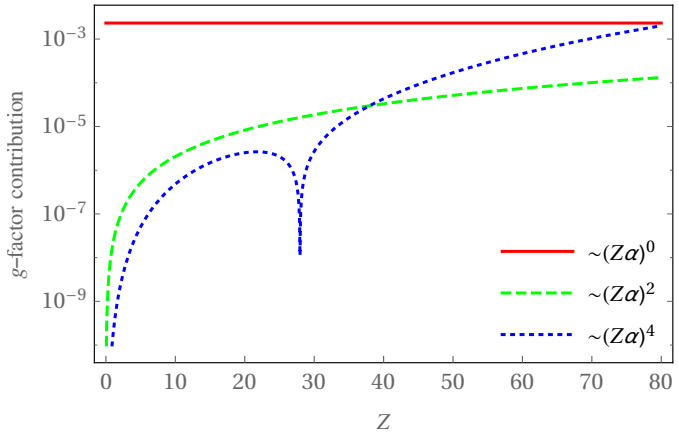

Figure 2.2: Moduli of one-loop contributions of order $(Z\alpha)^0$ (red line), $(Z\alpha)^2$ (green dashed line) and $(Z\alpha)^4$ (blue dotted line) to the electron g-factor [6, 56, 114]. The dip of the $(Z\alpha)^4$ contribution is caused by the change of sign due to logarithmic terms.

Such an expansion can certainly not be considered a good approximation for high nuclear charge numbers because the expansion parameter $Z\alpha$ is close to unity in this case. In Fig. 2.2, the modulus of the order $(Z\alpha)^2$ and $(Z\alpha)^4$ contributions to the one-loop diagrams are plotted. One can see that for $Z > 38$, the modulus of the order $(Z\alpha)^4$ contribution is larger than that of the order $(Z\alpha)^2$. Furthermore, in the evaluation of the $Z\alpha$ expansion for the two-loop self-energy correction to the Lamb shift, some coefficients of the perturbation expansion turned out to be rather large, suggesting a slow convergence of the $Z\alpha$ expansion even for low Z [63]. This might also be the case for the bound-electron g-factor, since the uncertainties of the bound-electron g-factor do not seem to decrease after the succesful evaluation of the order $(Z\alpha)^5$ corrections (see the uncertainties estimated for the bound-electron g-factor in different ions in Ref. [1, 62]). Thus, methods to take into account the interaction with the nuclear potential non-perturbatively in $Z\alpha$ are also required.

3 Non-perturbative treatment of the nuclear interaction

In this Chapter, we give an introduction to the non-perturbative treatment of the interaction of the bound fermion with the nuclear potential. We first introduce the Furry picture on which the non-perturbative method is based. We then introduce the basic building blocks of the Furry picture approach, namely the bound fermion's wavefunction and Green's function. To determine g-factor contributions from Feynman diagrams, we use the two-time Green's function method which we will briefly introduce here. We then use this method to discuss the leading g-factor diagram. Corrections to this diagram due to the nuclear structure and mass are briefly discussed at the end of this Chapter.

3.1 Furry picture

The QED Lagrangian, expressed not in terms of bare fields but in terms of the physical fields, is (see Ref. [6]):

$$\begin{aligned}\mathcal{L} =& -\frac{1}{4}(F^{\mu\nu})^2 + \overline{\Psi}(i\partial\!\!\!/ - m)\Psi \\ & - e\overline{\Psi}\gamma^\mu\Psi A_{r\mu} \\ & - \frac{1}{4}\delta_3(F^{\mu\nu})^2 + \overline{\Psi}(i\delta_2\partial\!\!\!/ - \delta_m)\Psi - e\delta_1\overline{\Psi}\gamma^\mu\Psi A_{r\mu}. \end{aligned} \tag{3.1}$$

Here, Ψ is the fermion field, $\overline{\Psi} = \Psi^\dagger\gamma^0$, $p\!\!\!/ = p^\mu\gamma_\mu$, $A_{r\mu}$ is the photon field and $F_{\mu\nu} = \partial_\mu A_{r\nu} - \partial_\nu A_{r\mu}$ is the photon field tensor. δ_1, δ_2, δ_3 and δ_m are renormalization counterterms [6]. $\mu, \nu \in \{0, 1, 2, 3\}$, $i \in \{1, 2, 3\}$. We choose the following representation of the Dirac matrices (see e.g. Ref. [69, 118]).

$$\gamma^0 = \begin{pmatrix} \mathbb{1} & 0 \\ 0 & -\mathbb{1} \end{pmatrix}, \qquad \gamma^i = \begin{pmatrix} 0 & \sigma^i \\ -\sigma^i & 0 \end{pmatrix},$$

$$\alpha^\mu = \gamma^0\gamma^\mu. \tag{3.2}$$

$\mathcal{L}$ consists of the free Lagrangian (first line), the interaction Lagrangian (second line) and renormalization counterterms (third line) which cancel UV divergences that appear in Feynman diagrams with closed loops [6, 119]. We now split the photon field into three components as follows: the quantum photon field A_μ, the classical nuclear (Coulomb) potential $eA_{e_\mu} = (V, \mathbf{0})$ and the classical magnetic potential $A_{m_\mu} = (0, \frac{1}{2}\mathbf{B} \times \mathbf{x})$ which

Figure 3.1: Furry picture: The double line represents a bound fermion. It corresponds to the infinite sum of a free fermion, a free fermion with one inetraction with the nuclear potential, a free fermion with two interactions etc. A wave line terminated by a cross represents the interaction with the nuclear potential [69].

corresponds to a constant magnetic field $\mathbf{B} = B\mathbf{e}_z$ (see Ref. [69]). The interaction Lagrangian now reads:

$$\mathcal{L}_I = -e\overline{\Psi}\gamma^\mu\Psi A_\mu - e\overline{\Psi}_r\gamma^\mu\Psi_r A_{e_\mu} - e\overline{\Psi}_r\gamma^\mu\Psi_r A_{m_\mu}. \tag{3.3}$$

The aim is to treat the magnetic potential perturbatively up to first order, and the nuclear potential exactly, i.e. non-perturbatively. The quantum field is treated perturbatively. The interaction term between the fermion field and the nuclear potential thus has to be "shifted" into the "free" (i.e. exactly solvable) Lagrangian [69]. Expressed in terms of Feynman diagrams, the bound fermion corresponds to the infinite series indicated in Fig. 3.1. It is a sum of a free fermion line, a free fermion line with one interaction with the nuclear potential, a free fermion line with two interactions and so on. We are going to represent a bound fermion with a double line (e.g. [69]). One can show that the entire series solves the Dirac equation with the nuclear potential. We therefore have to use solutions of the Dirac equation with the nuclear potential to represent fermion lines [120, 121]. To be precise, external fermion lines have to be represented by wave functions of the bound fermion. Internal fermion lines are represented by the Green's function of a fermion in the nuclear potential [69]. This approach is referred to as the Furry picture [122].

3.2 Solution of the Dirac equation - wavefunction

Just as the Dirac spinor representing free fermions [6], the wave function has four components. The Green's function can be represented as a 4×4 matrix. The procedure to solve the Dirac equation in the Coulomb potential is described in detail in Ref. [118]. In a general spherically symmetric potential, the four components of the wave function can be expressed as a product of a radial wave function which depends only on the radial coordinate r and a spherical spinor which depends on angular coordinates Ω as follows

[118]:

$$\Psi_{n\kappa m}(r,\Omega) = \begin{pmatrix} ig_{n\kappa}(r)\chi_{\kappa m}(\Omega) \\ -f_{n\kappa}(r)\chi_{-\kappa m}(\Omega) \end{pmatrix}. \tag{3.4}$$

This is a generalization of the non-relativistic case, where a similar separation of variables can be made [74, 75]. $g_{n\kappa}(r)$ and $f_{n\kappa}(r)$ are the radial wave functions [118]. The spherical two-component spinors $\chi_{\pm\kappa m}$ are defined in e.g. Ref. [118, 123]. Various summation formulae for spherical spinors can be found in Ref. [124]. $n \in \{1, 2, 3, \ldots\}$. κ is the relativistic angular momentum quantum number which is related to the orbital angular momentum l [123] and the total angular momentum j [118] as follows:

$$l = |\kappa + \frac{1}{2}| - \frac{1}{2}, \tag{3.5}$$

$$j = |\kappa| - \frac{1}{2}. \tag{3.6}$$

The radial functions can be determined analytically for the case of a Coulomb potential ($V(r) = -\frac{Z\alpha}{r}$), i.e. the model of a point-like nucleus. The procedure to determine the radial wave functions is described in detail in Ref. [118]. The wave functions for arbitrary quantum numbers are given in Ref. [69, 118]. For a detailed discussion of the Dirac equation, see also Ref. [125–127]

The above definition of the wavefunction is the definition of $\Psi_{n\kappa m}(r,\Omega)$ introduced in the textbooks by Greiner [118]. We employed this convention in all our calculations, although it differs from a more commonly used convention in the literature (specifically [57, 63, 72]). $|a\rangle$ will refer to the ground state of the electron with quantum numbers $(n,\kappa,m) = (1,-1,\frac{1}{2})$ and $|a_m\rangle$ will refer to the ground state $(n,\kappa) = (1,-1)$ with arbitrary angular momentum projection quantum number m.

We also employ the ground state wave functions perturbed linearly by a magnetic field $|\delta a\rangle$ [57]:

$$|\delta a\rangle = \sum_{n\neq a} \frac{|n\rangle\langle n|\gamma^0 e\not{A}_m|a\rangle}{E_a - E_n}, \tag{3.7}$$

$$|\delta_D a\rangle = -\sum_{n\neq a} \frac{|n\rangle\langle n|\gamma^0 e\not{A}_m|a\rangle}{(E_a - E_n)^2}. \tag{3.8}$$

In this work, we only require the $\kappa_n = -1$ contribution to $|\delta a\rangle$ and $|\delta_D a\rangle$ due to angular momentum selection rules. The $\kappa_n = -1$ contribution to $|\delta a\rangle$ can be expressed as:

$$\delta a(r,\Omega) = \frac{eB}{3}\begin{pmatrix} iX_a(r)\chi_{\kappa_a m_a}(\Omega) \\ -Y_a(r)\chi_{-\kappa_a m_a}(\Omega) \end{pmatrix}. \tag{3.9}$$

A closed analytical expression for $X_a(r)$ and $Y_a(r)$ is given in Ref. [128] for the model of a point-like nucleus.

The $\kappa_n = -1$ contribution to $|\delta_D a\rangle$ can be expressed as:

$$\delta_D a(r,\Omega) = \frac{eB}{3}\begin{pmatrix} iX_\delta(r)\chi_{\kappa_a m_a}(\Omega) \\ -Y_\delta(r)\chi_{-\kappa_a m_a}(\Omega)\end{pmatrix}. \tag{3.10}$$

The derivation of a closed analytical expression for $X_\delta(r)$ and $Y_\delta(r)$ is outlined in the appendix of this thesis for the model of a point-like nucleus.

The momentum space representation of $|a\rangle$ is (e.g. [6, 72]):

$$\Psi(p,\Omega_p) = \int \mathrm{d}^3 r e^{-i\boldsymbol{pr}}\Psi(r,\Omega) = \begin{pmatrix} ig(p)\chi_{\kappa m}(\Omega_p) \\ if(p)\chi_{-\kappa m}(\Omega_p)\end{pmatrix}. \tag{3.11}$$

Ω and Ω_p refer to angular coordinates in position and momentum space, respectively. The radial components $g(p)$ and $f(p)$ are (here, we do not give the subscripts $_{n,\kappa}$, since we need only the Fourier transform of the ground-state wave function) [69]:

$$g(p) = 4\pi \int \mathrm{d}r r^2 j_0(pr) g_{1,-1}(r) \tag{3.12}$$

$$f(p) = 4\pi \int \mathrm{d}r r^2 j_1(pr) f_{1,-1}(r). \tag{3.13}$$

$j_0(pr)$ and $j_1(pr)$ are the spherical Bessel functions. In the derivation of the momentum representation of the ground-state wavefunction, we employed the identity (see equation (8.178) in Ref. [75], and Ref. [129]):

$$e^{-i\boldsymbol{pr}} = 4\pi \sum_{l=0}^{\infty}\sum_{m=-l}^{l} (-i)^l Y_{lm}(\Omega_p) j_l(pr) Y^*_{lm}(\Omega). \tag{3.14}$$

The momentum space representations of $|\delta a\rangle$ and $|\delta_D a\rangle$ can be defined analogously:

$$\delta a(p,\Omega_p) = \frac{eB}{3}\begin{pmatrix} iX_a(p)\chi_{\kappa m}(\Omega_p) \\ iY_a(p)\chi_{-\kappa m}(\Omega_p)\end{pmatrix}, \tag{3.15}$$

$$X_a(p) = 4\pi \int \mathrm{d}r r^2 j_0(pr) X_a(r), \tag{3.16}$$

$$Y_a(p) = 4\pi \int \mathrm{d}r r^2 j_1(pr) Y_a(r), \tag{3.17}$$

$$\delta_D a(p,\Omega_p) = \frac{eB}{3}\begin{pmatrix} iX_\delta(p)\chi_{\kappa m}(\Omega_p) \\ iY_\delta(p)\chi_{-\kappa m}(\Omega_p)\end{pmatrix}, \tag{3.18}$$

$$X_\delta(p) = 4\pi \int \mathrm{d}r r^2 j_0(pr) X_\delta(r), \tag{3.19}$$

$$Y_\delta(p) = 4\pi \int \mathrm{d}r r^2 j_1(pr) Y_\delta(r). \tag{3.20}$$

Fully analytic expressions for $g(p)$, $f(p)$, $X_a(p)$, $Y_a(p)$, $X_\delta(p)$ and $Y_\delta(p)$ were determined using tabulated integrals in Ref. [130]. As can be seen, we usually choose to represent the position space and the momentum space representation of a function using the same symbol.

3.3 Solution of the Dirac equation - Green's function

The Green's function of a fermion in a nuclear potential $G(\mathbf{x}, \mathbf{y}, E)$ is defined as [69]:

$$(E + i\boldsymbol{\alpha}\nabla - m\gamma^0 - V(\mathbf{x}))G(\mathbf{x}, \mathbf{y}, E) = \delta(\mathbf{x} - \mathbf{y}). \tag{3.21}$$

For a detailed discussion of the Green's function of a fermion in a Coulomb potential, see [123]. The Green's function can be represented as a sum over the entire spectrum of the Dirac Hamiltonian [69]:

$$G(E) = \sum_n \frac{|n\rangle\langle n|}{E - E_n}. \tag{3.22}$$

For simplicity, $\sum\limits_n$ usually refers to a sum over the principal quantum number n, the angular momentum quantum number κ and the angular momentum projection quantum number m, with the latter two just assumed implicitly. $|n\rangle$ are eigenstates of the Dirac Hamiltonian. The spectral representation in position space is [69]:

$$G(\mathbf{x}, \mathbf{y}, E) = \sum_n \frac{a_n(\mathbf{x})a_n^\dagger(\mathbf{y})}{E - E_n(1 - i\eta)}. \tag{3.23}$$

It can be expressed as a partial wave series [123]:

$$G(\mathbf{x_1}, \mathbf{x_2}, E) = \sum_{\kappa,m} \begin{pmatrix} g_{11\kappa}(r_1, r_2, E)\chi_{\kappa m}\chi_{\kappa m}^\dagger & g_{12\kappa}(r_1, r_2, E)\chi_{\kappa m}\chi_{-\kappa m}^\dagger \\ g_{21\kappa}(r_1, r_2, E)\chi_{-\kappa m}\chi_{\kappa m}^\dagger & g_{22\kappa}(r_1, r_2, E)\chi_{-\kappa m}\chi_{-\kappa m}^\dagger \end{pmatrix}. \tag{3.24}$$

For the point-like nuclear model, the four radial components $g_{ij\kappa}(r_1, r_2, E)$ can be expressed as products of confluent hypergeometric functions [123] or in terms of Whittaker functions [72]. We will also occasionally employ a slight modification of the Green's function: $S_F(\mathbf{x}, \mathbf{y}, E) = G(\mathbf{x}, \mathbf{y}, E)\gamma^0$ [69].

The free fermion Green's function can also be expressed as a partial wave series like equation (3.24), albeit with different radial functions [127]. Other known representations of the free-fermion Green's function are the momentum space representation (see textbooks on quantum field theory, e.g. [6]) and the position-space representation in closed analytical form (without partial wave expansion) (see Ref. [131]). Such representations are not known for the Green's function of a fermion in the Coulomb potential [131].

For a detailed discussion of the bound fermion's wavefunction and Green's function, see also refs. [125, 132–135].

3.4 Two-time Green's function method

A possible method to discuss energy levels in the Furry picture is the adiabatic S-matrix formalism. This method was developed by Gell-Mann, Low and Sucher (see refs. [136, 137]) and was widely used in g-factor calculations [138–141]. It is also described in some detail in the review articles abount bound-state QED by Mohr et al [127] and Beier [69]. A detailed derivation of this method can also be found in Ref. [142]. However,

there are certain doubts about the applicability of this theoretical framework in the renormalization of complex diagrams (see Ref. [68] for details).

In this thesis, we employed the two-time Green's function (TTGF) method [68] to compute energy shifts from Feynman diagrams. This approach is discussed in detail in Ref. [68]. See also Ref. [69] for a brief introduction to the two-time Green's function method. We are going to discuss this method here, closely following the derivation in Ref. [68], for the special case of a one-electron system. The two-time Green's function for the case of a one-electron ion or atom is defined as [68]

$$G(x_1, x_2) = \langle 0|T[\Psi(x_1)\overline{\Psi(x_2)}]|0\rangle\,. \tag{3.25}$$

Here, $|0\rangle$ is the vauum state. We perform the partial Fourier transform [68]:

$$\frac{1}{2\pi i}\int \mathrm{d}t_1 \int \mathrm{d}t_2 e^{i(Et_1 - E't_2)} G(t_1, \mathbf{x}_1, t_2, \mathbf{x}_2). \tag{3.26}$$

Here, we work in the Heisenberg picture, i.e. the time-evolution of operators is described by $\Psi(t_1, \mathbf{x}_1) = e^{iHt_1}\Psi(0, \mathbf{x}_1)e^{-iHt_1}$ [6]. Integrations over time variables are performed from $-\infty$ to $+\infty$ unless otherwise stated. The eigenvalues of the Hamiltonian H are E_n: $H|n\rangle = E_n|n\rangle$, where the eigenstates $|n\rangle$ form an orthonormal basis of the corresponding Hilbert space [68, 74]. We choose the energy of the vacuum state to be $E_0 = 0$ [68]. The time-ordered product in the expression for $G(x_1, x_1')$ is defined as [6]:

$$T[\Psi(t_1, x_1)\overline{\Psi(t_2, x_2)}] = \Theta(t_1 - t_2)\Psi(t_1, x_1)\overline{\Psi(t_2, x_2)} - \Theta(t_2 - t_1)\Psi(t_2, x_2)\overline{\Psi(t_1, x_1)}. \tag{3.27}$$

Inserting this into the expression for the partial Fourier transform, and using [68]

$$\int \mathrm{d}t_1 \int \mathrm{d}t_2 e^{i(E - E_n)t_1} e^{-i(E' - E_n)t_2}\Theta(t_1 - t_2) = \frac{2\pi i\delta(E - E')}{E - E_n + i\eta}, \tag{3.28}$$

$$\int \mathrm{d}t_1 \int \mathrm{d}t_2 e^{i(E + E_n)t_1} e^{-i(E' + E_n)t_2}\Theta(t_2 - t_1) = -\frac{2\pi i\delta(E - E')}{E + E_n - i\eta}, \tag{3.29}$$

we obtain [68]:

$$\frac{1}{2\pi i}\int \mathrm{d}t_1 \int \mathrm{d}t_2 e^{i(Et_1 - E't_2)} G(t_1, \mathbf{x}_1, t_2, \mathbf{x}_2) = \mathcal{G}(\mathbf{x}_1, \mathbf{x}_2, E)\delta(E - E'), \tag{3.30}$$

with

$$\mathcal{G}(\mathbf{x}_1, \mathbf{x}_2, E) = \sum_n \frac{\langle 0|\Psi(0, \mathbf{x}_1)|n\rangle\langle n|\overline{\Psi}(0, \mathbf{x}_2)|0\rangle}{E - E_n + i\eta} + \sum_n \frac{\langle 0|\overline{\Psi}(0, \mathbf{x}_2)|n\rangle\langle n|\Psi(0, \mathbf{x}_1)|0\rangle}{E + E_n - i\eta}. \tag{3.31}$$

In this derivation, we assumed the eigenenergies E_n to have an infinitesimal add-on [63]: $E_n \longrightarrow E_n - i\eta$. $\sum_n$ corresponds to a summation over the entire spectrum. We now

calculate the diagonal matrix element of $\mathcal{G}(\mathbf{x}_1, \mathbf{x}_2, E)$ with the reference state [68]. In our case, we consider only the ground state $|a\rangle$ as the reference state.

$$g_{aa}(E) = \langle a|\mathcal{G}(E)\gamma^0|a\rangle \tag{3.32}$$

Splitting the sum in the expression for $\mathcal{G}(E)$ into the reference-state contribution and a term due to the rest of the spectrum, we can express $g_{aa}(E)$ as follows [68]:

$$\begin{aligned} g_{aa}(E) =& \frac{\int \mathrm{d}^3x_1 \int \mathrm{d}^3x_2 a^\dagger(\mathbf{x}_1)\langle 0|\Psi(0,\mathbf{x}_1)|a\rangle\langle a|\overline{\Psi}(0,\mathbf{x}_2)|0\rangle\gamma^0 a(\mathbf{x}_2)}{E - E_a} \\ &+ (\text{terms regular at } E = E_a) \end{aligned} \tag{3.33}$$

Now, defining $A_a = \mathrm{d}^3x_1 \int \mathrm{d}^3x_2 a^\dagger(\mathbf{x}_1)\langle 0|\Psi(0,\mathbf{x}_1)|a\rangle\langle a|\overline{\Psi}(0,\mathbf{x}_2)|0\rangle\gamma^0 a(\mathbf{x}_2)$ and performing the following contour integrations in the complex E plane [68],

$$\frac{1}{2\pi i}\oint_\Gamma \mathrm{d}E g_{aa}(E) = A_a \tag{3.34}$$

$$\frac{1}{2\pi i}\oint_\Gamma \mathrm{d}E E g_{aa}(E) = E_a A_a, \tag{3.35}$$

using a closed contour Γ which encloses the reference-state energy, but no other eigenvalue of H, we obtain [68]

$$\frac{\frac{1}{2\pi i}\oint_\Gamma \mathrm{d}E E g_{aa}(E)}{\frac{1}{2\pi i}\oint_\Gamma \mathrm{d}E g_{aa}(E)} = E_a. \tag{3.36}$$

We thus see that the information about the exact energy level is contained in the exact but unknown two-time Green's function. In order to obtain the energy level perturbatively, we now assume that the Hamiltonian splits into two parts, $H = H^{(0)} + V$, where the spectrum of $H^{(0)}$ can be determined exactly. Taking into account that $E_a = E_a^{(0)} + \Delta E$, and a similar relation for $g_{aa} = g_{aa}^{(0)} + \Delta g_{aa}$, with $E^{(0)}$ corresponding to the "unperturbed" ground-state energy obtained via the Dirac equation, i.e. to the ground-state energy according to the Dirac Hamiltonian, we obtain the following expression for the energy shift ΔE [68]:

$$\Delta E = \frac{\frac{1}{2\pi i}\oint_\Gamma \mathrm{d}E (E - E_a^{(0)})\Delta g_{aa}(E)}{1 + \frac{1}{2\pi i}\oint_\Gamma \mathrm{d}E \Delta g_{aa}(E)}. \tag{3.37}$$

In order to compute perturbations to the energy level of the bound fermion, we need to consider all Feynman diagrams with exactly one incoming and one outgoing fermion line, representing the bound fermion. The interaction with the magnetic field is represented in Feynman diagrams by an external photon (wave) line terminated by a triangle [69]. Furthermore, there can be interactions between the bound fermion and the quantum photon field. This is shown schematically in Fig. 3.2, where the black box represents all such interaction processes. Terms without the magnetic interaction correspond to contributions

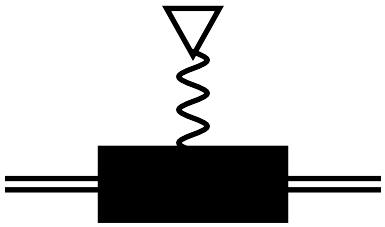

Figure 3.2: g-factor Feynman diagram for bound fermions: The incoming and outgoing double lines represent the bound fermion, the wave line terminated with a triangle represents the magnetic field [69]. The black box represents schematically all possible processes that can occur in Feynman diagrams with the previously mentioned building blocks.

to the Lamb shift and terms with one magnetic interaction correspond to corrections to the g-factor. We therefore consider the magnetic interaction perturbatively up to first order, i.e. only diagrams which contain zero or one magnetic interaction. Wick's theorem [143] dictates that all such diagrams contain an even number of interaction vertices between the bound fermion and the quantum photon field [6]. From equations (10.2) and (10.3) in Ref. [6], one can derive the following: a diagram with $2n$ vertices (which is of order e^{2n}) and which has no incoming or outgoing photon lines contains n closed loops, a diagram of order e^{2n+1} with one interaction with the magnetic potential contains n closed loops.

Both numerator and denominator of equation (3.37) can be expressed as series in powers of e. (Here, we deviate from the usual approach in the literature, where numerator and denominator are considered to be power series in α [68, 69].) Denoting a numerator and denominator contribution of order $\mathcal{O}\left(e^n\right)$ as Z_n and N_n, respectively, and expanding the expression for ΔE (3.37) in powers of e, we obtain:

$$\begin{aligned}\Delta E =& Z_1 + \\ & Z_2 + \\ & Z_3 - Z_1 N_2 + \\ & Z_4 - Z_2 N_2 + \\ & Z_5 - Z_3 N_2 - Z_2 N_3 - Z_1 N_4 - Z_1 N_2^2 + \\ & \mathcal{O}\left(e^6\right).\end{aligned} \tag{3.38}$$

$$\begin{aligned}\frac{1}{2\pi i}\oint_\Gamma \mathrm{d}E(E - E_a^{(0)})\Delta g_{aa}(E) &= \sum_{n=1}^{\infty} Z_n \\ \frac{1}{2\pi i}\oint_\Gamma \mathrm{d}E\Delta g_{aa}(E) &= \sum_{n=1}^{\infty} N_n\end{aligned} \tag{3.39}$$

Here, we already used the fact that $N_1 = 0$, which will be shown later. Furthermore, products of two terms with odd indices (e.g. $Z_1 N_3$) were ignored since such terms correspond to second order corrections in the magnetic interaction. In our approach, the order e^1 contribution corresponds to the tree-level g-factor diagram (Fig. 3.3), the e^2 contribution corresponds to the one-loop Lamb shift [69] (one closed loop or renormalization counterterm, no magnetic interaction, Fig. 4.1), the order e^3 corresponds to the one-loop g-factor correction [57, 69] (one closed loop or renormalization counterterm, one magnetic interaction, Fig. 4.2), the order e^4 contribution corresponds to the two-loop Lamb shift correction [63] (two closed loops or renormalization counterterms, no magnetic interaction) and the order e^5 contribution corresponds to the two-loop g-factor correction (two closed loops or renormalization counterterms, one magnetic interaction).

We see that the tree-level g-factor contribution and the one-loop Lamb shift correction consist only of "numerator terms". For the one-loop g-factor correction, we also need to take into account subtraction terms which correspond to products of lower-order (in perturbation theory) Feynman diagrams [69]. A similar subtraction term appears in the calculation of the two-loop correction to the Lamb shift. For the computation of the two-loop g-factor correction, various subtraction terms need to be taken into account.

To conclude this section, we briefly summarize the following procedure to determine the energy shift from Feynman diagrams:

- calculate the Two-time Green's function $G(x_1, x_2)$,
- perform the partial Fourier transform,
- calculate diagonal matrix elements with the reference state,
- perform contour integration.

We can compute the Green's function using Wick's theorem [143]. The relevant expressions for Wick contractions in bound-state QED are [69]:

$$\overbrace{\Psi(x)\bar{\Psi}}(y) = i \int \frac{\mathrm{d}E}{2\pi} e^{-iE(t_x - t_y)} S_F(\mathbf{x}, \mathbf{y}, E) \tag{3.40}$$

$$\overbrace{A_\mu(x_1) A_\nu}(x_2) = i \int \frac{\mathrm{d}\omega}{2\pi} e^{-i\omega(t_{x_1} - t_{x_2})} D_{\mu\nu}(\mathbf{x}_1, \mathbf{x}_2, \omega) \tag{3.41}$$

$D_{\mu\nu}(\mathbf{x}_1, \mathbf{x}_2, \omega)$ is the photon Green's function, as defined e.g. in Ref. [63, 72]. In this work, we employ the Feynman gauge [6, 72]. Three different useful representations of the photon Green's function are [63, 72]:

$$\begin{aligned} D_{\mu\nu}(\mathbf{x}_1, \mathbf{x}_2, \omega) &= g_{\mu\nu} \frac{\exp(i\sqrt{\omega^2 + i\eta} x_{12})}{4\pi x_{12}} \\ &= \int \frac{\mathrm{d}^3 q}{(2\pi)^3} \frac{-g_{\mu\nu} e^{i\mathbf{q}(\mathbf{x}_1 - \mathbf{x}_2)}}{\omega^2 - \mathbf{q}^2 + i\eta} \\ &= \int \frac{\mathrm{d}q}{2\pi^2} \frac{-g_{\mu\nu} |\mathbf{q}| \sin(|\mathbf{q}| x_{12})}{(\omega^2 - \mathbf{q}^2 + i\eta) x_{12}}. \end{aligned} \tag{3.42}$$

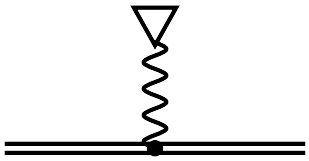

Figure 3.3: Tree-level g-factor diagram corresponding to the Dirac value $g_{\rm D}$ [69].

Here, $x_{12} = |\mathbf{x}_1 - \mathbf{x}_2|$ and $\mathrm{Im}(\sqrt{\omega^2 + i\eta}) > 0$. We will also occasionally use the function $D(\mathbf{x}_1, \mathbf{x}_2, \omega)$ to represent the photon propagator, defined by [63]

$$D_{\mu\nu}(\mathbf{x}_1, \mathbf{x}_2, \omega) = g_{\mu\nu} D(\mathbf{x}_1, \mathbf{x}_2, \omega). \tag{3.43}$$

3.5 Dirac value of the bound-electron g-factor

We will now demonstrate the two-time Green's function formalism using the least complicated Feynman diagram as an application, the tree-level g-factor diagram shown in Fig. 3.3. See also Ref. [68, 69] The Green's function corresponding to this diagram is:

$$G(x_1, x_2) = -ie \int \mathrm{d}^4x \langle 0|T\Psi(x_1)\overline{\Psi}(x_2)\overline{\Psi}(x)\gamma^\mu A_{m_\mu}(x)\Psi(x)|0\rangle. \tag{3.44}$$

Inserting explicit expressions for Wick contractions and using the time-independence of the magnetic potential, we obtain:

$$\begin{aligned} G(x_1, x_2) = &- ie \int \mathrm{d}^4x\, i \int \frac{\mathrm{d}E}{2\pi} e^{-iE(t_1 - t_x)} S_F(\mathbf{x}_1, \mathbf{x}, E)\gamma^\mu A_{m_\mu}(\mathbf{x}) \\ & i \int \frac{\mathrm{d}E}{2\pi} e^{-iE(t_x - t_2)} S_F(\mathbf{x}, \mathbf{x}_2, E). \end{aligned} \tag{3.45}$$

In this expression, we can identify a Dirac delta function [6] $\delta(E - E') = \int \frac{\mathrm{d}t_x}{2\pi} e^{i(E-E')t_x}$. Carrying out the integration over one energy variable, we obtain the final expression for the Green's function.

$$G(x_1, x_2) = ie \int \mathrm{d}^3x \int \frac{\mathrm{d}E}{2\pi} e^{-ie(t_1 - t_2)} S_F(\mathbf{x}_1, \mathbf{x}, E)\gamma^\mu A_{m_\mu}(\mathbf{x}) S_F(\mathbf{x}, \mathbf{x}_2, E) \tag{3.46}$$

In the next step, we have to carry out the partial Fourier transform $\frac{1}{2\pi i} \int \mathrm{d}t_1 \int \mathrm{d}t_2 e^{iEt_1} e^{-iE't_2} G(x_1, x_2)$. Inserting the above Green's function into this expression, we can identify a delta function as it was done above. We obtain the following:

$$\begin{aligned} &\frac{1}{2\pi i} \int \mathrm{d}t_1 \int \mathrm{d}t_2 e^{iEt_1} e^{-iE't_2} G(x_1, x_2) \\ =&\delta(E - E') e \int \mathrm{d}^3x S_F(\mathbf{x}_1, \mathbf{x}, E)\gamma^\mu A_{m_\mu}(\mathbf{x}) S_F(\mathbf{x}, \mathbf{x}_2, E). \end{aligned} \tag{3.47}$$

In the next step, we calculate the diagonal matrix element of the above expression (without the delta function factor) with the reference state wave function. In our case, the reference state is the ground state. Using the spectral representation for the Green's functions, $S_F(\mathbf{x},\mathbf{y},E) = \sum_n \frac{a_n(\mathbf{x})\overline{a}_n(\mathbf{y})}{E-E_n}$, we obtain the following expression for $g_{aa}(E)$:

$$g_{aa}(E) = \int \mathrm{d}^3x_1 \int \mathrm{d}^3x_2 a^\dagger(\mathbf{x}_1) e \int \mathrm{d}^3x \sum_{n_1} \frac{a_{n_1}(\mathbf{x}_1)\overline{a}_{n_1}(\mathbf{x})}{E-E_{n_1}} \gamma^\mu A_{m_\mu}(\mathbf{x}) \sum_{n_2} \frac{a_{n_2}(\mathbf{x})\overline{a}_{n_2}(\mathbf{x}_2)}{E-E_{n_2}} \gamma^0 a(\mathbf{x}_2). \tag{3.48}$$

Using the orthogonality of different eigenstates [74], $\langle n|a\rangle = \delta_{na}$[1], we obtain:

$$g_{aa}(E) = \frac{e\int \mathrm{d}^3x \overline{a}(\mathbf{x})\gamma^\mu A_{m_\mu}(\mathbf{x}) a(\mathbf{x})}{(E-E_a)^2}. \tag{3.49}$$

Now we can determine the expressions for Z_1 and N_1. Schematically, the contour integrations can be expressed as follows [69]:

$$\frac{1}{2\pi i}\oint \mathrm{d}z \frac{f(z)}{z} = f(0), \tag{3.50}$$

$$\frac{1}{2\pi i}\oint \mathrm{d}z \frac{f(z)}{z^2} = f'(0), \tag{3.51}$$

$$\frac{1}{2\pi i}\oint \mathrm{d}z \frac{f(z)}{z^3} = \frac{f''(0)}{2}. \tag{3.52}$$

Here, $f(z)$ is assumed to be regular at $z = z_0$. The integration path is a closed path around $z = 0$. For the tree-level Feynman diagram, we find [69]

$$Z_1 = \int \mathrm{d}^3x \overline{a}(\mathbf{x})\gamma^\mu e A_{m_\mu}(\mathbf{x}) a(\mathbf{x}) =: \Delta E_{\mathrm{mag}}, \tag{3.53}$$

and, since there is no energy-dependent term in the numerator of $g_{aa}(E)$, $N_1 = 0$. This justifies the omission of N_1 in the perturbative expansion of ΔE, equation (3.38). Z_1 is the energy shift due to the magnetic field to first order of perturbation theory which could also have been obtained from the formalism of relativistic quantum mechanics [69]. We can insert the known expressions for the ground state wave functions into equation (3.53) to obtain:

$$\Delta E_{\mathrm{mag}} = -i \int \mathrm{d}^3x f(r) g(r) \frac{Bier\sin^2(\Theta)}{4\pi}. \tag{3.54}$$

[1] $\sum_n$ refers to a sum over all quantum numbers. Therefore, the Kronecker delta is to be understood as a product of several Kronecker deltas, one for each quantum number.

Carrying out the integration over the angular variables and using equation (2.5), we obtain the following expression for the g-factor contribution [69]:

$$g_{\rm D} = -\frac{8m}{3}\int\limits_0^\infty {\rm d}r r^3 f(r) g(r). \tag{3.55}$$

For the model of a point-like nuclear charge distribution, the radial wave functions are known analytically and the remaining integration can be carried out to yield the so-called Dirac value of the bound-fermion g-factor which was first derived by G. Breit in 1928 [144]:

$$g_{\rm D} = \frac{2}{3} + \frac{4}{3}\sqrt{1-(Z\alpha)^2}. \tag{3.56}$$

For a more detailed derivation, see also Ref. [145]. As can be expected, for the free-fermion limit, i.e. $Z \longrightarrow 0$, we obtain the free-fermion value [6] $g_{\rm D} \overset{Z\to 0}{\longrightarrow} 2$. We see that the leading g-factor contribution is modified by binding corrections [56].

3.6 Nuclear effects on the bound-electron g factor

By using the Coulomb potential, we made three approximations. The static Coulomb potential corresponds to the approximation of an infinitely heavy nucleus. Furthermore, the nucleus is assumed to be point-like. Finally, vacuum polarization effects lead to further modifications of the nuclear potential. In this Chapter, we discuss the effects due to the finite size and finite mass of the nucleus. Vacuum polarization corrections will be discussed in the next Chapter along with other radiative corrections.

3.6.1 Finite-size effect

The finite size (FS) of the atomic nucleus causes the interaction potential between the nucleus and the fermion to deviate from the Coulomb potential on the femtometer scale, which in turn modifies the wavefunction of the bound fermion [69, 146], and, consequently, a correction $\Delta g_{\rm FS}$ to its g-factor. This effect can be approximated as (see [99, 147, 148]):

$$\Delta g_{\rm FS} = \frac{8m_{\rm f}^2}{3}(Z\alpha)^4\langle r^2\rangle + \mathcal{O}\left((Z\alpha)^6\right). \tag{3.57}$$

Accurate analytical formulas for the determination of the FS effect on the binding energy were developed in Ref. [149]. Using a method described in Ref. [150], these formulas can be adjusted for the computation of the FS correction to the g-factor. An analytical treatment of the FS correction to the g-factor was also performed in Ref. [147]. The FS effect can also be determined numerically using equation (3.55) with wavefunctions determined numerically [151] for an extended nuclear charge distribution.

The theoretical uncertainty of the FS effect is due to the uncertainty of the root mean square radius $\sqrt{\langle r^2\rangle}$ of the nucleus and to the uncertainty of the nuclear charge

distribution model used (see also Ref. [54]). Nuclear radii can be found e.g. in Ref. [152–158]. The uncertainty of the FS effects defines the limit of the theoretical accuracy achievable in g-factor predictions.

If QED is assumed to be correct, one can use the experimental fine-structure transition energies [159] or g-factor values to g-factor value to determine the nuclear radius. In this case, the theoretical g-factor value would be computed with the nuclear radius as a free parameter. The free parameter would be fitted in such a way that the total theoretical g-factor matches the experimental value. This requires all other contributions to the theoretical value of the g-factor to be known with sufficient accuracy. Such an investigation was performed for the g-factor of hydrogenlike $^{28}Si^{13+}$ [33]. In this investigation, a nuclear radius of 3.18(15) fm was found which is in agreement with the literature value 3.1223(24) fm cited in Ref. [33]. This shows that it is in principle possible to determine nuclear radii from g-factor measurements.

The muon's Bohr orbital is approx. 200 times smaller than that of the electron [75], and, therefore, the FS correction is much larger for bound muons than for bound electrons.

3.6.2 Finite-mass effect

Calculations of the bound-fermion g-factor are usually performed in the Furry picture which uses a static external potential to describe the nucleus. This corresponds to the approximation of an infinitely large nuclear mass. The correction to the g-factor due to the finite nuclear mass is called recoil contribution. It can be parametrized as an expansion in powers of $Z\alpha$, α and the ratio $\frac{m_\mathrm{f}}{M_\mathrm{nucl}}$ of fermion and nuclear mass [69].

$$\delta g_\mathrm{recoil} = (Z\alpha)^2 \left(\frac{m_\mathrm{f}}{M_\mathrm{nucl}}\right) - \frac{1}{3}(Z\alpha)^2 \left(\frac{\alpha}{\pi}\right) \left(\frac{m_\mathrm{f}}{M_\mathrm{nucl}}\right) + \cdots \tag{3.58}$$

Quantum mechanical calculations which take into account the finite nuclear mass have been performed in e.g. Ref. [160–164]. The QED theory of the nuclear recoil to all orders in $Z\alpha$ was developed in Ref. [165, 166].

The order $\frac{m_\mathrm{f}}{M_\mathrm{nucl}}$-contribution to the leading Feynman diagram can be computed to all orders in $(Z\alpha)$ according to [167]. Contributions to the leading diagram of order $\left(\frac{m_\mu}{M_\mathrm{nucl}}\right)^2$ and higher can be computed to first order in $(Z\alpha)$ [168]. Recoil corrections to loop diagrams (radiative recoil) can be computed using formulas from Ref. [69]. Nuclear masses can be computed using data from e.g. Ref. [169–173].

3.6.3 Nuclear deformation and polarization

Closely related to the FS effect is an additional correction in the case of a nuclear charge distribution which is not spherically symmetric. The g-factor correction due to the deviation of the shape of a nucleus from spherical symmetry (the so-called nuclear deformation (ND) correction) was investigated in great detail in Ref. [148, 174].

There are also contributions to the bound-fermion g-factor due to the nucleus exchanging virtual photons with the bound fermion, undergoing excitation in the process

[69]. Such Nuclear polarization (NP) effects to atomic energy levels were investigated in Ref. [175, 176]. The contribution to the bound-electron g-factor due to nuclear polarization was investigated in Ref. [177, 178]. NP constitutes another nuclear effect which limits the total accuracy of theoretical g-factors, especially in the case of heavy elements [177].

4 One-loop quantum electrodynamic corrections

In this Chapter, we explain one-loop radiative corrections to the bound-fermion g-factor. Before turning our attention to the g-factor, we use the one-loop self-energy correction to the Lamb shift in order to demonstrate the cancellation of a certain class of renormalization counterterms in bound-state QED calculations. We then explain the one-loop self-energy correction to the bound-fermion g-factor in detail. After illustrating the determination of all contributions with the two-time Green's function method, we explain the cancellations of UV divergences in this contribution in some detail. We then explain the methods used to compute the one-loop self-energy correction to the g-factor numerically. After the discussion of the one-loop self-energy correction, we rederive the formal expressions of previously mentioned radiative corrections using the framework of energy-dependent perturbation theory. After this, we discuss one-loop vacuum polarization corrections to the bound-fermion g-factor. We will focus on the case where the virtual particle is different from the bound fermion.

4.1 One-loop Lamb shift

We now turn to the Feynman diagrams contributing to Z_2 and N_2, as defined in equation (3.38). Z_2 corresponds to the one-loop correction to the Lamb shift and N_2 will be relevant for g-factor calculations [69]. Not taking into account renormalization counterterms, there are two diagrams contributing to Z_2, shown in Fig. 4.1:

- Self-energy (SE): interaction of the electron with the photon field;
- Vacuum polarization (VP): creation of a virtual charged particle-antiparticle pair.

In this section, we investigate only the SE diagram and the corresponding SE counterterms. It is our goal to illustrate that all contributions due to the renormalization counterterms δ_1 and δ_2 from the Lagrangian (3.1) cancel. First, we investigate the contribution due to the δ_1 counterterm diagram. The corresponding interaction term in the Lagrangian (3.1) is $-e\delta_1\overline{\Psi}_r\gamma^\mu\Psi_r A_{e_\mu}$. Using the same procedure as in the previous Chapter, we derive the following expression for $g_{aa}(E)$:

$$g_{aa,\delta_1}(E) = \frac{e\delta_1 \int \mathrm{d}^3x \overline{a}(\mathbf{x})\gamma^0 V(\mathbf{x})a(\mathbf{x})}{(E-E_a)^2}. \tag{4.1}$$

Figure 4.1: Feynman diagrams representing the one-loop Lamb shift: self-energy (left) and vacuum polarization (right) [69].

From this, we derive the following contributions to Z_2 and N_2:

$$Z_{2,\delta_1} = e\delta_1 \int \mathrm{d}^3x a^\dagger(\mathbf{x})V(\mathbf{x})a(\mathbf{x}), \tag{4.2}$$

$$N_{2,\delta_1} = 0. \tag{4.3}$$

For the other counterterm contribution (corresponding to the interaction term $\overline{\Psi}_r(i\delta_2\partial\!\!\!/ - \delta_m)\Psi_r$ in the Lagrangian (3.1)), we obtain the following expression for $g_{aa}(E)$:

$$g_{aa,\delta_2}(E) = \frac{-\int \mathrm{d}^3x \overline{a}(\mathbf{x}) \left(\delta_2(E-E_a)\gamma^0 + \gamma^0 V(\mathbf{x})\delta_2 + \delta m\right) a(\mathbf{x})}{(E-E_a)^2}. \tag{4.4}$$

In the derivation of $g_{aa\delta_2}(E)$, we used the Dirac equation [69] $(-i\boldsymbol{\alpha}\nabla + m\gamma^0 + V(\mathbf{x}))a(\mathbf{x}) = E_a a(\mathbf{x})$, and (see Ref. [6]) $\delta_m = m\delta_2 - \delta m$. Note that δ_m and δm are different. We will define the mass counterterm δm in the following section. The corresponding contributions to Z_2 and N_2 are:

$$Z_{2,\delta_2} = -\delta_2 \int \mathrm{d}^3x a^\dagger(\mathbf{x})V(\mathbf{x})a(\mathbf{x}) - \int \mathrm{d}^3x \overline{a}(\mathbf{x})\delta m a(\mathbf{x}), \tag{4.5}$$

$$N_{2,\delta_2} = -\delta_2. \tag{4.6}$$

Adding the two counterterm contributions to Z_2 and taking into account the identity $\delta_1 = \delta_2$ [6], we obtain:

$$Z_{2,\delta_1} + Z_{2,\delta_2} = -\int \mathrm{d}^3x \overline{a}(\mathbf{x})\delta m a(\mathbf{x}). \tag{4.7}$$

We observe that, within Z_2, the contributions due to the counterterm δ_1 cancel. Keeping in mind that Z_2 corresponds to the complete one-loop Lamb shift correction, we conclude that there is no δ_1 counterterm contribution to the one-loop Lamb shift. In a similar way, one can show that all δ_1 counterterm contributions cancel in $Z_3 - Z_1N_2$, i.e. the one-loop g-factor corrections as well as in $Z_4 - Z_2N_2$ (two-loop Lamb shift correction) and $Z_5 - Z_3N_2 - Z_2N_3 - Z_1N_4 - Z_1N_2^2$ (two-loop g-factor correction), although the number of contributing diagrams is much higher in these cases. In the latter two cases, this holds true both for the order $\mathcal{O}\left(e^2\right)$ and the order $\mathcal{O}\left(e^4\right)$ contributions to the counterterm

δ_1. The cancellation of all δ_1 counterterm contributions to the two-loop SE correction to the g-factor served as an important consistency check for our two-loop calculations. For a discussion of renormalization and bound states in QFT, see als o Ref. [179][1].

The actual one-loop self-energy diagram gives the following contributions to Z_2 and N_2 (see equation (3.38)): [69, 72]

$$Z_{2,\mathrm{SE}} = 2i\alpha \int \mathrm{d}^3x \int \mathrm{d}^3y \int \mathrm{d}\omega a^\dagger(\mathbf{x})\alpha^\mu G(\mathbf{x},\mathbf{y},E_a-\omega)\alpha^\nu a(\mathbf{y}) D_{\mu\nu}(\mathbf{x},\mathbf{y},\omega), \tag{4.8}$$

$$N_{2,\mathrm{SE}} = 2i\alpha \int \mathrm{d}^3x \int \mathrm{d}^3y \int \mathrm{d}\omega a^\dagger(\mathbf{x})\alpha^\mu \left.\frac{\partial G(\mathbf{x},\mathbf{y},E-\omega)}{\partial E}\right|_{E_a} \alpha^\nu a(\mathbf{y}) D_{\mu\nu}(\mathbf{x},\mathbf{y},\omega). \tag{4.9}$$

Using the following definition of the self-energy function [63],

$$\Sigma(\mathbf{x}_1,\mathbf{x}_2,E) = 2i\alpha\gamma^0 \int_{-\infty}^{\infty} \mathrm{d}\omega \alpha^\mu G(\mathbf{x}_1,\mathbf{x}_2,E-\omega)\alpha^\nu D_{\mu\nu}(\mathbf{x}_1,\mathbf{x}_2,\omega), \tag{4.10}$$

we can write the total self-energy contributions to Z_2 and N_2 as [57, 69]

$$Z_{2,\mathrm{SE}} = \langle a|\gamma^0\Sigma|a\rangle, \tag{4.11}$$

$$N_{2,\mathrm{SE}} = \langle a|\gamma^0 \left.\frac{\partial\Sigma}{\partial E}\right|_{E_a} |a\rangle. \tag{4.12}$$

Keeping the counterterm contributions in mind, we see that the self-energy function is accompanied by the mass renormalization term δm. It can be shown that every self-energy function is accompanied by a mass renormalization term in the cases of the one-loop g-factor correction [57, 69] and the two-loop self-energy corrections to the Lamb shift [63]. Our analysis of the two-loop SE correction to the g-factor showed the same occurence of an SE function along with the mass counterterm in all cases. Therefore, we can assume mass renormalization implicitly, i.e. consider the "mass renormalized" self-energy function $\widetilde{\Sigma} := \Sigma - \delta m$ instead of Σ. This will be applied to both the order $\mathcal{O}\left(e^2\right)$ and the order $\mathcal{O}\left(e^4\right)$ mass counterterms δm and $\delta m^{(2)}$.

The one-loop SE correction to the Lamb shift has been studied extensively in the literature. See e.g. Ref. [72, 131, 180–185].

4.2 One-loop self-energy correction to the g-factor

The one-loop SE correction to the g-factor has been investigated in detail in the literature, e.g. [57, 64, 69, 139–141, 186–189]. The one-loop diagrams representing Z_3 (as defined in equation (3.38)) are shown in Fig. 4.2 [69]:

- **SE-ver**: self-energy vertex correction

[1] The submission history suggests that this paper was uploaded in 2005, while the date found in the paper is 2013.

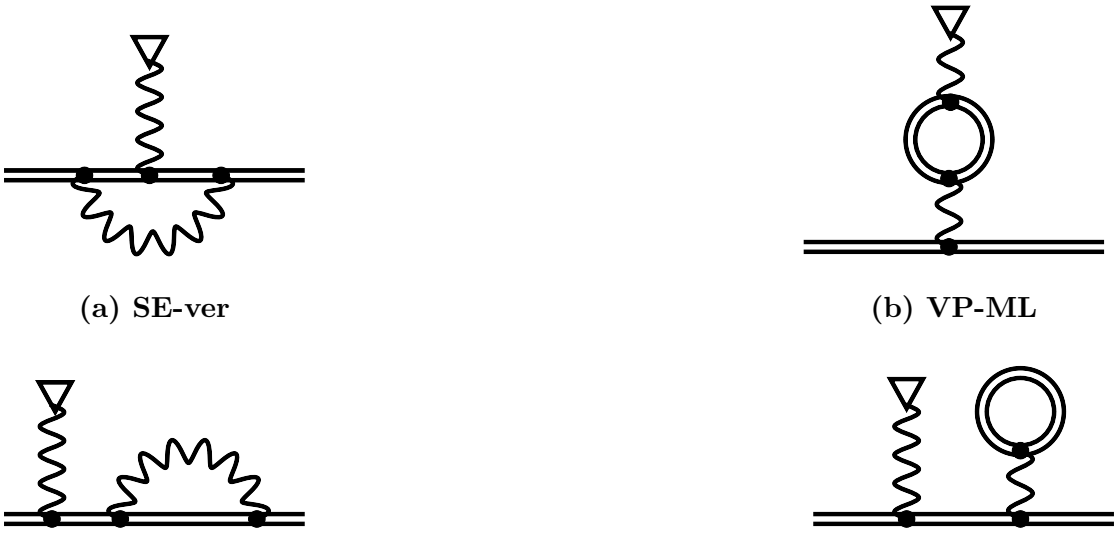

(a) SE-ver **(b) VP-ML**

(c) SE-wf **(d) VP-EL**

Figure 4.2: One-loop Feynman diagrams contributing to the bound-fermion g-factor: self-energy vertex correction (a), magnetic loop vacuum polarization correction (b), self-energy wavefunction correction (c) and the electric loop vacuum polarization correction (d) [69].

- **SE-wf**: modification of the fermion wave function due to the fermion's interaction with the photon field (self-energy)
- **VP-EL**: modification of the nuclear potential due to vacuum polarization
- **VP-ML**: influence of vacuum polarization on the interaction with the magnetic field

4.2.1 One-loop self-energy diagrams

We now investigate the one-loop self-energy contribution to the g-factor. Following the discussion of the one-loop SE correction to the Lamb shift, we can ignore the contributions due to the counterterm δ_2, since all such contributions cancel in the sum. Furthermore, we can assume mass renormalization implicitly, i.e. replace every one-loop SE function Σ by $\widetilde{\Sigma} = \Sigma - \delta m$ [57].

In principle, there are two SE diagrams with the magnetic interaction inserted in the external fermion lines, with the magnetic interaction in the left and right external fermion line (Fig. 4.2 (c)). However, both diagrams give the same contribution. We therefore consider only one of these diagrams and multiply its g-factor contribution by a factor of 2.

The diagram with the magnetic interaction inserted in the internal fermion line (Fig. 4.2 (a)) is called the vertex diagram. Using the two-time Green's function method, we obtain the following contribution to Z_3 [57, 69]:

$$\begin{aligned} Z_{3,\mathrm{ver}} = \Delta E_{\mathrm{ver}} =& \langle a|\gamma^0\Gamma^\mu eA_{m\mu}|a\rangle \\ =& \int \mathrm{d}^3x_1 \int \mathrm{d}^3x_2 \int \mathrm{d}^3x_3 a^\dagger(\mathbf{x}_1)\gamma^0\Gamma^\mu(\mathbf{x}_1,\mathbf{x}_2,\mathbf{x}_3,E_a,E_a)eA_{m\mu}(\mathbf{x}_2)a(\mathbf{x}_3), \end{aligned} \tag{4.13}$$

where the one-loop vertex function $\Gamma^\mu(\mathbf{x}_1,\mathbf{x}_2,\mathbf{x}_3,E_a,E_a)$ is defined as [63]:

$$\begin{aligned} \Gamma^\rho(\mathbf{x}_1,\mathbf{x}_2,\mathbf{x}_3,E_1,E_2) =& 2i\alpha\gamma^0 \int_{-\infty}^{\infty} \mathrm{d}\omega \alpha^\mu G(\mathbf{x}_1,\mathbf{x}_2,E_1-\omega)\alpha^\rho G(\mathbf{x}_2,\mathbf{x}_3,E_2-\omega)\alpha^\nu \\ & D_{\mu\nu}(\mathbf{x}_1,\mathbf{x}_3,\omega). \end{aligned} \tag{4.14}$$

Performing the two-time Green's function approach for the other one-loop SE diagrams (Fig. 4.2 (c)), we obtain the following expression for $g_{aa}(E)$ [68, 69]:

$$\begin{aligned} g_{aa,\mathrm{SE,wf}} =& 2ie^3 \int \mathrm{d}^3x \int \mathrm{d}^3y \int \mathrm{d}^3z \int \frac{\mathrm{d}\omega}{2\pi} \sum_{n,n\neq a} \\ & \frac{\overline{a}(\mathbf{x})\gamma^\mu S_F(\mathbf{x},\mathbf{y},E-\omega)\gamma^\nu a_n(\mathbf{y})\overline{a}_n(\mathbf{z})\gamma^\rho A_{m_\rho}(\mathbf{z})a(\mathbf{z})D_{\mu\nu}(\mathbf{x},\mathbf{y},\omega)}{(E-E_a)^2(E-E_n)}. \end{aligned} \tag{4.15}$$

Note that angular momentum conservation dictates that $m_n = m_a$. In order to determine the energy shift, we have to distinguish between the cases $E_n \neq E_a$ and $E_n = E_a$ in the spectral representation of the Green's function between the SE loop and the magnetic interaction, i.e. whether the energy level is different from the ground-state energy or identical to it. As it is done in the literature (e.g. [57, 69]), we call these two contributions the irreducible and reducible contributions, respectively. The irreducible contribution to Z_3 is [57, 69]:

$$\Delta E_{\mathrm{irred}} = Z_{3,\mathrm{irred}} = 2\langle a|\gamma^0\Sigma|\delta a\rangle. \tag{4.16}$$

Here, $|\delta a\rangle$ is the wave function perturbed linearly by the magnetic field, defined in Chapter 3, equation (3.7).

The reducible energy shift can be represented as a product of two lower-order perturbation theory contributions as follows [69]:

$$Z_{3,\mathrm{red}} = 2\Delta E_{\mathrm{mag}}\langle a|\gamma^0 \left.\frac{\partial\Sigma_i}{\partial E}\right|_{E_a} |a\rangle\,. \tag{4.17}$$

ΔE_{mag} is the energy shift that corresponds to the Dirac value g_{D}, see equation 3.53. We also need to take into account the subtraction term $-Z_1 N_2$. Using the expressions for Z_1 and N_2 from equations (3.53) and (4.9), we obtain [69]:

$$-Z_1 N_2 = -\Delta E_{\mathrm{mag}} \langle a|\gamma^0 \left.\frac{\partial \Sigma_i}{\partial E}\right|_{E_a} |a\rangle \,. \tag{4.18}$$

We see that those two terms (4.17) and (4.18) partially cancel each other [69]:

$$\Delta E_{\mathrm{red}} = \Delta E_{\mathrm{mag}} \langle a|\gamma^0 \left.\frac{\partial \Sigma}{\partial E}\right|_{E_a} |a\rangle \,. \tag{4.19}$$

One can see that the reducible contribution from Z_3 can be represented as a product of diagrams, multiplied by a factor of two because of identical contributions coming from two equivalent diagrams. The subtraction term ensures that the product term appears only once in the final expression. Such partial cancellations will also occur in the two-loop SE correction to the g-factor, as will be discussed in Chapter 6.

4.2.2 Renormalization

We now discuss the regularization of ultraviolet (UV) divergences in the one-loop g-factor correction. Both the one-loop SE and vertex functions are UV divergent. In order to deal with UV divergences, we expand the internal fermion line in the SE loop in powers of interactions with the nuclear potential. This approach is discussed in great detail in the literature e.g. [57, 69, 72, 190, 191].

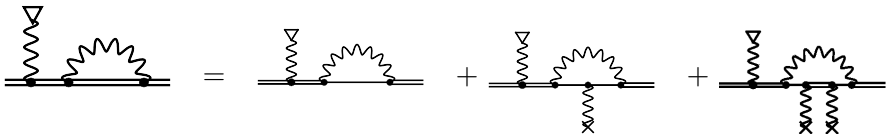

Figure 4.3: Decomposition of the SE-wavefunction correction to the g-factor correction into zero-, one-, and many-potential terms [69]. A single line stands for a free Dirac electron propagator.

The self-energy loop with a free internal fermion line and with n interactions between the internal electron line and the nuclear potential is called the n-potential contribution [72]. Using the superficial degree of divergence d, as defined in Ref. [6], we conclude that the zero- and one-potential diagrams are UV divergent and all n-potential diagrams with $n \geq 2$ do not contain UV divergences. Therefore, the irreducible contribution is expanded in the zero-potential, the one-potential and the many-potential contribution. Many in this case means two or more. The self-energy function Σ is expanded as $\Sigma = \Sigma^{(0)} + \Sigma^{(1)} + \Sigma^{(2+)}$, where the superscript $^{(n)}$ indicates n interactions with the nuclear potential. The zero-potential contribution to the g-factor reads

$$\Delta E^{(0)}_{\mathrm{irred}} = 2\langle \delta a|\gamma^0 \Sigma^{(0)}|a\rangle \,. \tag{4.20}$$

The zero-potential contribution to the one-loop SE function can be computed in momentum space using dimensional regularization [6] in $D = 4 - 2\epsilon$ dimensions [63, 72]:

$$\Sigma^{(0)}(p) = \delta m + B^{(1)}(\not{p} - m_{\rm f}) + \Sigma^{(0)}_{\rm R}(p). \tag{4.21}$$

The mass counterterm is $\delta m = \Sigma^{(0)}(m_{\rm f}) = \frac{\alpha C_\epsilon}{4\pi\epsilon}\frac{3-2\epsilon}{1-2\epsilon} m_{\rm f}$,
$B^{(1)} = -\frac{\alpha C_\epsilon}{4\pi\epsilon}$ and $C_\epsilon = \Gamma(1+\epsilon)(4\pi)^\epsilon \left(\frac{\mu^2}{m_{\rm f}^2}\right)^\epsilon$. Analytic formulas for the renormalized part of the free one-loop SE function are given in the appendix of Ref. [72], the computation of the SE function in $D = 4 - 2\epsilon$ dimensions is described in detail in the appendix of Ref. [63]. As discussed before, the contribution due to δm can be ignored because it is removed by mass renormalization. The finite remainder which needs to be calculated numerically can be expressed as [69]

$$\Delta g^{(0)}_{\rm SE,wf,irred,ren} = -\frac{8 m_{\rm f}}{3} \langle \delta a | \gamma^0 \Sigma_{\rm R} | a \rangle \,. \tag{4.22}$$

The one-potential contribution can be expressed in terms of the vertex function of free QED [6], $\Sigma^{(1)} = \Gamma^{(0)0} V$, where $\Gamma^{(0)0}$ corresponds to the vertex function defined in equation (4.14), with the full fermion Green's functions replaced by free fermion Green's functions.

$$\Delta E^{(1)}_{\rm irred} = 2 \langle \delta a | \gamma^0 \Gamma^{(0)0} V | a \rangle \,. \tag{4.23}$$

The vertex function of free QED can be separated into a UV divergent constant and a finite remainder [57]:

$$\Gamma^{(0)\mu}(p', p) = \frac{\alpha C_\epsilon}{4\pi\epsilon} \gamma^\mu + \Gamma^{(0)\mu}_{\rm R}(p', p) \,. \tag{4.24}$$

The g-factor contribution due to the first term can be represented as

$$\Delta g^{(1)}_{\rm SE,wf,irred,div} = -\frac{8 m_{\rm f}}{3} \langle \delta a | \frac{\alpha C_\epsilon}{4\pi\epsilon} V | a \rangle \,. \tag{4.25}$$

The g-factor contribution due to the divergent contribution to the zero-potential term is (see equations (4.20) and (4.21)):

$$\Delta g^{(1)}_{\rm SE,wf,irred,div} = \frac{8 m_{\rm f}}{3} \langle \delta a | \frac{\alpha C_\epsilon}{4\pi\epsilon} V | a \rangle \,. \tag{4.26}$$

Here, we used the Dirac equation in momentum space (see Ref. [72]):

$$(\not{p} - m_{\rm f}) a(\mathbf{p}) = \int \frac{{\rm d}^3 p'}{(2\pi)^3} \gamma^0 V(\mathbf{p} - \mathbf{p}') a(\mathbf{p}'). \tag{4.27}$$

We see that the charge divergent contributions from the zero- and one-potential contributions cancel each other [72].

The g-factor contribution due to the finite remainder is [69] (see equations (4.23) and (4.24))

$$\Delta g^{(1)}_{\rm SE,wf,irred,ren} = -\frac{8 m_{\rm f}}{3} \langle \delta a | \gamma^0 \Gamma^{(0)0}_{\rm R} V | a \rangle \,. \tag{4.28}$$

The reducible g-factor contribution can be calculated by performing straightforward derivatives of the SE function [69].

$$\Delta g_{\rm red} = g_{\rm D}\,\frac{\partial}{\partial E}\langle a|\gamma^0\Sigma(E)|a\rangle\Big|_{E=E_a}\,. \tag{4.29}$$

It can be separated in principle into the zero-, one- and many-potential parts. However, taking the derivative with respect to energy of the one-loop vertex function, we see that the divergent constant is cancelled. Therefore, the one-potential contribution to the reducible diagram is finite and does not need to be separated [69]. The many-potential term (many, in this case, means one or more), just as in the case of the SE wavefunction correction, does not contain UV divergences. Taking the derivative of the zero-potential contribution to the one-loop SE function, we obtain (see equation (4.21)):

$$\frac{\partial\Sigma^{(0)}}{\partial E}\bigg|_{E_a} = -\frac{\alpha C_\epsilon}{4\pi\epsilon}\gamma^0 \;+ (\text{UV finite terms}). \tag{4.30}$$

The g-factor contribution due to the divergent term is:

$$g_{\rm red,div} = -\frac{\alpha C_\epsilon}{4\pi\epsilon} g_{\rm D}. \tag{4.31}$$

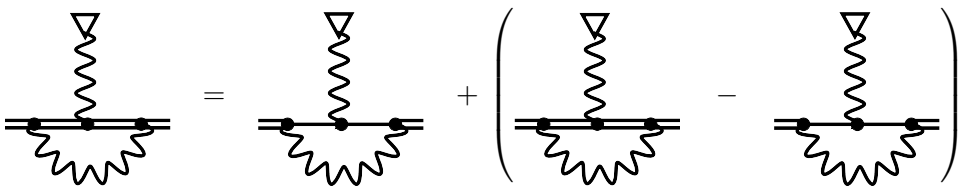

Figure 4.4: Separation of the SE vertex diagram into the zero- and many-potential terms [69].

The SE vertex correction is given in equation (4.13). We again expand this diagram in powers of interactions with the nuclear potential. Analyzing the superficial degree of divergence [6] in this case, we find that the vertex diagram with at least one interaction with the nuclear potential does not contain UV divergences [69]. Therefore, we separate the vertex diagram into the zero- and the many-potential contributions (see Fig. 4.4). Many, in this case, means one or more. Inserting expression (4.24) into the expression for the vertex diagram, we find the following divergent g-factor contribution:

$$g_{\rm ver,div} = \frac{\alpha C_\epsilon}{4\pi\epsilon} g_{\rm D}. \tag{4.32}$$

The UV divergent contribution of the vertex diagram cancels the UV divergent part of the reducible SE diagram [69]. We thus see that all charge divergences in the one-loop SE contribution to the g-factor cancel.

4.2.3 Evaluation of the individual terms

Since the UV regularization is carried out in momentum space, we calculate the irreducible zero- and one-potential contribution as well as the zero-potential reducible SE and the zero-potential vertex corrections using the momentum space representation [63]. A formula for the irreducible zero-potential contribution can be obtained by a straightforward replacement of the radial components of the bound-fermion wavefunction $g(p)$ and $f(p)$ in the formula for the zero-potential contribution to the Lamb shift (equation (15) in Ref. [72]) by the radial components of the magnetic wave function $X_a(p)$ and $Y_a(p)$.

$$\begin{aligned}\Delta g^{(0)}_{\mathrm{SE,irred}} = &- \frac{m_\mathrm{f}\alpha}{12\pi^4}\int_0^\infty \mathrm{d}p p^2 \{a(\rho)(g(p)X_a(p) - f(p)Y_a(p)) \\ &+ b(\rho)[E(g(p)X_a(p) + f(p)Y_a(p)) \\ &+ p(g(p)Y_a(p) + f(p)X_a(p))]\}\end{aligned} \tag{4.33}$$

Expressions for $a(\rho)$ and $b(\rho)$ can be found e.g. in Ref. [72]. The formula for the irreducible one-potential contribution is:

$$\begin{aligned}\Delta g^{(1)}_{\mathrm{SE,irred}} = &\frac{m_\mathrm{f} Z\alpha^2}{12\pi^5}\int_0^\infty \mathrm{d}p \int_0^\infty \mathrm{d}p' \int_{-1}^{1} \mathrm{d}\xi \frac{p^2 p'^2}{q^2} \times \\ &(G_1(p,p',\xi)P_0(\xi) + G_2(p,p',\xi)P_1(\xi)).\end{aligned} \tag{4.34}$$

$G_1(p,p',\xi)$ and $G_2(p,p',\xi)$ can be obtained from the expressions of $F_1(p,p',\xi)$ and $F_2(p,p',\xi)$ in the formula for the one-loop contribution to the Lamb shift (equations (B19) and (B20) in Ref. [72]) by replacing the wavefunction at momentum p or p' by the magnetic wave function. $P_0(\xi)$ and $P_1(\xi)$ are Legendre polynomials [72, 74].

Many-potential contributions can be calculated in position space, employing methods introduced for atomic structure calculations in Ref. [72, 192–194]. The Lamb-shift calculation presented in Ref. [72] can be modified into a g-factor calculation in a straightforward manner. The many-potential Green's function $G^{(2+)}$ was computed as $G^{(2+)} = G - G^{(0)} - G^{(1)}$, where $G^{(1)} = \int \mathrm{d}^3 z G^{(0)} V G^{(0)}$ [131]. It is known only as a partial wave expansion in κ in the position space representation, as pointed out in chapter 3, requiring the computation of the many-potential term to be carried out in position space. The integration contour for the $\mathrm{d}\omega$ integration was rotated into the complex plane as follows [57, 63, 72]: $[E_0 - i\infty, E_0 - i\cdot 0]$, $[E_0 - i\cdot 0, -i\cdot 0]$, $[i\cdot 0, E_0 + i\cdot 0]$, $[E_0 + i\cdot 0, E_0 + i\infty]$. The so-called Low-energy part corresponds to the integration contour $[E_0 - i\cdot 0, -i\cdot 0]$, $[i\cdot 0, E_0 + i\cdot 0]$ and the High-energy part corresponds to $[E_0 - i\infty, E_0 - i\cdot 0]$, $[E_0 + i\cdot 0, E_0 + i\infty]$. E_0 was chosen as $E_0 = 0.1E_a$ for high nuclear charge numbers according to the procedure described in ref. [72], and as $E_0 = Z\alpha E_a$ for low nuclear charge numbers according to the procedure described in Ref. [57]. We performed all integrations and then computed the summation over κ.

The computation of the partial-wave expansion of the low-energy part can be stopped at $\kappa \approx 10$ because of the fast convergence of this series. The partial wave expansion of the high-energy part was computed till $\kappa \approx 40$. Because of the slow convergence, the remainder of the expansion was estimated by means of the Richardson extrapolation procedure [195].

The final formula for the many-potential contribution to the irreducible diagram is [72]:

$$\begin{aligned}\Delta g^{(2+)}_{\rm SE,irred} = &- \frac{4i\alpha m_{\rm f}}{3\pi\,(2j_a+1)} \sum_{\kappa_i,J} (2J+1) \int {\rm d}\omega \int_0^\infty {\rm d}r r^2 \int_0^\infty {\rm d}r' r'^2 \times \\ &\big\{ g_J(r,r',\omega)(C_J(\kappa_i,\kappa_a))^2 [g(r) g^{(2+)}_{11}(r,r',E-\omega) X_a(r') + \\ &g(r) g^{(2+)}_{12}(r,r',E-\omega) Y_a(r') + f(r) g^{(2+)}_{21}(r,r',E-\omega) X_a(r') + \\ &f(r) g^{(2+)}_{22}(r,r',E-\omega) Y_a(r')] - \sum_L g_L(r,r',\omega) \times \\ &[f(r) g^{(2+)}_{11}(r,r',E-\omega) Y_a(r') (S_{JL}(-\kappa_a,\kappa_i))^2 - \\ &\{f(r) g^{(2+)}_{12}(r,r',E-\omega) X_a(r') + g(r) g^{(2+)}_{21}(r,r',E-\omega) Y_a(r')\} \times \\ &S_{JL}(-\kappa_a,\kappa_i) S_{JL}(\kappa_a,-\kappa_i) + \\ &g(r) g^{(2+)}_{22}(r,r',E-\omega) X_a(r') (S_{JL}(\kappa_a,-\kappa_i))^2]\big\},\end{aligned} \tag{4.35}$$

with the radial components of the fermion wave function $g(r)$ and $f(r)$, the wave function perturbed by the magnetic field $X_a(r)$ and $Y_a(r)$ and the radial components $g^{(2+)}_{ij}(r,r',E-\omega)$ of the Green's function, defined in Chapter 3. The angular coefficients [72, 192] are given in Appendix 3.

The renormalized zero-potential contribution to the reducible SE diagram can be computed from the expression of the zero-potential Lamb shift diagram [72] by taking the derivative with respect to energy [57]. The renormalized zero-potential part of the SE vertex diagram can be computed using the momentum-space representation of the vector potential corresponding to the constant magnetic field [57] $\mathbf{A}(\mathbf{p}'-\mathbf{p}) = -\frac{i}{2}(2\pi)^3 \mathbf{B} \times \nabla_{\mathbf{p}} \delta(\mathbf{p}'-\mathbf{p})$. We obtain the following expression [57]:

$$\Delta g^{(0)}_{\rm ver} = -\,2im_{\rm f} \int \frac{{\rm d}^3 p}{(2\pi)^3} \int {\rm d}^3 p' \overline{a}(\mathbf{p}) \left(\nabla_{\mathbf{p}'} \delta(\mathbf{p}-\mathbf{p}') \times \mathbf{\Gamma}_R(p,p')\right)_z a(\mathbf{p}')\,.$$

The derivative of the δ function can be dealt with by means of integration by parts. A detailed description of the computation of the zero-potential vertex diagram can be found in Ref. [57].

In order to compute the many-potential term of the reducible SE diagram, we insert the spectral representation of the Green's function into the expression for the energy shift. For the reducible contribution, we obtain

$$\Delta E^{(1+)}_{\rm red} = -\,\Delta E_{\rm mag}\frac{i}{2\pi}\int {\rm d}\omega \sum_{n_1}\frac{\langle an_1|I(\omega)|n_1a\rangle}{(E_a-\omega-E_{n_1}(1-i\eta))^2} - \text{zero pot}, \tag{4.36}$$

$I(\omega) = e^2\alpha^\mu\alpha_\mu D(\omega)$. "Zero pot" indicates that the expression for the corresponding diagram with free fermion propagators has to be subtracted. The integrations over angular variables can be performed according to [63, 72]:

$$\langle ab|I(\omega)|cd\rangle = \alpha\sum_{J=0}^{\infty} I_J(abcd)R_J(\omega,abcd), \tag{4.37}$$

$$I_J(abcd) = \sum_{m_J}(-1)^{j_a-m_a+J-m_J+j_b-m_b}\begin{pmatrix} j_a & J & j_c\\ -m_a & m_J & m_c\end{pmatrix}\begin{pmatrix} j_b & J & j_d\\ -m_b & -m_J & m_d\end{pmatrix} \tag{4.38}$$

Here, $\begin{pmatrix} j_1 & j_2 & j_3\\ m_1 & m_2 & m_3\end{pmatrix}$ are Wigner three-j symbols [193, 194]. Formulas for $I_J(abcd)$ and $R_J(\omega,abcd)$ and their derivation can be found in Ref. [63, 72, 192]. We give the formula for $R_J(\omega,abcd)$ in Appendix 3. Using equation (4.37), the reducible contribution for the g-factor can be expressed as a partial wave expansion as follows:

$$\Delta g^{(1+)}_{\rm red} = -g_{\rm D}\frac{i\alpha}{2\pi}\sum_{n_1,\kappa_1,J}\frac{(-1)^{J+j_1-j_a}R_j(\omega,an_1n_1a)}{(2j_a+1)(E_a-\omega-E_{n_1\kappa_1})^2} - \text{zero pot}. \tag{4.39}$$

Note that this expression contains infrared (IR) divergences for $(n_i,\kappa_i) = (n_a,\kappa_a)$. To determine $\Delta g^{(1+)}_{\rm ver}$, we use the same procedure as for the reducible diagram. This yields

$$\Delta E_{\rm ver} = \frac{i}{2\pi}\int {\rm d}\omega \sum_{n_1,n_2}\frac{\langle an_2|I(\omega)|n_1a\rangle\langle n_1|\gamma^0 e\not{A}_m|n_2\rangle}{(E_a-\omega-E_{n_1}(1-i\eta))(E_a-\omega-E_{n_2}(1-i\eta))} - \text{zero pot}. \tag{4.40}$$

This can be further evaluated using equation (4.37) [57, 196]. The energy shift corresponding to the vertex diagram also contains reference-state IR divergences for $(n_1,\kappa_1) = (n_2,\kappa_2) = (n_a,\kappa_a)$, whereas the sum of the vertex and reducible contributions is finite [57] as will be shown in the next section.

Finally, we would like to mention that there have been other schemes for the evaluation of many-potential terms. In the vertex and reducible diagrams, the (finite) one-potential contribution can be computed exactly (without partial-wave expansion) in momentum space. The partial-wave expansion of the remaining many-potential term (with at least two Coulomb interactions) converges faster than the $^{(1+)}$ many-potential term [57]. The many-potential part of the one-loop Lamb shift diagram has been evaluated by splitting it into two terms. One term can be evaluated without partial wave expansion, the partial wave expansion of the other term converges faster than with the method described above [131]. In our calculations, however, we did not use these schemes.

4.2.4 Reference-state infrared divergences

We discuss the cancellation of IR divergences in the one-loop SE correction to the g-factor in some detail. The IR divergent diagrams are the vertex and the reducible SE contributions (see Ref. [57]). Using the spectral representation for the Green's functions, we obtain the following expression for the combined energy shift of the vertex and reducible diagrams:

$$\Delta E_{\rm vr} = \Delta E_{\rm red} + \Delta E_{\rm ver} \tag{4.41}$$

$$= \frac{i}{2\pi}\int {\rm d}\omega \sum_{n_1,n_2} \frac{\langle an_2|I(\omega)|n_1a\rangle\langle n_1|\gamma^0 e\not{A}_m|n_2\rangle}{(E_a-\omega-E_{n_1}(1-i\eta))(E_a-\omega-E_{n_2}(1-i\eta))} - \tag{4.42}$$

$$\Delta E_{\rm mag}\frac{i}{2\pi}\int {\rm d}\omega \sum_{n_1} \frac{\langle an_1|I(\omega)|n_1a\rangle}{(E_a-\omega-E_{n_1}(1-i\eta))^2}\,.$$

Here, $I(\omega) = e^2\alpha^\mu\alpha^\nu D_{\mu\nu}(\omega)$ is the operator representing the electron-electron interaction [63]. Integrations over photon energies extend from $-\infty$ to ∞ unless stated otherwise. Considering the reference state $n_1 = n_2 = a$, and keeping in mind that $\langle a_m|\gamma^0 e\not{A}_m|a_m\rangle = {\rm sgn}(m)\Delta E_{\rm mag}$ ($m_a = \frac{1}{2}$), we obtain the expression

$$\Delta E_{\rm IR} = \Delta E_{\rm mag}\frac{i}{2\pi}\int {\rm d}\omega \sum_m \frac{\langle aa_m|I(\omega)|a_ma\rangle}{(-\omega+i\eta)^2}({\rm sgn}(m)-1)\,. \tag{4.43}$$

We see that there is no $m = m_a$ contribution, while the $m = -m_a$ contribution remains and requires further investigation. Inserting the momentum-space representation of the photon propagator, equation (3.42) (see [63]) into this expression, we obtain

$$\Delta E_{\rm IR} = \frac{2i\alpha}{\pi^2}\Delta E_{\rm mag}\int {\rm d}\omega \frac{1}{(-\omega+i\eta)^2}\int_0^\infty {\rm d}q \frac{q}{\omega^2-q^2+i\eta}\langle aa_{-m_a}|\alpha^\mu\alpha_\mu\frac{\sin(qx_{12})}{x_{12}}|a_{-m_a}a\rangle\,. \tag{4.44}$$

We can perform the integration over ω [63], yielding

$$\Delta E_{\rm IR} = 2\Delta E_{\rm mag}\frac{\alpha}{\pi}\int \frac{{\rm d}q}{(q-i\eta)^2}4\pi{\rm Im}\langle aa_{-m_a}|\alpha^\mu\alpha_\mu D(q)|a_{-m_a}a\rangle\,. \tag{4.45}$$

We can expand the matrix element using the multipole expansion (4.37):

$$\langle aa_{-m_a}|\alpha^\mu\alpha_\mu D(q)|a_{-m_a}a\rangle = \alpha\sum_{J=0}^\infty I_J(aa_{-m_a}a_{-m_a}a)R_J(q,aa_{-m_a}a_{-m_a}a). \tag{4.46}$$

Formulas for $I_J(aa_{-m_a}a_{-m_a}a)$ and $R_J(q,a,aa_{-m_a}a_{-m_a}a)$ can be found e.g. in ref [72]. Angular momentum selection rules dictate that only the term with $J = 1$ contributes. The only q-dependent term in $R_1(q,aa_{-m_a}a_{-m_a}a)$ is the photon Green's function. The expression for $R_1(q,aa_{-m_a}a_{-m_a}a)$ contains contributions from the partial waves of the

photon Green's function with $L = 0$, $L = 1$ and $L = 2$ in principle. However, analyzing the angular coefficients in $R_1(q, aa_{-m_a}a_{-m_a}a)$, we find that all contributions with $L = 0$ and $L = 2$ vanish, leaving only terms which contain the partial wave of the photon Green's function with $L = 1$. For the computation of ΔE_{IR}, we need to determine the imaginary part of $R_1(q, aa_{-m_a}a_{-m_a}a)$, which is equivalent to using the imaginary part of the photon Green's function. It can be easily seen that the imaginary part of the photon Green's function with $L = 1$ is proportional to q^3 for small q, which means that the integrand in equation (4.45) is proportional to q and therefore, ΔE_{IR} is IR finite. We thus see that IR divergences are completely cancelled in the sum of the vertex and reducible SE diagrams.

4.3 Energy-dependent perturbation theory - a consistency check

In this section, we are going to rederive the formal expressions for the contributions to the energy shift corresponding to the leading Feynman diagram Z_1, the one-loop SE contribution to the Lamb shift Z_2 and the one-loop SE contribution to the g-factor $Z_3 - Z_1 N_2$ (see equation (3.38)) using the formalism of quantum mechanical perturbation theory by treating self-energy and vertex corrections as energy-dependent potentials. We used this formalism to check our expressions for the two-loop SE correction to the g-factor.

Perturbation theory is an approximate calculation method in quantum mechanics, described in standard textbooks (e.g. Ref. [75]). The general procedure is to split the full Hamiltonian H of the system, which cannot be solved exactly, into two parts, $H = H_0 + V$. The eigenstates and eigenenergies of H_0 are known. The task is to determine the eigenstates $|\Psi\rangle$ and eigenenergies E of H, $H|\Psi\rangle = E|\Psi\rangle$, beginning with the eigenstates $|a\rangle$ and eigenenergies E_0 of H_0, $H_0|a\rangle = E_0|a\rangle$: $|\Psi\rangle = |a\rangle + |\Delta\Psi\rangle$, $E = E_0 + \Delta E$. ΔE and $|\Delta\Psi\rangle$ are expressed as power series of the coupling constant of the perturbation term V. (See Ref. [75])

The approach usually discussed in textbooks does not take into account the possibility of the perturbation being energy-dependent [75]. An approach which includes the possibility $V = V(E)$ is described in Ref. [197]. We quote the results from Ref. [197] for the energy shift up to second order in perturbation theory, namely:

$$\Delta E^{(1)} = \langle a|V(E_a)|a\rangle, \tag{4.47}$$

$$\Delta E^{(2)} = \sum_{n\neq a} \frac{\langle aV(E_a)|n\rangle\langle n|V(E_a)|a\rangle}{E_a - E_n} + \langle a|V(E_a)|a\rangle\langle a| \left.\frac{\partial V}{\partial E}\right|_{E_a} |a\rangle. \tag{4.48}$$

$\Delta E^{(1)}$ and the first term in $\Delta E^{(2)}$ correspond to the expressions for the energy shift in the usual (energy-independent) perturbation theory approach [75]. We will now consider the Dirac Hamiltonian as H_0, and the magnetic interaction potential V_{mag} as an (energy-independent) perturbation potential. The one-loop SE and vertex functions will be

considered as energy-dependent perturbations. The total perturbation potential reads:

$$V(E) = V_{\mathrm{mag}} + V_{\mathrm{SE}}(E) + V_{\mathrm{ver}}(E). \tag{4.49}$$

Here, $V_{\mathrm{mag}} = e\gamma^0 \not{A}_m$, $V_{\mathrm{SE}}(E) = \gamma^0 \Sigma(E)$ and $V_{\mathrm{ver}}(E) = \gamma^0 \Gamma^\mu(E) A_{m_\mu}$. The first, second and third term in $V(E)$ are of order $\mathcal{O}(e)$, $\mathcal{O}(e^2)$ and $\mathcal{O}(e^3)$, respectively. Note that the word "order" has a three distinct meanings in this section. It will refer to the order of perturbation theory, as defined above, the power of e in a term, and the number of magnetic interactions in a term. We now determine the energy shift up to second order in perturbation theory, up to third order in e and up to first order in the magnetic interaction. The first-order energy shift reads:

$$\Delta E^{(1)} = \langle a|V_{\mathrm{mag}}|a\rangle + \langle a|V_{\mathrm{SE}}(E)|a\rangle + \langle a|V_{\mathrm{ver}}(E)|a\rangle. \tag{4.50}$$

The first term is the energy shift due to a single interaction with the magnetic field and corresponds to the tree-level g-factor Feynman diagram Fig. 3.3. The second term corresponds to the one-loop SE correction to the Lamb shift shown in Fig. 4.1 (left). The third term corresponds to the one-loop vertex correction to the g-factor, Fig. 4.2 (a).

For the determination of $\delta E^{(2)}$, we can ignore the contribution due to $V_{\mathrm{ver}}(E)$ since this would lead to terms of order $\mathcal{O}(e^4)$. Inserting $V(E) = V_{\mathrm{mag}} + V_{\mathrm{SE}}(E)$ into equation (4.48), we obtain:

$$\Delta E^{(2)} = 2 \sum_{n,n\neq a} \frac{\langle a|V_{\mathrm{mag}}|n\rangle\langle n|V_{\mathrm{SE}}(E_a)|a\rangle}{E_a - E_n} + \langle a|V_{\mathrm{mag}}|a\rangle\langle a| \left.\frac{\partial V_{\mathrm{SE}}}{\partial E}\right|_{E=E_a} |a\rangle. \tag{4.51}$$

Here, we ignored the contribution from the term where V_{mag} appears in both factors, since this would be of second order in the magnetic interaction, and the case of $V_{\mathrm{SE}}(E)$ in both factors, since this is of order $\mathcal{O}(e^4)$. The first term in $\delta E^{(2)}$ corresponds to the irreducible SE correction (equation (4.16)). The second term in $\delta E^{(2)}$ corresponds to the reducible SE contribution (equation (4.19)).

Note that the term Z_3 (see equation (3.38)) contains the contribution $2\langle a|V_{\mathrm{mag}}|a\rangle$ $\langle a| \left.\frac{\partial V_{\mathrm{SE}}}{\partial E}\right|_{E_a} |a\rangle$. The subtraction term $-Z_1 N_2 = -\langle a|V_{\mathrm{mag}}|a\rangle\langle a| \left.\frac{\partial V_{\mathrm{SE}}}{\partial E}\right|_{E_a} |a\rangle$ ensures that the final result for the energy shift contains the product term only once.

Having established this correspondence between energy dependent perturbation theory and the energy shift due to loop diagrams, we can extend this approach to check our TTGF calculations for the two-loop SE contribution to the bound-fermion g-factor. We performed this energy-dependent perturbation theory calculation as a consistency check for our results obtained using the TTGF method. We will discuss this in more detail in Chapter 6.

4.4 Vacuum polarization

The effect of vacuum polarization (VP), i.e. the creation and subsequent annihilation of a virtual charged particle-antiparticle pair, contributes to the free-fermion g-factor only

in Feynman diagrams with at least two loops, e.g. by inserting a vacuum polarization loop in the virtual photon line of the vertex diagram shown in Fig. 2.1 [56]. For bound fermions, however, there are also one-loop vacuum polarization diagrams. There are two different one-loop VP diagrams contributing to the g-factor, shown in Fig. 4.2:

- Electric loop (VP-EL): The interaction potential between the bound fermion and the nucleus is corrected by VP. The corresponding correction to the bound-fermion g-factor due to the correction of the nuclear potential is called the "electric loop" VP correction. (Fig. 4.2 (d)) [189]
- Magnetic loop (VP-ML): This diagram descries the g-factor correction due to the influence of VP on the magnetic interaction. (Fig. 4.2 (b)) [189]

In principle, the VP-EL diagram would have to be split into the irreducible and the reducible part. However, since the VP potential does not depend on energy, the reducible part vanishes.

The effect of vacuum polarization in atomic physics calculations has been widely investigated, e.g. in Ref. [198–206]

4.4.1 Renormalization

The closed VP loop is UV divergent [69]. In order to deal with the divergences, we expand the virtual fermion loop in powers of interactions with the nuclear Coulomb potential. Due to the Furry theorem [207], only those diagrams with an even number of photon lines attached to the VP loop, are non-zero. This means that those contributions to the VP-EL diagram with an even number of Coulomb interactions attached to the VP loop vanish (due to the virtual photon line connecting the VP loop with the bound fermion line) [69]. In particular the "tadpole" [6] diagram (zero interactions with the Coulomb potential) vanishes. The leading contribution to the VP-EL diagram is the diagram with one Coulomb interaction attached to the VP loop, and it is UV divergent [69]. The VP potential in this diagram, i.e the Coulomb potential corrected by a free-fermion VP loop, is called the Uehling potential [208]. Its calculation and renormalization are described in detail in textbooks (e.g. [6, 79]). The corresponding VP-EL g-factor contribution is called the Uehling contribution [69]. Higher-order terms contain three or more Coulomb interactions attached to the VP loop. The sum of all such terms is called the "Wichmann-Kroll" contribution [69, 209] and is finite. The separation of the VP-EL diagram into the Uehling and the Wichmann-Kroll contribution is shown in Fig. 4.5.

The VP-ML diagram can be expanded in the same way into the "Uehling" type and the "Wichmann-Kroll" type contribution, with only the latter being finite [69] (see Fig. 4.6). It can be shown that the "Uehling" type contribution is cancelled exactly by renormalization [69]. This means that the magnetic interaction itself is not corrected by vacuum polarization, only in the background of the Coulomb potential does VP have an influence on the magnetic interaction [210].

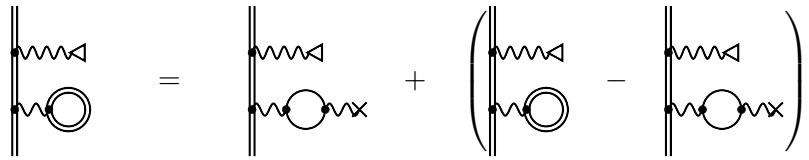

Figure 4.5: Separation of the VP-EL diagram in the divergent Uehling and the finite Wichmann-Kroll contribution [69]

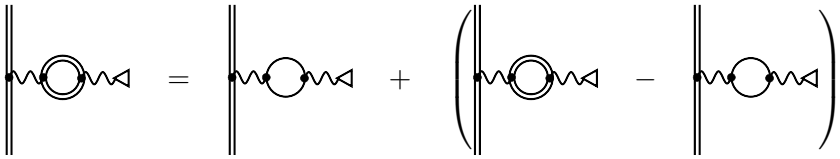

Figure 4.6: Separation of the VP-ML diagram into the "Uehling type" and the "Wichmann-Kroll type" contribution. The "Uehling type" contribution vanishes due to renormalization [69].

4.4.2 Uehling contribution

The Uehling contribution to the VP-EL diagram was computed in different ways. According to the two-time Green's function method, the Uehling g-factor contribution is [69]

$$\Delta g_{\mathrm{Ueh}} = -\frac{8m_{\mathrm{f}}}{3}\langle a|V_{\mathrm{Ueh}}|\delta a\rangle\,. \tag{4.52}$$

The Uehling potential depends on the mass of the virtual particle in the fermion loop, but it is independent of the mass of the bound particle. Therefore, the Uehling g-factor contribution can also be computed according to the following formula:

$$\Delta g_{\mathrm{Ueh}} = -\frac{4}{3m_{\mathrm{f}}}\langle a|\frac{\partial V_{\mathrm{Ueh}}}{\partial r}|a\rangle\,. \tag{4.53}$$

The derivation of this formula can be found in Ref. [150]. The results for the Uehling contribution by means of both methods were in excellent agreement with each other, and, for the model of the point-like nuclei, with the exact analytic formula for the Uehling contribution [70].

The lowest-order in $Z\alpha$ expansion VP term of order $(Z\alpha)^4$ is (e.g. [56, 70]):

$$\Delta g_{\mathrm{VP}} = -\frac{16}{15}\frac{\alpha}{\pi}(Z\alpha)^4 + \mathcal{O}\left((Z\alpha)^5\right). \tag{4.54}$$

It is due to the Uehling contribution only and can be derived using the delta function approximation of the Uehling potential [6]. In this form, it only takes into account the case of the bound particle and the virtual particle being identical. Deriving this

Z	$g^{\mathrm{Ue}}_{\mathrm{VP,approx}}$	$g^{\mathrm{Ue}}_{\mu\mathrm{VP,pt}}$	$g^{\mathrm{Ue}}_{\mu\mathrm{VP}}$ [4]
1	$-1.64 \cdot 10^{-16}$	$-1.64 \cdot 10^{-16}$	$-1.63 \cdot 10^{-16}$
2	$-2.63 \cdot 10^{-15}$	$-2.63 \cdot 10^{-15}$	$-2.66 \cdot 10^{-15}$
6	$-2.13 \cdot 10^{-13}$	$-2.17 \cdot 10^{-13}$	$-2.22 \cdot 10^{-13}$
14	$-6.31 \cdot 10^{-12}$	$-6.89 \cdot 10^{-12}$	$-7.13 \cdot 10^{-12}$
18	$-1.73 \cdot 10^{-11}$	$-1.98 \cdot 10^{-11}$	$-1.99 \cdot 10^{-11}$
20	$-2.63 \cdot 10^{-11}$	$-3.12 \cdot 10^{-11}$	$-3.09 \cdot 10^{-11}$
36	$-2.76 \cdot 10^{-10}$	$-4.65 \cdot 10^{-10}$	$-4.33 \cdot 10^{-10}$
70	$-3.95 \cdot 10^{-9}$	$-2.67 \cdot 10^{-8}$	$-1.48(1) \cdot 10^{-8}$
82	$-7.43 \cdot 10^{-9}$	$-1.06 \cdot 10^{-7}$	$-4.07(1) \cdot 10^{-8}$
92	$-1.18 \cdot 10^{-8}$	$-3.60 \cdot 10^{-7}$	$-9.44(1) \cdot 10^{-8}$

Table 4.1: Muonic VP-EL Uehling correction to the bound-electron g-factor according to the approximation formula (4.55) (first column), numerical calculations for the point-like (second column) and extended nuclear models (third column) for different nuclear charge numbers Z.

contribution for the loop particle with mass m_l and a bound particle with mass m_b, we obtain:

$$\Delta g_{\mathrm{VP}} \approx -\frac{16}{15}\frac{\alpha}{\pi}(Z\alpha)^4 \frac{m_b^2}{m_l^2}. \tag{4.55}$$

We now investigate two cases of the Uehling contributions with the loop particle being different from the bound particle.

Muonic VP correction to the bound-electron g-factor

The creation of muon antimuon pairs was investigated in Ref. [211, 212]. The effect of muonic VP to the Lamb shift was investigated in Ref. [213]. We investigated the muonic VP correction to the bound-electron g-factor in Ref. [4]. Previously, the same effect had been investigated by R. Weis [214].

For low Z, the above formula (4.55) can be expected to give a good approximation for the muonic VP correction to the bound-electron g-factor for low Z. In Table 4.1, we compare the results of the approximate formula (4.55) with numerical determinations of the Uehling contribution for point-like nuclei following equations (4.52) and (4.53). The results obtained with both numerical methods are in excellent agreement. Furthermore, we list the Uehling contribution for extended nuclear charge distributions, obtained in Ref. [4] by the first author N. A. Belov.

We see that all three methods are in good agreement for low Z. We also find that, for high Z, the numerical result for point-like nuclei overestimates the result for extended nuclei by a factor of three to four. In Ref. [69], for $Z = 90$ a relative deviation of only 5% is found between the e^-e^+ Uehling contributions to the bound-electron g-factor for point-like and extended nuclear charge distributions. Therefore, the effect of the

finite nuclear size on the muonic VP correction is much larger than on the electronic VP correction.

However, the total Uehling contribution of muonic VP is still smaller than the uncertainty of the g-factor due to the FS effect [4]. Therefore, we conclude that the muonic VP effect will be observable in principle after an improvement of the nuclear radius uncertainty by some independent means.

Electronic VP correction to the bound-muon g-factor

The electronic VP correction in muonic $^4He^+$, calculated according to equations (4.52) and (4.53) for point-like nuclei, was found to be $-4.807 \cdot 10^{-7}$ [2]. The same contribution was investigated for the extended nuclear model by the co-authors H. Cakir and N. Michel in Ref. [2] and was found to be $-4.796 \cdot 10^{-7}$. The approximation formula (4.55) would give the result $-4.8061 \cdot 10^{-6}$, one order of magnitude larger than the numerical results. We therefore conclude that the $Z\alpha$ expansion formulas, obtained for the case of electronic VP in electronic ions cannot be expected to give good approximations for the electronic VP contribution in muonic ions when scaled with the appropriate power of the mass ratio. This holds true even for low Z.

4.4.3 Wichmann-Kroll contribution and magnetic loop

For completeness, we note that the Wichmann-Kroll contribution and the VP-ML contributions were studied for a wide range of nuclear charge numbers in e.g. Ref. [69, 141]. In Ref. [4], the Wichmann-Kroll and the VP-ML contributions due to muonic VP in electronic ions was investigated by N. A. Belov. In Ref. [59], the muonic VP-ML contribution was studied perturbatively in $Z\alpha$.

5 Mass determinations by means of the bound-fermion g-factor

5.1 Determination of the electron mass

We describe the method to determine the atomic mass of the electron. The work described in this section was previously published in Ref. [1]. The underlying article has been written predominantly by the co-authors J. Zatorski, Z. Harman, S. Sturm, K. Blaum and C. H. Keitel. Table 5.1 of g-factor values, including the complete caption, was taken from Ref. [1].

As described in the introduction, the electron mass can be determined from the bound-electron g-factor using equation (1.3). To achieve a high accuracy for the electron mass, the theoretical g-factor value g_{theo}, the frequency ratio $\Gamma = \frac{\omega_{\mathrm{c}}}{\omega_{\mathrm{L}}}$ and the ion mass M need to be determined with at least an equally high accuracy. $^{12}\mathrm{C}^{5+}$ ions were chosen for the electron mass determination [31, 43], and in an earlier investigation [30], because the mass of $^{12}\mathrm{C}^{5+}$ ions is known with an extremely high accuracy since the atomic mass unit is defined by the $^{12}\mathrm{C}$ atom. The experimental determination of Γ was presented in Ref. [43].

Theoretical g-factor values were computed taking into account the perturbative (in $Z\alpha$) corrections, nuclear terms as well as non-perturbative one-loop contributions. The theory of the bound-electron g-factor was tested in an earlier investigation using the $^{28}\mathrm{Si}^{13+}$ ion in Ref. [33], where the theoretical prediction was found to be in excellent agreement with the experimental value. Since binding corrections are magnified in $^{28}\mathrm{Si}^{13+}$ compared to $^{12}\mathrm{C}^{5+}$ due to the higher nuclear charge, one can rely on the theoretical prediction for the bound-electron g-factor in $^{12}\mathrm{C}^{5+}$. Further contributions which were computed only after the previous electron mass determination [31] were taken into account. These are non-perturbative (in $Z\alpha$) contributions from two-loop diagrams with at least one VP loop [58] and a two-loop light-by-light scattering contribution of order $(Z\alpha)^4$ [59]. Remaining two-loop higher-order contributions were estimated by assuming the correctness of QED for the $^{28}\mathrm{Si}^{13+}$ ion. The difference between the sum of all theoretical g-factor contributions and the experimental value for $^{28}\mathrm{Si}^{13+}$ was assumed to account for uncalculated higher-order two-loop corrections. These two-loop corrections were scaled with the fifth power in $Z\alpha$ to determine their value for $^{12}\mathrm{C}^{5+}$. For details of this procedure, see Ref. [1]. The value for the electron mass obtained in Ref. [1], given in atomic mass units, is:

$$m_e = 0.000548579909065(16). \tag{5.1}$$

This electron mass value is slightly different (0.3 σ) from the one obtained in the previ-

ous investigation [19, 43] because of the inclusion of the above mentioned light-by-light scattering term. It is possible that the inclusion of the recently computed order $(Z\alpha)^5$ contribution to the two-loop diagrams [62] (which was completed only after the determination of the electron mass) would further shift the electron mass.

A further improvement of the electron mass m_e value is possible if the frequency ration Γ can be measured with higher accuracy. Such a measurement is expected to be possible at the ALPHATRAP Penning-trap experiment at the Max Planck Institute for Nuclear Physics [35, 39].

An electron mass determination is also possible by employing the $^4He^+$ ion. The accuracy of the theoretical g-factor is better than for $^{12}C^{5+}$ because uncalculated higher-order in $Z\alpha$ contributions are strongly suppressed in $^4He^+$ compared to $^{12}C^{5+}$. A limitation to the electron mass determination in this approach is the uncertainty of the Helium mass [19]. In case the electron mass can be improved by a measurement of $^{12}C^{5+}$ or some independent experiment, a measurement of the bound-electron g-factor in $^4He^+$ can be used to determine the ion mass. A high-precision measurement of the ^{4}He mass is planned at the THe-Trap experimental facility [40].

We now briefly discuss possibilities to determine α in bound-electron g-factor experiments. As pointed out in section 3.6, the theoretical accuracy of the bound-electron g-factor is limited by nuclear effects. For this reason, it has been suggested to not just consider the g-factor of one ion, but instead the weighted difference of g-factors of the same ion in different charge states, schematically represented by

$$\Delta_\xi g = g_{\text{state 1}} - \xi g_{\text{state 2}}. \tag{5.2}$$

Specifically, weighted differences have been suggested for hydrogenlike and boronlike ions with high Z [53] and between hydrogenlike and lithiumlike ions for small and medium Z [54, 55]. In these cases, the weight ξ is determined such that the uncertainty of $\Delta_\xi g$ due to the nuclear structure is strongly suppressed, making the determination of α with an accuracy higher than the current literature value feasible. A determination of α from the bound-electron g-factor without employing a weighted difference is possible if the uncertainty of the g-factor due to nuclear parameters is smaller than the uncertainty due to α. $^4He^+$ is the only ion which offers this possibility [1]. Therefore, it is in principle possible to determine α with an improved accuracy from the g-factor of the $^4He^+$ ion. For this, an improvement of the experimental frequency ratio Γ is required as well as an independent improvement of the electron mass and the mass of the ^{4}He nucleus.

5.2 Muon mass and magnetic moment anomaly from the bound-muon g-factor

In the current section, we put forward a method to determine the muon mass and the muon anomaly from the bound-muon g-factor. Major parts of this section are based on Ref. [2]. Fig. 5.1 (along with the caption) and table 5.2 (along with the caption) were taken from Ref. [2].

Table 5.1: Values of individual contributions to $g\left({}^{4}\mathrm{He}^{+}\right)$, $g\left({}^{12}\mathrm{C}^{5+}\right)$ and $g\left({}^{28}\mathrm{Si}^{13+}\right)$, and some relevant nuclear parameters. The abbreviations stand for: M_{atom}, M: mass of the atom and the hydrogenlike ion, respectively; $\left\langle r^2\right\rangle^{1/2}$: root-mean-square nuclear charge radius; "SE-FS" – mixed self-energy and nuclear finite size correction. An experimental value for $g\left({}^{28}\mathrm{Si}^{13+}\right)$ is given as published in Ref. [34], i.e. evaluated with a former, less accurate value of m_e, which defines the last error given. This table, including the complete caption, was taken from Ref. [1]. Notes: [1] Ref. [157], [2] Extrapolation of the cited results

Contribution	${}^{4}\mathrm{He}^{+}$	${}^{12}\mathrm{C}^{5+}$	${}^{28}\mathrm{Si}^{13+}$	Ref.
$\left\langle r^2\right\rangle^{1/2}$ [fm]	1.681(4)[1]	2.4703(22)	3.1223(24)	[156]
M_{atom} [u]	4.002 603 254 130(63)	12 (exact)	27.976 926 534 65(44)	[171]
M [u]	4.002 054 700 617(63)	11.997 257 680 293 69(97)	27.969 800 594 24(50)	
Dirac value	1.999 857 988 825 37(7)	1.998 721 354 392 0(6)	1.993 023 571 557(3)	[144]
Finite nuclear size	0.000 000 000 002 30(1)	0.000 000 000 407 4(7)	0.000 000 020 468(31)	[148]
One-loop QED				
$(Z\alpha)^0$	0.002 322 819 464 85(54)	0.002 322 819 464 9(5)	0.002 322 819 465(1)	[19, 76]
$(Z\alpha)^2$	0.000 000 082 462 19	0.000 000 742 159 7	0.000 004 040 647	[160]
$(Z\alpha)^4$	0.000 000 001 976 70	0.000 000 093 422 2	0.000 001 244 596	[56]
$(Z\alpha)^{5+}$ SE	0.000 000 000 035 42(68)	0.000 000 008 282 6(37)	0.000 000 542 856(60)	[57, 186][2]
SE FS	-0.000 000 000 000 00	-0.000 000 000 000 7	-0.000 000 000 068	[189]
$\geq (Z\alpha)^5$ VP-EL	0.000 000 000 002 52	0.000 000 000 555 9	0.000 000 032 531	[70, 189]
VP-EL FS	0.000 000 000 000 00	0.000 000 000 000 2	0.000 000 000 022	[189]
$(Z\alpha)^{5+}$ VP-ML	0.000 000 000 000 16	0.000 000 000 038 1	0.000 000 002 540(10)	[117, 215]
$(Z\alpha)^{5+}$ VP-ML FS	0.000 000 000 000 00	0.000 000 000 000 0	-0.000 000 000 001	[189, 215]
Two-loop QED				
$(Z\alpha)^0$	-0.000 003 544 604 49	-0.000 003 544 604 5	-0.000 003 544 604	[83, 85]
$(Z\alpha)^2$	-0.000 000 000 125 84	-0.000 000 001 132 5	-0.000 000 006 166	[160]
$(Z\alpha)^4$ (w/o LBL)	0.000 000 000 002 41	0.000 000 000 060 1	-0.000 000 001 318	[56, 116]
LBL at $(Z\alpha)^4$	-0.000 000 000 000 39	-0.000 000 000 031 5	-0.000 000 000 933	[59]
$(Z\alpha)^{5+}$ S(VP)E	0.000 000 000 000 00	0.000 000 000 000 0(1)	0.000 000 000 009(2)	[58]
$(Z\alpha)^{5+}$ SEVP	0.000 000 000 000 03	0.000 000 000 006 9(3)	0.000 000 000 458(1)	[58]
$(Z\alpha)^{5+}$ VPVP	0.000 000 000 000 03	0.000 000 000 005 5	0.000 000 000 315	[58, 60]
$(Z\alpha)^{5+}$ SESE (estimate)	0.000 000 000 000 00(2)	-0.000 000 000 001 2(33)	-0.000 000 000 082(139)	
$\geq$ Three-loop QED				
$(Z\alpha)^0$	0.000 000 029 497 95	0.000 000 029 497 9	0.000 000 029 498	[21, 86, 87]
$(Z\alpha)^2$	0.000 000 000 001 05	0.000 000 000 009 4	0.000 000 000 051	[160]
Recoil				
$(m/M)^1$ all-orders in $(Z\alpha)$	0.000 000 029 202 51	0.000 000 087 725 1	0.000 000 206 100	[167]
$(m/M)^{2+}$ at $(Z\alpha)^2$	-0.000 000 000 012 01	-0.000 000 000 028 1	-0.000 000 000 060	[168]
Radiative-recoil	-0.000 000 000 022 61	-0.000 000 000 067 9	-0.000 000 000 159	[69, 160]
Nuclear polarizability	0.000 000 000 000 00	0.000 000 000 000 0	0.000 000 000 000(20)	[177][2]
Nuclear susceptibility	0.000 000 000 000 00	0.000 000 000 000 0(1)	0.000 000 000 000(3)	[44]
Weak interaction at $(Z\alpha)^0$	0.000 000 000 000 06	0.000 000 000 000 1	0.000 000 000 000	[19, 92]
Hadronic effects at $(Z\alpha)^0$	0.000 000 000 003 47	0.000 000 000 003 5	0.000 000 000 003	[89–91]
Total w/o SESE $(Z\alpha)^5$	2.002 177 406 711 68(87)	2.001 041 590 166 3(39)	1.995 348 957 791(71)	
Total w/ SESE $(Z\alpha)^5$ from exp.	2.002 177 406 711 68(87)	2.001 041 590 165 2(51)	1.995 348 957 708(156)	
Experiment			$1.995\,348\,959\,10(7)_{\mathrm{stat}}(7)_{\mathrm{syst}}(80)_{m_e}$	[34]

5.2.1 Muonic systems

The g-factor of bound muons was previously investigated theoretically in Ref. [216, 217] and experimentally in Ref. [218]. In the latter investigation, the system under consideration consisted out of a nucleus, a bound muon and bound electrons. However, we consider a muonic ion consisting only of an atomic nucleus and one bound muon in the ground state, without any bound electrons.

As pointed out in the introduction, there are several discrepancies between theoretical predictions and experimental findings involving muons. These are the deviation between the theoretical and experimental free-muon g-factors by about 3σ [94] and an even larger deviation between the proton radii, determined with electronic and muonic systems [23,

24] (see also [28]). In this Chapter, we put forward a method to determine the muon mass from the bound-muon g-factor similar to the electron mass determination. The muon mass is known only from muonium spectroscopy [219] with a relative accuracy of 2.2×10^{-8} [19, 20]. Our scheme constitutes an alternative method to determine the muon mass or the muon anomaly a_μ, which is defined by [19]

$$g_{\mu\text{free}} = 2(1 + a_\mu). \tag{5.3}$$

In an experimental setup which enables the Larmor and cyclotron frequancy determination, the muon mass can be expressed similar to the electron mass (see also equation (1.3)):

$$m_\mu = \frac{g}{2}\frac{e}{Q}\frac{\omega_\text{c}}{\omega_\text{L}}M\,. \tag{5.4}$$

Just as in the case of the bound-electron, the theoretical value for the bound-muon g-factor has to be employed. Alternatively, one can compare the theoretical and experimental bound-muon g-factors. The experimental g-factor would be determined from equations (1.1) and (1.2):

$$g = 2\frac{m_\mu}{M}\frac{Q}{e}\Gamma\,. \tag{5.5}$$

The experimental value for the bound-muon g-factor is limited by the accuracy of the muon mass, determined using independent methods. The theoretical g-factor can be expressed as $g = 2 + 2a_\mu + \Delta g_\text{bind}$, where a_μ is the muon anomaly and Δg_bind is the sum of all binding corrections. Provided the binding corrections can be determined with sufficient accuracy, this method is an alternative access to the free-muon anomaly. In this Chapter, we calculate the binding corrections.

As indicated in section 3.6.1, the accuracy of the theoretical bound-muon g-factor prediction is limited by the uncertainty due to nuclear effects which are strongly enhanced in muonic ions compared to electronic ions. In order to minimize this uncertainty, a light ion needs to be chosen for the muon-mass determination. We present the theory of the bound-muon g-factor using the muonic $^4\text{He}^+$ which is the lightest muonic ion which has a nucleus with zero spin. We demonstrate that the theoretical prediction of the bound-muon g-factor can be determined with a relative accuracy of 10^{-9}. This allows the determination of the muon mass or the free-muon anomaly with the same relative accuracy, provided a comparable experimental precision can be achieved. This allows an improvement of the accuracy of the muon mass by one order of magnitude.

5.2.2 Theory of the bound-muon g-factor

The theoretical descriptions of the bound electron and the bound muon are similar. The one-loop SE contribution and the Uehling VP contribution were computed as described in Chapter 4. Here, we describe the computation of additional contributions relevant for the bound-muon g-factor.

The electronic VP-ML and Wichmann-Kroll contributions for the muonic ion $^4\text{He}^+$ was investigated in Ref. [2] by the co-authors V. Debierre and H. Cakir. The Wichmann-Kroll contribution was computed using the method of Ref. [220]. It was found that the

Wichmann-Kroll contribution is negligible. The light-by-light (LBL) scattering approximation of the VP-ML term was calculated as in Ref. [71, 221]. However, in our case, the FS effect was included in the bound-muon wavefunction.

Apart from one-loop SE and VP corrections, we took into account the leading diagrams with two VP loops for the case of electronic VP and further two-loop corrections in order to determine the total g-factor of muonic $^4He^+$ with an absolute accuracy of the order 10^{-9}. The two-loop contribution to the free-muon g-factor can be found in Ref. [19]. Binding corrections to the two-loop self-energy diagrams were determined perturbatively in $Z\alpha$ up to order $\mathcal{O}\left((Z\alpha)^5\right)$ using formulas from [56, 62, 114].

One further way to determine the contribution due to the Uehling potential allows the determination of two-loop VP corrections as follows. The Uehling contribution was evaluated by the co-author N. Michel by solving the radial Dirac equation numerically, with the Uehling potential added to the nuclear potential. The B-spline representation was used for the bound-muon wavefunction [222], as described in Ref. [223]. By subtracting the one-loop Uehling correction from this contribution, the effect of the higher-order Uehling contributions which correspond to the diagrams shown in Fig. 5.1 (a), could be determined. See also Ref. [4, 224] for this approach.

The two-loop VP correction corresponding to the diagrams in Fig. 5.1 (b), the Källén-Sabry contribution [225], was evaluated using B-splines by N. Michel. The effective potential given in Ref. [226, 227] was employed.

Furthermore, the mixed magnetic and electric loop effect was calculated by the co-authors V. Debierre and H. Cakir. For this, the calculation of the LBL contribution to the VP-ML diagram (Fig. 4.2 (b)) was repeated, with the bound-muon wave function corrected by the Uehling potential. This corresponds to a modified version of the diagram shown on the left side of Fig. 5.1 (a), with the magnetic interaction attached not to the bound muon line but to one of the VP loops.

We also investigated diagram on the right hand side of Fig. 5.1 (b) for the case of one electronic and one muonic VP loop. The corresponding VP potential was determined by generalizing the computation of the Uehling potential of Ref. [6]. The contribution due to the mixed electronic and muonic vacuum polarization was found to be negligible. We checked our approach by computing the case of electronic VP in both loops for the bound electron. Our numerical results for low Z were in reasonable agreement with the results obtained with the $Z\alpha$ expansion formula for this contribution given in Ref. [60].

Finally, there is the two-loop S(VP)E diagram [58], i.e. the two-loop diagram with a vacuum polarization loop inserted in the virtual photon line of the vertex diagram, for the case of electronic VP. The order $\mathcal{O}\left((Z\alpha)^0\right)$ contribution of this diagram is included in the free-muon g-factor contributions from Ref. [19]. Binding corrections of order $\mathcal{O}\left((Z\alpha)^2\right)$ were computed according to Ref. [114].

The ≥ 3 loop QED term contains all three to five loop corrections to the free-muon g-factor [19]. Binding corrections to this contribution were computed according to Ref. [114] and were found to be irrelevant for the level of accuracy to be achieved.

For the bound muon, there are several sources of hadronic VP corrections to the g-factor. First, there is the above mentioned S(VP)E diagram, with the VP loop replaced by hadronic VP [90], and other hadronic VP contributions to the free-muon g-factor.

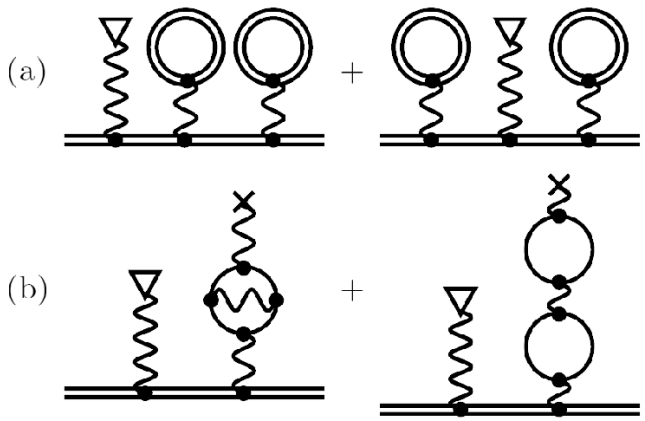

Figure 5.1: Feynman diagrams of two-loop VP corrections to the bound-muon g factor: (a) 2nd-order electric-loop VP (Uehling and Wichmann-Kroll) terms, and (b) the Källén-Sabry diagrams. A single internal line represents a free Dirac propagator, and the wave line terminated by a cross stands for the interaction with the nuclear potential. This figure, including the complete caption, was taken from Ref. [2].

The total hadronic VP correction, as given in Ref. [19], is $1.393(12) \cdot 10^{-7}$. Binding corrections to the hadronic VP contribution were computed according to Ref. [114] and found to be negligible.

Another source of hadronic VP is the Uehling contribution to the VP-EL diagram, with the VP loop replaced by hadronic VP. A corresponding hadronic VP contribution to the Lamb-Shift was computed in Ref. [228]. See also Ref. [229–231]. Adapting this method to g-factor calculations, we express the hadronic VP contribution in terms of the muonic VP contribution, $\Delta g_{\mathrm{hadrVP}} \approx 0.671(15) \Delta g_{\mu\mathrm{VP}}$ (see also Ref. [4]).

5.2.3 Results and discussion

Our numerical results in table 5.2 show that the bound-muon g-factor can be calculated with a relative accuracy of 10^{-9}. The muon mass and the anomaly of the free muon can therefore be determined with the same accuracy. In case of the muon mass, this accuracy corresponds to an improvement by one order of magnitude. Because of the muon's short lifetime, determining the required cyclotron and Larmor frequencies is challenging. However, considering recent advances in the precision spectroscopy of muonic atoms [23, 24, 27] and Penning-trap techniques [35, 38], this method can be used as an independent determination of the muon anomaly or the muon mass, in the latter case with a greatly improved accuracy compared to the currently accepted CODATA value [19].

Effect	Term	Numerical value	Ref.
Dirac value		1.999 857 988 8	[19, 144]
Finite nuclear size		0.000 000 094 6(4)	[156]
One-loop SE	$(Z\alpha)^0$	0.002 322 819 5	[19, 76]
	all-order binding	0.000 000 084 9(10)	
One-loop VP	eVP, Uehling	-0.000 000 479 6	
	eVP, magnetic loop	0.000 000 127 2(4)	
	μVP, Uehling	-0.000 000 000 1	
	hadronic VP, Uehling	-0.000 000 000 1(1)	
Two-loop QED	$(Z\alpha)^0$	0.000 008 264 4	[83, 85]
	SE-SE, $(Z\alpha)^2$— $(Z\alpha)^5$	-0.000 000 000 1	[56, 62, 114, 115]
	S(eVP)E, $(Z\alpha)^2$	0.000 000 000 4	[83, 85, 114, 115]
	2nd-order Uehling	-0.000 000 001 1(4)	
	Källén-Sabry	-0.000 000 003 5	
	magnetic loop+Uehling	0.000 000 000 3	
$\geq$ Three-loop QED	$(Z\alpha)^0$	0.000 000 610 6	[19, 21, 86, 87]
Nuclear recoil	$\left(\frac{m}{M}\right)^1$, all orders in $Z\alpha$	0.000 006 038 2	[167]
	$\left(\frac{m}{M}\right)^{2+}$, $(Z\alpha)^2$	-0.000 000 488 7	[168]
	radiative recoil	-0.000 000 004 7	[160]
Weak interaction	$(Z\alpha)^0$	0.000 000 003 1	[19, 92]
Hadronic contributions	$(Z\alpha)^0$	0.000 000 139 3(12)	[19, 89–91]
Sum		2.002 195 193 4(20)	

Table 5.2: Various contributions to the g factor of $\mu^4\mathrm{He}^+$. The abbreviations are: "eVP"/"μVP": VP due to virtual $e^-e^+/\mu^-\mu^+$ pairs. The estimated uncertainty of the nuclear size effect stems from the error bar of the root-mean-square nuclear radius and the uncertainty of the nuclear charge distribution model. This table, including the complete caption, was taken from ref. [2].

6 Theory of the two-loop self-energy corrections to the g-factor

There are no less than fifty Feynman diagrams (excluding counterterms) with two loops contributing to the bound-fermion g-factor [69]. There are three types of two-loop diagrams [58]:

- VPVP: diagrams with two vacuum polarization loops,
- SEVP: diagrams with one vacuum polarization and one self-energy loop,
- SESE: diagrams with two self-energy loops.

In Ref. [58], SEVP and VPVP diagrams were computed non-perturbatively in $Z\alpha$. In some cases, the VP loop(s) were treated in the Uehling approximation in Ref. [58], i.e. the free-electron approximation was employed for the particles in the VP loop(s). Keeping in mind that the ML VP loop vanishes in the Uehling approximation, all two-loop diagrams with such a ML VP loop were left out in that analysis. Currently, efforts are underway to compute two-loop SEVP and VPVP diagrams with a ML-VP loop [5].

In this chapter, we investigate those two-loop Feynman diagrams with two SE loops non-perturbatively in $Z\alpha$ [3]. We will first give basic formulas derived with the TTGF method, and compare our results with energy-dependent perturbation theory calculations. Then we discuss the cancellation of UV and IR divergences. We will then discuss the separation of the SESE diagrams into different categories suitable for numerical evaluation, namely the LAL contribution and the F, P and M term which will be defined later. Finally, we will discuss in detail the methods for the evaluation of the LAL contribution. A description of the methods to compute the F term and the presentation of our numerical results for the F term follow in the next chapter.

6.1 Two-loop self-energy diagrams

There are three two-loop self-energy diagrams contributing to the *binding energy* of a hydrogenlike ion, namely, the loop-after-loop (LAL), the nested loops (N) and the overlapping loops (O) diagrams [63]. They are presented in Fig. 6.1. A calculation of all terms has been presented in detail in Ref. [63]. The renormalization of the two-loop SE contribution to the Lamb shift was discussed in detail in Ref. [197, 232]. Further investigations of the two-loop SE correction to the Lamb shift were performed in Ref. [65–67, 233–246]. Experiments involving Lamb shift measurements with highly charged ions were performed in Ref. [247–249].

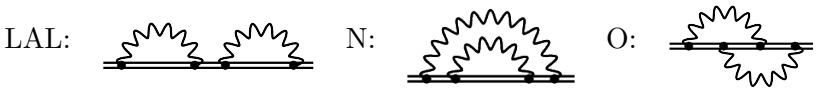

Figure 6.1: Furry-picture Feynman diagrams of two-loop self-energy corrections to the Lamb shift: the loop-after-loop (LAL), the nested-loops (N) and the overlapping-loops (O) diagrams, respectively [63]. Double lines represent Coulomb-Dirac wave or Green's functions, and the wave line represents a virtual photon.

The diagrams of the SESE corrections for the g-factor can be generated by magnetic vertex insertions into the corresponding Lamb shift diagrams. Therefore, in this case we differentiate between loop-after-loop, nested-loop and overlapping-loop terms as well. However, this time we have three diagrams of each type. The nine non-equivalent diagrams obtained this way are shown in Fig. 6.2.

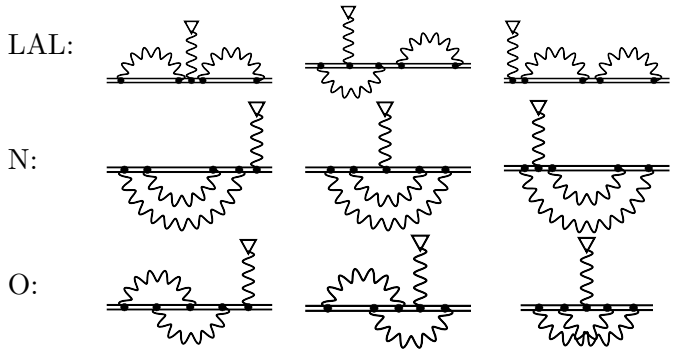

Figure 6.2: Furry-picture Feynman diagrams of two-loop self-energy corrections to the g-factor [69]. A wave line terminated by a triangle represents a magnetic interaction vertex.

Just as in our one-loop calculations, we consider an electron bound in the ground state of a hydrogenlike ion, with the angular momentum projection quantum number being $m_a = \frac{1}{2}$. The energy shift ΔE of the ground state in an external magnetic field $\boldsymbol{B} = B\boldsymbol{e}_z$ can be computed for each diagram using the two-time Green's function method [68]. The corresponding g-factor contribution Δg is related to the energy shift by $\Delta E = -\frac{eB}{4m_e}\Delta g$, where e and m_e are the electron's charge and mass, respectively.

6.1.1 Nested-loop and overlapping-loop diagrams

We will now give basic formulas for all Feynman diagrams relevant for the two-loop SE correction to the bound-electron g-factor. The diagrams in the second and third lines of Fig. 6.2 are called the nested-loop (N) and overlapping-loop (O) diagrams, respectively. The first diagram in the second and third line needs to be split into two contributions.

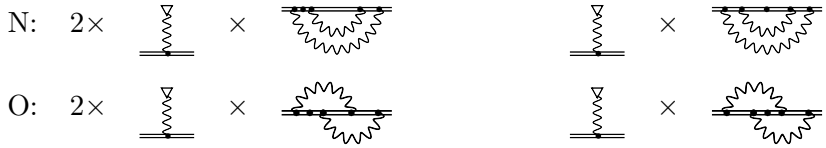

Figure 6.3: Reducible N and O g-factor diagrams. A double line with a dot denotes a derivative of a Green's function with respect to the energy [63]: $\left.\frac{\partial G(E)}{\partial E}\right|_{E=E_a}$.

In the spectral representation of the propagator $\sum_n \frac{|n\rangle\langle n|}{E_a - E_n}$ between the SE loops and a magnetic vertex, when the intermediate state $|n\rangle$ equals the reference state $|a\rangle$, the expression can be reduced to products of matrix elements appearing in a lower order of perturbation theory. This contribution is called reducible, and the rest of the sum, i.e. the term containing the reduced Green's function $\sum_{n,n\neq a} \frac{|n\rangle\langle n|}{E_a - E_n}$ [63] is called the irreducible contribution. We will refer to the irreducible contributions as "N, irred" and "O, irred", and to the reducible parts as "N, red" and "O, red". The energy shifts corresponding to these diagrams are

$$\Delta E_{i,\,\mathrm{irred}} = 2\langle a|\gamma^0 \Sigma_i|\delta a\rangle, \tag{6.1}$$

$$\Delta E_{i,\,\mathrm{red}} = \Delta E_{\mathrm{mag}} \langle a|\gamma^0 \left.\frac{\partial \Sigma_i}{\partial E}\right|_{E=E_a} |a\rangle\,, \tag{6.2}$$

with $\Delta E_{\mathrm{mag}} = \langle a|\gamma^0 e \not{A}_m|a\rangle$ being the leading energy shift in the first order of perturbation theory, induced by the external magnetic field described by its 4-vector potential A_{m_μ}. Furthermore, $i \in \{\mathrm{N}, \mathrm{O}\}$, and the Σ_i are the two-loop SE functions which are discussed in detail in Ref. [63]. We obtain the following expressions for the two-loop SE functions:

$$\begin{aligned}\Sigma_{\mathrm{N}}(\mathbf{x}_1, \mathbf{x}_4, E_a) =& 2i\alpha\gamma^0 \int \mathrm{d}\mathbf{x}_2 \int \mathrm{d}\mathbf{x}_3 \int \mathrm{d}\omega \alpha^\mu G(\mathbf{x}_1, \mathbf{x}_2, E_a - \omega)\gamma^0 \Sigma(\mathbf{x}_2, \mathbf{x}_3, E_a - \omega) \\ & G(\mathbf{x}_3, \mathbf{x}_4, E_a - \omega)\alpha^\sigma D_{\mu\sigma}(\mathbf{x}_1, \mathbf{x}_4, \omega)\,, \end{aligned} \tag{6.3}$$

$$\begin{aligned}\Sigma_{\mathrm{O}}(\mathbf{x}_1, \mathbf{x}_4, E_a) =& 2i\alpha\gamma^0 \int \mathrm{d}\mathbf{x}_2 \int \mathrm{d}\mathbf{x}_3 \int \mathrm{d}\omega \alpha^\mu G(\mathbf{x}_1, \mathbf{x}_2, E_a - \omega)\gamma^0 \\ & \Gamma^\rho(\mathbf{x}_2, \mathbf{x}_3, \mathbf{x}_4, E_a - \omega, E_a) D_{\mu\rho}(\mathbf{x}_1, \mathbf{x}_3, \omega)\,. \end{aligned} \tag{6.4}$$

$|\delta a\rangle$ is the wave function perturbed linearly by the magnetic field, $|\delta a\rangle = \sum_{n,n\neq a} \frac{|n\rangle\langle n|\gamma^0 e \not{A}_m|a\rangle}{E_a - E_n}$. A closed analytical expression for the part diagonal in κ of this function is given in Ref. [128]. The "N, red" and "O, red" diagrams are shown in Fig. 6.3. As can be seen in this Figure, the derivative in $\Delta E_{i,\,\mathrm{red}}$ can act on the central electron propagator or on one of the propagators on the side. Following the nomenclature of Ref. [63], we refer to these contributions as the "ladder" and "side" contributions, respectively.

The remaining diagrams in the second and third lines of Fig. 6.2 are called the vertex diagrams. Just as in the reducible case, we will refer to these contributions as "side"

and "ladder" vertex diagrams if the magnetic interaction is connected to the side or central electron propagator, respectively. The energy shifts corresponding to the vertex diagrams can be represented as

$$\Delta E_{\mathrm{ver},ij} = \langle a|\gamma^0 \Gamma^\mu_{ij} e A_{m\mu}|a\rangle \,. \tag{6.5}$$

Here, $j \in \{\mathrm{side}, \mathrm{ladder}\}$, and Γ^μ_{ij} are the two-loop vertex functions. These can be expressed as follows:

$$\begin{aligned}
\Gamma^\mu_{\mathrm{N,side}}(\mathbf{x}_1,\mathbf{x}_4,\mathbf{x}_5,E_a) =& 4i\alpha\gamma^0 \int \mathrm{d}\mathbf{x}_2 \int \mathrm{d}\mathbf{x}_3 \int \mathrm{d}\omega \alpha^\nu G(\mathbf{x}_1,\mathbf{x}_2,E_a-\omega)\gamma^0 \Sigma(\mathbf{x}_2,\mathbf{x}_3,E_a-\omega) \\
& G(\mathbf{x}_3,\mathbf{x}_4,E_a-\omega)\alpha^\mu G(\mathbf{x}_4,\mathbf{x}_5,E_a-\omega)\alpha^\rho D_{\nu\rho}(\mathbf{x}_1,\mathbf{x}_5,\omega)\,, \qquad (6.6) \\
\Gamma^\mu_{\mathrm{N,ladder}}(\mathbf{x}_1,\mathbf{x}_3,\mathbf{x}_5,E_a) =& 2i\alpha\gamma^0 \int \mathrm{d}\mathbf{x}_2 \int \mathrm{d}\mathbf{x}_4 \int \mathrm{d}\omega \alpha^\nu G(\mathbf{x}_1,\mathbf{x}_2,E_a-\omega)\gamma^0 \qquad (6.7) \\
& \Gamma^\mu(\mathbf{x}_2,\mathbf{x}_3,\mathbf{x}_4,E_a-\omega,E_a-\omega) G(\mathbf{x}_4,\mathbf{x}_5,E_a-\omega)\alpha^\rho D_{\nu\rho}(\mathbf{x}_1,\mathbf{x}_5,\omega)\,, \\
\Gamma^\mu_{\mathrm{O,side}}(\mathbf{x}_1,\mathbf{x}_4,\mathbf{x}_5,E_a) =& 4i\alpha\gamma^0 \int \mathrm{d}\mathbf{x}_2 \int \mathrm{d}\mathbf{x}_3 \int \mathrm{d}\omega \Gamma^\nu(\mathbf{x}_1,\mathbf{x}_2,\mathbf{x}_3,E_a,E_a-\omega) \qquad (6.8) \\
& G(\mathbf{x}_3,\mathbf{x}_4,E_a-\omega)\alpha^\mu G(\mathbf{x}_4,\mathbf{x}_5,E_a-\omega)\alpha^\rho D_{\nu\rho}(\mathbf{x}_2,\mathbf{x}_5,\omega)\,, \\
\Gamma^\mu_{\mathrm{O,ladder}}(\mathbf{x}_1,\mathbf{x}_3,\mathbf{x}_5,E_a) =& (2i\alpha)^2\gamma^0 \int \mathrm{d}\mathbf{x}_2 \int \mathrm{d}\mathbf{x}_4 \int \mathrm{d}\omega_1 \int \mathrm{d}\omega_2 \alpha^\nu G(\mathbf{x}_1,\mathbf{x}_2,E_a-\omega_1)\alpha^\rho \\
& G(\mathbf{x}_2,\mathbf{x}_3,E_a-\omega_1-\omega_2)\alpha^\mu G(\mathbf{x}_3,\mathbf{x}_4,E_a-\omega_1-\omega_2)\alpha^\sigma \\
& G(\mathbf{x}_4,\mathbf{x}_5,E_a-\omega_2)\alpha^\beta D_{\nu\sigma}(\mathbf{x}_1,\mathbf{x}_4,\omega_1) D_{\rho\beta}(\mathbf{x}_2,\mathbf{x}_5,\omega_2)\,. \qquad (6.9)
\end{aligned}$$

6.1.2 The loop-after-loop diagrams

The three loop-after-loop (LAL) diagrams shown in the first line of Fig. 6.2 can be further cast into 3 categories. In the spectral representation of the propagator $\sum_n \frac{|n\rangle\langle n|}{E_a - E_n}$ between the two SE loops or between a magnetic vertex and an SE loop, if the intermediate state $|n\rangle$ equals the reference state $|a\rangle$, the expression can again be reduced to products of matrix elements appearing in a lower order of perturbation theory. This contribution is called reducible, and the rest of the sum, i.e. the term containing the reduced Green's function $\sum_{n,n\neq a} \frac{|n\rangle\langle n|}{E_a - E_n}$ is called the irreducible contribution. As in the case of the LAL diagrams we have two Green's functions where the separation into reducible and irreducible parts can be made. We differentiate between irreducible-irreducible ("irred-irred"), irreducible-reducible ("irred-red") and reducible-reducible ("red-red") parts. These contributions are illustrated in Fig. 6.4 and 6.5 in a diagrammatic form.

As will be discussed later, it is convenient to consider the "irred-irred" LAL diagrams along with those "irred-red" LAL diagrams which contain the LAL structure, i.e. in which two loops are connected by a reduced Green's function. In the following, we will refer to these diagrams simply as the LAL contribution. The remaining "irred-red" as well as the "red-red" diagrams will be referred to as the "LAL, red" contribution. The complete LAL contribution, defined in this way, is shown in Fig. 6.4.

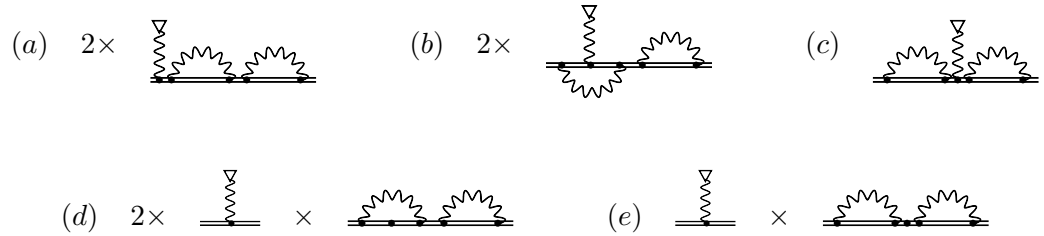

Figure 6.4: Two-loop SE diagrams with the loop-after-loop structure ("LAL" contribution). Double lines between two SE loops or between an SE loop and the magnetic interaction represent reduced Green's functions. A double line with a dot denotes a derivative of a (full or reduced) Green's function with respect to the energy: $\frac{\partial G(E)}{\partial E}\Big|_{E=E_a}$.

The energy shifts corresponding to the LAL diagrams, following the notation of Fig. 6.4, are as follows:

$$\Delta E_{\mathrm{LAL},a} = 2\langle a|\gamma^0\Sigma \sum_{n,n\neq a} \frac{|n\rangle\langle n|}{E_a - E_n}\gamma^0\Sigma|\delta a\rangle\,, \tag{6.10}$$

$$\Delta E_{\mathrm{LAL},b} = 2\langle a|\gamma^0\Sigma \sum_{n,n\neq a} \frac{|n\rangle\langle n|}{E_a - E_n}\gamma^0 e\Gamma^\mu A_{m_\mu}|a\rangle\,, \tag{6.11}$$

$$\Delta E_{\mathrm{LAL},c} = \langle a|\gamma^0\Sigma \sum_{n_1,n_1\neq a} \frac{|n_1\rangle\langle n_1|}{E_a - E_{n_1}}\gamma^0 e\not{A}_m \sum_{n_2,n_2\neq a} \frac{|n_2\rangle\langle n_2|}{E_a - E_{n_2}}\gamma^0\Sigma|a\rangle\,, \tag{6.12}$$

$$\Delta E_{\mathrm{LAL},d} = 2\Delta E_{\mathrm{mag}}\langle a|\gamma^0\Sigma \sum_{n,n\neq a} \frac{|n\rangle\langle n|}{E_a - E_n}\gamma^0 \left.\frac{\partial\Sigma}{\partial E}\right|_{E=E_a}|a\rangle\,, \tag{6.13}$$

$$\Delta E_{\mathrm{LAL},e} = -\,\Delta E_{\mathrm{mag}}\langle a|\gamma^0\Sigma \sum_{n,n\neq a} \frac{|n\rangle\langle n|}{(E_a - E_n)^2}\gamma^0\Sigma|a\rangle\,. \tag{6.14}$$

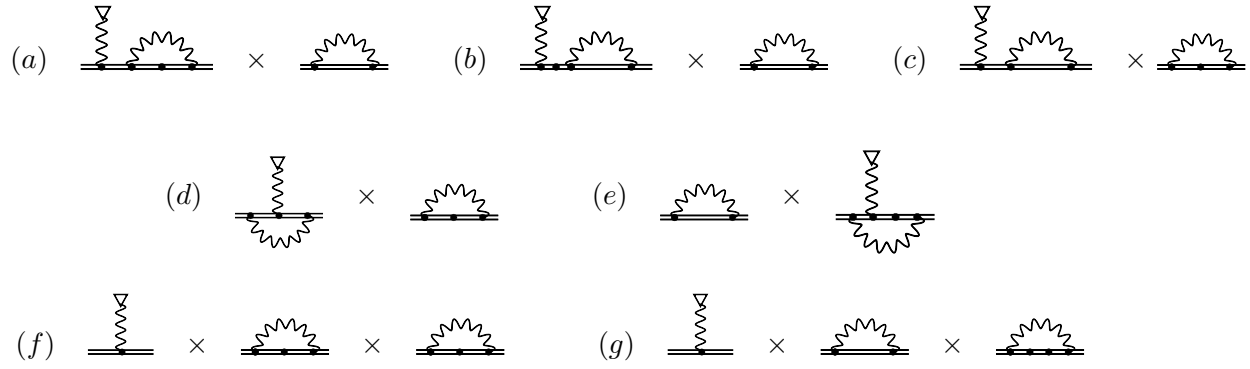

Figure 6.5: Reducible two-loop SE diagrams which can be represented as products of one-loop diagrams ("LAL, red" contribution).

For the "LAL, red" diagrams, shown in Fig. 6.5, we find the following energy shifts:

$$\Delta E_{\mathrm{LAL,red},a} = 2\langle a|\gamma^0 \left.\frac{\partial\Sigma}{\partial E}\right|_{E=E_a} |\delta a\rangle\langle a|\gamma^0\Sigma|a\rangle\,, \tag{6.15}$$

$$\Delta E_{\mathrm{LAL,red},b} = 2\langle a|\gamma^0\Sigma|\delta_D a\rangle\langle a|\gamma^0\Sigma|a\rangle\,, \tag{6.16}$$

$$\Delta E_{\mathrm{LAL,red},c} = 2\langle \delta a|\gamma^0\Sigma|a\rangle\langle a|\gamma^0 \left.\frac{\partial\Sigma}{\partial E}\right|_{E=E_a} |a\rangle\,, \tag{6.17}$$

$$\Delta E_{\mathrm{LAL,red},d} = \langle a|\gamma^0 \left.\frac{\partial\Sigma}{\partial E}\right|_{E=E_a} |a\rangle\langle a|\gamma^0\Gamma^\mu A_{m_\mu}|a\rangle\,, \tag{6.18}$$

$$\Delta E_{\mathrm{LAL,red},e} = \langle a|\gamma^0\Sigma|a\rangle\langle a|\gamma^0 \left.\frac{\partial\Gamma^\mu}{\partial E}\right|_{E=E_a} eA_{m_\mu}|a\rangle\,, \tag{6.19}$$

$$\Delta E_{\mathrm{LAL,red},f} = \Delta E_{\mathrm{mag}}\langle a|\gamma^0 \left.\frac{\partial\Sigma}{\partial E}\right|_{E=E_a} |a\rangle^2\,, \tag{6.20}$$

$$\Delta E_{\mathrm{LAL,red},g} = \Delta E_{\mathrm{mag}}\langle a|\gamma^0\Sigma|a\rangle\langle a|\gamma^0 \left.\frac{\partial^2\Sigma}{\partial E^2}\right|_{E=E_a} |a\rangle\,. \tag{6.21}$$

Here, Σ and Γ^μ are the one-loop SE and vertex functions [57], respectively, and $|\delta a\rangle$ and $|\delta_D a\rangle$ are bound-electron wave functions perturbed by the magnetic field: $|\delta a\rangle = \sum_{n,n\neq a} \frac{|n\rangle\langle n|\gamma^0 e\not{A}_m|a\rangle}{E_a-E_n}$, $|\delta_D a\rangle = -\sum_{n,n\neq a} \frac{|n\rangle\langle n|\gamma^0 e\not{A}_m|a\rangle}{(E_a-E_n)^2}$.

We would like to point out that our formulas, containing the results of our two-time Green's function calculations, are the result of partial cancellations between Z_5 and subtraction terms, defined in equation (3.38). In table 6.1 we give a schematic overview of all terms contributing to the two-loop SE correction to the g-factor originating from Z_5 and various subtraction terms.

	Z_5	$-Z_1N_4$	$+Z_1N_2^2$	$-Z_3N_2$	$-Z_2N_3$	total
N & O, ver	1	0	0	0	0	1
N & O, irred	2	0	0	0	0	2
N & O, red	2	-1	0	0	0	1
LAL, a	2	0	0	0	0	2
LAL, b	2	0	0	0	0	2
LAL, c	1	0	0	0	0	1
LAL, d	4	-2	0	0	0	2
LAL, e	2	-1	0	0	0	1
LAL, red a	4	0	0	0	-2	2
LAL, red b	4	0	0	0	-2	2
LAL, red c	4	0	0	-2	0	2
LAL, red d	2	0	0	-1	0	1
LAL, red e	2	0	0	0	-1	1
LAL, red f	3	-1	1	-2	0	1
LAL, red g	3	-1	0	0	-1	1

Table 6.1: Overview of all contributions to the two-loop SE correction to the g-factor. E.g. the energy shift due to the reducible N and O contribution originating from Z_5 is twice the value given in equation (6.2), an energy shift of minus the value given in equation (6.2) originates from the subtraction term $-Z_1N_4$, hence the total value. Z_i and N_i were defined in equation (3.38).

6.2 Energy-dependent perturbation theory for two-loop SE diagrams

Having established the correspondence between energy dependent perturbation theory and the energy shift due to loop diagrams in section 4.3, we can extend this approach to check our TTGF calculations for the two-loop SE contribution to the bound-fermion g-factor. The relevant diagrams are of first order in the magnetic field, order $\mathcal{O}\left(e^5\right)$ and of first to third order in perturbation theory. We have to include two-loop SE $V_{\mathrm{SE2}}(E)$ and vertex functions $V_{\mathrm{ver2}}(E)$ ($\mathcal{O}\left(e^4\right)$ and $\mathcal{O}\left(e^5\right)$ respectively) into the perturbation term. We define the "two-loop vertex potential" as $V_{\mathrm{ver,2loop}} = \gamma^0 \sum\limits_{ij} \Gamma^{\mu}_{ij} e A_{m_\mu}$ and the two-loop SE potential as $V_{\mathrm{SE,2loop}} = \sum\limits_{i} \gamma^0 \Sigma_i$ to obain the total perturbation potential:

$$V(E) = V_{\mathrm{mag}} + V_{\mathrm{SE}}(E) + V_{\mathrm{ver}}(E) + V_{\mathrm{SE2}}(E) + V_{\mathrm{ver2}}(E). \tag{6.22}$$

$V_{\mathrm{mag}} = e\gamma^0 \not{A}_m$, $V_{\mathrm{SE}}(E) = \gamma^0 \Sigma(E)$ and $V_{\mathrm{ver}}(E) = \gamma^0 \Gamma^{\mu}(E) A_{m_\mu}$ are the same as in section 4.3. The two-loop contribution to $\delta E^{(1)}$ reads:

$$\Delta E^{(1)}_{\mathrm{2loop}} = \langle a | V_{\mathrm{ver2}}(E) | a \rangle. \tag{6.23}$$

The second-order energy shift reads:

$$\begin{aligned}
\Delta E^{(2)}_{\mathrm{2loop}} =& 2 \sum_{n \neq a} \frac{\langle a | V_{\mathrm{SE}}(E_a) | n \rangle \langle n | V_{\mathrm{ver}} | a \rangle}{E_a - E_n} + 2 \sum_{n \neq a} \frac{\langle a | V_{\mathrm{mag}}(E_a) | n \rangle \langle n | V_{\mathrm{SE2}} | a \rangle}{E_a - E_n} + \\
& \langle a | V_{\mathrm{SE}}(E_a) | a \rangle \langle a | \left. \frac{\partial V_{\mathrm{ver}}}{\partial E} \right|_{E_a} | a \rangle + \langle a | V_{\mathrm{ver}}(E_a) | a \rangle \langle a | \left. \frac{\partial V_{\mathrm{SE}}}{\partial E} \right|_{E_a} | a \rangle + \\
& \langle a | V_{\mathrm{mag}} | a \rangle \langle a | \left. \frac{\partial V_{\mathrm{SE2}}}{\partial E} \right|_{E_a} | a \rangle.
\end{aligned} \tag{6.24}$$

We see that the sum of all vertex diagrams corresponds to the first-order energy shift obtained in the framework of energy-dependent perturbation theory. Similarly, the sum of the irreducible and reducible N and O contributions correspond to a part of the second-order energy shift.

Of all contributions to $V(E)$, only V_{mag} and $V_{\mathrm{SE}}(E)$ can combine to third order perturbation theory terms of order $\mathcal{O}\left(e^5\right)$. Inserting the potential $V(E) = V_{\mathrm{mag}} + V_{\mathrm{SE}}(E)$ into the expression for $\delta E^{(3)}$ [197], we obtain:

$$
\begin{aligned}
\delta E^{(3)}_{\text{2loop}} =& 2 \sum_{n_1 \neq a} \sum_{n_2 \neq a} \frac{\langle a|V_{\text{mag}}|n_1\rangle\langle n_1|V_{\text{SE}}(E_a)|n_2\rangle\langle n_2|V_{\text{SE}}(E_a)|a\rangle}{(E_a - E_{n_1})(E_a - E_{n_2})} \\
&+ \sum_{n_1 \neq a} \sum_{n_2 \neq a} \frac{\langle a|V_{\text{SE}}(E_a)|n_1\rangle\langle n_1|V_{\text{mag}}|n_2\rangle\langle n_2|V_{\text{SE}}(E_a)|a\rangle}{(E_a - E_{n_1})(E_a - E_{n_2})} \\
&+ 2\langle a|V_{\text{mag}}|a\rangle \sum_{n \neq a} \frac{\langle a|V_{\text{SE}}(E_a)|n\rangle\langle n| \left.\frac{\partial V_{\text{SE}}}{\partial E}\right|_{E_a} |a\rangle}{E_a - E_n} \\
&- \langle a|V_{\text{mag}}|a\rangle \sum_{n \neq a} \frac{\langle a|V_{\text{SE}}(E_a)|n\rangle\langle n|V_{\text{SE}}(E_a)|a\rangle}{(E_a - E_n)^2} \\
&+ 2\langle a| \left.\frac{\partial V_{\text{SE}}}{\partial E}\right|_{E_a} |a\rangle \sum_{n \neq a} \frac{\langle a|V_{\text{SE}}(E_a)|n\rangle\langle n|V_{\text{mag}}|a\rangle}{E_a - E_n} \\
&+ 2\langle a|V_{\text{SE}}(E_a)|a\rangle \sum_{n \neq a} \frac{\langle a|V_{\text{mag}}|n\rangle\langle n| \left.\frac{\partial V_{\text{SE}}}{\partial E}\right|_{E_a} |a\rangle}{E_a - E_n} \\
&- 2\langle a|V_{\text{SE}}(E_a)|a\rangle \sum_{n \neq a} \frac{\langle a|V_{\text{mag}}|n\rangle\langle n|V_{\text{SE}}(E_a)|a\rangle}{(E_a - E_n)^2} \\
&+ \langle a|V_{\text{mag}}|a\rangle\langle a| \left.\frac{\partial V_{\text{SE}}}{\partial E}\right|_{E_a} |a\rangle^2 \\
&+ \langle a|V_{\text{mag}}|a\rangle\langle a|V_{\text{SE}}(E_a)|a\rangle\langle a| \left.\frac{\partial^2 V_{\text{SE}}}{\partial E^2}\right|_{E_a} |a\rangle. \qquad (6.25)
\end{aligned}
$$

We found a perfect agreement between the energy shifts $\delta E^{(1)}_{\text{2loop}}$, $\delta E^{(2)}_{\text{2loop}}$, $\delta E^{(3)}_{\text{2loop}}$ and our results obtained with the two-time Green's function method in the previous section. This energy-dependent perturbation theory calculation was an important consistency check for our results obtained using the TTGF method.

6.3 Two-loop self-energy, renormalization

6.3.1 Mass renormalization

Analyzing counterterm Feynman diagrams, one observes that every SE function $\Sigma(p)$ is accompanied by the corresponding mass renormalization counterterm δm. This applies to the one-loop SE function $\Sigma(p)$, when it appears in LAL diagrams and as a subgraph of the N SE or vertex functions, as well as the N and O SE functions $\Sigma_N(p)$ and $\Sigma_O(p)$. The latter two are always accompanied by a two-loop mass renormalization counterterm $\delta m^{(2)}_N$ and $\delta m^{(2)}_O$ respectively [63]. We therefore assume mass renormalization implicitly, i.e. instead of considering $\Sigma(p)$, we consider the mass-renormalized SE function $\widetilde{\Sigma}(p) := \Sigma(p) - \delta m$. We apply this to both the one-loop and the two-loop SE functions.

6.3.2 Charge renormalization

One-loop diagrams

We begin the discussion of charge divergences by analyzing the one-loop SE function using a compact notation. The one-loop SE function has been analyzed thoroughly in the literature (see Ref. [63, 72]), but we will repeat this discussion because it is essential for the understanding of the two-loop case.

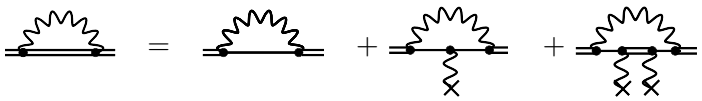

Figure 6.6: Decomposition of the Lamb shift self-energy correction into zero-, one-, and many-potential terms [72]. A single line stands for a free Dirac electron propagator, and a wave line terminated by a cross represents a Coulomb interaction.

Expanding the one-loop SE function in powers of interactions with the nuclear potential A_e, we find [63]

$$\widetilde{\Sigma} = \widetilde{\Sigma}^{(0)} + \Sigma^{(1)} + \Sigma^{(2+)}\,, \tag{6.26}$$

where the index $^{(n)}$ denotes the number of interactions (see Fig. 6.6). The zero-potential SE function was defined in Chapter 4. Using the notation from Chapter 4, the one-potential SE function is defined as $\Sigma^{(1)} = \Gamma^{(0)0}V$. The many-potential SE function is similar to the full SE function, with the electron Green's function replaced by the many-potential Green's function. One can show that $\Sigma^{(2+)}$ is finite, while $\widetilde{\Sigma}^{(0)}$ and $\Sigma^{(1)}$ contain charge divergences as follows [63]:

$$\widetilde{\Sigma}^{(0)} = B^{(1)}(\not{p} - m) + \Sigma^{(0)}_{\rm R}\,, \tag{6.27}$$

$$\Sigma^{(1)} = L^{(1)} e\not{A}_e + \Sigma^{(1)}_{\rm R}\,. \tag{6.28}$$

Here,

$$B^{(1)} = -L^{(1)} \tag{6.29}$$

are divergent renormalization constants and $\Sigma^{(0)}_{\rm R}(p)$ and $\Sigma^{(1)}_{\rm R}(p)$ are the finite (regular, R) remainders [63]. $A_{e\mu}$ is the 4-vector potential containing the Coulomb potential of the nucleus. Therefore, the one-loop SE function reads [63]

$$\widetilde{\Sigma} = B^{(1)}(\not{p} - e\not{A}_e - m) + \Sigma^{(0)}_{\rm R} + \Sigma^{(1)}_{\rm R} + \Sigma^{(2+)}\,. \tag{6.30}$$

Since $(\not{p} - e\not{A}_e - m)|a\rangle = 0$, the above one-loop SE function does not contain charge divergences as long as it acts on the bound-electron wave function $|a\rangle$ [63].

In the forthcoming calculations, the derivative of the one-loop SE function with respect to energy, $\left.\dfrac{\partial\widetilde{\Sigma}}{\partial E}\right|_{E=E_a}$, will also be required. Taking this derivative of the expression (6.30)

for the one-loop SE function, we find that the energy derivative contains the following charge-divergent term:

$$\left.\frac{\partial\widetilde{\Sigma}}{\partial E}\right|_{E=E_a} = B^{(1)}\gamma^0 + (\text{UV finite terms}). \tag{6.31}$$

We also need the knowledge of charge divergences in the one-loop vertex function. The one-loop vertex function can be expanded as

$$\Gamma^\mu = \Gamma^{(0)\mu} + \Gamma^{(1+)\mu}, \tag{6.32}$$

where only the zero-potential contribution contains charge divergences [57]:

$$\Gamma^{(0)\mu} = L^{(1)}\gamma^\mu + \Gamma_{\rm R}^{(0)\mu}. \tag{6.33}$$

It is easy to see that the second derivative of the one-loop SE function and the derivative of the one-loop vertex function with respect to energy do not contain UV divergences. With this, we can begin the analysis of charge divergences in the individual two-loop diagrams.

Loop-after-loop diagrams

It is convenient to consider the "irred, irred" LAL diagrams together with those "irred, red" LAL diagrams which contain the LAL structure. These diagrams are shown in Fig. 6.4. We will show that this subset of two-loop SE diagrams is UV finite:

(i) In diagrams (c) and (e), both SE operators act on the bound-electron wave function. According to the above analysis of the one-loop SE function, these diagrams are finite.

(ii) Diagram (d) contains both the one-loop SE function and its derivative with respect to energy. While the SE function does not give a UV divergent contribution (since it acts on the bound-electron wave function), its derivative contains a charge-divergent term. Calculating the energy shift that corresponds to this divergent term, we find

$$\Delta E_{\mathrm{LAL},d,\mathrm{div}} = 2\Delta E_{\rm mag}\langle a|\gamma^0\widetilde{\Sigma}\sum_{n,n\neq a}\frac{|n\rangle\langle n|}{E_a-E_n}\gamma^0 B^{(1)}\gamma^0|a\rangle\,. \tag{6.34}$$

Here, and in the following, the subscript "div" indicates that we are considering the contribution due to divergent renormalization constants only. This expression contains the scalar products $\langle n|a\rangle$ (note that $\gamma^0\gamma^0$ is the unity matrix [6]), which are all zero because the sum excludes the reference state ($n \neq a$). Therefore, the charge-divergent contribution to this diagram vanishes.

(iii) In diagram (b), the SE function gives a finite contribution. Charge divergences are possible only because of the charge divergence in the one-loop vertex function. The corresponding charge-divergent contribution to the energy shift reads

$$\Delta E_{\mathrm{LAL},b,\mathrm{div}} = 2\langle a|\gamma^0\widetilde{\Sigma}\sum_{n,n\neq a}\frac{|n\rangle\langle n|}{E_a-E_n}\gamma^0 L^{(1)}e\not{A}_m|a\rangle = 2L^{(1)}\langle a|\gamma^0\widetilde{\Sigma}|\delta a\rangle\,. \tag{6.35}$$

We see that the charge-divergent contribution to this diagram does not vanish.

(iv) Diagram (a) can also contain charge divergences because one of the SE functions in this diagram does not act on the bound-electron wave function but is "sandwiched" by two reduced Green's functions $G_{\rm red} = \sum_{n,n\neq a} \frac{|n\rangle\langle n|}{E_a - E_n}$. To determine the charge-divergent contribution, we use the identity (see Ref. [197])

$$(\not{p} - m)G_{\rm red} = \gamma^0 + e\not{A}_e G_{\rm red}\,. \tag{6.36}$$

We find the following expression for the divergent contribution to the energy shift:

$$\Delta E_{{\rm LAL},a,{\rm div}} = 2B^{(1)}\langle a|\gamma^0\widetilde{\Sigma}|\delta a\rangle\,, \tag{6.37}$$

which, because of Eq. (6.29), cancels the charge-divergent contribution of diagram (b).

Finally, we can conclude that the total contribution of all diagrams with the LAL structure is finite. It is therefore possible to analyze the LAL contribution independently from the remaining diagrams.

LAL, reducible diagrams

The remaining "irred, red" and "red, red" diagrams can be represented as products of two one-loop diagrams. These diagrams are shown in Fig 6.5. Some of these diagrams do not contain charge divergences:

- Diagram (b) contains only the one-loop SE function acting on at least one bound-electron wave function.
- Diagrams (e) and (g) contain the one-loop SE function acting on bound-electron wave functions as well as one-loop functions which are UV finite.
- Diagram (a) does not contain charge divergences for the same reason as the LAL diagram (d).

The remaining diagrams do contain charge divergences. There is a partial cancellation of charge divergences between diagrams (d) and (f). The combined energy shift due to both diagrams can be represented as

$$\begin{aligned}\Delta E_{{\rm LAL,red},df} =& \Delta E_{{\rm LAL,red},d} + \Delta E_{{\rm LAL,red},f} \\ =& \langle a|\gamma^0 \left.\frac{\partial\widetilde{\Sigma}}{\partial E}\right|_{E=E_a}|a\rangle \left(\langle a|\gamma^0\Gamma^\mu A_{m\mu}|a\rangle + \Delta E_{\rm mag}\langle a|\gamma^0 \left.\frac{\partial\widetilde{\Sigma}}{\partial E}\right|_{E=E_a}|a\rangle\right).\end{aligned} \tag{6.38}$$

While both terms inside the round brackets contain charge divergences, their sum is finite and corresponds to the combined energy shift $\Delta E_{\rm vr} = \Delta E_{\rm red} + \Delta E_{\rm ver}$ of the one-loop vertex diagram and the reducible one-loop SE diagram which is known from one-loop g-factor calculations [57]. Inserting the charge-divergent contribution to $\left.\frac{\partial\widetilde{\Sigma}}{\partial E}\right|_{E=E_a}$ into the above equation, we obtain the following charge-divergent contribution to the energy shift:

$$\Delta E_{{\rm LAL,red},df,{\rm div}} = B^{(1)}\Delta E_{\rm vr}\,. \tag{6.39}$$

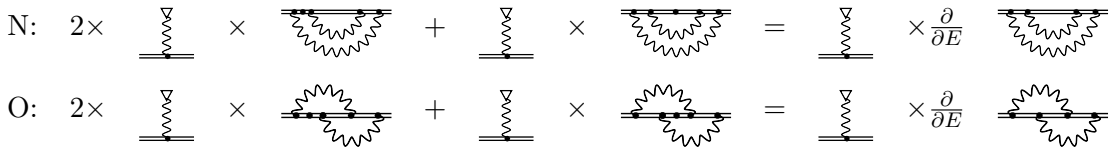

Figure 6.7: Reducible parts of the nested-loop and overlapping-loop diagrams.

In diagram (c), the derivative of the one-loop SE function contains charge divergences, while the SE function is finite. The corresponding energy shift is the product of the divergent renormalization constant and the irreducible SE contribution to the one-loop g-factor:

$$\Delta E_{\mathrm{LAL,red},c,\mathrm{div}} = 2B^{(1)}\langle a|\gamma^0\widetilde{\Sigma}|\delta a\rangle\,. \tag{6.40}$$

Nested-loop and overlapping-loop diagrams, irreducible contribution

The N and O SE functions Σ_{N} and Σ_{O}, which appear in the N and O irreducible diagrams, have been analyzed in detail in Ref. [63]. We just quote the relevant results here:

$$\widetilde{\Sigma}_{\mathrm{N}} = B^{(2\mathrm{N})}(\not{p} - e\not{A}_e - m) + B^{(1)}\widetilde{\Sigma} + \Sigma_{\mathrm{N,R}}\,, \tag{6.41}$$

$$\widetilde{\Sigma}_{\mathrm{O}} = B^{(2\mathrm{O})}(\not{p} - e\not{A}_e - m) + 2L^{(1)}\widetilde{\Sigma} + \Sigma_{\mathrm{O,R}}\,, \tag{6.42}$$

where $B^{(2N)}$ and $B^{(2O)}$ are divergent two-loop renormalization constants. Their contributions to the energy shift are zero because the two-loop SE functions act on a bound-electron wave function in all two-loop g-factor diagrams. The energy shifts due to the respective second terms of the above equations are

$$\Delta E_{\mathrm{N,irred,div}} = 2B^{(1)}\langle a|\gamma^0\widetilde{\Sigma}|\delta a\rangle\,, \tag{6.43}$$

$$\Delta E_{\mathrm{O,irred,div}} = 4L^{(1)}\langle a|\gamma^0\widetilde{\Sigma}|\delta a\rangle\,. \tag{6.44}$$

We see that the sum $\Delta E_{\mathrm{N,irred,div}} + \Delta E_{\mathrm{O,irred,div}}$ exactly cancels the charge-divergent contribution from the LAL, reducible diagram (c) in Eq. (6.40).

Nested-loop and overlapping-loop diagrams, reducible contribution

The N and O reducible diagrams are shown in Fig. 6.7. The sum of side and ladder diagrams corresponds to

$$\Delta E_{i,\mathrm{red}} = \Delta E_{\mathrm{mag}}\langle a|\gamma^0\left.\frac{\partial\widetilde{\Sigma}_i}{\partial E}\right|_{E=E_a}|a\rangle\,. \tag{6.45}$$

	N	O
side	-2	2
ladder	1	0

Table 6.2: Integer factors $a_{i,j}$ for the zero-potential vertex functions.

Using the above parameterizations (6.41) and (6.42) of the two-loop SE functions, we obtain the following representations for their energy derivatives:

$$\frac{\partial\widetilde{\Sigma}_{\rm N}}{\partial E} = B^{(2{\rm N})}\gamma^0 + B^{(1)}\frac{\partial\widetilde{\Sigma}}{\partial E} + \frac{\partial\widetilde{\Sigma}_{\rm N,R}}{\partial E}\,, \tag{6.46}$$

$$\frac{\partial\widetilde{\Sigma}_{\rm O}}{\partial E} = B^{(2{\rm O})}\gamma^0 + 2L^{(1)}\frac{\partial\widetilde{\Sigma}}{\partial E} + \frac{\partial\widetilde{\Sigma}_{\rm O,R}}{\partial E}\,. \tag{6.47}$$

The first two terms of both expressions contain charge divergences. The energy shift that corresponds to the charge-divergent terms of the sum of N and O reads

$$\sum_i \Delta E_{i,\rm red,div} = \Delta E_{\rm mag} B^{(2)} + \Delta E_{\rm mag} L^{(1)} \langle a|\gamma^0 \left.\frac{\partial\widetilde{\Sigma}}{\partial E}\right|_{E=E_a} |a\rangle. \tag{6.48}$$

Here, $B^{(2)} = B^{(2{\rm N})} + B^{(2{\rm O})}$ is the sum of the charge-divergent renormalization constants of the N and O terms.

Nested-loop and overlapping-loop vertex diagrams

The N and O vertex diagrams are shown in the second and third line of Fig. 6.2. The discussion of charge divergences in vertex diagrams requires a thorough analysis of the two-loop vertex functions. Just as in the one-loop case, we expand the vertex functions in powers of interactions with the nuclear potential. All zero-potential contributions can be parameterized as

$$\Gamma^{(0)\mu}_{i,j} = \gamma^\mu L^{(2)}_{i,j} + L^{(1)} a_{i,j} \Gamma^{(0)\mu} + \Gamma^{(0)\mu}_{i,j,\rm R}\,, \tag{6.49}$$

where $j \in \{\text{side, ladder}\}$ (see [63]). The $a_{i,j}$ are integers given in table 6.2. We would like to emphasize the similarity between the zero-potential vertex functions and the one-potential SE functions. The latter were analyzed thoroughly in the calculation of the two-loop SE correction to the Lamb shift [63]. The total two-loop renormalization constant is

$$L^{(2)} = \sum_{i,j} L^{(2)}_{i,j} = -B^{(2)}\,. \tag{6.50}$$

Vertex functions with nn interactions with the nuclear potential $\Gamma^{(n)\mu}_{ij}$ contain charge divergences only if they contain a divergent subgraph:

- "O, ladder": This diagram does not contain a divergent subgraph. Therefore, all $\Gamma^{(n)\mu}_{\mathrm{O,ladder,div}}$ with $n \geq 1$ are free from charge divergences.
- "O, side": If all interactions with the nuclear potential are on the extreme right (orientation as in Fig. 6.2), the diagram contains the one-loop vertex function as a subdiagram. Its charge divergences are due to the divergent term in the one-loop vertex function only. The divergent part of the n-potential contribution to the "O, side" vertex function therefore is $\Gamma^{(n)\mu}_{\mathrm{O,side,div}} = 2L^{(1)}\Gamma^{(n)\mu}$.
- "N, ladder": The diagram contains the one-loop vertex function as a divergent subdiagram only if all interactions with the nuclear potential are outside the inner loop. The corresponding divergent part of the n-potential contribution reads $\Gamma^{(n)\mu}_{\mathrm{N,ladder,div}} = L^{(1)}\Gamma^{(n)\mu}$.
- "N, side": Here, we have to distinguish between the cases of zero or one interactions with the nuclear potential inside the inner loop. Diagrams with two or more interactions in the inner loop do not contain charge divergences. n-potential diagrams with zero potentials in the inner loop contain the divergent contribution $2(n+1)B^{(1)}\Gamma^{(n)\mu}$. Those with one potential in the inner loop contain the divergent term $2nL^{(1)}\Gamma^{(n)\mu}$. The total divergent part of the n-potential contribution therefore is $\Gamma^{(n)\mu}_{\mathrm{N,side,div}} = 2B^{(1)}\Gamma^{(n)\mu}$.

Adding all divergences of the N and O vertex functions, we find the total charge divergent contribution to be

$$\sum_{i,j} \Gamma^{\mu}_{i,j,\mathrm{div}} = L^{(2)}\gamma^{\mu} + L^{(1)}\Gamma^{\mu}\,, \tag{6.51}$$

which corresponds to the energy shift

$$\sum_{i,j} \Delta E_{\mathrm{ver},i,j,\mathrm{div}} = L^{(2)}\Delta E_{\mathrm{mag}} + L^{(1)}\langle a|\gamma^0\Gamma^{\mu}A_{m\mu}|a\rangle\,. \tag{6.52}$$

The first divergent term is canceled by the corresponding $B^{(2)}$ term in the N and O reducible diagrams (see Eq. (6.48)). The sum of the charge-divergent contributions of the N and O vertex and reducible diagrams is

$$\sum_{i,j} \Delta E_{\mathrm{ver},i,j,\mathrm{div}} + \sum_{i} \Delta E_{i,\mathrm{red,div}} = L^{(1)}\Delta E_{\mathrm{vr}}\,. \tag{6.53}$$

This term is canceled by the remaining charge-divergent contribution to the "LAL, red" diagrams (see Eq. (6.39)). We thus see that all charge divergences in the two-loop SE diagrams cancel, and the two-loop SE correction to the g-factor is UV finite.

6.4 Reference-state infrared divergences

Reference-state infrared (IR) divergences appear in bound-state QED calculations whenever at least two electron propagators with identical energy value appear in an SE loop. Such IR divergences are present in the one-loop g-factor correction [57] as well as in the two-loop Lamb shift [63]. In both cases, it is possible to identify two Feynman diagrams which are each IR divergent on their own but whose sum is IR finite [57, 63]. The situation for the two-loop SE correction to the bound-electron g-factor is somewhat more complicated.

Not all contributions to the two-loop SE correction are IR divergent. The one-loop SE function $\widetilde{\Sigma}$ and the two-loop O SE function $\widetilde{\Sigma}_{\rm O}$ are IR finite [63]. Therefore, all diagrams which contain only these SE functions are IR finite. These are the irreducible O contribution, the LAL diagrams (a), (c) and (e) in Fig. 6.4, as well as the "LAL, red" diagram (b) in Fig. 6.5.

The remaining contributions contain IR divergences. We keep in mind that in the case of the one-loop SE correction to the g-factor, both the vertex and the reducible SE contriburtion are IR divergent, but the sum of the two diagrams is finite [57].

Replacing one external electron wave function $|a\rangle$ in the above mentioned one-loop g-factor diagrams with $\sum_{n,n\neq a} \frac{|n\rangle\langle n|\Sigma|a\rangle}{E_a-E_n}$, and multiplying by a factor of two, we obtain the energy shifts corresponding to the LAL diagrams (b) and (d) in Fig. 6.4. The cancellation of IR divergences between these two diagrams works in exactly the same way as for the one-loop g-factor correction. This means that the LAL contribution, shown to be UV finite in the previous section, is also IR finite. Analogously, one can show that the IR divergences of the "O, ver" and "O, red" contributions also cancel each other.

The two-loop N SE function $\widetilde{\Sigma}_{\rm N}$ is IR divergent, which leads to divergences in the two-loop Lamb shift. This IR divergence was found to be canceled by the reducible Lamb shift contribution (see [63] for details). Replacing one external electron line by the magnetic wave function in both Lamb shift diagrams, and multiplying by a factor of two, we obtain the "N, irred" diagram and the "LAL, red" diagram (a) of Fig. 6.5. The cancellation of IR divergences between these two diagrams is identical to the case of the Lamb shift. This case has been studied in detail in the literature [63], so we will not repeat this analysis here.

For the remaining diagrams, it is not sufficient to form the sum of two diagrams in order to cancel IR divergences. E.g. the "LAL, red" diagrams (d) and (f) (see Fig. 6.5) each consist of two IR-divergent factors. The energy shift which corresponds to the sum of both diagrams is still IR divergent:

$$\Delta E_{\rm LAL,red,}{}_{df} = -\frac{i}{2\pi}\int {\rm d}\omega \sum_n \frac{\langle an|I(\omega)|na\rangle}{(E_a-\omega-E_n(1-i\eta))^2}\Delta E_{\rm vr}\,. \tag{6.54}$$

The reference-state contribution to this energy shift is

$$\Delta E_{\rm LAL,red,}{}_{df,{\rm ref}} = -\frac{i}{2\pi}\int {\rm d}\omega \sum_m \frac{\langle aa_m|I(\omega)|a_m a\rangle}{(-\omega+i\eta)^2}\Delta E_{\rm vr}\,. \tag{6.55}$$

$\sum_m$ is a sum over the angular momentum projection quantum number. Comparing this expression with equation (4.43), we conclude that the $m = m_a$ term in this sum is IR divergent, and the $m = -m_a$ term is finite.

It is convenient to consider a "N, ver" diagram along with a corresponding reducible diagram, although each such pair is IR divergent. Let us now consider the sum of the "N, ver" ladder and the "N, red" ladder contributions. Performing an analysis similar to the one-loop case, we find that the IR divergences due to the inner loop cancel in the sum. However, this sum is IR divergent because of the reference state contributions to the electron propagators to the left and right of the inner loop. Using the spectral representation of the bound-electron Green's function, we obtain the following expression for the combined energy shift of the "N, ver" ladder and "N, red" ladder contributions:

$$\begin{aligned}\Delta E_{\mathrm{N,vr,lad}} = \left(\frac{i}{2\pi}\right)^2 \int \mathrm{d}\omega_1 \int \mathrm{d}\omega_2 \frac{\langle a n_4|I(\omega_1)|n_1 a\rangle}{(E_a-\omega_1-E_{n_1}(1-i\eta))(E_a-\omega_1-E_{n_4}(1-i\eta))} \\ \times \left(\frac{\langle n_2|\gamma^0 e\not{A}_m|n_3\rangle\langle n_1 n_3|I(\omega_2)|n_2 n_4\rangle}{(E_a-\omega_1-\omega_2-E_{n_2}(1-i\eta))(E_a-\omega_1-\omega_2-E_{n_3}(1-i\eta))} - \right. \\ \left. \frac{\Delta E_{\mathrm{mag}}\langle n_1 n_2|I(\omega_2)|n_2 n_4\rangle}{(E_a-\omega_1-\omega_2-E_{n_2}(1-i\eta))^2}\right). \end{aligned} \tag{6.56}$$

Here, $\Delta E_{\mathrm{N,vr,lad}} = \Delta E_{\mathrm{ver,N,lad}} + \Delta E_{\mathrm{N,lad,red}}$. We will analyze the two reference-state terms with $(n_1,\kappa_1,m_1) = (n_4,\kappa_4,m_4) = (n_a,\kappa_a,m_a)$ and $(n_1,\kappa_1,m_1) = (n_4,\kappa_4,m_4) = (n_a,\kappa_a,-m_a)$ separately. The reference-state contribution with $(n_1,\kappa_1,m_1) = (n_4,\kappa_4,m_4) = (n_a,\kappa_a,-m_a)$ is

$$\begin{aligned}\Delta E_{\mathrm{N,vr,lad,IR-}} = \left(\frac{i}{2\pi}\right)^2 \int \mathrm{d}\omega_1 \frac{\langle a a_{-m_a}|I(\omega_1)|a_{-m_a} a\rangle}{(-\omega_1+i\eta)^2} \\ \int \mathrm{d}\omega_2 \sum_{n_2} \left(- \frac{\Delta E_{\mathrm{mag}}\langle a_{-m_a} n_2|I(\omega_2)|n_2 a\rangle}{(E_a-\omega_1-\omega_2-E_{n_2}(1-i\eta))^2} \right. \\ \left. + \sum_{n_3} \frac{\langle a_{-m_a} n_3|I(\omega_2)|n_2 a_{-m_a}\rangle\langle n_2|\gamma^0 e\not{A}_m|n_3\rangle}{(E_a-\omega_1-\omega_2-E_{n_2}(1-i\eta))(E_a-\omega_1-\omega_2-E_{n_3}(1-i\eta))}\right). \end{aligned} \tag{6.57}$$

In order to investigate whether this expression is IR divergent or IR finite, it is sufficient to consider the reference-state term of the expression in brackets ($(n_2,\kappa_2) = (n_3,\kappa_3) = (n_a,\kappa_a)$). The result is

$$\begin{aligned}\Delta E_{\mathrm{N,vr,lad,IR-,ref}} = \left(\frac{i}{2\pi}\right)^2 \int \mathrm{d}\omega_1 \frac{\langle a a_{-m_a}|I(\omega_1)|a_{-m_a} a\rangle}{(-\omega_1+i\eta)^2} \\ \int \mathrm{d}\omega_2 \sum_{m_2} \left(\frac{\Delta E_{\mathrm{mag}}\langle a_{-m_a} a_{m_2}|I(\omega_2)|a_{m_2} a\rangle}{(-\omega_1-\omega_2+i\eta))^2}\right)(\mathrm{sgn}(m_2)-1) \end{aligned} \tag{6.58}$$

One can see that there is a contribution due to $m_2 = -m_a$ only. Just like in the one-loop case, we can insert the momentum space representation of the photon Green's function

and perform the integrations over ω_1 and ω_2 to obtain (see also Ref. [63])

$$\Delta E_{\mathrm{N,ver,lad,IR-,ref}} = \Delta E_{\mathrm{mag}} \left(\frac{\alpha}{\pi}\right)^2 \int_0^\infty \mathrm{d}q_1 \int_0^\infty \mathrm{d}q_2 \frac{1}{q_1^2(q_1+q_2)^2} \langle aa_{-m_a}|\alpha^\mu \alpha_\mu \frac{\sin(q_1 x_{14})}{x_{14}}|a_{-m_a}a\rangle \tag{6.59}$$

$$\langle a_{-m_a}a_{-m_a}|\alpha^\nu \alpha_\nu \frac{\sin(q_2 x_{23})}{x_{23}}|a_{-m_a}a_{-m_a}\rangle\,.$$

With an analysis similar to the one-loop case above, we conclude that the first matrix element is proportional to q_1^3 and the second matrix element is proportional to q_2 for small q_1 and q_2. Therefore, $\Delta E_{\mathrm{N,vr,lad,IR-}}$ is finite.

The reference-state contribution with $(n_1,\kappa_1,m_1) = (n_4,\kappa_4,m_4) = (n_a,\kappa_a,m_a)$ is

$$\Delta E_{\mathrm{N,ver,lad,IR+}} = \frac{i}{2\pi}\int \mathrm{d}\omega_1 \frac{\langle aa|I(\omega_1)|aa\rangle}{(-\omega_1+i\eta)^2}\Delta E_{\mathrm{J}}(\omega_1)\,, \tag{6.60}$$

where

$$\Delta E_{\mathrm{J}}(\omega_1) = \frac{i}{2\pi}\int \mathrm{d}\omega_2 \sum_{n_2}\Bigg(-\frac{\Delta E_{\mathrm{mag}}\langle an_2|I(\omega_2)|n_2a\rangle}{(E_a-\omega_1-\omega_2-E_{n_2}(1-i\eta))^2} \tag{6.61}$$

$$+\sum_{n_3}\frac{\langle an_3|I(\omega_2)|n_2a\rangle\langle n_2|\gamma^0 e\not{A}_m|n_3\rangle}{(E_a-\omega_1-\omega_2-E_{n_2}(1-i\eta))(E_a-\omega_1-\omega_2-E_{n_3}(1-i\eta))}\Bigg)\,.$$

Note that $\Delta E_{\mathrm{J}}(0) = \Delta E_{\mathrm{vr}}$ corresponds to the unrenormalized energy shift of the one-loop vertex and reducible SE diagrams. Therefore, the remaining contribution of the "N, ver" ladder, the "N, red" ladder and the "LAL, red" diagrams d and f in Fig. 6.5 is

$$\Delta E_{\mathrm{IR}} = \frac{i}{2\pi}\int \mathrm{d}\omega_1 \frac{\langle aa|I(\omega_1)|aa\rangle}{(-\omega_1+i\eta)^2}(\Delta E_{\mathrm{J}}(\omega_1)-\Delta E_{\mathrm{J}}(0))\,. \tag{6.62}$$

In order to show that this is IR finite, it is sufficient to analyze the reference-state contribution to $\Delta E_{\mathrm{J}}(\omega) - \Delta E_{\mathrm{J}}(0)$:

$$\Delta E_{\mathrm{N,vr,lad,IR+,ref}} = -2\Delta E_{\mathrm{mag}}\left(\frac{i}{2\pi}\right)^2 \int \mathrm{d}\omega_1 \frac{\langle aa|I(\omega_1)|aa\rangle}{(-\omega_1+i\eta)^2} \tag{6.63}$$

$$\int \mathrm{d}\omega_2 \left(\frac{\langle aa_{-m_a}|I(\omega_2)|a_{-m_a}a\rangle}{(-\omega_1-\omega_2+i\eta)^2} - \frac{\langle aa_{-m_a}|I(\omega_2)|a_{-m_a}a\rangle}{(-\omega_2+i\eta)^2}\right)\,.$$

Inserting the momentum-space photon propagator and carrying out the integrations $\int \mathrm{d}\omega_1$ and $\int \mathrm{d}\omega_2$ analytically [63], we obtain

$$\Delta E_{\mathrm{N,vr,lad,IR+,ref}} = \Delta E_{\mathrm{mag}}\frac{2\alpha^2}{\pi^2}\int_0^\infty \mathrm{d}q_1 \int_0^\infty \mathrm{d}q_2 \frac{q_1+2q_2}{q_1 q_2^2 (q_1+q_2)^2}$$

$$\langle aa|\alpha^\mu\alpha_\mu \sin(q_1 x_{14})|aa\rangle\langle aa_{-m_a}|\alpha^\nu\alpha_\nu \sin(q_2 x_{23})|a_{-m_a}a\rangle\,. \tag{6.64}$$

Keeping in mind that, following the discussion of IR divergences in the one-loop SE correction, the first matrix element is proportional to q_1 and the second one is proportional to q_2^3, we see that the entire expression is finite.

In a similar way, it can be shown that the sum of the "N, ver" side, the "N, red" side and the "LAL, red" contributions c and e in Fig. 6.5 is finite. Thus, we see that the entire two-loop SE correction to the bound-electron g-factor is both UV and IR finite, with the LAL diagrams constituting a subset of the two-loop SE diagrams which is both UV and IR finite on its own. A specific subtraction procedure to deal with IR divergences, comparable to the subtraction procedure employed in the two-loop SE correction to the Lamb shift [63], will be developed in a future analysis.

6.5 Separation of the two-loop terms into categories

In order to deal with UV divergences, we split all diagrams into different contributions. One-loop functions can simply be split into the zero-, one- (if applicable) and many-potential functions (see Fig. 6.6 and 4.4) [69]. The zero- and, in some cases, the one-potential contributions are UV divergent. These UV divergent contributions are evaluated in the momentum space, using the dimensional regularization procedure to isolate UV-divergent terms. The many-potential functions which are UV finite are computed in the coordinate representation, since these involve the Coulomb-Dirac propagator which is known only in coordinate space [63]. A position-space renormalization scheme for position-space representations [250–253] has not yet been generalized for two-loop calculations [63, 246].

The LAL and the "LAL, red" contributions can be dealt with using a straightforward generalization of this procedure. The situation is more complicated for the N and O diagrams. While in the one-loop case, diagrams can always be divided into UV-divergent contributions and contributions which contain the bound-electron propagator, two-loop diagrams need to be divided into three different categories: (i) Diagrams which contain UV divergences, (ii) diagrams which contain the bound-electron propagator, and (iii) diagrams which contain both [63]. Using the nomenclature which was introduced for the computation of the two-loop SE correction to the Lamb shift, we refer to these categories as the F, M and P term, respectively [65].

Replacing $|\delta a\rangle$ with $|a\rangle$ in the "N, irred" and "O, irred" contributions, we obtain the known Lamb shift diagrams [63]. Therefore, the separation of the "N, irred" and "O, irred" diagrams into F, P and M term is identical to the case of the Lamb shift. This separation is illustrated in Fig. 6.8 and 6.9.

For the N and O, red and vertex diagrams, we consider the expansion of the electron propagators in powers of interactions with the nuclear potential, and analyze the superficial degree of divergence d, as defined in Ref. [6]. According to Ref. [6], if $d \geq 0$, a diagram is expected to contain UV divergences unless it is a tree-level diagram or divergences cancel due to symmetries. If $d < 0$, a diagram is expected to be finite unless it contains a UV divergent subdiagram [6]. We divided the contributions into F, P and

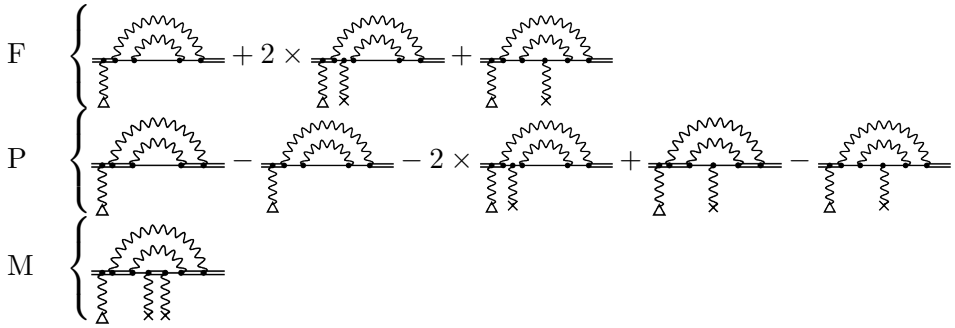

Figure 6.8: Separation of the "N, irred" contributions into F (first line), P (second line) and M term (third line) [63].

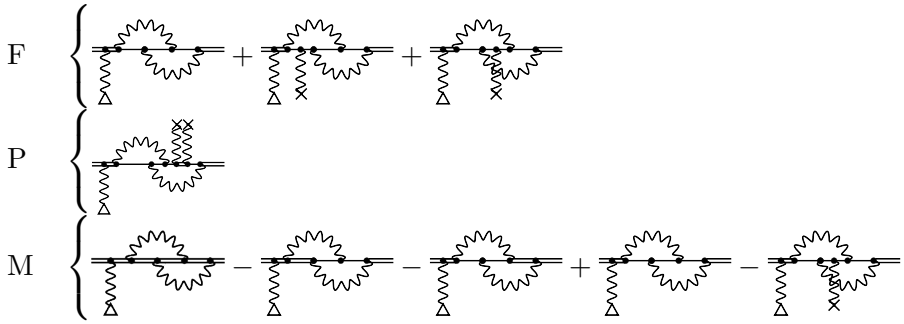

Figure 6.9: Separation of the "O, irred" contributions into F, P and M terms [63].

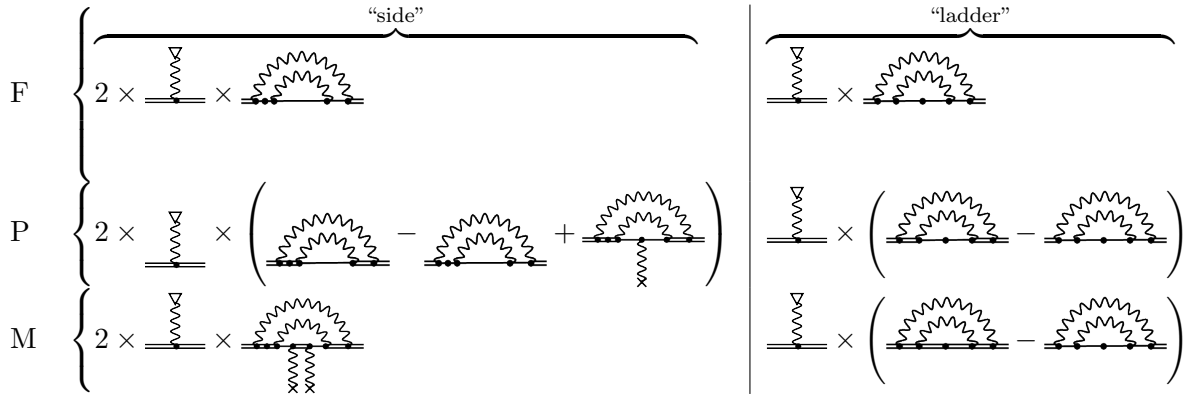

Figure 6.10: Separation of the "N, red" contributions into F, P and M terms.

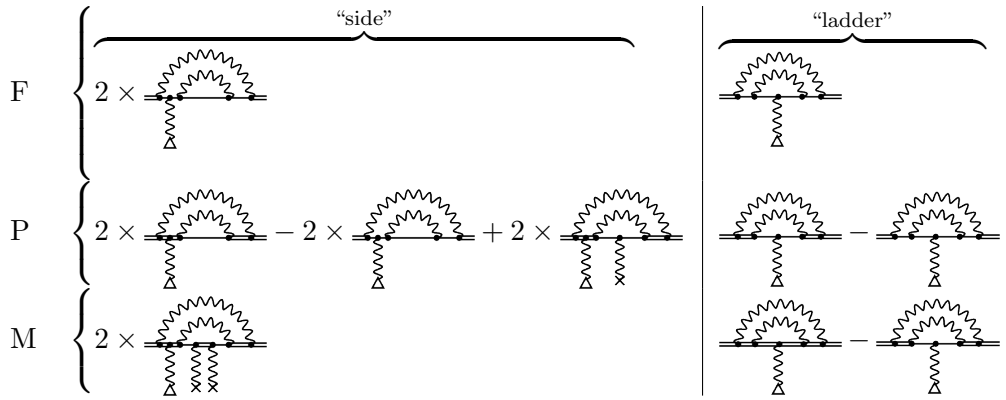

Figure 6.11: Separation of the "N, vertex" contributions into F, P and M terms.

M terms according to the definitions

$$d \geq 0 \Leftrightarrow \text{F term},$$
$$d < 0, \text{ UV divergent subgraph} \Leftrightarrow \text{P term},$$
$$d < 0, \text{ no UV divergent subgraph} \Leftrightarrow \text{M term}.$$

The separation of the N and O, red and vertex diagrams is depicted in Fig. 6.10 to 6.13. Formulas for the (unrenormalized) F, P and M term contributions can be obtained by replacing the full Green's functions in the basic formulas for all contributions by zero-, one - and many-potential Green's functions where necessary, according to the figures 6.10 to 6.13.

F term diagrams need to be calculated in momentum space because of the appearance of UV divergences, M term diagrams need to be evaluated in position space because of the many-potential propagators, and P term diagrams need to be evaluated by employing a mixed position-momentum space representation since they contain both UV divergent subdiagrams and many-potential electron propagators [63].

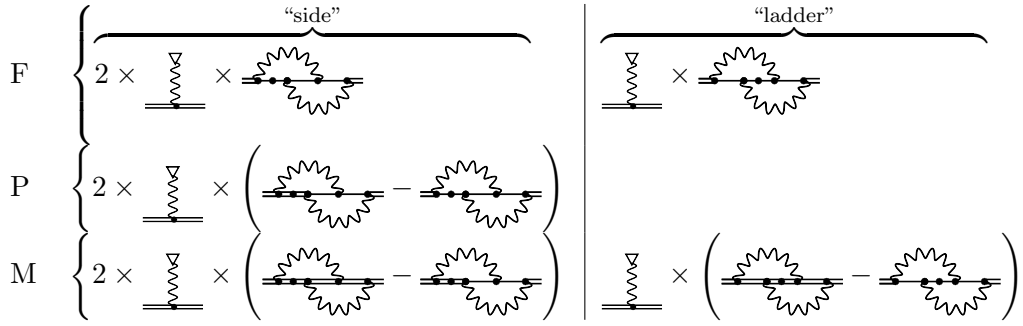

Figure 6.12: Separation of the "O, red" contribution into F, P and M terms. Note that the "ladder" diagram does not contain a P term contribution because there is no divergent subgraph in this diagram.

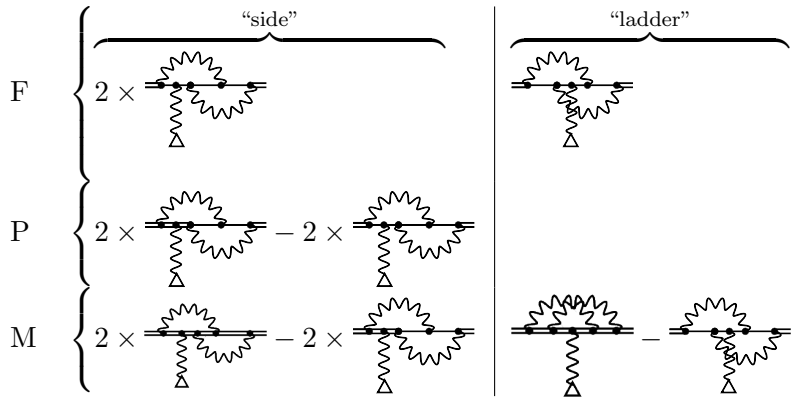

Figure 6.13: Separation of the "O, vertex" contribution into F, P and M terms. The "ladder" diagram does not contribute to the P term because there is no divergent subgraph within this diagram.

We demonstrated the separation of all two-loop SE g-factor Feynman diagrams into different categories, namely, the LAL contribution, the "LAL, red" contribution, and the F, P and M terms. Some of the "LAL, red" contributions are conveniently included in the F term, as will be discussed below. The remaining "LAL, red" contributions shall be included in the M term. In this Chapter, we will give a description of the methods for the computation of the LAL diagrams. In the next Chapter, we present a detailed description of the calculation method and our numerical results of the F term. The evaluation of the P and M terms and the LAL contribution will be presented in a future work.

6.6 Loop-after-loop diagrams

In this section, we discuss the methods to compute the loop-after-loop diagrams shown in Fig. 6.4. Following the discussion about UV divergences, it is sufficient to consider the renormalized part of all relevant loop functions since all UV divergences in the LAL contribution cancel. The contributions to the energy shift by the various renormalized loop after loop diagrams are as follows:

$$\Delta E_{\mathrm{LAL,a,R}} = 2\langle a|\gamma^0\Sigma_R \sum_{n,n\neq a} \frac{|n\rangle\langle n|}{E_a - E_n}\gamma^0\Sigma_R|\delta a\rangle\,, \tag{6.65}$$

$$\Delta E_{\mathrm{LAL,b,R}} = 2\langle a|\gamma^0\Sigma_R \sum_{n,n\neq a} \frac{|n\rangle\langle n|}{E_a - E_n}\gamma^0 e\Gamma^\mu A_{m\mu}|a\rangle\,, \tag{6.66}$$

$$\Delta E_{\mathrm{LAL,c,R}} = \langle a|\gamma^0\Sigma_R \sum_{n_1,n_1\neq a} \frac{|n_1\rangle\langle n_1|}{E_a - E_{n_1}}\gamma^0 e\not{A}_m \sum_{n_2,n_2\neq a} \frac{|n_2\rangle\langle n_2|}{E_a - E_{n_2}}\gamma^0\Sigma_R|a\rangle\,, \tag{6.67}$$

$$\Delta E_{\mathrm{LAL,d,R}} = 2\Delta E_{\mathrm{mag}}\langle a|\gamma^0\Sigma_R \sum_{n,n\neq a} \frac{|n\rangle\langle n|}{E_a - E_n}\gamma^0 \left.\frac{\partial\Sigma_R}{\partial E}\right|_{E_a}|a\rangle\,, \tag{6.68}$$

$$\Delta E_{\mathrm{LAL,e,R}} = -\Delta E_{\mathrm{mag}}\langle a|\gamma^0\Sigma_R \sum_{n,n\neq a} \frac{|n\rangle\langle n|}{(E_a - E_n)^2}\gamma^0\Sigma_R|a\rangle\,. \tag{6.69}$$

The subscript $_{\mathrm{R}}$ indicates that we consider only the UV finite remainders of all SE and vertex functions involved. For this computation, it is convenient to define a "self-energy perturbed wave function" $|\delta_\Sigma a\rangle$ (see [190, 254]), analogously to the wave function perturbed by the magnetic field $|\delta a\rangle$:

$$|\delta_\Sigma a\rangle = \sum_{n,n\neq a} \frac{|n\rangle\langle n|\Sigma_R|a\rangle}{E_a - E_n}\,. \tag{6.70}$$

The most challenging aspect of the loop-after-loop calculation is the numerical determination of $|\delta_\Sigma a\rangle$ using B-splines [222, 255]. $|\delta_\Sigma a\rangle$ corresponds to the sum of the zero-, one- and many-potential contributions to the self-energy function according to $\widetilde{\Sigma}_R = \widetilde{\Sigma}^0_R + \Sigma^1_R + \Sigma^{(2+)}$.

The configuration space representation of $|\delta_\Sigma a\rangle$ is:

$$\delta_\Sigma a(r,\Omega) = \begin{pmatrix} i g_\Sigma(r)\chi_{\kappa m}(\Omega) \\ -f_\Sigma(r)\chi_{-\kappa m}(\Omega) \end{pmatrix}. \tag{6.71}$$

The radial components of $|\delta_\Sigma a\rangle$ are:

$$g_\Sigma(r) = \sum_{n,n\neq a} \frac{g_n(r)\langle n|\Sigma_R|a\rangle}{E_a - E_n}, \tag{6.72}$$

$$f_\Sigma(r) = \sum_{n,n\neq a} \frac{f_n(r)\langle n|\Sigma_R|a\rangle}{E_a - E_n}. \tag{6.73}$$

For the LAL calculations, it is necessary to determine $|\delta_\Sigma a\rangle$ in both configuration and momentum space. The configuration space representation of $|\delta_\Sigma a\rangle$ was determined numerically using the finite basis set method [222, 255]. The momentum space representation of $|\delta_\Sigma a\rangle$ was determined by performing the Fourier transform of the configuration space representation numerically. The determination of $|\delta_\Sigma a\rangle$, both in position and momentum space, was carried out by Dr. N. S. Oreshkina und H. Cakir. The values of g_Σ and f_Σ were stored at certain grid points in a file and determined at arbitrary values of r and p by interpolation.

We tested the precision of $|\delta_\Sigma a\rangle$ using different methods. We computed the orthogonal scalar product $\langle a|\delta_\Sigma a\rangle = 0$ numerically to test the coding and to assess the numerical accuracy of the wave functions and their integration. Furthermore, we computed the $g_{\mathrm{SEwf,irred}}$ contribution to the one-loop g-factor as well as the LAL contribution to the Lamb shift using $|\delta_\Sigma a\rangle$ and compared with literature values [63, 69].

We now turn to expressing the g-factor contributions of the different LAL diagrams in terms of $|\delta_\Sigma a\rangle$. The simplest diagram is diagram (e). We can make the replacement

$$\sum_{n_1,n_1\neq a} \frac{|n_1\rangle\langle n_1|}{(E_a - E_{n_1})^2} = \sum_{n_1,n_1\neq a} \frac{|n_1\rangle\langle n_1|}{E_a - E_{n_1}} \sum_{n_2,n_2\neq a} \frac{|n_2\rangle\langle n_2|}{E_a - E_{n_2}} \tag{6.74}$$

in Eq. (6.69) and find the following formula for its g-factor contribution:

$$\Delta E_{\mathrm{LAL,e,R}} = -\Delta E_{\mathrm{mag}} \langle \delta_\Sigma a|\delta_\Sigma a\rangle\,. \tag{6.75}$$

The corresponding g-factor contribution is:

$$\Delta g_{\mathrm{LAL,e}} = -g_{\mathrm{D}} \langle \delta_\Sigma a|\delta_\Sigma a\rangle. \tag{6.76}$$

This contribution can be computed both with the position- and momentum-space representations of $|\delta_\Sigma a\rangle$. Diagram (c) can now also be computed in a straightforward manner. Rewriting formula (6.67) using equation (6.70), we find

$$\Delta E_{LAL,c,R} = \langle \delta_\Sigma a|\gamma^0 e\not{A}_m|\delta_\Sigma a\rangle\,. \tag{6.77}$$

This is similar to the formula for the computation of the Dirac value g_{D} (see equation (3.53)), with the bound-electron wave function replaced by $|\delta_\Sigma a\rangle$.

The LAL, c contribution can also be computed in momentum space using the momentum space representation of the magnetic potential [57]:

$$\Delta E_{\rm LAL,c} = \int \frac{{\rm d}^3p_1}{(2\pi)^3} \int \frac{{\rm d}^3p_2}{(2\pi)^3} \overline{\delta_\Sigma a}(\boldsymbol{p}_1)(-e)\boldsymbol{\gamma}\boldsymbol{A}(\boldsymbol{p}_1-\boldsymbol{p}_2)\delta_\Sigma a(\boldsymbol{p}_2) \tag{6.78}$$

The evaluation of this g-factor contribution can be carried out along the lines of the discussion of the zero-potential vertex contributions in Chapter 7 (see also Ref. [57]), replacing the two-loop vertex functions Γ^μ_{ij} in these contributions by the "zero loop" vertex function $\Gamma^\mu_{0\,\rm loop}(p_1,p_2)=\gamma^\mu$. The final formula for the g-factor contribution is:

$$\Delta g_{\rm LAL,c} = -\frac{m}{6\pi^3}\int {\rm d}p p^2 \left(\frac{2g_\Sigma f_\Sigma}{p} + g_\Sigma f'_\Sigma - f_\Sigma g'_\Sigma\right). \tag{6.79}$$

Here, $()' = \frac{d()}{dp}$. Making the replacement $g_\Sigma \to g$, $f_\Sigma \to f$, we obtain a formula for the Dirac value $g_{\rm D}$. We made this replacement in our code in order to assess the accuracy of our momentum integration procedure.

The remaining diagrams can be rewritten as a one-loop SE or vertex diagram, sandwiched by either the bound-electron wave function or $|\delta a\rangle$ on one side and the self-energy perturbed wave function $|\delta_\Sigma a\rangle$ on the other. The one-loop operator has to be expanded into zero-, one- (if applicable), and many-potential terms. The energy shift that corresponds to diagram (a) can be rewritten as

$$\Delta E_{\rm LAL,a,R} = 2\langle \delta_\Sigma a|\Sigma_R|\delta a\rangle\,. \tag{6.80}$$

The formula contains the one-loop SE function. It is expanded into zero-, one- and many-potential terms, as discussed in detail in the literature (e.g. [72]). Formulas for the zero-, one- and many-potential contributions to the one-loop Lamb shift are given in Ref. [72]. Corresponding formulas for the LAL contributions to the g-factor can be obtained from the Lamb shift formulas by replacing the bound-electron wave function by $|\delta a\rangle$ and $|\delta_\Sigma a\rangle$ in a straightforward way.

The diagram (d) contains the energy derivative of the SE operator:

$$\Delta E_{\rm LAL,d,R} = 2\Delta E_{\rm mag}\langle a|\left.\frac{\partial\Sigma_R}{\partial E}\right|_{E_a}|\delta_\Sigma a\rangle\,. \tag{6.81}$$

This operator has to be also expanded into zero- and many-potential terms, as discussed in Ref. [57]. The formula above is a straightforward generalization of the corresponding contribution to the one-loop g-factor. It must be mentioned that the many-potential contribution cannot be computed directly since the derivative of the SE operator contains reference-state IR divergences.

Finally, diagram (b) is the generalization of the one-loop vertex diagram, with one of the bound-electron wave functions replaced by $|\delta_\Sigma a\rangle$. It has to be expanded into zero- and many-potential terms. The zero-potential contribution can be computed by inserting the explicit expression for the magnetic potential in momentum space [57],

$$\boldsymbol{A}(\boldsymbol{p}_1-\boldsymbol{p}_2) = -\frac{i}{2}(2\pi)^3\left(\boldsymbol{B}\times\nabla_{\boldsymbol{p}_2}\delta^3(\boldsymbol{p}_1-\boldsymbol{p}_2)\right), \tag{6.82}$$

into equation (6.66). After integrating by parts, we obtain two terms with the derivative acting on the vertex function and the bound-electron wave function, respectively [57].

$$\Delta g^{(0)}_{\mathrm{LAL,b}} = 2im \int \frac{\mathrm{d}^3p}{(2\pi)^3} \overline{\delta_\Sigma a}(\boldsymbol{p}_1)\Xi(p)a(\boldsymbol{p}) - \qquad \}g^{(0)}_{\mathrm{LAL,b1}} \tag{6.83}$$

$$- 2im \int \frac{\mathrm{d}^3p}{(2\pi)^3} \overline{\delta_\Sigma a}(\boldsymbol{p}_1) \left(\boldsymbol{\Gamma}(p,p) \times \nabla_{\boldsymbol{p}}\right)_z a(\boldsymbol{p}) \qquad \}g^{(0)}_{\mathrm{LAL,b2}}$$

Here, $\boldsymbol{\Xi}(p) = \left(\nabla_{\boldsymbol{p}_2} \times \boldsymbol{\Gamma}_{\mathrm{R}}(p,p_2)\big|_{\boldsymbol{p}_2=\boldsymbol{p}} \right)_z$ [57]. The evaluation of $\boldsymbol{\Xi}(p)$ is discussed in detail in Ref. [57]. The result, as given in Ref. [57], is:

$$\boldsymbol{\Xi}(p) = \frac{\alpha A(\rho)}{2\pi m^2} \left(2(\boldsymbol{p}\times\boldsymbol{\gamma})_z + (\boldsymbol{\gamma}\times\boldsymbol{\gamma})_z \not{p}\right), \tag{6.84}$$

$$A(\rho) = \frac{1}{1-\rho}\left(1 + \frac{\log(\rho)}{1-\rho}\right). \tag{6.85}$$

The subsequent integration of angular variables can be performed using equations (25), (26), (34) and (35) from Ref. [57]. It should be noted that the final formula for the $g_{\mathrm{ver},1}$ contribution cannot be obtained by a straightforward replacement of $g \to g_{SE},\ f \to f_{SE}$ in equation (27) in Ref. [57]. This formula is obtained after angular integration, using the fact that the angular integral over the $(\boldsymbol{p}\times\boldsymbol{\gamma})_3$ term vanishes if it is sandwiched by identical wave functions. Therefore, the corresponding angular integral does not vanish in the LAL case.

The formula for the many-potential term can be obtained by a straightforward generalization of the formula for the one-loop g-factor diagram [57]. It should be noted that this term also contains reference-state IR divergences. However, it can be shown that the IR divergences in the many-potential terms of diagrams (b) and (d) cancel each other, similarly to the case of the one-loop g-factor. It is therefore possible to compute the sum of the many-potential terms of diagrams (c) and (e) directly [57]. Alternatively, one can explicitly subtract the reference state contribution to both diagrams to obtain "IR-regularized" contributions of both terms separately. Such a subtraction procedure was performed in the computation of the two-loop SE contribution to the Lamb shift [63].

7 Evaluation of the F term

The F term, as mentioned in the previous Chapter, consists of contributions from O and N irreducible and reducible diagrams, as well as such reducible LAL diagrams which can be split into two one-loop diagrams. The reducible LAL diagrams can be computed using methods for one-loop diagrams. The O and N contributions are either zero- or one-potential diagrams. We begin this Chapter by describing the "LAL, red" terms which we included in the F term, and methods to evaluate them. Then, we analyze the zero-potential contributions to the two-loop SE functions. We present our calculation of the zero-potential O, SE function in great detail and then describe our evaluation of the irreducible zero-and one-potential F terms which are straightforward generalizations of two-loop Lamb shift diagrams. After this, we turn to the zero-potential reducible and vertex diagrams. For some of the vertex contributions, we will describe an alternative calculation method which we used as a consistency check. We conclude this Chapter by presenting our numerical results for the F term.

7.1 LAL, reducible contributions

We included contributions from those "LAL, red" diagrams into the F term which contain UV divergent one-loop functions in both factors. These are the "LAL, red" diagrams a, b, c, d, and f in Fig. 6.5. In the following, we briefly outline the methods used to evaluate these contributions.

Diagram a

The energy shift corresponding to this diagram is

$$\begin{aligned}\Delta E_{\mathrm{LAL,red},a,\mathrm{R}} =& 2\langle a|\gamma^0 \left.\frac{\partial\Sigma_\mathrm{R}}{\partial E}\right|_{E=E_a} |\delta a\rangle\langle a|\gamma^0\Sigma_\mathrm{R}|a\rangle \\ =& 2\left(\langle a|\gamma^0 \left.\frac{\partial\Sigma^{(0)}}{\partial E}\right|_{E=E_a} |\delta a\rangle + \langle a|\gamma^0 \left.\frac{\partial\Sigma^{(1+)}}{\partial E}\right|_{E=E_a} |\delta a\rangle\right) \\ & \times\left(\Delta E^{(0)}_\mathrm{SE} + \Delta E^{(1)}_\mathrm{SE} + \Delta E^{(2+)}_\mathrm{SE}\right),\end{aligned} \tag{7.1}$$

where the $\Delta E^{(n)}_\mathrm{SE} = \langle a|\gamma^0\Sigma^{(n)}_\mathrm{R}|a\rangle$ correspond to the one-loop SE corrections to the Lamb shift with n intermediate-state interactions with the nuclear Coulomb potential [63]. We included the zero-potential contribution of the first factor as well as the zero-, one- and

many-potential contributions of the second factor into the F term:

$$\Delta E_{\mathrm{LAL,red},a,\mathrm{F}} = 2\langle a|\gamma^0 \left.\frac{\partial\Sigma^{(0)}}{\partial E}\right|_{E=E_a} |\delta a\rangle \left(\Delta E^{(0)}_{\mathrm{SE}} + \Delta E^{(1)}_{\mathrm{SE}} + \Delta E^{(2+)}_{\mathrm{SE}}\right). \tag{7.2}$$

The remainder, $\Delta E_{\mathrm{LAL,red},a,\mathrm{R}} - \Delta E_{\mathrm{LAL,red},a,\mathrm{F}}$, will be included in the M term. We tested our results for these terms by replacing $|\delta a\rangle$ with $|a\rangle$ in the first factor. By doing so, we obtain $\langle a|\gamma^0 \left.\frac{\partial\Sigma}{\partial E}\right|_{E=E_a} |a\rangle$, a quantity which appears both in the one-loop correction to the g-factor [57] and in the two-loop correction to the Lamb shift [63].

We needed to compute the one-loop SE correction to the Lamb shift. We compared our numerical results with the $Z\alpha$ expansion formula with terms up to order $(Z\alpha)^6$ [110]. Our numerical results for low Z are in good agreement with the $Z\alpha$-expansion results, except for $Z = 1$. For $Z = 1$, we used the $Z\alpha$ expansion result for the computation of the reducible F term. For some Z, we used the very precise numerical results for the one-loop SE diagram from Ref. [131].

Diagram b

The corresponding energy shift is given by

$$\Delta E_{\mathrm{LAL,red},b,\mathrm{R}} = 2\langle a|\gamma^0\Sigma_{\mathrm{R}}|\delta_{\mathrm{D}} a\rangle\langle a|\gamma^0\Sigma_{\mathrm{R}}|a\rangle\,. \tag{7.3}$$

Here, the perturbed wave function is $|\delta_{\mathrm{D}} a\rangle = -\sum_{n,n\neq a} \frac{|n\rangle\langle n|\gamma^0 e\not{A}_m|a\rangle}{(E_a-E_n)^2}$. We derived an analytic expression for $|\delta_{\mathrm{D}} a\rangle$ using the method of generalized virial relations [128]. The resulting formula was tested by computing scalar products of $|\delta_{\mathrm{D}} a\rangle$ with the ground state and several excited states $|m\rangle$ numerically:

$$\begin{aligned}
&\langle a|\delta_{\mathrm{D}} a\rangle = 0\,,\\
&\langle m|\delta_{\mathrm{D}} a\rangle = -\frac{\langle m|\gamma^0 e\not{A}_m|a\rangle}{(E_a - E_m)^2}\,.
\end{aligned} \tag{7.4}$$

Our numerical results for the left-hand side and the right-hand side of the above equations were in excellent agreement.

We included the zero- and one-potential contributions of the first factor of Eq. (7.3), and, as with diagram a, the zero-, one- and many-potential contributions of the second factor in the F term:

$$\Delta E_{\mathrm{LAL,red},b,\mathrm{F}} = 2\langle a|\gamma^0 \left(\Sigma^{(0)}_{\mathrm{R}} + \Sigma^{(1)}_{\mathrm{R}}\right) |\delta_{\mathrm{D}} a\rangle \left(\Delta E^{(0)}_{\mathrm{SE}} + \Delta E^{(1)}_{\mathrm{SE}} + \Delta E^{(2+)}_{\mathrm{SE}}\right). \tag{7.5}$$

The remainder, $\Delta E_{\mathrm{LAL,red},b,\mathrm{R}} - \Delta E_{\mathrm{LAL,red},b,\mathrm{F}}$, will be included in the M term.

One can also compute the "LAL,red,b" contribution in a different way. Inserting the explicit expression of $|\delta_{\mathrm{D}} a\rangle$ into equation (7.3), we find

$$\begin{aligned}
\Delta E_{\mathrm{LAL,red},b,\mathrm{F}} = &-2\langle a|\gamma^0 \left(\Sigma^{(0)}_{\mathrm{R}} + \Sigma^{(1)}_{\mathrm{R}}\right) \sum_n \frac{|n\rangle\langle n|\gamma^0 e\not{A}_m|a\rangle}{(E_a - E_n)^2}\\
&\left(\Delta E^{(0)}_{\mathrm{SE}} + \Delta E^{(1)}_{\mathrm{SE}} + \Delta E^{(2+)}_{\mathrm{SE}}\right).
\end{aligned} \tag{7.6}$$

Rewriting this expression, using identity (6.74), we find

$$\Delta E_{\mathrm{LAL,red},b,\mathrm{R}} = -2\langle a|\gamma^0\left(\Sigma^{(0)}_{\mathrm{R}}+\Sigma^{(1)}_{\mathrm{R}}\right)\sum_{n_1}\frac{|n_1\rangle\langle n_1|}{E_a-E_{n_1}}\sum_{n_2}\frac{|n_2\rangle\langle n_2|\gamma^0 e\not{A}_m|a\rangle}{E_a-E_{n_2}} \times\left(\Delta E^{(0)}_{\mathrm{SE}}+\Delta E^{(1)}_{\mathrm{SE}}+\Delta E^{(2+)}_{\mathrm{SE}}\right). \tag{7.7}$$

In this expression, we can identify both $|\delta a\rangle$ and the zero- and one-potential contributions to $|\delta_\Sigma a\rangle$, the self-energy corrected wave function also useful for the computation of the LAL diagrams:

$$\Delta E_{\mathrm{LAL,red},b,\mathrm{R}} = -2\langle\delta_\Sigma a^{(0+1)}|\delta a\rangle\,. \tag{7.8}$$

Here, $|\delta_\Sigma a^{(n)}\rangle$ corresponds to the part of the self-energy corrected wave function due to the n-potential contribution to the one-loop SE function.

Diagram c

The energy shift induced by this diagram is

$$\Delta E_{\mathrm{LAL,red},c} = 2\langle\delta a|\gamma^0\widetilde{\Sigma}|a\rangle\langle a|\gamma^0\left.\frac{\partial\Sigma}{\partial E}\right|_{E=E_a}|a\rangle\,. \tag{7.9}$$

We included the zero-potential contribution of the second factor and the zero-, one- and many-potential contributions of the first factor in the F term. Inserting the D-dimensional parameterization (see [63])

$$\Sigma^{(i)}_{\mathrm{R},D} = C_\epsilon\left(\Sigma^{(i)}_{\mathrm{R},4}+\epsilon\Sigma^{(i)}_{\mathrm{R},\epsilon}+\mathcal{O}\left(\epsilon^2\right)\right) \tag{7.10}$$

for the zero- and one-potential SE functions into the expression for the energy shift, and expanding in powers of ϵ up to order $\mathcal{O}\left(\epsilon^0\right)$, we obtain

$$\begin{aligned}\Delta E_{\mathrm{LAL,red},c,\mathrm{F}} =& -\frac{\alpha C_\epsilon^2}{2\pi\epsilon}\langle\delta a|\gamma^0\left(\Sigma^{(0)}_{\mathrm{R},4}+\Sigma^{(1)}_{\mathrm{R},4}\right)|a\rangle + 2B^{(1)}\langle\delta a|\gamma^0\Sigma^{(2+)}|a\rangle \\ &-\frac{\alpha C_\epsilon^2}{2\pi}\langle\delta a|\gamma^0\left(\Sigma^{(0)}_{\mathrm{R},\epsilon}+\Sigma^{(1)}_{\mathrm{R},\epsilon}\right)|a\rangle + 2\langle\delta a|\gamma^0\Sigma_{\mathrm{R},4}|a\rangle\langle a|\gamma^0\left.\frac{\partial\Sigma^{(0)}_{\mathrm{R},4}}{\partial E}\right|_{E=E_a}|a\rangle\,.\end{aligned} \tag{7.11}$$

Here, $\Sigma^{(i)}_{\mathrm{R},4}$ and $\Sigma^{(i)}_{\mathrm{R},D}$ are the renormalized SE functions, computed in 4 and $D=4-2\epsilon$ dimensions, respectively. Note that this term contains UV divergences. The remainder, $\Delta E_{\mathrm{LAL,red},c} - \Delta E_{\mathrm{LAL,red},c,\mathrm{F}}$, is UV finite and will be included in the M term. The UV-finite contribution to the F term is

$$\Delta E_{\mathrm{LAL,red},c,\mathrm{F,R}} = -\frac{\alpha C_\epsilon^2}{2\pi}\langle\delta a|\gamma^0\left(\Sigma^{(0)}_{\mathrm{R},\epsilon}+\Sigma^{(1)}_{\mathrm{R},\epsilon}\right)|a\rangle + 2\langle\delta a|\gamma^0\Sigma_{R,4}|a\rangle\langle a|\gamma^0\left.\frac{\partial\Sigma^{(0)}_{\mathrm{R},4}}{\partial E}\right|_{E=E_a}|a\rangle\,. \tag{7.12}$$

We computed $\Sigma^{(0)}_{\mathrm{R},\epsilon}$ and $\Sigma^{(1)}_{\mathrm{R},\epsilon}$ according to [63]. We checked our formulas by reproducing published results for the reducible two-loop SE correction to the Lamb shift by replacing $|\delta a\rangle$ with $|a\rangle$ [63]. The factor $\langle a|\gamma^0\Sigma_{\mathrm{R}}|\delta a\rangle$ corresponds to the irreducible one-loop SE correction to the g-factor, considered in Chapter 4.

Diagrams d and f

It is convenient to directly consider the sum of the diagrams d and f. For the corresponding energy shift one obtains

$$\Delta E_{\mathrm{LAL,red},df} = \langle a|\gamma^0 \left.\frac{\partial\Sigma}{\partial E}\right|_{E=E_a} |a\rangle \Delta E_{\mathrm{vr},D}\,, \tag{7.13}$$

where $\Delta E_{\mathrm{vr},D} = C_\epsilon\left(\Delta E_{\mathrm{vr},4} + \epsilon\Delta E_{\mathrm{vr},\epsilon} + \mathcal{O}\left(\epsilon^2\right)\right)$ [63] is the sum of the one-loop vertex ΔE_{ver} (see equation (4.13)) and the reducible ΔE_{red} (equation (4.19)) one-loop SE contribution to the g-factor, $\Delta E_{\mathrm{vr}} = \Delta E_{\mathrm{ver}} + \Delta E_{\mathrm{red}}$ (see [57]), evaluated in D space-time dimensions. We included the zero-potential contribution of the first factor and all contributions to the second factor in the F term. Keeping only these terms and performing an expansion in powers of ϵ similarly to diagram c, we obtain

$$\begin{aligned}\Delta E_{\mathrm{LAL,red},df,\mathrm{F}} =& -\frac{\alpha C_\epsilon^2}{4\pi\epsilon}\Delta E^{(0)}_{\mathrm{vr},4} + B^{(1)}\Delta E^{(1+)}_{\mathrm{vr},D} \\ &- \frac{\alpha C_\epsilon^2}{4\pi}\Delta E^{(0)}_{\mathrm{vr},\epsilon} + \langle a|\gamma^0 \left.\frac{\partial\Sigma^{(0)}_{\mathrm{R},4}}{\partial E}\right|_{E=E_a} |a\rangle \Delta E_{\mathrm{vr},4}\,.\end{aligned} \tag{7.14}$$

Note that also this contribution contains UV divergences. The last term consists of contributions which are a part of the one-loop SE correction to the g-factor [57] and the two-loop SE correction to the Lamb shift [63].

For the calculation of $\Delta E^{(0)}_{\mathrm{vr},\epsilon}$, we repeated the derivation of the zero-potential contribution to ΔE_{vr} which is carried out in Ref. [57], working in D dimensions and keeping terms up to $\mathcal{O}(\epsilon)$. We split the finite part of this contribution into two parts as follows:

$$\Delta E_{\mathrm{LAL,red},df,\mathrm{F,R1}} = -\frac{\alpha C_\epsilon^2}{4\pi}\Delta E^{(0)}_{\mathrm{vr},\epsilon} + \langle a|\gamma^0 \left.\frac{\partial\Sigma^{(0)}_{\mathrm{R},4}}{\partial E}\right|_{E=E_a} |a\rangle \Delta E^{(0)}_{\mathrm{vr},4}\,; \tag{7.15}$$

$$\Delta E_{\mathrm{LAL,red},df,\mathrm{F,R2}} = \langle a|\gamma^0 \left.\frac{\partial\Sigma^{(0)}_{\mathrm{R},4}}{\partial E}\right|_{E=E_a} |a\rangle \Delta E^{(1+)}_{\mathrm{vr},4}\,. \tag{7.16}$$

The remainder, $\Delta E_{\mathrm{LAL,red},df} - \Delta E_{\mathrm{LAL,red},df,\mathrm{F}}$, is UV finite and will be included in the M term.

Forming the sum of equations (7.12) and (7.16), we obtain:

$$\Delta E_{\mathrm{LAL,red},c,\mathrm{F,R}} + \Delta E_{\mathrm{LAL,red},df,\mathrm{F,R2}} = \tag{7.17}$$
$$-\frac{\alpha C_\epsilon^2}{2\pi}\langle\delta a|\gamma^0\left(\Sigma^{(0)}_{R,\epsilon}+\Sigma^{(1)}_{R,\epsilon}\right)|a\rangle + \langle a|\gamma^0\left.\frac{\partial\Sigma^{(0)}_{R,4}}{\partial E}\right|_{E=E_a}|a\rangle\left(2\langle\delta a|\gamma^0\Sigma_{R,4}|a\rangle+\Delta E^{(1+)}_{\mathrm{vr},4}\right).$$

It contains the product of the energy derivative of the one-loop SE diagram and the one-loop SE correction to the g-factor, minus the zero-potential contribution to the vertex and reducible diagrams [57]. For $Z \leq 20$, we obtained the second factor following Ref. [64] in the following way.

The numbers tabulated in Ref. [64] cannot be used directly since these numbers were computed for a value of the fine-structure constant $\alpha = 139.036^{-1}$ which does not correspond to the current literature value for α [19]. We computed the zero-potential contribution to the reducible and vertex diagrams for $\alpha = 139.036^{-1}$ and made sure that we are able to match the accuracy of this contribution given in Ref. [64]. We then used equation (9) in Ref. [64] to compute the total one-loop SE contribution to the g-factor for the current literature value of α and subtracted our zero-potential contributions to the vertex and reducible diagrams, computed for the present value of α.

For higher Z, we computed the irreducible and the sum of the reducible and vertex corrections separately with our computer codes. Whenever possible, we compared the results of our codes with literature values given in Ref. [57].

7.2 Evaluation of the zero-potential two-loop self-energy functions

In Ref. [63], the computation of the nested loop self-energy function is described in some detail. According to Ref. [63], the overlapping loop self-energy function can be computed analogously. Here, we are going to present our evaluation of the overlapping loop self-energy function.

The overlapping loop self-energy function can be parameterized as [63]:

$$\Sigma^{(0)}_{\mathrm{O}}(p) = -4\pi i\alpha\mu^{2\epsilon}\int\frac{\mathrm{d}^D q}{(2\pi)^D}\gamma_\rho\frac{1}{\not p-\not q-m}\Gamma^\rho(p-q,p)\frac{1}{q^2}. \tag{7.18}$$

It contains the one-loop vertex $\Gamma^\rho(p_1,p_2)$ function as a subdiagram. We choose the parameterization of the vertex function given in the appendix of Ref. [63], Eq. (252) there. It can be expressed as

$$\begin{aligned}\Gamma^\rho(p_1,p_2) =& \frac{\alpha C_\epsilon}{4\pi} m^{2\epsilon} \int_0^1 \mathrm{d}x \int_0^1 \mathrm{d}y \frac{(2-2\epsilon)^2}{2\epsilon} \gamma^\rho \frac{x^{1-\epsilon}}{D^\epsilon} - \\ & \frac{\alpha C_\epsilon}{4\pi} m^{2\epsilon} \int_0^1 \mathrm{d}x \int_0^1 \mathrm{d}y \frac{x^{-\epsilon}(\not{p}_1 - m)\left(\gamma^\rho(\not{p}_2 - m)\mathcal{L}_2 + \mathcal{L}_{1r}^\rho\right)}{D^{1+\epsilon}} - \\ & \frac{\alpha C_\epsilon}{4\pi} m^{2\epsilon} \int_0^1 \mathrm{d}x \int_0^1 \mathrm{d}y \frac{x^{-\epsilon}\left(\mathcal{L}_{1l}^\rho(\not{p}_2 - m) + \mathcal{L}_0^\rho\right)}{D^{1+\epsilon}}\,, \end{aligned} \tag{7.19}$$

where $\mathcal{L}_2, \mathcal{L}_{1l}^\rho, \mathcal{L}_{1r}^\rho$ and $\mathcal{L}_0^\rho$ can be computed as described in Ref. [63]. We begin by determining D for the case $p_1 = p-q, p_2 = p$, using the relevant (unnumbered) equations in the appendix of Ref. [63]. We find:

$$D = -yuD' := -yu\left(q^2 - \frac{2(1-x)}{u}pq + \frac{(1-x)}{yu}p^2 - \frac{m^2}{yu}\right), \tag{7.20}$$

with $u = 1 - xy$. We now insert the three terms in our formula (7.19) for the vertex function into the expression (7.18) for the two-loop self-energy function one by one.

Inserting the first term, we obtain:

$$\Sigma_{O1}^{(0)}(p) = -i\alpha C_\epsilon \mu^{2\epsilon} m^{2\epsilon} \frac{(2-2\epsilon)^2}{2\epsilon} \int_0^1 \mathrm{d}x \int_0^1 \mathrm{d}y \frac{x^{1-\epsilon}}{(-yu)^\epsilon} \int \frac{\mathrm{d}^D q}{(2\pi)^D} \frac{\gamma_\rho(\not{p} - \not{q} + m)\gamma^\rho}{q^2\left((p-q)^2 - m^2\right)D'^\epsilon}. \tag{7.21}$$

We combine the denominators using Feynman parameters, using formula (281) in Ref. [63] to obtain:

$$\frac{1}{q^2\left((p-q)^2 - m^2\right)D'^\epsilon} = \frac{\Gamma(2+\epsilon)}{\Gamma(\epsilon)} \int_0^1 \mathrm{d}z \int_0^1 \mathrm{d}w \frac{z^\epsilon w^{\epsilon-1}}{(l^2 - z\Delta)^{2+\epsilon}}, \tag{7.22}$$

with $l = q - zAp$, $\Delta = m^2\left(d_{11} - d_{12}(1-\rho) + zA^2(1-\rho)\right)$, $d_{11} = 1 - w + \frac{w}{yu}$, $d_{12} = 1 - w + \frac{(1-x)w}{yu}$, $A = 1 - w + \frac{(1-x)w}{u}$ and $\rho = \frac{m^2 - E_a^2 + p^2}{m^2}$ [72]. Performing the corresponding substitution in the numerator, we obtain:

$$\gamma_\rho(\not{p} - \not{q} + m)\gamma^\rho = -2(1-z)(1-\epsilon)\not{p} + (4-2\epsilon)m - 2w(z - \frac{1-x}{u}z)(1-\epsilon)\not{p}\,. \tag{7.23}$$

Now we can perform the integration over the loop momentum:

$$\Sigma^{(0)}_{\mathrm{O1}}(p) = \frac{\alpha^2 C_\epsilon^2}{16\pi^2}\frac{(2-2\epsilon)^2\Gamma(2\epsilon)}{2\Gamma^2(1+\epsilon)}\int\limits_0^1 \mathrm{d}x\int\limits_0^1 \mathrm{d}y\int\limits_0^1 \mathrm{d}z\int\limits_0^1 \mathrm{d}w \frac{x^{1-\epsilon}z^{-\epsilon}w^{\epsilon-1}}{(yu)^\epsilon} \frac{-2(1-z)(1-\epsilon)\not{p} + (4-2\epsilon)m - 2w(z-\frac{1-x}{u}z)(1-\epsilon)\not{p}}{\left(\frac{\Delta}{m^2}\right)^{2\epsilon}}. \tag{7.24}$$

There are two ways in which UV divergences manifest themselves in this expression: first, in the Gamma function $\Gamma(2\epsilon)$ and second, in the integration over w: $\int\limits_0^1 \mathrm{d}w w^{\epsilon-1}$. We deal with these divergences following procedures described in Ref. [6, 63]. We split the integrand in a way which can be schematically represented as follows: $\int\limits_0^1 \mathrm{d}w w^{\epsilon-1}N(w)f(w) = \int\limits_0^1 \mathrm{d}w w^{\epsilon-1}N(w)[f(0) + (f(w)-f(0))]$. $N(w)$ is the numerator in Eq. (7.24) and $f(w) = \left(\frac{\Delta}{m^2}\right)^{-2\epsilon}$. We consider the contributions due to $f(0)$ and $f(w)-f(0)$ separately.

The $f(0)$ term corresponds to

$$\Sigma^{(0)}_{\mathrm{O1}}(p) = \frac{\alpha^2 C_\epsilon^2}{16\pi^2}\frac{(2-2\epsilon)^2\Gamma(2\epsilon)}{2\Gamma^2(1+\epsilon)}\int\limits_0^1 \mathrm{d}x\int\limits_0^1 \mathrm{d}y\int\limits_0^1 \mathrm{d}z\int\limits_0^1 \mathrm{d}w \frac{x^{1-\epsilon}z^{-\epsilon}w^{\epsilon-1}}{(yu)^\epsilon} \frac{-2(1-z)(1-\epsilon)\not{p} + (4-2\epsilon)m - 2w(z-\frac{1-x}{u}z)(1-\epsilon)\not{p}}{\Upsilon^{2\epsilon}(z)}, \tag{7.25}$$

where $\Upsilon(z) = \rho + z - z\rho$. In this case, the denominator is independent of w, and the $\int \mathrm{d}w$ integration can be performed easily:

$$\int\limits_0^1 \mathrm{d}w w^{\epsilon-1} = \frac{1}{\epsilon}, \tag{7.26}$$

$$\int\limits_0^1 \mathrm{d}w w^{\epsilon-1} w = \frac{1}{1+\epsilon}, \tag{7.27}$$

$$\int\limits_0^1 \mathrm{d}w w^{\epsilon-1} w^2 = \frac{1}{2+\epsilon}. \tag{7.28}$$

This can be obtained e.g. from Eq. (7.82) in Ref. [6] for the special case $a \in \{1,2,3\}$ and $b = 1$. The expression obtained after the $\int \mathrm{d}w$ integration is expanded in powers of ϵ up to order $\mathcal{O}\left(\epsilon^0\right)$. The result is

$$\Sigma^{(0)}_{O1a}(p) = \frac{\alpha^2 C_\epsilon^2}{16\pi^2}\left(\frac{3m}{2\epsilon^2} - \frac{1}{2\epsilon^2}(\not{p} - m) + \frac{3m}{\epsilon}\right) + \frac{\alpha C_\epsilon^2}{4\pi\epsilon}\Sigma^{(0)}_{R,4}(p) + \delta m^{(2)}_{O1a} + \Sigma^{(0)}_{O1aR}(p). \quad (7.29)$$

The mass counterterm contribution was found to be $\delta m^{(2)}_{O1a} = 11m$. We could perform all Feynman parameter integrations in $\Sigma^{(0)}_{O1aR}(p)$ analytically using Mathematica.

For the computation of the $f(w) - f(0)$ contribution, we introduce an additional Feynman parameter according to equation (284) in Ref. [63] as follows:

$$\frac{1}{\left(\frac{\Delta}{m^2}\right)^{2\epsilon}} - \frac{1}{\Upsilon^{2\epsilon}(z)} = -\int_0^1 \mathrm{d}t \frac{2\epsilon\left(\frac{\Delta}{m^2} - \Upsilon(z)\right)}{\left(\left(\frac{\Delta}{m^2} - \Upsilon(z)\right)t + \Upsilon(z)\right)^{1+2\epsilon}}. \quad (7.30)$$

By definition, $\frac{\Delta}{m^2} - \Upsilon(z)$ is proportional to w. We therefore see that, due to the additional factors 2ϵ and w in the numerator, the contribution of this expression to $\Sigma^{(0)}_{O1}(p)$ is UV finite. We can therefore compute this contribution for the case $\epsilon = 0$. We obtain the following result:

$$\Sigma^{(0)}_{O1b}(p) = -\frac{\alpha^2 C_\epsilon^2}{16\pi^2} 2 \int_0^1 \mathrm{d}x \int_0^1 \mathrm{d}y \int_0^1 \mathrm{d}z \int_0^1 \mathrm{d}w \int_0^1 \mathrm{d}t \frac{x}{w} \frac{-2(1 - zA)\not{p} + 4m}{\left(\frac{\Delta}{m^2} - \Upsilon(z)\right)t + \Upsilon(z)} \left(\frac{\Delta}{m^2} - \Upsilon(z)\right). \quad (7.31)$$

The $\int \mathrm{d}t$ integration can be performed easily. The remaining Feynman parameter integrations were carried out numerically. The contribution to the mass counterterm was determined by numerical integration:

$$\delta m^{(2)}_{O1b} = \frac{\alpha^2 C_\epsilon^2}{16\pi^2}(-10.526958...m). \quad (7.32)$$

In order to check the validity of our formulas, we also computed $\Sigma^{(0)}_{O1}(p)$ using an alternative parametrization for the one-loop vertex function, Eq. (253) in Ref. [63]. According to this equation,

$$\Gamma^\mu_1(p_1, p_2) = \frac{\alpha C_\epsilon m^{2\epsilon}}{4\pi}\left(\frac{(2-2\epsilon)^2}{2\epsilon(2-\epsilon)} \int_0^1 \mathrm{d}y \frac{\gamma^\rho}{D^\epsilon(x=1)} + \int_0^1 \mathrm{d}x \int_0^1 \mathrm{d}y \frac{x^{2-\epsilon}}{D^{1+\epsilon}} \frac{(2-2\epsilon)^2}{2(2-\epsilon)} b^2 \gamma^\mu\right), \quad (7.33)$$

where $b = yp_1 + (1-y)p_2$. Our numerical results for the mass counterterm and g-factor contributions containing $\Sigma^{(0)}_{O1}(p)$ obtained by both methods are in good agreement with each other.

We now insert the second term of $\Gamma^\mu(p_1, p_2)$ into the expression for $\Sigma^{(0)}_O(p)$. Note that the factor $(\not{p}_1 - m) = (\not{p} - \not{q} - m)$ in this expression cancels the fermion propagator

$\frac{1}{\not p-\not l-m}$ in the expression for $\Sigma_O^{(0)}(p)$, allowing a significant simplification of the γ matrix algebra in this term. We obtain:

$$\Sigma_{\rm O2}^{(0)}(p) = -i\alpha^2 C_\epsilon \mu^{2\epsilon} m^{2\epsilon} \int_0^1 {\rm d}x \int_0^1 {\rm d}y \frac{-x^{-\epsilon}}{(-yu)^{1+\epsilon}} \int \frac{{\rm d}^D q}{(2\pi)^D} \frac{\gamma_\rho \gamma^\rho (\not p - m)\mathcal{L}_2 + \gamma_\rho \mathcal{L}_{1r}^\rho}{q^2 D'^{1+\epsilon}}. \quad (7.34)$$

In this case, we need only one additional Feynman parameter to combine denominators:

$$\frac{1}{q^2 D'^{1+\epsilon}} = \frac{\Gamma(2+\epsilon)}{\Gamma(1+\epsilon)} \int_0^1 {\rm d}z \frac{z^\epsilon}{(l^2 - z\Delta_2)^{2+\epsilon}}. \quad (7.35)$$

The shifted loop momentum in this case is $l = q - z\frac{1-x}{u}p$, and $\Delta_2 = m^2\left(\frac{1}{yu} - \frac{1-x}{yu}(1-\rho) + z\frac{(1-x)^2}{u^2}(1-\rho)\right)$. Performing this substitution in the numerator, one obtains

$$\gamma_\rho \gamma^\rho (\not p - m)\mathcal{L}_2 + \gamma_\rho \mathcal{L}_{1r}^\rho = N_0 + N_1 y, \quad (7.36)$$

with $N_0 = 4(-1-\epsilon+\epsilon^2)(-1+x)\not p + 4(-2+\epsilon)\epsilon m$ and $N_1 = -4(-1+\epsilon)(-1+x)xy(-1+z)\not p$. Now we perform the integration over the loop momentum to obtain:

$$\Sigma_{O2}^{(0)}(p) = \frac{\alpha^2 C_\epsilon^2}{16\pi^2} \frac{\Gamma(2\epsilon)}{\Gamma^2(1+\epsilon)} \int_0^1 {\rm d}x \int_0^1 {\rm d}y \int_0^1 {\rm d}z \frac{x^{-\epsilon} z^{-\epsilon}}{y^{1-\epsilon} u^{1-3\epsilon}} \frac{N_0 + N_1 y}{\Delta_2'^{2\epsilon}}. \quad (7.37)$$

Here, $\Delta_2' = u - (1-x)u(1-\rho) + zy(1-x)^2(1-\rho)$. This expression contains UV divergences due to $\Gamma(2\epsilon)$ and $\int {\rm d}y \frac{1}{y^{1-\epsilon}}$. We deal with the UV divergences, schematically, as follows: $f(y)g(y) = f(0)g(0) + (f(y)-f(0))g(0) + f(y)(g(y)-g(0))$. $f(y) = \frac{1}{u^{1-3\epsilon}}$ and $g(y) = \frac{1}{\Delta_2'^{2\epsilon}}$. The $f(0)g(0)$ term leads to:

$$\Sigma_{O2a}^{(0)}(p) = \frac{\alpha^2 C_\epsilon^2}{16\pi^2} \frac{\Gamma(2\epsilon)}{\Gamma^2(1+\epsilon)} \int_0^1 {\rm d}x \int_0^1 {\rm d}y \int_0^1 {\rm d}z \frac{x^{-\epsilon} z^{-\epsilon}}{y^{1-\epsilon}} \frac{N_0 + N_1 y}{\Upsilon^{2\epsilon}(x)}. \quad (7.38)$$

Now, the $\int {\rm d}y$ integration can be performed analytically using equations (7.26) to (7.28). The result is expanded in powers of ϵ:

$$\begin{aligned}\Sigma_{O2a}^{(0)}(p) =& \frac{\alpha^2 C_\epsilon^2}{16\pi^2}\left(\frac{m}{\epsilon^2} + \frac{1}{\epsilon^2}(\not p - m) - \frac{m}{3\epsilon} + \frac{11}{3\epsilon}(\not p - m)\right) + \\ & \frac{\alpha C_\epsilon^2}{16\pi^2 \epsilon} \int_0^1 {\rm d}x \left(-4\not p (1-x)\log\Upsilon(x)\right) + \delta m_{O2a}^{(2)} + \Sigma_{O2aR}^{(0)}(p), \end{aligned} \quad (7.39)$$

where

$$\delta m^{(2)}_{O2a} = \frac{\alpha^2 C_\epsilon^2}{16\pi^2}\frac{m}{12}(145 + 2\pi^2). \tag{7.40}$$

The Feynman parameter integrations in $\Sigma^{(0)}_{O2aR}(p)$ could be performed analytically using Mathematica. For the computation of the $f(y) - f(0)$ term, we introduce an additional Feynman parameter using equation (284) in Ref. [63]:

$$\frac{1}{u^{1-3\epsilon}} - \frac{1}{1^{1-3\epsilon}} = \int_0^1 \mathrm{d}t \frac{(1-3\epsilon)xy}{(1-xyt)^{2-3\epsilon}}. \tag{7.41}$$

With this, we obtain the following expression:

$$\Sigma^{(0)}_{O2b}(p) = \frac{\alpha^2 C_\epsilon^2}{16\pi^2}\frac{(1-3\epsilon)\Gamma(2\epsilon)}{\Gamma^2(1+\epsilon)}\int_0^1 \mathrm{d}x \int_0^1 \mathrm{d}y \int_0^1 \mathrm{d}z \int_0^1 \mathrm{d}t \frac{x^{1-\epsilon} y z^{-\epsilon}}{y^{1-\epsilon}(1-xyr)^{2-3\epsilon}} \frac{N_0 + N_1 y}{\Upsilon^{2\epsilon}(x)}. \tag{7.42}$$

Due to the additional factor of y in the numerator, there are no UV divergences due to the $\int \mathrm{d}y$ integration in $\Sigma^{(0)}_{O2b}(p)$. Therefore, we can expand this expression in powers of ϵ:

$$\Sigma^{(0)}_{O2b}(p) = \frac{\alpha^2 C_\epsilon^2}{16\pi^2}\left(\frac{7m}{12\epsilon} + \frac{7}{12\epsilon}(\not{p} - m)\right) + \delta m^{(2)}_{O2b} + \Sigma^{(0)}_{O2bR}(p), \tag{7.43}$$

with

$$\delta m^{(2)}_{O2b} = \frac{\alpha^2 C_\epsilon^2}{16\pi^2}\frac{-m}{24}(-247 + 36\pi^2). \tag{7.44}$$

The Feynman parameter integrations in $\Sigma^{(0)}_{O2b}(p)$ were performed again analytically by the help of Mathematica. For the computation of the $g(y) - g(0)$ term, we introduce a Feynman parameter as follows:

$$\frac{1}{\Delta_2^{'2\epsilon}} - \frac{1}{\Upsilon^{2\epsilon}(x)} = -\int_0^1 \mathrm{d}t \frac{2\epsilon(\Delta_2^{'} - \Upsilon(x))}{((\Delta_2^{'} - \Upsilon(x))t + \Upsilon(x))^{1+2\epsilon}}. \tag{7.45}$$

Using this, we obtain the expression

$$\Sigma^{(0)}_{O2c}(p) = -\frac{\alpha^2 C_\epsilon^2}{16\pi^2}\frac{2\epsilon\Gamma(2\epsilon)}{\Gamma^2(1+\epsilon)}\int_0^1 \mathrm{d}x \int_0^1 \mathrm{d}y \int_0^1 \mathrm{d}z \int_0^1 \mathrm{d}t \frac{x^{-\epsilon} z^{-\epsilon}(N_0 + N_1 y)}{y^{1-\epsilon} u^{1-3\epsilon}} \frac{(\Delta_2^{'} - \Upsilon(x))}{((\Delta_2^{'} - \Upsilon(x))t + \Upsilon(x))^{1+2\epsilon}}. \tag{7.46}$$

$\Delta_2' - \Upsilon(x)$ contains, by definition, a factor of y. This factor and the additional factor of 2ϵ make sure that $\Sigma^{(0)}_{O2c}(p)$ is free of UV divergences. We can therefore evaluate this expression for $\epsilon = 0$:

$$\Sigma^{(0)}_{O2c}(p) = \delta m^{(2)}_{O2c} + \Sigma^{(0)}_{O2cR}(p), \tag{7.47}$$

with

$$\delta m^{(2)}_{O2c} = \frac{\alpha^2 C_\epsilon^2}{16\pi^2} m \left(\frac{15}{2} + \pi^2 \left(-\frac{5}{2} + \log(16) \right) - 10\zeta(3) \right). \tag{7.48}$$

The Feynman parameters in $\Sigma^{(0)}_{O2cR}(p)$ were integrated numerically.

In order to check the validity of our results, we also computed $\Sigma^{(0)}_{O2}(p)$ in a different way. One can rewrite equation (7.37) as follows:

$$\Sigma^{(0)}_{O2}(p) = \frac{\alpha^2 C_\epsilon^2}{16\pi^2} \frac{\Gamma(2\epsilon)}{\Gamma^2(1+\epsilon)} \int_0^1 \mathrm{d}x \int_0^1 \mathrm{d}y \int_0^1 \mathrm{d}z \frac{x^{-\epsilon} z^{-\epsilon} (N_0 + N_1 y)}{y^{1-\epsilon} u^{1-\epsilon} \Delta_{22}^{2\epsilon}}. \tag{7.49}$$

Here, $\Delta_{22} = \Upsilon(x) + yz\frac{(1-x)^2}{u}(1-\rho)$. In order to deal with UV divergences, we split this expression into two terms now instead of three terms:

$$\begin{aligned} \Sigma^{(0)}_{O2}(p) =& \frac{\alpha^2 C_\epsilon^2}{16\pi^2} \frac{\Gamma(2\epsilon)}{\Gamma^2(1+\epsilon)} \int_0^1 \mathrm{d}x \int_0^1 \mathrm{d}y \int_0^1 \mathrm{d}z \frac{x^{-\epsilon} z^{-\epsilon} (N_0 + N_1 y)}{y^{1-\epsilon}} \\ & \left(\frac{1}{\Upsilon^{2\epsilon}(x)} + \left(\frac{1}{u^{1-\epsilon} \Delta_{22}^{2\epsilon}} - \frac{1}{\Upsilon^{2\epsilon}(x)} \right) \right). \end{aligned} \tag{7.50}$$

The first term is identical to the previously computed $\Sigma^{(0)}_{O2a}(p)$. For the computation of the second term, we introduce an additional Feynman parameter according to:

$$\frac{1}{\left(u \Delta_{22}^{\frac{2\epsilon}{1-\epsilon}} \right)^{1-\epsilon}} - \frac{1}{\left(\Upsilon^{\frac{2\epsilon}{1-\epsilon}} \right)^{1-\epsilon}} = - \int_0^1 \mathrm{d}t \frac{(1-\epsilon) \left(u \Delta_{22}^{\frac{2\epsilon}{1-\epsilon}} - \Upsilon^{\frac{2\epsilon}{1-\epsilon}} \right)}{\left(\left(u \Delta_{22}^{\frac{2\epsilon}{1-\epsilon}} - \Upsilon^{\frac{2\epsilon}{1-\epsilon}} \right) t + \Upsilon^{\frac{2\epsilon}{1-\epsilon}} \right)}. \tag{7.51}$$

After this replacement, we obtain:

$$\begin{aligned} \Sigma^{(0)'}_{O2b}(p) =& - \frac{\alpha^2 C_\epsilon^2}{16\pi^2} \frac{\Gamma(2\epsilon)(1-\epsilon)}{\Gamma^2(1+\epsilon)} \int_0^1 \mathrm{d}x \int_0^1 \mathrm{d}y \int_0^1 \mathrm{d}z \int_0^1 \mathrm{d}t \frac{x^{-\epsilon} z^{-\epsilon} (N_0 + N_1 y)}{y^{1-\epsilon}} \\ & \frac{\left(u \Delta_{22}^{\frac{2\epsilon}{1-\epsilon}} - \Upsilon^{\frac{2\epsilon}{1-\epsilon}} \right)}{\left(\left(u \Delta_{22}^{\frac{2\epsilon}{1-\epsilon}} - \Upsilon^{\frac{2\epsilon}{1-\epsilon}} \right) t + \Upsilon^{\frac{2\epsilon}{1-\epsilon}} \right)}. \end{aligned} \tag{7.52}$$

We can expand this in powers of ϵ:

$$\Sigma^{(0)'}_{O2b}(p) = \frac{\alpha^2 C_\epsilon^2}{16\pi^2}\left(\frac{7m}{12\epsilon} + \frac{7}{12\epsilon}(\not{p} - m)\right) + \delta m^{(2)'}_{O2b} + \Sigma^{(0)'}_{O2bR}(p), \tag{7.53}$$

with

$$\delta m^{(2)'}_{O2b} = \frac{\alpha^2 C_\epsilon^2}{16\pi^2}\left(\frac{m}{24}(427 + 96\pi^2(-1 + \log 2) - 240\zeta(3))\right). \tag{7.54}$$

The divergent terms and $\delta m^{(2)'}_{O2b}$ are identical to the sum of the corresponding contributions of $\Sigma^{(0)}_{O2b}(p)$ and $\Sigma^{(0)}_{O2c}(p)$ from the previous calculation. Our numerical results for both methods were in good agreement with each other.

Inserting the third term of $\Gamma^\mu(p_1, p_2)$ into equation (7.18), we obtain:

$$\Sigma^{(0)}_{O3}(p) = -i\alpha^2 C_\epsilon \mu^{2\epsilon} m^{2\epsilon} \int_0^1 \mathrm{d}x \int_0^1 \mathrm{d}y \frac{-x^{-\epsilon}}{(-yu)^{1+\epsilon}} \int \frac{\mathrm{d}^D q}{(2\pi)^D} \frac{\gamma_\rho(\not{p} - \not{q} + m)(\mathcal{L}^\rho_{1l}(\not{p} - m) + \mathcal{L}^\rho_0)}{q^2\left((p-q)^2 - m^2\right) D'^{1+\epsilon}}. \tag{7.55}$$

Combining the denominator terms works similarly as for the first term:

$$\frac{1}{q^2\left((p-q)^2 - m^2\right) D'^{1+\epsilon}} = \frac{\Gamma(3+\epsilon)}{\Gamma(1+\epsilon)} \int_0^1 \mathrm{d}z \int_0^1 \mathrm{d}w \frac{z^{1+\epsilon} w^\epsilon}{(l^2 - z\Delta)^{2+\epsilon}}. \tag{7.56}$$

Here, l and Δ are the same as in the case of the first term. Performing this substitution in the numerator requires some tedious γ matrix algebra. The result can be represented as $\gamma_\rho(\not{p} - \not{q} + m)(\mathcal{L}^\rho_{1l}(\not{p} - m) + \mathcal{L}^\rho_0) = N_0 + N_2 l^2$. Performing the integration over the loop momentum, we obtain:

$$\Sigma^{(0)}_{O3}(p) = \frac{\alpha^2 C_\epsilon^2}{16\pi^2} \frac{m^{4\epsilon}}{\Gamma^2(1+\epsilon)} \int_0^1 \mathrm{d}x \int_0^1 \mathrm{d}y \int_0^1 \mathrm{d}z \int_0^1 \mathrm{d}w \frac{x^{-\epsilon} z^{1+\epsilon} w^\epsilon}{(yu)^{1+\epsilon}} \left(\frac{D\Gamma(2\epsilon) N_2}{2z^{2\epsilon}\Delta^{2\epsilon}} - \frac{\Gamma(1+2\epsilon) N_0}{(Z\Delta)^{1+2\epsilon}}\right). \tag{7.57}$$

The first term can be rewritten as

$$\Sigma^{(0)}_{O3}(p) = \frac{\alpha^2 C_\epsilon^2}{16\pi^2} \frac{D\Gamma(2\epsilon)}{2\Gamma^2(1+\epsilon)} \int_0^1 \mathrm{d}x \int_0^1 \mathrm{d}y \int_0^1 \mathrm{d}z \int_0^1 \mathrm{d}w \frac{x^{-\epsilon} z^{1-\epsilon} w^\epsilon}{y^{1-\epsilon} u^{1-3\epsilon}} \frac{N_2}{\Delta_3^{2\epsilon}}, \tag{7.58}$$

with $\Delta_3 = yu^2 \frac{\Delta}{m^2}$. It contains UV divergences to $\Gamma(2\epsilon)$ and $\int \mathrm{d}y \frac{1}{y^{1-\epsilon}}$. We employ a similar procedure to the one used in the computation of $\Sigma^{(0)}_{O2}(p)$, with $f(y) = \frac{1}{u^{1-3\epsilon}}$, $g(y) = \frac{1}{\Delta_3^{2\epsilon}}$. The $f(0)g(0)$ term corresponds to:

$$\Sigma^{(0)}_{O3a}(p) = \frac{\alpha^2 C_\epsilon^2}{16\pi^2}\frac{D\Gamma(2\epsilon)}{2\Gamma^2(1+\epsilon)}\int\limits_0^1 \mathrm{d}x \int\limits_0^1 \mathrm{d}y \int\limits_0^1 \mathrm{d}z \int\limits_0^1 \mathrm{d}w \frac{x^{-\epsilon} z^{1-\epsilon} w^{-\epsilon} N_2}{y^{1-\epsilon}\Upsilon^{2\epsilon}(x)}. \tag{7.59}$$

The $\int \mathrm{d}y$ integration can be performed analytically. Then we expand the result in powers of ϵ:

$$\begin{aligned}\Sigma^{(0)}_{O3a}(p) =& \frac{\alpha^2 C_\epsilon^2}{16\pi^2}\left(\frac{m}{2\epsilon^2} - \frac{3}{2\epsilon^2}(\not{p}-m) - \frac{13m}{6\epsilon} - \frac{7}{2\epsilon}(\not{p}-m)\right) + \\ & \frac{\alpha C_\epsilon^2}{16\pi^2\epsilon}\int\limits_0^1 \mathrm{d}x \left(-4m\log\Upsilon + 6\not{p}(1-x)\log\Upsilon\right) + \delta m^{(2)}_{O3a} + \Sigma^{(0)}_{O3aR}(p).\end{aligned} \tag{7.60}$$

Here,

$$\delta m^{(2)}_{O3a} = \frac{\alpha^2 C_\epsilon^2}{16\pi^2}\frac{m}{24}(2\pi^2 - 145). \tag{7.61}$$

Combining the two integral expressions from $\Sigma^{(0)}_{O2a}(p)$ and $\Sigma^{(0)}_{O3a}(p)$, we obtain [63]

$$\begin{aligned}&\frac{\alpha C_\epsilon^2}{16\pi^2\epsilon}\int\limits_0^1 \mathrm{d}x \left(-4\not{p}(1-x)\log\Upsilon\right) + \frac{\alpha C_\epsilon^2}{16\pi^2\epsilon}\int\limits_0^1 \mathrm{d}x \left(-4m\log\Upsilon + 6\not{p}(1-x)\log\Upsilon\right) \\ &\qquad = \frac{\alpha C_\epsilon^2}{4\pi\epsilon}\Sigma^{(0)}_{\mathrm{R},4}(p) + \frac{\alpha^2 C_\epsilon^2}{16\pi^2}\left(\frac{5m}{2\epsilon} + \frac{1}{2\epsilon}(\not{p}-m)\right).\end{aligned} \tag{7.62}$$

The Feynman parameter integrations in $\Sigma^{(0)}_{O3a}(p)$ can be performed analytically using Mathematica. For the computation of the $f(y) - f(0)$ term, we use Eq. (7.41), and obtain the following:

$$\Sigma^{(0)}_{O3b}(p) = \frac{\alpha^2 C_\epsilon^2}{16\pi^2}\frac{D\Gamma(2\epsilon)(1-3\epsilon)}{2\Gamma^2(1+\epsilon)}\int\limits_0^1 \mathrm{d}x \int\limits_0^1 \mathrm{d}y \int\limits_0^1 \mathrm{d}z \int\limits_0^1 \mathrm{d}w \int\limits_0^1 \mathrm{d}t \frac{x^{1-\epsilon} z^{1-\epsilon} w^{-\epsilon}}{y^{-\epsilon}(1-xyt)^{2-3\epsilon}}\frac{N_2}{\Upsilon^{2\epsilon}(x)}. \tag{7.63}$$

We expand this expression in powers of ϵ:

$$\Sigma^{(0)}_{O3b}(p) = \frac{\alpha^2 C_\epsilon^2}{16\pi^2}\left(-\frac{13m}{12\epsilon} - \frac{3}{4\epsilon}(\not{p}-m)\right) + \delta m^{(2)}_{O3b} + \Sigma^{(0)}_{O3bR}(p). \tag{7.64}$$

Here,

$$\delta m^{(2)}_{O3b} = \frac{\alpha^2 C_\epsilon^2}{16\pi^2}\frac{m}{12}(17\pi^2 - 94). \tag{7.65}$$

The Feynman parameter integrations in $\Sigma^{(0)}_{O3b}(p)$ were again performed analytically using Mathematica. We compute the $g(y) - g(0)$ term by the help of an additional Feynman

parameter, similar to Eq. (7.30). As in the case of the contributions $\Sigma^{(0)}_{O1b}$ and $\Sigma^{(0)}_{O2c}$, this is finite and we can compute $\Sigma^{(0)}_{O3c}(p)$ for $\epsilon = 0$:

$$\Sigma^{(0)}_{O3c}(p) = \delta m^{(2)}_{O3c} + \Sigma^{(0)}_{O3cR}(p). \tag{7.66}$$

$\delta m^{(2)}_{O3c} = \frac{\alpha^2 C_\epsilon^2}{16\pi^2} m \cdot 0.869...$ was determined numerically. Just as in the case of $\Sigma^{(0)}_{O2}(p)$, we also computed $\Sigma^{(0)}_{O3}(p)$ using a second method. We split the first term in $\Sigma^{(0)}_{O3}(p)$ as follows:

$$\Sigma'^{(0)}_{O3b}(p) = \frac{\alpha^2 C_\epsilon^2}{16\pi^2} \frac{D\Gamma(2\epsilon)}{2\Gamma^2(1+\epsilon)} \int_0^1 \mathrm{d}x \int_0^1 \mathrm{d}y \int_0^1 \mathrm{d}z \int_0^1 \mathrm{d}w \frac{x^{-\epsilon} z^{1-\epsilon} w^\epsilon N_2}{y^{1-\epsilon}} \left(\frac{1}{b^{1-\epsilon}} + \left(\frac{1}{a^{1-\epsilon}} - \frac{1}{b^{1-\epsilon}} \right) \right), \tag{7.67}$$

with $a = u\left(\frac{\Delta}{m^2}\right)^{\frac{2\epsilon}{1-\epsilon}}$, $b = (w\Upsilon(x))^{\frac{2\epsilon}{1-\epsilon}}$. The first term in this expression is identical to $\Sigma^{(0)}_{O3a}(p)$. For the computation of the second term, we introduce the usual additional Feynman parameter as in the case of $\Sigma^{(0)}_{O3c}(p)$:

$$\Sigma'^{(0)}_{O3b}(p) = -\frac{\alpha^2 C_\epsilon^2}{16\pi^2} \frac{D\Gamma(2\epsilon)(1-\epsilon)}{2\Gamma^2(1+\epsilon)} \int_0^1 \mathrm{d}x \int_0^1 \mathrm{d}y \int_0^1 \mathrm{d}z \int_0^1 \mathrm{d}w \int_0^1 \mathrm{d}t \frac{x^{-\epsilon} z^{1-\epsilon} w^\epsilon N_2}{y^{1-\epsilon}} \frac{a-b}{((a-b)t+b)^{2-\epsilon}}. \tag{7.68}$$

Expanding this in powers of ϵ, we obtain:

$$\Sigma^{(0)'}_{O3b}(p) = \frac{\alpha^2 C_\epsilon^2}{16\pi^2} \left(-\frac{13m}{12\epsilon} - \frac{3}{4\epsilon}(\not{p} - m) \right) + \delta m^{(2)'}_{O3b} + \Sigma^{(0)'}_{O3bR}(p). \tag{7.69}$$

$\delta m^{(2)'}_{O3b} = \frac{\alpha^2 C_\epsilon^2}{16\pi^2} m \cdot 7.0177...$ was determined numerically and is in good agreement with the sum $\delta m^{(2)}_{O3b} + \delta m^{(2)}_{O3c}$. Also, our numerical results for g-factor contributions obtained with $\Sigma^{(0)'}_{O3b}(p)$ and $\Sigma^{(0)}_{O3b}(p) + \Sigma^{(0)}_{O3c}(p)$ were in good agreement with each other.

Finally, we have to compute the term proportional to N_0 in $\Sigma^{(0)}_{O3}(p)$. This contribution is finite and can be evaluated in four dimensions:

$$\Sigma^{(0)}_{O3d}(p) = \delta m^{(2)}_{O3d} + \Sigma^{(0)}_{O3dR}(p). \tag{7.70}$$

$\delta m^{(2)}_{O3d} = \frac{\alpha^2 C_\epsilon^2}{16\pi^2} m(-10.732471...)$ was determined numerically. Adding all divergent terms, we obtain:

$$\begin{aligned} \Sigma^{(0)}_{O}(p) =& \frac{\alpha^2 C_\epsilon^2}{16\pi^2} \left(\left(\frac{3}{\epsilon^2} + \frac{5}{2\epsilon} \right) m + \left(-\frac{1}{\epsilon^2} + \frac{1}{2\epsilon} \right) (\not{p} - m) \right) + \\ & 2\frac{\alpha C_\epsilon^2}{4\pi\epsilon} \Sigma^{(0)}_{\mathrm{R},4}(p) + \text{UV finite terms} \end{aligned} \tag{7.71}$$

which is in agreement with the result in Ref. [63]. The sum of all finite mass counterterm contributions is

$$\delta m^{(2)}_{O,\mathrm{fin}} = \frac{\alpha^2 C_\epsilon^2}{16\pi^2} m(-1.0756...) \tag{7.72}$$

which is in good agreement with the exact value known analytically [63, 256]:

$$\delta m^{(2)}_{O,\mathrm{fin}} = \frac{\alpha^2 C_\epsilon^2}{16\pi^2} m \left(12\zeta(3) + 24(1-2\log 2)\zeta(2) - \frac{1}{4} \right) . \tag{7.73}$$

Having passed this consistency check, we used the analytically determined value for $\delta m^{(2)}_{O,\mathrm{fin}}$ in our codes which were used to compute g-factor contributions due to $\Sigma^{(0)}_O(p)$.

7.3 N and O irreducible, zero-potential contributions

The zero-potential contribution to the energy shift reads

$$\Delta E^{(0)}_{i,\,\mathrm{irred}} = 2\langle \delta a | \Sigma^{(0)}_i | a \rangle \,, \tag{7.74}$$

where $i \in \{N, O\}$. The unrenormalized SE functions can be represented as (see Ref. [63])

$$\Sigma^{(0)}_i(p) = \delta m^{(2)}_i + B^{(2)}_i(\not{p} - m) + a_i \frac{\alpha C_\epsilon^2}{4\pi\epsilon} \Sigma^{(0)}_{R,4}(p) + \Sigma^{(0)}_R(p) \,. \tag{7.75}$$

Here, $a_N = -1$ and $a_O = 2$. $B^{(2)}_i$ are divergent renormalization constants. The first three terms are UV divergent. The first term is canceled by mass renormalization. The energy shift corresponding to the sum of the second and third terms of the N and O contributions is

$$\sum_i \Delta E^{(0)}_{i,\mathrm{irred,div}} = 2B^{(2)} \langle \delta a | \gamma^0 (\not{p} - m) | a \rangle + \frac{\alpha C_\epsilon^2}{2\pi\epsilon} \langle \delta a | \gamma^0 \Sigma^{(0)}_{\mathrm{R},4} | a \rangle \,. \tag{7.76}$$

The second term of this equation is cancelled by a divergent contribution to the LAL, reducible diagrams (see Eq. (7.11)).

The renormalized part of the SE functions can be parameterized as [63]

$$\Sigma^{(0)}_{i,R}(p) = \frac{\alpha^2}{16\pi^2} (a_i(\rho) + \not{p} b_i(\rho)) \,. \tag{7.77}$$

The corresponding g-factor contribution is computed by inserting the renormalized SE functions into Eq. (7.74). The integration over angular variables is identical to the one-loop case [72]. The final formula for the g-factor contribution can be obtained from the corresponding one-loop formula (4.33) by replacing $a \longrightarrow a_i, b \longrightarrow b_i$ and multiplying with an additional factor of $\frac{\alpha}{4\pi}$. This means that, apart from Feynman parameter integrations, only a one-dimensional momentum integration is left to be done numerically. In the nested-loop case, all Feynman parameter integrations could be performed analytically using the computer algebra software Mathematica [257]. In the formulas for

the overlapping-loop diagram, there are up to four Feynman parameters. We performed all four Feynman parameter integrations numerically for the overlapping-loop diagram using the extended Gauss-Legendre quadrature rules [258].

We tested our numerical codes by replacing the magnetic wave function with the bound-electron wave function which corresponds to the computation of Lamb shift diagrams. We found a good agreement with previously published contributions to the two-loop Lamb shift [63].

7.4 N and O irreducible, one-potential term

The computation of the two-loop one-potential SE functions is discussed in some detail in Ref. [63]. We shall only quote some results here. The one-potential SE function can be parameterized as

$$\Sigma^{(1)}_{ij}(p_1,p_2) = \gamma^0 L^{(2)}_{i,j} + a_{i,j}\frac{\alpha C_\epsilon^2}{4\pi\epsilon}\Gamma^{(0)^0}_{\mathrm{R},4}(p_1,p_2) + \Sigma^{(1)}_{i,j,\mathrm{R}}(p_1,p_2)\,. \tag{7.78}$$

The energy shift corresponding to the sum of all divergent N and O contributions is

$$\sum_{i,j}\Delta E^{(1)}_{ij,\mathrm{irred,div}} = 2L^{(2)}\langle\delta a|\gamma^0 e\not{A}_e|a\rangle + \frac{\alpha C_\epsilon^2}{2\pi\epsilon}\langle\delta a|\gamma^0\Sigma^{(1)}_{\mathrm{R},4}|a\rangle. \tag{7.79}$$

Using $L^{(2)} = -B^{(2)}$ and the Dirac equation $(\not{p} - e\not{A}_e - m)|a\rangle = 0$ [63], we see that the first term is cancelled by the irreducible zero-potential contribution. The second term is cancelled by a divergent contribution to the LAL, reducible diagrams [see equation (7.11)].

We evaluated the one-potential contribution by using a Fortran Code provided by V. A. Yerokhin which was used for the computation of the corresponding Lamb shift contribution and modifying this code for the purpose of calculating g-factor contributions.

7.5 Zero-potential, N and O reducible contribution

Instead of computing the "side" and "ladder" contributions separately, we use the fact that the sum of the g-factor contributions of "side" and "ladder" corresponds to

$$\Delta E^{(0)}_{i,\mathrm{red}} = \Delta E_{\mathrm{mag}}\langle a|\gamma^0\left.\frac{\partial\Sigma^{(0)}_i}{\partial E}\right|_{E=E_a}|a\rangle\,. \tag{7.80}$$

Inserting the derivatives of the unrenormalized SE functions (7.75) into equation (7.80), we obtain the following g-factor contributions:

$$\Delta E^{(0)}_{i,\mathrm{red}} = B^{(2)}_i\Delta E_{\mathrm{mag}} + a_i\frac{\alpha C_\epsilon^2}{4\pi\epsilon}\Delta E_{\mathrm{mag}}\langle a|\gamma^0\left.\frac{\partial\Sigma^{(0)}_{R,4}}{\partial E}\right|_{E=E_a}|a\rangle + \Delta E_{\mathrm{mag}}\langle a|\gamma^0\left.\frac{\partial\Sigma^{(0)}_{i,R}}{\partial E}\right|_{E=E_a}|a\rangle\,. \tag{7.81}$$

The first two terms are UV divergent. Having calculated the renormalized SE functions, it is straightforward to determine the required derivative of the SE functions:

$$\left.\frac{\partial\Sigma^{(0)}_{i,\mathrm{R}}}{\partial E}\right|_{E=E_a} = \frac{\alpha^2}{16\pi^2}\left(-\frac{2E_a}{m^2}\frac{\partial a_i}{\partial\rho} + \gamma^0 b_i(\rho) - \frac{2E_a}{m^2}\frac{\partial b_i(\rho)}{\partial\rho}\right). \tag{7.82}$$

Inserting this expression into Eq. (7.80), the integration over angular variables is identical to the one-loop case (see Ref. [57]). The final expression for the finite part of the reducible contribution reads

$$\begin{aligned}\Delta E^{(0)}_{i,\mathrm{red,R}} =& \Delta E_{\mathrm{mag}}\frac{\alpha^2}{128\pi^5}\int \mathrm{d}pp^2\Bigg(-\frac{2E_a}{m^2}\frac{\partial a_i}{\partial\rho}\left(g^2-f^2\right) + b_i(\rho)\left(g^2+f^2\right)\\ &-\frac{2E_a}{m^2}\frac{\partial b_i}{\partial\rho}\left[E_a\left(g^2+f^2\right)+2pfg\right]\Bigg).\end{aligned} \tag{7.83}$$

This formula can also be obtained from the reducible one-loop SE correction to the g-factor [57], with the replacement $a \longrightarrow a_i, b \longrightarrow b_i$ and multiplication with an additional factor of $\frac{\alpha}{4\pi}$.

7.6 Zero-potential, vertex contribution

For the vertex diagrams, we found it more convenient to give formulas for the g-factor contribution instead of the energy shift. There are four zero-potential N and O diagrams. The corresponding g-factor contributions read

$$g^{(0)}_{ij,\mathrm{ver}} = -\frac{4m}{eB}\langle a|\gamma^0\Gamma^{(0)\mu}_{ij}eA_{m\mu}|a\rangle, \tag{7.84}$$

where $i \in \{N,0\}$, $j \in \{\mathrm{side},\mathrm{ladder}\}$, and $\Gamma^{(0)\mu}_{ij}$ refers to the zero-potential contribution to the vertex functions only. Following the discussion of the one-loop vertex diagram in Ref. [57], we insert the momentum-space representation of the magnetic potential

$$\boldsymbol{A}(\boldsymbol{p}_1-\boldsymbol{p}_2) = -\frac{i}{2}(2\pi)^3\left(\boldsymbol{B}\times\nabla_{\boldsymbol{p}_2}\delta^3(\boldsymbol{p}_1-\boldsymbol{p}_2)\right) \tag{7.85}$$

into Eq. (7.84) and obtain

$$g^{(0)}_{ij,\mathrm{ver}} = -2im\int\frac{d^3p_1}{(2\pi)^3}\int d^3p_2\overline{a}(p1)\left(\nabla_{p_2}\delta(\boldsymbol{p}_1-\boldsymbol{p}_2)\times\boldsymbol{\Gamma}^{(0)}_{i,j}(p_1,p_2)\right)_z a(\boldsymbol{p}_2). \tag{7.86}$$

In order to deal with the derivative of the δ function, we integrate expression (7.86) by parts [57]. After that, we can integrate over one momentum variable to obtain [57]

$$\begin{aligned}g^{(0)}_{ij,\mathrm{ver}} =& 2im\int\frac{d^3p}{(2\pi)^3}\overline{a}(\boldsymbol{p})\Xi_{i,j}(p)a(\boldsymbol{p}) -\\ &-2im\int\frac{d^3p}{(2\pi)^3}\overline{a}(\boldsymbol{p})\left(\boldsymbol{\Gamma}^{(0)}_{i,j}(p,p)\times\nabla_p\right)_z a(\boldsymbol{p}),\end{aligned} \tag{7.87}$$

where $\Xi_{i,j}(p) = \left(\nabla_{p_2} \times \boldsymbol{\Gamma}^{(0)}_{i,j}(p,p_2)\Big|_{p_2=p} \right)_z$.

Contributions with the derivative acting on the vertex function and the bound-electron wave function will be called $g_{\mathrm{ver},1}$-type and $g_{\mathrm{ver},2}$-type contributions, respectively, following the nomenclature of Ref. [57]. We will discuss these two types of contributions separately.

$g_{\mathrm{ver},2}$-type contributions

Since these contributions contain the vertex functions with equal momenta, we employ a generalization of the one-loop Ward identity (e.g. Ref. [6, 57, 79]) which corresponds to two-loop diagrams:

$$\sum_j \Gamma^{(0)\,\beta}_{ij}(p,p) = -\partial^\beta \Sigma^{(0)}_i(p)\,. \tag{7.88}$$

Using this identity, we can compute the sum of "side" and "ladder" contributions directly. Inserting the unrenormalized expression of the SE functions into equation (7.87), we obtain

$$g^{(0)}_{\mathrm{ver},i,2} = -B^{(2)}_i g_{\mathrm{D}} + a_i \frac{\alpha C_\epsilon^2}{4\pi\epsilon} \Delta g^{(0)}_{\mathrm{ver},2} - 2im \int \frac{d^3p}{(2\pi)^3} \overline{a}(\boldsymbol{p}) \left((\nabla \Sigma_i(p)) \times \nabla \right)_z a(\boldsymbol{p})\,. \tag{7.89}$$

The first two terms of this expression are divergent. The first term is cancelled by the N and O reducible contribution [see equation (7.81)]. The second term contains the $g^{(0)}_{\mathrm{ver},2}$ contribution, known from the one-loop self-energy contribution to the g-factor, equation (36) in Ref. [57]. The finite part of equation (7.89) can be determined by taking the derivative of the SE functions:

$$\partial^\mu \Sigma^{(0)}_i(p) = \frac{\alpha^2}{16\pi^2} \left(\frac{2p^\mu}{m^2} \frac{\partial a_i(\rho)}{\partial \rho} - \gamma^\mu b_i(\rho) + \frac{2p^\mu}{m^2} \frac{\partial b_i(\rho)}{\partial \rho} \right)\,. \tag{7.90}$$

After inserting this expression into Eq. (7.89), the integration over angular variables can be performed identically to the one-loop case [57]. After angular integration, we obtain the following formula for the renormalized part of $g_{\mathrm{ver},i,2}$:

$$\begin{aligned} g^{(0)}_{\mathrm{ver},i,2,\mathrm{R}} =& \frac{\alpha^2 m}{96\pi^5} \int dp p^2 \Bigg(-\frac{2}{m^2} \frac{\partial a_i(\rho)}{\partial \rho} f^2 + b_i(\rho) \left(\frac{2gf}{p} + gf' - fg' \right) + \\ & \frac{2}{m^2} \frac{\partial b_i(\rho)}{\partial \rho} f(Ef + pg) \Bigg)\,. \end{aligned} \tag{7.91}$$

Here, $()' = \frac{\mathrm{d}()}{\mathrm{d}p}$ denotes the derivative with respect to momentum. This formula can also be obtained from the one-loop vertex, 2 correction to the g-factor [57], with the replacement $a \longrightarrow a_i, b \longrightarrow b_i$ and multiplication with an additional factor of $\frac{\alpha}{4\pi}$.

$g_{\text{ver},1}$-type contributions

These contributions require the computation of new loop integrals. While power counting suggests that these contributions are finite, they can contain UV divergences due to a UV divergent subgraph.

N, side term

This type of calculation will be illustrated using the "N, side" term as an example. The corresponding function $\Xi_{\text{N,side}}(p)$ reads

$$\Xi_{\text{N,side}} = -8\pi i\alpha \int \frac{d^D q}{(2\pi)^4}\gamma^\mu \frac{1}{\not p - \not q - m}\widetilde{\Sigma}(p-q)\frac{1}{\not p - \not q - m}\,(\boldsymbol{\gamma}\times\nabla)_z\,\frac{1}{\not p - \not q - m}\gamma_\mu\frac{1}{q^2}\,. \tag{7.92}$$

We use the following parameterization of the "N, side" vertex function [63]:

$$\Gamma^{(0),\nu}_{\text{N,side}}(p_1,p_2) = -8\pi i\alpha\mu^{2\epsilon}\int \frac{d^D q}{(2\pi)^4}\gamma^\mu \frac{1}{\not p_1 - \not q - m}\widetilde{\Sigma}(p_1-q)\frac{1}{\not p_1 - \not q - m}\gamma^\nu\frac{1}{\not p_2 - \not q - m}\gamma_\mu\frac{1}{q^2}\,. \tag{7.93}$$

In this case, the derivative in equation (7.87) acts only on one factor in the vertex function. Using the following equivalent parameterization of the "N, side" vertex function,

$$\Gamma^{(0),\nu}_{\text{N,side}}(p_1,p_2) = -8\pi i\alpha\mu^{2\epsilon}\int \frac{d^D q}{(2\pi)^4}\gamma^\mu \frac{1}{\not p_1 - \not q - m}\gamma^\nu\frac{1}{\not p_2 - \not q - m}\widetilde{\Sigma}(p_2-q)\frac{1}{\not p_2 - \not q - m}\gamma_\mu\frac{1}{q^2}, \tag{7.94}$$

the derivative acts on three terms. We used both parameterization of the N, side vertex function to compute the corresponding g-factor contribution in order to check the validity of our formulas. Both characterizations gave the same formulas for $g_{N,\text{side},1}$. We use formulas (245) to (247) in Ref. [63] for the one-loop SE function $\widetilde{\Sigma}^{(0)}(p-q)$. Using this parameterization, $\widetilde{\Sigma}^{(0)}(p-q)$ consists of three terms. Inserting the first term into equation (7.92), we obtain

$$\Xi_{\text{N,side},1}(p) = \frac{i\alpha^2 C_\epsilon \mu^{2\epsilon}}{\epsilon(1-2\epsilon)}\int \frac{d^D q}{(2\pi)^D}\frac{\gamma^\mu(-2((\boldsymbol{p}-\boldsymbol{q})\times\boldsymbol{\gamma})_z - (\not p - \not q + m)(\boldsymbol{\gamma}\times\boldsymbol{\gamma})_z)\gamma_\mu}{q^2[(p-q)^2-m^2]}\,. \tag{7.95}$$

We simplified the numerator of this expression using the identity [6]

$$\gamma^k(\not p + m) = 2p^k - (\not p - m)\gamma^k\,, \tag{7.96}$$

and exploiting $\boldsymbol{p}\times\boldsymbol{p} = \boldsymbol{0}$, as it was done in Ref. [57]. Combining denominators using Feynman parameters, we can compute the momentum integral using well-known formulas for loop integrals (e.g. Ref. [6]). In Ref. [57], the identity $\boldsymbol{\gamma}\times\boldsymbol{\gamma} = 2i\gamma^0\gamma_5\boldsymbol{\gamma}$ is used. Since γ_5 is a well-defined quantity only in exactly 4 dimensions, this replacement can only be made after the ϵ expansion [259]. Therefore, we will not make this replacement

and instead keep terms of the form $\boldsymbol{\gamma} \times \boldsymbol{\gamma}$. Performing the ϵ expansion, we obtain

$$\Xi_{\mathrm{N,side,1}}(p) = 2\frac{\alpha^2 C_\epsilon^2}{16\pi^2 m^2} \int_0^1 \mathrm{d}z \frac{N_0}{\Upsilon \epsilon} + 2\frac{\alpha^2 C_\epsilon^2}{16\pi^2 m^2} \int_0^1 \mathrm{d}z \frac{N_0(2 - \log(\Upsilon) - \log(z)) + N_1}{\Upsilon} \,. \tag{7.97}$$

Here, $\Upsilon = z + \rho - z\rho$, and N_0 and N_1 are the $\mathcal{O}\left(\epsilon^0\right)$ and $\mathcal{O}\left(\epsilon^1\right)$ contributions to the numerator, respectively:

$$N_0 = 2(1-z)(2(\boldsymbol{p} \times \boldsymbol{\gamma})_z - (\boldsymbol{\gamma} \times \boldsymbol{\gamma})_z \not{p}), \tag{7.98}$$

$$N_1 = 4m(\boldsymbol{\gamma} \times \boldsymbol{\gamma})_z - 2(1-z)(2(\boldsymbol{p} \times \boldsymbol{\gamma})_z + \not{p}(\boldsymbol{\gamma} \times \boldsymbol{\gamma})_z). \tag{7.99}$$

We can perform the integrations over angular variables using formulas for elementary angular integrals, equations (25) and (26) in Ref. [57]. The divergent g-factor contribution is

$$g^{(0)}_{\mathrm{ver,N,side,1,div}} = -2\frac{\alpha C_\epsilon^2}{4\pi\epsilon} \Delta g^{(0)}_{\mathrm{ver},1} \,, \tag{7.100}$$

where $g^{(0)}_{\mathrm{ver},1}$ is the contribution to the one-loop vertex correction (equation (27) in Ref. [57]). The result for the finite part, after angular integration, reads

$$g^{(0)}_{\mathrm{N,side,1R}} = \frac{\alpha^2}{16\pi^5 m} \int \mathrm{d}p p^2 (A_1(\rho) I_1 + A_2(\rho) I_2) \,, \tag{7.101}$$

where

$$A_1(\rho) = \int_0^1 \mathrm{d}z \frac{(1-z)(3 - \log(\Upsilon) - \log(z)}{\Upsilon} \,, \tag{7.102}$$

$$A_2(\rho) = \int_0^1 \mathrm{d}z \frac{-m}{\Upsilon} \,, \tag{7.103}$$

$$I_1 = g(E_a g + p f) - \frac{1}{3} f(E_a f + p g) \,, \tag{7.104}$$

$$I_2 = g^2 + \frac{1}{3} f^2 \,. \tag{7.105}$$

The contributions due to the second and third term of $\widetilde{\Sigma}^{(0)}(p-q)$ are finite and can therefore be computed in 4 dimensions in a similar way. The results are:

$$g^{(0)}_{\mathrm{N,side,2}} = -\frac{\alpha^2}{4\pi^5 m} \int \mathrm{d}p p^2 A_{N2}(\rho) I_1 \,, \tag{7.106}$$

$$g^{(0)}_{\mathrm{N,side,3}} = -\frac{\alpha^2}{8\pi^5 m} \int \mathrm{d}p p^2 A_{N3}(\rho) I_1 \,, \tag{7.107}$$

with

$$A_{N2}(\rho) = \int_0^1 \mathrm{d}x \int_0^1 \mathrm{d}z \int_0^1 \mathrm{d}w \frac{(2+x)(1-x)(1-z)(1-w)}{(1-x(1-w)-(1-x)(1-z)(1-\rho))^2}, \tag{7.108}$$

$$A_{N3}(\rho) = \int_0^1 \mathrm{d}x \int_0^1 \mathrm{d}z \int_0^1 \mathrm{d}w \frac{(2-x)(1-z)}{1-x(1-w)-(1-x)(1-z)(1-\rho)}. \tag{7.109}$$

N, ladder contribution

Beginning with the "N, ladder" vertex function [63], we find that the "N, ladder" contribution consists of two terms, corresponding to

$$\begin{aligned}\Xi_{\mathrm{N,ladder}}(p) = &-4\pi i\alpha \int \frac{\mathrm{d}^4q}{(2\pi)^4}\gamma^\mu \frac{1}{\not p - \not q - m}\boldsymbol{\Omega}(p,q)_z \frac{1}{\not p - \not q - m}\gamma_\mu \frac{1}{q^2} - \\ &4\pi i\alpha\mu^{2\epsilon} \int \frac{\mathrm{d}^Dq}{(2\pi)^D}\gamma^\mu \frac{1}{\not p - \not q - m}\left(\boldsymbol{\Gamma}(p-q,p-q)\times\boldsymbol{\nabla}\right)_z \frac{1}{\not p - \not q - m}\gamma_\mu \frac{1}{q^2}\,,\end{aligned} \tag{7.110}$$

where

$$\boldsymbol{\Omega}(p,q) = 4\pi i\alpha \int \frac{\mathrm{d}^4q'}{(2\pi)^4}\gamma^\nu \frac{1}{\not p - \not q - \not q' - m}\left(\boldsymbol{\gamma}\times\frac{1}{\not p - \not q - \not q' - m}\boldsymbol{\gamma}\right)\frac{1}{\not p - \not q - \not q' - m}\gamma_\nu \frac{1}{q'^2}\,. \tag{7.111}$$

The second term in Eq. (7.110) contains the one-loop vertex function (with equal momenta) as a subdiagram. We can use the one-loop Ward identity $\Gamma^{(0)\,\beta}(p,p) = -\partial^\beta \Sigma^{(0)}(p)$ [57] to compute this contribution. For this, one has to take the derivative of equations (245) and (247) in Ref. [63] and insert this expression into equation (7.110). Alternatively, one can use representation (252) in Ref. [63] for the one-loop vertex function, evaluate it for equal momenta and insert this expression into equation (7.110). Since we did not find a way to match the representations for $\Gamma^{(0)\,\mu}(p,p)$ and $\partial^\mu\Sigma^{(0)}(p)$, we computed the second term of the "N, ladder" contribution using both methods to check the validity of our formulas. We found identical formulas using both methods. The divergent contribution to the g-factor is

$$g_{\mathrm{ver,N,ladder,1,div}} = \frac{\alpha C_\epsilon^2}{4\pi\epsilon}\Delta g^{(0)}_{\mathrm{ver},1}\,. \tag{7.112}$$

The first term of the "N, ladder" contribution contains neither the one-loop SE nor the one-loop vertex function as a subdiagram. Since the entire contribution is finite, we can perform our calculation in 4 dimensions. We first computed the function $\boldsymbol{\Omega}(p,q)_z$ and inserted this expression into equation (7.110). Alternatively, we computed the first term of the "N, ladder" contribution by using $\boldsymbol{\Omega}(p,q)_z = \left(\boldsymbol{\nabla}_{\boldsymbol{p}_2}\times\boldsymbol{\Gamma}(p-q,p_2-q)\big|_{\boldsymbol{p}_2=\boldsymbol{p}}\right)_z$. We computed the derivative of the one-loop vertex function using equation (252) in Ref. [63]. The numerical results for the "N, ladder" contribution computed with both methods were in excellent agreement.

O, side contribution

The evaluation of the O contributions can be performed in a similar way. Just as in the nested loop case, there are two ways to express the "O, side" vertex functions [63]:

$$\Gamma^{(0),\mu}_{\text{side},1}(p_1,p_2) = -4\pi i\alpha\mu^{2\epsilon}\int\frac{d^Dq}{(2\pi)^D}\Gamma^{\nu}_D(p_1,p_1-q)\frac{1}{\not p_1-\not q-m}\gamma^\mu\frac{1}{\not p_1-\not q-m}\gamma_\nu\frac{1}{q^2}\,, \tag{7.113}$$

$$\Gamma^{(0),\mu}_{\text{side},2}(p_1,p_2) = -4\pi i\alpha\mu^{2\epsilon}\int\frac{d^Dq}{(2\pi)^D}\gamma_\sigma\frac{1}{\not p_1-\not q-m}\gamma^\mu\frac{1}{\not p_1-\not q-m}\Gamma^{\sigma}_D(p_2-q,p_2)\frac{1}{q^2}\,. \tag{7.114}$$

The total "O, side" vertex function is $\Gamma^{(0),\mu}_{\text{side}}(p_1,p_2)=\Gamma^{(0),\mu}_{\text{side},1}(p_1,p_2)+\Gamma^{(0),\mu}_{\text{side},2}(p_1,p_2)$. The O, side term is UV divergent due to the UV divergence in the one-loop vertex function. We can use parameterization (252) from [63] for the vertex function in order to compute this contribution.

Unlike in the nested-loop case, these two vertex functions do not lead to identical results for the $g_{\text{ver},1}$ contribution. The corresponding expressions for $\Xi_{\text{O,side}}(p)$ are

$$\Xi_{\text{O,side}\,1}(p) = -4\pi i\alpha\mu^{2\epsilon}\int\frac{d^Dq}{(2\pi)^D}\Gamma^{\nu}_D(p,p-q)\frac{1}{\not p-\not q-m}\left(\boldsymbol{\gamma}\times\nabla_p\right)_z\frac{1}{\not p-\not q-m}\gamma_\nu\frac{1}{q^2}\,, \tag{7.115}$$

$$\begin{aligned}\Xi_{\text{O,side}\,2}(p) = &-4\pi i\alpha\mu^{2\epsilon}\int\frac{d^Dq}{(2\pi)^D}\gamma_\sigma\frac{1}{\not p-\not q-m}\left(\boldsymbol{\gamma}\times\nabla_p\frac{1}{\not p-\not q-m}\right)_z\Gamma^{\sigma}_D(p-q,p)\frac{1}{q^2}\,, \\ &-4\pi i\alpha\mu^{2\epsilon}\int\frac{d^Dq}{(2\pi)^D}\gamma_\sigma\frac{1}{\not p-\not q-m}\left(\boldsymbol{\gamma}\times\frac{1}{\not p-\not q-m}\nabla_p\Gamma^{\sigma}_D(p-q,p)\right)_z\frac{1}{q^2}\,.\end{aligned} \tag{7.116}$$

$\Xi_{\text{O,side}\,1}(p)$ and the first line of $\Xi_{\text{O,side}\,2}(p)$ give identical contributions to the g-factor. Since the g-factor contribution of the second line of $\Xi_{\text{O,side}\,2}(p)$ was found to be non-vanishing, the g-factor contributions of the two overlapping loop, side vertex functions are not equal. In order to compute this contribution, we determined the derivative of the one-loop vertex function from equation (252) in Ref. [63] and inserted this into equation (7.116).

The total divergent "O, side" contribution to the g-factor is

$$g_{\text{ver,O,side,1,div}} = 2\frac{\alpha C_\epsilon^2}{4\pi\epsilon}\Delta g^{(0)}_{\text{ver},1}\,. \tag{7.117}$$

O, ladder contribution

The most difficult contribution is the "O, ladder" one. The "O, ladder" contribution is finite and can therefore be evaluated in 4 dimensions. The most challenging aspect of this calculation is the γ matrix algebra in the numerators. The program Mathematica was used to facilitate such computations.

Formulas and results

The sum of all divergent contributions of the N and O, red and vertex diagrams is [see equations (7.81),(7.89),(7.100), (7.112) and (7.117)] $\frac{\alpha C_\epsilon^2}{4\pi\epsilon}\Delta g_{\rm ver}^{(0)}$, where $\Delta g_{\rm ver}^{(0)}$ is the sum of the g-factor contributions of the one-loop vertex and reducible SE diagrams (see Ref. [57]). This divergent contribution is cancelled by a corresponding divergence of the "LAL, red" diagrams d and f (see Eq. (7.14)).

In all cases considered, the finite part of $\Xi_{ij}(p)$ can be expressed as:

$$\Xi_{ij,\mathrm{R}}(p) = A_{0,ij}(\rho)(\boldsymbol{p}\times\boldsymbol{\gamma})_z + A_{1,ij}(\rho)(\boldsymbol{\gamma}\times\boldsymbol{\gamma})_z\not{p} + A_{2,ij}(\rho)(\boldsymbol{\gamma}\times\boldsymbol{\gamma})_z + A_{3,ij}(\rho)(\boldsymbol{p}\times\boldsymbol{\gamma})_z\not{p}, \tag{7.118}$$

where $A_{3,ij}(\rho)$ is non-zero only for overlapping loop diagrams. In order to compute the renormalized g-factor contributions, the integration over angular variables can be performed analytically using the formulas for angular integrals in Ref. [57]. We obtain the following expression for a $g_{\rm ver}$-type 1 contribution:

$$g_{ij,\mathrm{ver},1}^{(0)} = \frac{\alpha^2 m_e}{32\pi^5}\int \mathrm{d}pp^2\left(A_{1,ij}(\rho)I_1 + A_{2,ij}(\rho)I_2 + A_{3,ij}(\rho)I_3\right). \tag{7.119}$$

Here, $I_3 = \frac{1}{3}\left(2E_a pgf + p^2\left(g^2+f^2\right)\right)$. I_1 and I_2 are the same as above [equations (7.104) and (7.105)].

For the N contributions, all Feynman parameter integrations can be performed analytically using Mathematica. The remaining momentum integration was performed numerically. In the O case, Feynman parameter integrations were performed using the extended Gauss-Legendre quadrature formulas from Ref. [258]. The remaining momentum integration was performed using the standard Gauss-Legendre procedure [130].

7.7 Alternative computation of the vertex type 1 contributions

Instead of computing the functions $\boldsymbol{\Xi}_{ij}(p)$ as new loop integrals, one can also begin with the expressions for the zero-potential vertex functions and take the derivative with respect to momentum. The general expression for the renormalized part of the zero-potential two-loop vertex functions is:

$$\begin{aligned}\Gamma_{ij\mathrm{R}}^{(0)\mu}(p_1,p_2) =& \frac{\alpha^2}{16\pi^2}\Big(A\gamma^\mu + (B_1p_1^\mu + B_2p_2^\mu)\not{p}_1 + (C_1p_1^\mu + C_2p_2^\mu)\not{p}_2 + D\not{p}_1\gamma^\mu\not{p}_2 + \\ & (E_1p_1^\mu + E_2p_2^\mu)\not{p}_1\not{p}_2 + F\not{p}_1\gamma^\mu + G\gamma^\mu\not{p}_2 + (H_1p_1^\mu + H_2p_2^\mu)\Big).\end{aligned} \tag{7.120}$$

This expression was generalized from the expression for the one-loop vertex function given in Ref. [72] and taking into account information about the time component of the two-loop vertex function given in Ref. [63] (where it is called the one-potential SE function). The coefficient functions A, B_1, B_2, C_1, C_2, D, E_1, E_2, F, G, H_1, H_2 are functions of p_1 and p_2.

Taking the derivative of expression (7.120), and subsequently evaluating the result at $p_1 = p_2 = p$, we obtain:

$$\begin{aligned}\Xi(p) =&\frac{\alpha^2}{16\pi^2}\Big(A_0(\rho)(\boldsymbol{p}\times\boldsymbol{\gamma})_z + D\not{p}(\boldsymbol{\gamma}\times\boldsymbol{\gamma})_z + G(\boldsymbol{\gamma}\times\boldsymbol{\gamma})_z + \\ &(E_1+E_2)\not{p}(\boldsymbol{p}\times\boldsymbol{\gamma})_z + (\nabla_{\boldsymbol{p}_2}(G-F)|_{\boldsymbol{p}_2=\boldsymbol{p}}\times\boldsymbol{\gamma})_z\not{p}\Big).\end{aligned} \tag{7.121}$$

We do not specify $A_0(\rho)$ here, since it does not give a contribution to the g-factor, as explained in the previous section. Comparing this result with the general expression for $\Xi(p)$, we find:

$$A_1(\rho) = D, \tag{7.122}$$

$$A_2(\rho) = G, \tag{7.123}$$

$$A_3(\rho)(\boldsymbol{p}\times\boldsymbol{\gamma})_z\not{p} = (\nabla_{\boldsymbol{p}_2}(G-F)|_{\boldsymbol{p}_2=\boldsymbol{p}}\times\boldsymbol{\gamma})_z\not{p} - (E_1+E_2)(\boldsymbol{p}\times\boldsymbol{\gamma})_z\not{p}. \tag{7.124}$$

The coefficient functions $A_1(\rho)$, $A_2(\rho)$ and $A_3(\rho)$ have to be inserted into the general formula for the computation of the vertex, type 1 contributions, Eq. (7.119).

We tested this procedure by computing the one-loop vertex 1 contribution to the g-factor, starting from the parameterization for the one-loop vertex function given in Ref. [72]. Since the coefficient functions E_1, E_2, F and G of the one-loop vertex function are zero, the only contribution is $A_1(\rho)$ due to the coefficient function D. Considering the case $p_1 = p_2 = p$ greatly simplifies the formulas given in Ref. [72], and the remaining Feynman parameter integration in these formulas becomes easy. The final formula for the vertex 1 contribution we obtained is identical to the one given in Ref. [57].

Nested loop

We computed the formulas for the "N, side" contribution beginning from our formulas for the vertex function. We managed to perform all Feynman parameter integrations using Mathematica. Our formulas obtained using this method agreed with our formulas obtained in the previous section.

For the "N, vertex" diagram, we could also perform all Feynman parameter integrations analytically. Our numerical results obtained by both methods are in excellent agreement.

Overlapping loop

We also computed the "O, side" and "O, ladder" contributions according to this method. Note that, by first computing the loop integral before considering the special case $p_1 = p_2$, we introduce an additional Feynman parameter compared to the previous method [6, 63]. For the overlapping-loop case, this means that our final formulas for the g-factor contributions contain up to five Feynman parameter integrations. Unfortunately, unlike the one-loop case, we did not find a Feynman parametrization in such a way that one

of the Feynman parameter integrations becomes easy. We computed the O, vertex type 1 contributions, integrating all five Feynman parameters numerically. Our results were in good agreement with the results obtained with the previous method. It should be mentioned that, due to the high computation time, we did not use a high number of integration points and did not include the results obtained with this method for the estimation of the numerical uncertainty.

7.8 Remaining UV-divergent term

Adding all UV divergent F term contributions [see equations (7.11), (7.14), (7.76), (7.79), (7.81), (7.89), (7.100), (7.112) and (7.117)], we obtain the following remaining UV divergent term:

$$\Delta E_{\mathrm{F,div}} = 2B^{(1)}\langle a|\gamma^0\Sigma_D^{(2+)}|\delta a\rangle + B^{(1)}\Delta E_{vr,D}^{(1+)}\,. \tag{7.125}$$

Since the total two-loop SE correction is UV-finite, and the M term contains only UV-finite diagrams, we can be sure that these divergences will be cancelled by corresponding contributions to the P term.

7.9 Numerical results and the free-electron limit

For the free electron case, i.e. in the limit of a vanishing Coulomb potential, all P and M term contributions as well as one-potential F term contributions vanish, since, by definition, they contain interactions with the nuclear potential. Furthermore, the irreducible N and O diagrams vanish because the SE correction is canceled exactly by mass renormalization [6]. We therefore expect these contributions to converge to zero in the limit $Z \longrightarrow 0$. For the same reason, we expect all LAL contributions to converge to zero in this limit, as well as those reducible LAL diagrams which contain the one-loop SE correction (a,b, e, and g), or the irreducible one-loop "SE,wf" correction to the one-loop g-factor (c) as one factor. The remaining diagrams are the N and O vertex and reducible diagrams and the following LAL, red diagrams: d and f. We expect the sum of the zero-potential contributions (zero-potential contributions of both factors for LAL, red) of these diagrams to converge to the two-loop SE contribution to the free-electron g-factor. This corresponds to the sum of equations (7.119), (7.91), (7.83) and (7.15). The free-electron g-factor contribution can be easily determined using the expressions for the form factors from Ref. [56]. Our numerical results for low-Z converge well to the free-electron g-factor contribution, as shown in Table 7.1.

We defined the total zero-potential F term contribution to consist of the above mentioned diagrams and the irreducible zero-potential N and O contributions. Table 7.2 shows a detailed breakdown of zero-potential F term contributions for $Z = 82$. The table highlights that all terms need to be evaluated, i.e. there is no simple way of estimating the F term.

The reducible F term contribution consists of the remaining LAL,red contributions, i.e. equations (7.2), (7.5), (7.12) and (7.16). The one-potential F term consists of the

irreducible one-potential N and O contributions. The corresponding numerical values, together with their numerical uncertainties are given in Table 7.9 for various different Z and are plotted in Fig.7.1. The figure shows that, at high Z values, the low-Z behaviour which can be described by a few $Z\alpha$-expansion terms, is not applicable. Therefore, for heavy ions, it is indeed mandatory to perform a non-perturbative calculation.

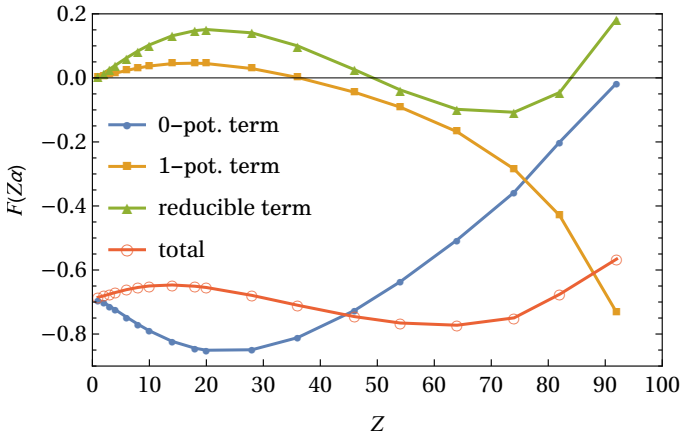

Figure 7.1: The zero- and one-potential and the reducible F term contributions, respectively, as a function of Z. Results are expressed in terms of the scaled function $F(Z\alpha)$, defined as $\Delta g = \frac{\alpha^2}{\pi^2} F(Z\alpha)$.

Z	$g^{\text{free}}_{\text{F,0pot}}$
1	-3.73645(7)
2	-3.77838(5)
3	-3.82963(5)
4	-3.88628(3)
6	-4.00745(3)
8	-4.13137(3)
10	-4.25262(3)
14	-4.47583(2)
18	-4.66407(2)
20	-4.74346(2)
36	-5.02289(1)
54	-4.69983(1)
82	-3.25804(1)
92	-2.78760(1)

Table 7.1: Subset of zero-potential F term diagrams which converges to the free-electron g-factor contribution $g_{\text{free,SESE}} = -3.71389279 \times 10^{-6}$ (see text for details). g-factor contributions are expressed in units of 10^{-6}.

Contribution	$g_{\text{F,0pot}}$
LAL,red,df	-0.70592
N,red	-3.35298
N, ver 2-type	4.99794
N, ver 1-type	-7.98377
O,red	-3.63951
O, ver 2-type	3.91721
O, ver 1-type	3.50898
N & O, irred	2.17644

Table 7.2: Individual contributions to the zero-potential F term for $Z = 82$ in units of 10^{-6}.

Z	$F_{\mathrm{F,0pot}}$	$F_{\mathrm{F,red}}$	$F_{\mathrm{F,1pot}}$
1	-0.693181(19)	0.005715(1)	0.00213(27)
2	-0.701989(10)	0.015596(2)	0.00576(27)
3	-0.712496(9)	0.026977(1)	0.01011(18)
4	-0.723816(6)	0.038885(2)	0.014544(44)
6	-0.747062(4)	0.062437	0.023242(27)
8	-0.769444(6)	0.084105	0.030852(6)
10	-0.789865(4)	0.103024	0.037022(16)
14	-0.822846(3)	0.131496(4)	0.044584(6)
18	-0.844231(3)	0.147488(2)	0.046072(2)
20	-0.850565(3)	0.151111(4)	0.044799(2)
28	-0.849133(4)	0.140733(8)	0.029121(2)
36	-0.811397(2)	0.100049(7)	0.001363
46	-0.726408(4)	0.025643(5)	-0.044823(1)
54	-0.636907(2)	-0.037442(12)	-0.091188(2)
64	-0.506144(4)	-0.098176(11)	-0.168186(2)
74	-0.357661(4)	-0.107297(12)	-0.284575(2)
82	-0.200464(4)	-0.045539(18)	-0.429814(2)
92	-0.016259(15)	0.183186(32)	-0.732700(4)

Table 7.3: The zero- and one-potential and reducible F term contributions for different atomic numbers. Results are expressed in terms of the scaled function $F(Z\alpha)$, defined as $\Delta g = \frac{\alpha^2}{\pi^2} F(Z\alpha)$. The zero-potential term contains all diagrams described in the free electron limit and the irreducible N and O diagrams. The reducible term contains the remaining "LAL, red" contributions. The one-potential term contains only the irreducible one-potential N and O diagrams.

8 Conclusions and outlook

In this thesis, the theory of the bound-fermion g-factor was discussed, with a special emphasis on methods for taking into account the interaction with the nuclear potential non-perturbatively. Such a treatment is required to achieve a highly accurate prediction of the g-factor for high-Z ions, and, in certain cases, even for medium- and low-Z ions. The theoretical framework developed here is mandatory for near-future stringent tests of quantum electrodynamics in strong electromagnetic fields, for a projected independent determination of the fine-structure constant [54], and for further substantial improvements of the electron mass value by means of Penning-trap experiments [1].

After the introductory Chapter, the theoretical treatment of the g-factor of free fermions was summarized, followed by a presentation of the quantum electrodynamic theory of bound states. In the forthcoming Chapter, we described in detail the analytical and numerical methods to evaluate the one-loop self-energy and vacuum polarization corrections, which were developed previously by several authors and presented in the literature, e.g. Ref. [57, 69, 71]. As an application of these methods, we investigated first the muonic vacuum polarization correction [4]. Our studies show that the effect of creation and annihilation of virtual muon pairs will become observable in g-factor experiments after an improvement of the uncertainty of nuclear radii in certain elements, e.g., with Ca ions.

As an additional application of bound-state quantum electrodynamic theory discussed thus far, we described the recent determination of the electron mass by a combined analysis of the theoretical bound-electron g-factor and the measurement of the Larmor and cyclotron frequencies in Penning trap experiments, and discussed possibilities for a further improvement of the accuracy of this fundamental quantity [1]. In particular, based on the treatment presented in the previous Chapters, we calculated the g-factor of the hydrogenlike $^4He^+$ ion. This light ion may serve as a helpful benchmark for the past determination of the electron mass with the $^{12}C^{5+}$ ion, and it also enables an accuracy improvement due to the fact in the lightest atomic systems, QED contributions are scaled down by high powers of the atomic number Z.

In the forthcoming Chapter, we put forward a method to determine the *muon* mass in analogy to the successful extraction of the *electron* mass as presented previously [2]. Such a determination necessitates an accurate theoretical prediction of the bound-muon g-factor. Therefore, we calculate all the relevant contributing terms at the one- and two-loop level, with special emphasis on vacuum polarization effects which are crucial in muonic systems. The scheme we suggest allows the improvement of the accuracy of the muon mass by one order of magnitude, provided that experiments with bound muons can achieve in near future the required accuracy. Furthermore, such an experiment will build a bridge between measurements of the free muon's magnetic moment anomaly

(i.e. the $(g-2)/2$) and its mass, and will thus shed new light on physics beyond the Standard Model. Presently, the discrepancy of the predicted and measured free-muon g factor values constitutes one of the most significant deviations of an electroweak physical observable [94]. With the subtraction of the QED binding corrections we calculated, the free-muon g-factor can be determined in the ionic experiments we propose, and contrasted to predictions including hadronic vacuum polarization and weak interaction contributions, and possible effects beyond the Standard Model [95].

As of now, in the H-like Si ion, the experimental error bar of the bound-electron g-factor is one order of magnitude lower than the theoretical uncertainty [34]. In order to improve the latter, it is necessary to calculate the two-loop SE correction to the g-factor non-perturbatively in $Z\alpha$, since the unknown higher-order terms in this coupling parameter constitute the dominant contribution to the theoretical uncertainty. This holds especially true for heavier elements which can be investigated in nearest future with the currently commissioned ALPHATRAP Penning-trap setup [35], and also for atomic numbers as low as $Z = 6$ [62]. Therefore, in the main chapters of this thesis, we developed the exact theory of the two-loop SE corrections [3]. We demonstrated the cancellation of UV and IR divergences in the relevant set of Feynman diagrams. The occurrence of UV divergences necessitates the separation of the two-loop SE diagrams into the loop-after-loop type diagrams, and into the F, M, and the P term diagrams, similar to the two-loop SE correction to the Lamb shift [63]. Each of these terms has to be evaluated with different techniques. The F term consists of diagrams with only free internal electron lines, with zero or one interaction with the nuclear potential in the intermediate states. The M term diagrams contain many-potential internal electron lines (i.e. higher than first order interactions with the nucleus), and do not contain UV divergences. The P term diagrams contain many-potential internal electron lines, as well as a subdiagram with only free internal electron lines. There are UV divergences in P term diagrams because of their subdiagrams containing free-electron propagators. Since both P and M term diagrams contain many-potential internal fermionic lines, these contributions vanish in the free-electron limit. Furthermore, the loop-after-loop contribution also vanish in this limit, since, for free electrons, one of the SE loops acts as a correction to an external on-shell electron line in the Feynman diagrams. Therefore, one may expect the F-term to converge to the well-known two-loop SE correction to the free-electron g-factor in the limit $Z \to 0$.

In the subsequent Chapter, we performed the numerical evaluation of the F-term diagrams. Our results were found to converge to the two-loop SE correction to the free-electron g-factor [56], yielding an important consistency check of our renormalization scheme and the overall theoretical formalism. Other tests included the calculation of the F-term contribution to the two-loop Lamb shift SE correction, and its comparison to published literature values [63].

The computation of the loop-after-loop g-factor diagrams is still an ongoing project. Defining a self-energy perturbed wave function, we can perform the calculation of the loop-after-loop contributions as a straightforward generalization of one-loop calculations. The implementation of the SE corrected wave function is the numerically most challenging aspect in the evaluation of the loop-after-loop terms. The M and P terms also need

to be computed numerically. The M terms include, just as in the case of the Lamb shift, summations over two independent angular momentum quantum numbers [63]. The P term will include one such angular momentum summation, as well as numerical Fourier transforms [63]. Therefore, the final numerical accuracy of the two-loop SE terms will be determined by the numerical uncertainty of these computationally expensive terms.

After a complete numerical evaluation of the two-loop SE diagrams for the ground state of hydrogenic ions, the calculations can be repeated for other atomic states. The projected independent determination of the fine-structure constant also requires accurate QED predictions for Li-like ions [54]. Therefore, the two-loop SE corrections have to be re-evaluated for the $2s$ state, which is the valence ground state of a three-electron ion. Besides the trivial replacement of the bound-electron wave functions entering the formulas, this can be done by a straightforward modification of the complex integration contours in the many-potential terms.

For a complete evaluation of all two-loop Furry picture Feynman diagrams, one also needs to take into account diagrams with virtual light-by-light scattering subgraphs. The calculation of these terms is in progress, in collaboration with V. Debierre [5]. Such nonlinear QED effects do play a role in the heaviest hydrogenic ions, with a prominent example being $^{208}Pb^{81+}$. Experiments on this very heavy element are also projected at the ALPHATRAP setup [35], with the highly charged ions created in the Heidelberg Electron Beam Ion Trap (EBIT) of the Max Planck Institute for Nuclear Physics, and transported to the Penning trap with a beamline constructed specifically for this purpose, enabling the study of QED effects in the strongest electric fields available in a laboratory.

Appendix

A.1 Calculation of loop integrals

The calculation of Feynman diagrams with free internal fermion lines necessitates the evaluation of loop functions known from free QED [63, 72]. E.g. for the computation of one-loop SE diagrams, one has to evaluate the free one-loop SE and vertex functions [72]. In standard textbooks, usually one-loop functions are discussed for the special case of all external momenta being on-shell $p^2 = m^2$, i.e. for free particles [6, 79]. However, this is not sufficient for bound-fermion calculations, where these loop functions need to be computed for more general four-momenta $p = (E_a, \mathbf{p})$ [72].

A loop integral $L(p_1, p_2, ...p_n)$ typically has the following form in D dimensions [63, 260]:

$$L(p_1, p_2, ...p_n) = \int \frac{\mathrm{d}^D q}{(2\pi)^D} \frac{N(q)}{(q^2 + 2p_1 q + M_1)^{\alpha_1} \cdots (q^2 + 2p_n q + M_n)^{\alpha_n}}. \tag{A.1}$$

Here, $N(q)$ is a polynomial in q. The expressions in the denominator can be combined using Feynman parameters (equation (281) in Ref. [63]). Some special cases of this equation are derived in Appendix J of Ref. [261] and Chapter 10 of Ref. [80]. Feynman parameters are also used in standard textbooks about QFT, e.g. Ref. [6, 77, 81]. After a substitution, we obtain expressions of the form $\int \frac{\mathrm{d}^D l}{(2\pi)^D} \frac{\{1, l_\mu l_\nu, l_\mu l_\nu l_\rho l_\sigma, ...\}}{(l^2 - \Delta)^\alpha}$, with $\alpha = \sum_i \alpha_i$. It can be shown that odd powers of l in the numerator lead to vanishing integrals, and integrals with even powers of l in the numerator can be simplified, e.g. $l_\mu l_\nu \to \frac{l^2 g_{\mu\nu}}{D}$ (see Ref. [6, 63]). The integrals over l can then be carried out using formulas from e.g.Ref. [6, 63].

One-loop functions are usually UV divergent. In order to deal with these divergences, we regularize the loop functions by computing them in $D = 4 - 2\epsilon$ dimensions, where ϵ is an infinitesimal positive number. Dimensional regularization is discussed in detail in textbooks, e.g. in Ref. [6]. The results obtained after integration are expanded in powers of ϵ. UV divergences manifest themselves as inverse powers of ϵ. In the final result for an observable quantity, all contributions due to inverse powers of ϵ cancel.

Mass divergences in SE functions are dealt with using a renormalization scheme in which the SE function, evaluated for $\not{p} = m$, is subtracted: $\widetilde{\Sigma}^{(0)}(p) = \Sigma^{(0)}(p) - \Sigma^{(0)}(m)$. The remainder is still UV divergent. We do not use the usual textbook renormalization scheme [6], i.e. subtract $\delta_2(\not{p} - m)$ to deal with the remaining divergences because $\delta_2 = \left.\frac{\mathrm{d}\Sigma(p)}{\mathrm{d}\not{p}}\right|_{\not{p}=m}$ is IR divergent in the Feynman gauge [72]. Instead, in order to avoid IR divergences, we just separate the remaining UV divergent terms. In the case of two-loop

diagrams, we also separate only the UV divergent term instead of identifying the order α^2 contribution to δ_2. In the final result for an observable quantity, all contributions due to inverse powers of ϵ cancel.

Many two-loop diagrams contain the one-loop SE and vertex functions as a subdiagram. As the expansion in powers of ϵ yields more complicated expressions than indicated in equantion (A.1), we perform the ϵ expansion only after all integrations over loop momenta have been performed. Since the one-loop SE and vertex functions are always accompanied by at least one electron propagator $\frac{1}{\not{p}-m}$ it is convenient to develop parametrizations of the one-loop functions in which $(\not{p}-m)$ has been explicitly factored out on at least one side. Such parametrizations were developed in the appendix of Ref. [63].

In our calculations, we followed the convention of Ref.[57, 63] and kept a constant factor $\frac{\alpha C_\epsilon}{4\pi}$ for one-loop functions and $\frac{\alpha^2 C_\epsilon^2}{16\pi^2}$ for two-loop functions and expanded only the remainder of the loop functions in ϵ. Here, $C_\epsilon = \Gamma(1+\epsilon)(4\pi)^\epsilon \frac{\mu^{2\epsilon}}{m_{\rm f}^{2\epsilon}}$, and μ defines the elementary charge in D dimensions: $e(D) = \mu^\epsilon e$.

A.2 The wave functions perturbed by a magnetic field

In this section, we explain the derivation of the wave functions $|\delta a\rangle$ and $|\delta_D a\rangle$ which is used in the computation of the reducible F term contribution to the two-loop self-energy using the method of virial relations:

$$|\delta a\rangle = \sum_{n,n\neq a} \frac{|n\rangle\langle n|\gamma^0 e\not{A}|a\rangle}{E_a - E_n}, \tag{A.2}$$

$$|\delta_D a\rangle = -\sum_{n,n\neq a} \frac{|n\rangle\langle n|\gamma^0 e\not{A}|a\rangle}{(E_a - E_n)^2}. \tag{A.3}$$

In all relevant cases, the perturbed wave functions act on operators which conserve angular momentum. Therefore, only the term with $\kappa_n = \kappa_a$ needs to be considered. For the model of a point-like nucleus, these wavefunctions can be determined analytically using the method of generalized virial relations [128].

Virial relations

In non-relativistic quantum mechanics, the average value for the kinetic energy of a particle moving in a central potential $V(r)$ is determined by the virial theorem [128]:

$$\langle T\rangle = \frac{1}{2}\langle r\frac{dV}{dr}\rangle. \tag{A.4}$$

In relativistic quantum mechanics, one can derive such virial relations for various operators (see Ref. [128, 262]). These provide relations between diagonal and off-diagonal matrix elements of different operators. See Ref. [128] for details.

Calculation of $|\delta a\rangle$

The general procedure to determine the perturbed wave functions is to rewrite the matrix elements $\langle n|\gamma^0 e\not{A}|a\rangle$ as a linear combination of the following form:

$$\langle n|\gamma^0 e\not{A}|a\rangle = (E_a - E_n)\sum_i \langle n|R_i|a\rangle. \tag{A.5}$$

Here, the R_i are a small set of different operators. This replacement allows the elimination of the energy difference $E_a - E_n$ from the expression for $|\delta a\rangle$. The perturbed wavefunction now reads:

$$|\delta a\rangle = \sum_{n\neq a}\sum_i |n\rangle\langle n|R_i|a\rangle. \tag{A.6}$$

The operator $\sum_{n\neq a}|n\rangle\langle n|$ can then be replaced by $\mathbb{1} - |a\rangle\langle a|$. The expression for $|\delta a\rangle$ is now:

$$|\delta a\rangle = \sum_i \left(R_i|a\rangle - \langle a|R_i|a\rangle|a\rangle\right). \tag{A.7}$$

The sums $\sum_i R_i|a\rangle$ and $\sum_i\langle a|R_i|a\rangle|a\rangle$ can be determined easily. The most complicated part of this derivation is the determination of the operators R_i using virial relations. This determination is presented in great detail in Ref. [128]. It shall not be repeated here.

Derivation of $|\delta_D a\rangle$

We insert a unity operator into expression (A.3) $|\delta_D a\rangle$ as follows:

$$\mathbb{1} = \sum_m |m\rangle\langle m|, \tag{A.8}$$

$$\begin{aligned}|\delta_D a\rangle = &-\sum_{m,m\neq a}\frac{|m\rangle\langle m|}{E_a - E_m}\sum_{n,n\neq a}\frac{|n\rangle\langle n|\gamma^0 e\not{A}|a\rangle}{E_a - E_n} = \\ &-\sum_{m\neq a}\frac{|m\rangle\langle m|\delta a\rangle}{E_a - E_m}.\end{aligned} \tag{A.9}$$

Inserting the well-known expression for $|\delta a\rangle$ into equation (A.9), we obtain:

$$\langle n|\delta a\rangle = \frac{eB}{3}\left(\frac{\kappa}{m}C^1_{n\kappa a\kappa} - \frac{m - 2\kappa E_a}{2m^2}D^1_{n\kappa a\kappa} + \frac{\alpha Z\kappa}{m^2}D^0_{n\kappa a\kappa} - \frac{\kappa^2}{m^2}B^0_{n\kappa a\kappa}\right). \tag{A.10}$$

For the definition of $B^0_{n\kappa a\kappa}, C^1_{n\kappa a\kappa}$ and $D^i_{n\kappa a\kappa}$, see Ref. [128]. We again use virial relations from [128] in order to replace the matrix elements by linear combinations of the same form as equation (A.5). $\langle m|\delta a\rangle$ can then be rewritten as follows:

$$\langle n|\delta a\rangle = \frac{eB}{3}(E_a - E_n)\langle n|\left(-\frac{\kappa}{2m^2}D^1_{n\kappa a\kappa} - \frac{m-2\kappa E_a}{4m^2}A^2_{n\kappa a\kappa} + \frac{\alpha Z\kappa}{m^2}A^1_{n\kappa a\kappa}\right)|a\rangle. \quad \text{(A.11)}$$

The definition of $A^i_{n\kappa a\kappa}$ can also be found in Ref. [128]. Inserting this expression into equation (A.11), replacing $\sum_{m,m\neq a}|m\rangle\langle m| = \mathbb{1} - |a\rangle\langle a|$, and evaluating the corresponding matrix elements analytically for the ground state, we obtain the following expression for the radial components of $|\delta_D a\rangle$:

$$X_\delta(r) = \frac{\kappa r}{2m^2}f(r) + \left(\frac{m-2\kappa E_a}{4m^2}r^2 - \frac{\alpha Z\kappa}{m^2}r - \left(\frac{m-2\kappa E_a}{4m^2}A^2 - \frac{\alpha Z\kappa}{m^2}A^1\right)\right)g(r), \quad \text{(A.12)}$$

$$Y_\delta(r) = -\frac{\kappa r}{2m^2}g(r) + \left(\frac{m-2\kappa E_a}{4m^2}r^2 - \frac{\alpha Z\kappa}{m^2}r - \left(\frac{m-2\kappa E_a}{4m^2}A^2 - \frac{\alpha Z\kappa}{m^2}A^1\right)\right)f(r). \quad \text{(A.13)}$$

We evaluated A^1 and A^2 for the 1s state only. We obtained $A^1 = \dfrac{2\gamma+1}{\lambda}$ and $A^2 = \frac{(2\gamma+1)(2\gamma+2)}{(2\lambda)^2}$.

A.3 Radial integrals

In this section, we give a definition of the integral $R_J(\omega, abcd)$ which is used in the computation of many-potential contributions and the analysis of reference-state IR divergences. All formulas in this section are taken (with small adjustments concerning the notation) from Appendix C of Ref. [72].

$$R_J(\omega, abcd) = (2J+1)\int_0^\infty \mathrm{d}r_1 r1^2 \int_0^\infty \mathrm{d}r_2 r_2^2 \Bigg((-1)^J C_J(\kappa_a,\kappa_c)C_J(\kappa_b,\kappa_d)g_J(\omega,r_<,r_>) W_{ac}(r_1)W_{bd}(r_2) - \sum_L (-1)^L g_L(\omega,r_<,r_>)X_{ac}(r_1)X_{bd}(r_2)\Bigg), \quad \text{(A.14)}$$

$$W_{ab}(r) = g_a(r)g_b(r) + f_a(r)f_b(r), \quad \text{(A.15)}$$

$$X_{ab}(r) = g_a(r)f_b(r)S_{JL}(-\kappa_b,\kappa_a) - f_a(r)g_b(r)S_{JL}(\kappa_b,-\kappa_a). \quad \text{(A.16)}$$

$g_l(\omega, x_<, x_>)$ can be expressed in terms of spherical Bessel functions [263] as follows:

$$g_l(\omega, x_<, x_>) = i\omega j_l(\omega x_<)h_l^{(1)}(\omega x_>). \quad \text{(A.17)}$$

$C_J(\kappa_b,\kappa_a)$ is nonzero only if $l_a + l_b + J$ is even:

$$C_J(\kappa_b,\kappa_a) = (-1)^{j_b}\sqrt{(2j_a+1)(2j_b+1)}\begin{pmatrix} j_a & J & j_b \\ \frac{1}{2} & 0 & -\frac{1}{2}\end{pmatrix}. \tag{A.18}$$

Non-zero $S_{JL}(\kappa_a,\kappa_b)$ are:

$$S_{01}(\kappa_a,\kappa_b) = C_0(-\kappa_b,\kappa_a), \tag{A.19}$$

for $J=0$, and

$$S_{JJ-1}(\kappa_a,\kappa_b) = \sqrt{\frac{J}{2J+1}}\left(-1+\frac{\kappa_a+\kappa_b}{J}\right)C_J(-\kappa_b,\kappa_a), \tag{A.20}$$

$$S_{JJ}(\kappa_a,\kappa_b) = \frac{\kappa_a-\kappa_b}{\sqrt{J(J+1)}}C_J(\kappa_b,\kappa_a), \tag{A.21}$$

$$S_{JJ+1}(\kappa_a,\kappa_b) = \sqrt{\frac{J+1}{2J+1}}\left(1+\frac{\kappa_a+\kappa_b}{J+1}\right)C_J(-\kappa_b,\kappa_a). \tag{A.22}$$

Bibliography

[1] J. Zatorski, B. Sikora, S. G. Karshenboim, S. Sturm, F. Köhler-Langes, K. Blaum, C. H. Keitel, and Z. Harman. Extraction of the electron mass from g-factor measurements on light hydrogenlike ions. *Phys. Rev. A*, 96:012502, 2017.

[2] B. Sikora, H. Cakir, N. Michel, V. Debierre, N. S. Oreshkina, N. A. Belov, V. A. Yerokhin, C. H. Keitel, and Z. Harman. Access to improve the muon mass and magnetic moment anomaly via the bound-muon g factor. *ArXiv High Energy Physics; Atomic Physics*, 2018. arXiv:1801.02501v1 [hep-ph] .

[3] B. Sikora, N. S. Oreshkina, H. Cakir, Z. Harman, V. A. Yerokhin, and C. H. Keitel. Theory of the two-loop self-energy correction to the g-factor in non-perturbative Coulomb fields, 2018. In preparation.

[4] N. A. Belov, B. Sikora, R. Weis, V. A. Yerokhin, S. Sturm, K. Blaum, C. H. Keitel, and Z. Harman. Muonic vacuum polarization correction to the bound-electron g-factor. *ArXiv Atomic Physics*, 2016. arXiv:1610.01340v1 [physics.atom-ph].

[5] V. Debierre, B. Sikora, H. Cakir, N. S. Oreshkina, Z. Harman, and C. H. Keitel. Two-loop virtual light-by-light scattering corrections to the bound-electron g factor. In preparation, 2018.

[6] M. E. Peskin and D. V. Schroeder. *An Introduction to Quantum Field Theory*. Westview Press, 1995.

[7] C. Burgess and G. Moore. *The Standard Model – A Primer*. Cambridge University Press, 2007.

[8] J. Beringer, J.-F. Arguin, R. M. Barnett, K. Copic, O. Dahl, D. E. Groom, C.-J. Lin, J. Lys, H. Murayama, C. G. Wohl, W.-M. Yao, P. A. Zyla, C. Amsler, M. Antonelli, D. M. Asner, H. Baer, H. R. Band, T. Basaglia, C. W. Bauer, J. J. Beatty, V. I. Belousov, E. Bergren, G. Bernardi, W. Bertl, S. Bethke, H. Bichsel, O. Biebel, E. Blucher, S. Blusk, G. Brooijmans, O. Buchmueller, R. N. Cahn, M. Carena, A. Ceccucci, D. Chakraborty, M.-C. Chen, R. S. Chivukula, G. Cowan, G. D'Ambrosio, T. Damour, de Florian, D., A. de Gouvêa, T. DeGrand, P. de Jong, G. Dissertori, B. Dobrescu, M. Doser, M. Drees, D. A. Edwards, S. Eidelman, J. Erler, V. V. Ezhela, W. Fetscher, B. D. Fields, B. Foster, T. K. Gaisser, L. Garren, H.-J. Gerber, G. Gerbier, T. Gherghetta, S. Golwala, M. Goodman, C. Grab, A. V. Gritsan, J.-F. Grivaz, M. Grünewald, A. Gurtu, T. Gutsche, H. E. Haber, K. Hagiwara, C. Hagmann, C. Hanhart, S. Hashimoto, K. G. Hayes, M. Heffner,

B. Heltsley, J. J. Hernández-Rey, K. Hikasa, A. Höcker, J. Holder, A. Holtkamp, J. Huston, J. D. Jackson, K. F. Johnson, T. Junk, D. Karlen, D. Kirkby, S. R. Klein, E. Klempt, R. V. Kowalewski, F. Krauss, M. Kreps, B. Krusche, Yu. V. Kuyanov, Y. Kwon, O. Lahav, J. Laiho, P. Langacker, A. Liddle, Z. Ligeti, T. M. Liss, L. Littenberg, K. S. Lugovsky, S. B. Lugovsky, T. Mannel, A. V. Manohar, W. J. Marciano, A. D. Martin, A. Masoni, J. Matthews, D. Milstead, R. Miquel, K. Mönig, F. Moortgat, K. Nakamura, M. Narain, P. Nason, S. Navas, M. Neubert, P. Nevski, Y. Nir, K. A. Olive, L. Pape, J. Parsons, C. Patrignani, J. A. Peacock, S. T. Petcov, A. Piepke, A. Pomarol, G. Punzi, A. Quadt, S. Raby, G. Raffelt, B. N. Ratcliff, P. Richardson, S. Roesler, S. Rolli, A. Romaniouk, L. J. Rosenberg, J. L. Rosner, C. T. Sachrajda, Y. Sakai, G. P. Salam, S. Sarkar, F. Sauli, O. Schneider, K. Scholberg, D. Scott, W. G. Seligman, M. H. Shaevitz, S. R. Sharpe, M. Silari, T. Sjöstrand, P. Skands, J. G. Smith, G. F. Smoot, S. Spanier, H. Spieler, A. Stahl, T. Stanev, S. L. Stone, T. Sumiyoshi, M. J. Syphers, F. Takahashi, M. Tanabashi, J. Terning, M. Titov, N. P. Tkachenko, N. A. Törnqvist, D. Tovey, G. Valencia, K. van Bibber, G. Venanzoni, M. G. Vincter, P. Vogel, A. Vogt, W. Walkowiak, C. W. Walter, D. R. Ward, T. Watari, G. Weiglein, E. J. Weinberg, L. R. Wiencke, L. Wolfenstein, J. Womersley, C. L. Woody, R. L. Workman, A. Yamamoto, G. P. Zeller, O. V. Zenin, J. Zhang, R.-Y. Zhu, G. Harper, V. S. Lugovsky, and P. Schaffner. Review of Particle Physics. *Phys. Rev. D*, 86: 010001, 2012.

[9] J. Beringer et al. Particle physics booklet, extracted from the review of particle physics. *Phys. Rev. D*, 86:010001, 2012.

[10] H. Georgi and S. L. Glashow. Unity of All Elementary-Particle Forces. *Phys. Rev. Lett.*, 32:438–441, 1974.

[11] A. Smetana. Role of right-handed neutrinos in the electroweak symmetry breaking. Particle and Astroparticle Theory Seminar, Max Planck Institute for Nuclear Physics, 2014. https://www.mpi-hd.mpg.de/lin/seminar_theory/talks/Talk_Smetana_160614.pdf.

[12] A. N. Artemyev. QED Effects and Challenges. In W. Liu, editor, *Handbook of Relativistic Quantum Chemistry*. Springer-Verlag, Berlin Heidelberg, 2016.

[13] A. N. Artemyev. Effective QED Hamiltonians. In W. Liu, editor, *Handbook of Relativistic Quantum Chemistry*. Springer-Verlag, Berlin Heidelberg, 2016.

[14] Peter J. Mohr and Barry N. Taylor. CODATA recommended values of the fundamental physical constants: 2002. *Rev. Mod. Phys.*, 77:1–107, 2005.

[15] P. J. Mohr, B. N. Taylor, and D. B. Newell. CODATA recommended values of the fundamental physical constants: 2006. *Rev. Mod. Phys.*, 80:633–730, 2008.

[16] P. J. Mohr, B. N. Taylor, and D. B. Newell. CODATA recommended values of the fundamental physical constants: 2006. *J. Phys. Chem. Ref. Data*, 37(3):1187–1284, 2008.

[17] P. J. Mohr, B. N. Taylor, and D. B. Newell. CODATA recommended values of the fundamental physical constants: 2010. *Rev. Mod. Phys.*, 84:1527–1605, 2012.

[18] P. J. Mohr, B. N. Taylor, and D. B. Newell. CODATA Recommended Values of the Fundamental Physical Constants: 2010. *J. Phys. Chem. Ref. Data*, 41(4):043109, 2012.

[19] Peter J. Mohr, David B. Newell, and Barry N. Taylor. CODATA recommended values of the fundamental physical constants: 2014. *Rev. Mod. Phys.*, 88:035009, 2016.

[20] P. J. Mohr, D. B. Newell, and B. N. Taylor. CODATA Recommended Values of the Fundamental Physical Constants: 2014. *J. Phys. Chem. Ref. Data*, 45(4):043102, 2016.

[21] T. Aoyama, M. Hayakawa, T. Kinoshita, and M. Nio. Tenth-Order QED Contribution to the Electron $g-2$ and an Improved Value of the Fine Structure Constant. *Phys. Rev. Lett.*, 109:111807, 2012.

[22] D. Hanneke, S. Fogwell, and G. Gabrielse. New Measurement of the Electron Magnetic Moment and the Fine Structure Constant. *Phys. Rev. Lett.*, 100:120801, 2008.

[23] R. Pohl, A. Antognini, F. Nez, F. D. Amaro, F. Biraben, J. M. R. Cardoso, D. S. Covita, A. Dax, S. Dhawan, L. M. P. Fernandes, A. Giesen, T. Graf, T. W. Hänsch, P. Indelicato, L. Julien, C.-Y. Kao, P. Knowles, E.-O. Le Bigot, Y.-W. Liu, J. A. M. Lopes, L. Ludhova, C. M. B. Monteiro, F. Mulhauser, T. Nebel, P. Rabinowitz, J. M. F. dos Santos, L. A. Schaller, K. Schuhmann, C. Schwob, D. Taqqu, J. F. C. A. Veloso, and F. Kottmann. The size of the proton. *Nature*, 466:213–216, 2010.

[24] A. Antognini, F. Nez, K. Schuhmann, F. D. Amar, F. Biraben, J. M. R. Cardoso, D. S. Covita, A. Dax, S. Dhawan, M. Diepold, L. M. P. Fernandes, A. Giesen, A. L. Gouvea, T. Graf, T. W. Hänsch, P. Indelicato, L. Julien, C.-Y. Kao, P. Knowles, F. Kottmann, E.-O. Le Bigot, Y.-W. Liu, J. A. M. Lopes, L. Ludhova, C. M. B. Monteiro, F. Mulhauser, T. Nebel, P. Rabinowitz, J. M. F. dos Santos, L. A. Schaller, C. Schwob, D. Taqqu, J. F. C. A. Veloso, J. Vogelsang, and R. Pohl. Proton Structure from the Measurement of $2S - 2P$ Transition Frequencies of Muonic Hydrogen. *Science*, 339:417–420, 2013.

[25] A. Antognini, K. Schuhmann, F. D. Amaro, P. Amaro, M. Abdou-Ahmed, F. Biraben, T.-L. Chen, D. S. Covita, A. J. Dax, M. Diepold, L. M. P. Fernandes, B. Franke, S. Galtier, A. L. Gouvea, J. Götzfried, T. Graf, T. W. Hänsch,

M. Hildebrandt, P. Indelicato, L. Julien, K. Kirch, A. Knecht, F. Kottmann, J. J. Krauth, Y.-W. Liu, J. Machado, C. M. B. Monteiro, F. Mulhauser, F. Nez, J. P. Santos, J. M. F. dos Santos, C. I. Szabo, D. Taqqu, J. F. C. A. Veloso, A. Voss, B. Weichelt, and R. Pohl. Experiments towards resolving the proton charge radius puzzle. *EPJ Web of Conferences*, 113:01006, 2016.

[26] K. Pachucki and A. Wienczek. Nuclear structure effects in light muonic atoms. *Phys. Rev. A*, 91:040503, 2015.

[27] R. Pohl, F. Nez, L. M. P. Fernandes, M. Abdou Ahmed, F. D. Amaro, P. Amaro, F. Biraben, J. M. R. Cardoso, D. S. Covita, A. Dax, S. Dhawan, M. Diepold, B. Frank, S. Galtier, A. Giesen, A. L. Gouvea, J. Götzfried, T. Graf, T. W. Hänsch, M. Hildebrandt, P. Indelicato, L. Julien, K. Kirch, A. Knecht, P. Knowles, F. Kottmann, J. J. Krauth, E.-O. Le Bigot, Y.-W. Liu, J. A. M. Lopes, L. Ludhova, J. Machado, C. M. B. Monteiro, F. Mulhauser, T. Nebel, P. Rabinowitz, J. M. F. dos Santos, J. P. Santos, L. A. Schaller, K. Schuhmann, C. Schwob, C. I. Szabó, D. Taqqu, J. F. C. A. Veloso, A. Voss, B. Weichelt, and A. Antognini. Laser Spectroscopy of Muonic Atoms and Ions. In *Proceedings of the 12th International Conference on Low Energy Antiproton Physics (LEAP2016)*, page 011021, 2017.

[28] A. Beyer, L. Maisenbacher, A. Matveev, R. Pohl, K. Khabarova, A. Grinin, T. Lamour, D. C. Yost, T. W. Hänsch, N. Kolachevsky, and T. Udem. The Rydberg constant and proton size from atomic hydrogen. *Science*, 358(6359):79–85, 2017.

[29] J. Ullmann, Z. Andelkovic, C. Brandau, A. Dax, W. Geithner, C. Geppert, C. Gorges, M. Hammen, V. Hannen, S. Kaufmann, K. König, Y. A. Litvinov, M. Lochmann, B. Maaß, J. Meisner, T. Murböck, R. Sánchez, M. Schmidt, S. Schmidt, M. Steck, Th. Stöhlker, R. C. Thompson, C. Trageser, J. Vollbrecht, J. Weinheimer, and W. Nörthershäuser. High precision hyperfine measurements in Bismuth challenge bound-state strong-field QED. *Nat. Commun.*, 8:15484, 2017.

[30] H. Häffner, T. Beier, N. Hermanspahn, H.-J. Kluge, W. Quint, S. Stahl, J. Verdú, and G. Werth. High-Accuracy Measurement of the Magnetic Moment Anomaly of the Electron Bound in Hydrogenlike Carbon. *Phys. Rev. Lett.*, 85(25):5308–5311, 2000.

[31] S. Sturm, F. Köhler, J. Zatorski, A. Wagner, Z. Harman, G. Werth, W. Quint, C. H. Keitel, and K. Blaum. High-precision measurement of the atomic mass of the electron. *Nature*, 506(7489):467–470, 2014.

[32] J. Verdú, S. Djekić, S. Stahl, T. Valenzuela, M. Vogel, G. Werth, T. Beier, H.-J. Kluge, and W. Quint. Electronic g Factor of Hydrogenlike Oxygen $^{16}O^{7+}$. *Phys. Rev. Lett.*, 92(9):093002, 2004.

[33] S. Sturm, A. Wagner, B. Schabinger, J. Zatorski, Z. Harman, W. Quint, G. Werth, C. H. Keitel, and K. Blaum. g Factor of Hydrogenlike $^{28}Si^{13+}$. *Phys. Rev. Lett.*, 107:023002, 2011.

[34] S. Sturm, A. Wagner, M. Kretzschmar, W. Quint, G. Werth, and K. Blaum. g-factor measurement of hydrogenlike $^{28}Si^{13+}$ as a challenge to QED calculations. *Phys. Rev. A*, 87:030501, 2013.

[35] S. Sturm, M. Vogel, F. Köhler-Langes, W. Quint, K. Blaum, and G. Werth. High-Precision Measurements of the Bound Electron's Magnetic Moment. *Atoms*, 5(1): 1–14, 2017.

[36] W. Quint, J. Dilling, S. Djekić, H. Häffner, N. Hermanspahn, H.-J. Kluge, G. Marx, R. Moore, D. Rodriguez, J. Schönfelder, G. Sikler, T. Valenzuela, J. Verdú, C. Weber, and G. Werth. HITRAP: A Facility for Experiments with Trapped Highly Charged Ions. *Hyperfine Interact.*, 132(1):457–461, 2001.

[37] H.-J. Kluge, T. Beier, K. Blaum, L. Dahl, S. Eliseev, F. Herfurth, B. Hofmann, O. Kester, S. Koszudowski, C. Kozhuharov, G. Maero, W. Nörtershäuser, J. Pfister, W. Quint, U. Ratzinger, A. Schempp, R. Schuch, Th. Stöhlker, R. C. Thompson, M. Vogel, G. Vorobjev, D. F. A. Winters, and G. Werth. HITRAP: A Facility at GSI for Highly Charged Ions. In S. Salomonson and E. Lindroth, editors, *Current Trends in Atomic Physics*, volume 53 of *Advances in Quantum Chemistry*, pages 83 – 98. Academic Press, 2008.

[38] S. Sturm, A. Wagner, B. Schabinger, and K. Blaum. Phase-Sensitive Cyclotron Frequency Measurements at Ultralow Energies. *Phys. Rev. Lett.*, 107:143003, 2011.

[39] S. Sturm, G. Werth, and K. Blaum. Electron g-factor determinations in Penning traps. *Ann. Phys.*, 525(8-9):620–635, 2013.

[40] S. Streubel, T. Eronen, M. Höcker, J. Ketter, M. Schuh, R. S. Van Dyck, and K. Blaum. Toward a more accurate Q value measurement of tritium: status of THe-Trap. *Appl. Phys. B*, 114(1):137–145, 2014.

[41] T. Beier, H. Häffner, N. Hermanspahn, S. G. Karshenboim, H.-J. Kluge, W. Quint, S. Stahl, J. Verdú, and G. Werth. New Determination of the Electron's Mass. *Phys. Rev. Lett.*, 88:011603, 2001.

[42] J. Zatorski. Determining the mass of the electron via measurement of the bound-electron g-factor in ^{12} C $^{5+}$. Seminar Theoretical Quantum Dynamics, Max Planck Institute for Nuclear Physics, 2014.

[43] F. Köhler, S. Sturm, A. Kracke, G. Werth, W. Quint, and K. Blaum. The electron mass from g-factor measurements on hydrogen-like carbon $^{12}C^{5+}$. *J. Phys. B*, 48 (14):144032, 2015.

[44] U. D. Jentschura, A. Czarnecki, K. Pachucki, and V. A. Yerokhin. Mass measurements and the bound-electron g factor. *Int. J. Mass. Spectrom.*, 251(2-3):102 – 108, 2006.

[45] T. Beier, H. Häffner, N. Hermanspahn, S. Djekić, H.-J. Kluge, W. Quint, S. Stahl, T. Valenzuela, J. Verdú, and G. Werth. The measurement of the electronic g-factor in hydrogen-like ions –A promising tool for determining fundamental and nuclear constants. *Eur. Phys. J. A*, 15(1):41–44, 2002.

[46] D. L. Moskovkin, N. S. Oreshkina, V. M. Shabaev, T. Beier, G. Plunien, W. Quint, and G. Soff. g factor of hydrogenlike ions with nonzero nuclear spin. *Phys. Rev. A*, 70:032105, 2004.

[47] V. M. Shabaev, D. A. Glazov, M. B. Shabaeva, V. A. Yerokhin, G. Plunien, and G. Soff. g factor of high-Z lithiumlike ions. *Phys. Rev. A*, 65:062104, 2002.

[48] D. A. Glazov, A. V. Volotka, V. M. Shabaev, I. I. Tupitsyn, and G. Plunien. Screened QED corrections to the g factor of Li-like ions. *Phys. Lett. A*, 357(4):330 – 333, 2006.

[49] A. V. Volotka, D. A. Glazov, V. M. Shabaev, I. I. Tupitsyn, and G. Plunien. Many-Electron QED Corrections to the g Factor of Lithiumlike Ions. *Phys. Rev. Lett.*, 112:253004, 2014.

[50] D. A. Glazov, A. V. Malyshev, A. V. Volotka, V. M. Shabaev, I. I. Tupitsyn, and G. Plunien. Higher-order perturbative relativistic calculations for few-electron atoms and ions. *Nucl. Instr. Meth. Phys. Res. B*, 408:46 – 49, 2017.

[51] A. Wagner, S. Sturm, F. Köhler, D. A. Glazov, A. V. Volotka, G. Plunien, W. Quint, G. Werth, V. M. Shabaev, and K. Blaum. g Factor of Lithiumlike Silicon $^{28}Si^{11+}$. *Phys. Rev. Lett.*, 110:033003, 2013.

[52] F. Köhler, K. Blaum, M. Block, S. Chenmarev, S. Eliseev, D. A. Glazov, M. Goncharov, J. Hou, A. Kracke, D. A. Nesterenko, Y. N. Novikov, W. Quint, E. Minaya Ramirez, V. M. Shabaev, S. Sturm, A. V. Volotka, and G. Werth. Isotope dependence of the Zeeman effect in lithium-like calcium. *Nat. Commun.*, 7:10246, 2016.

[53] V. M. Shabaev, D. A. Glazov, N. S. Oreshkina, A. V. Volotka, G. Plunien, H.-J. Kluge, and W. Quint. g-Factor of Heavy Ions: A New Access to the Fine Structure Constant. *Phys. Rev. Lett.*, 96:253002, 2006.

[54] V. A. Yerokhin, E. Berseneva, Z. Harman, I. I. Tupitsyn, and C. H. Keitel. g Factor of Light Ions for an Improved Determination of the Fine-Structure Constant. *Phys. Rev. Lett.*, 116:100801, 2016.

[55] V. A. Yerokhin, E. Berseneva, Z. Harman, I. I. Tupitsyn, and C. H. Keitel. Weighted difference of g factors of light Li-like and H-like ions for an improved determination of the fine-structure constant. *Phys. Rev. A*, 94:022502, 2016.

[56] K. Pachucki, A. Czarnecki, U. D. Jentschura, and V. A. Yerokhin. Complete two-loop correction to the bound-electron g factor. *Phys. Rev. A*, 72:022108, 2005.

[57] V. A. Yerokhin, P. Indelicato, and V. M. Shabaev. Evaluation of the self-energy correction to the g factor of S states in H-like ions. *Phys. Rev. A*, 69(5):052503, 2004.

[58] V. A. Yerokhin and Z. Harman. Two-loop QED corrections with closed fermion loops for the bound-electron g factor. *Phys. Rev. A*, 88:042502, 2013.

[59] Andrzej Czarnecki and Robert Szafron. Light-by-light scattering in the Lamb shift and the bound electron g factor. *Phys. Rev. A*, 94:060501, 2016.

[60] U. D. Jentschura. Binding two-loop vacuum-polarization corrections to the bound-electron g factor. *Phys. Rev. A*, 79:044501, 2009.

[61] K. Pachucki and M. Puchalski. One-loop binding corrections to the electron g factor. *Phys. Rev. A*, 96:032503, 2017.

[62] A. Czarnecki, M. Dowling, J. Piclum, and R. Szafron. Two-Loop Binding Corrections to the Electron Gyromagnetic Factor. *Phys. Rev. Lett.*, 120:043203, 2018.

[63] V. A. Yerokhin, P. Indelicato, and V. M. Shabaev. Evaluation of the two-loop self-energy correction to the ground state energy of H-like ions to all orders in $Z\alpha$. *Eur. Phys. J. D*, 25(3):203–238, 2003.

[64] V. A. Yerokhin and Z. Harman. One-loop electron self-energy for the bound-electron g factor. *Phys. Rev. A*, 95:060501, 2017.

[65] S. Mallampalli and J. Sapirstein. Fourth-order self-energy contribution to the Lamb shift. *Phys. Rev. A*, 57:1548–1564, 1998.

[66] S. Mallampalli and J. Sapirstein. Perturbed Orbital Contribution to the Two-Loop Lamb Shift in Hydrogen. *Phys. Rev. Lett.*, 80:5297–5300, 1998.

[67] V. A. Yerokhin and V. M. Shabaev. Two-loop self-energy correction in H-like ions. *Phys. Rev. A*, 64:062507, 2001.

[68] V. M. Shabaev. Two-time Green's function method in quantum electrodynamics of high-Z few-electron atoms. *Phys. Rep.*, 356(3):119 – 228, 2002.

[69] T. Beier. The g_j factor of a bound electron and the hyperfine structure splitting in hydrogenlike ions. *Phys. Rep.*, 339(2-3):79 – 213, 2000.

[70] S. G. Karshenboim, V. G. Ivanov, and V. M. Shabaev. Vacuum Polarization in a Hydrogen-like Relativistic Atom: g Factor of a Bound Electron. *J. Exp. Theor. Phys. Lett.*, 93:477, 2001.

[71] R. N. Lee, A. I. Milstein, I. S. Terekhov, and S. G. Karshenboim. Virtual light-by-light scattering and the g factor of a bound electron. *Phys. Rev. A*, 71:052501, 2005.

[72] V. A. Yerokhin and V. M. Shabaev. First-order self-energy correction in hydrogenlike systems. *Phys. Rev. A*, 60:800, 1999.

[73] J. D. Jackson. *Klassische Elektrodynamik*. Walter de Gruyter GmbH & Co. KG, 10785 Berlin, 2006.

[74] C. Cohen-Tannoudji, B. Diu, and F. Laloë. *Quantenmechanik, Band 1*. Walter de Gruyter GmbH & Co. KG, 10785 Berlin, 2007.

[75] C. Cohen-Tannoudji, B. Diu, and F. Laloë. *Quantenmechanik, Band 2*. Walter de Gruyter GmbH & Co. KG, 10785 Berlin, 2008.

[76] J. Schwinger. On Quantum-Electrodynamics and the Magnetic Moment of the Electron. *Phys. Rev.*, 73:416–417, 1948.

[77] M. Srednicki. *Quantum Field Theory*. Cambridge University Press, 2007.

[78] S. Weinberg. *The Quantum Theory of Fields*, volume I. Foundations. Cambridge University Press, 2005.

[79] W. Greiner and J. Reinhardt. *Theoretische Physik Band 7: Quantenelektrodynamik*. Verlag Harri Deutsch, Thun und Frankfurt am Main, 1984.

[80] F. Mandl and G. Shaw. *Quantum Field Theory*. John Wiley & Sons, Ltd, 2010.

[81] B. De Wit and J. Smith. *Field Theory in Particle Physics*, volume 1. North-Holland Physics Publishing, Amsterdam Oxford New York Tokyo, 1986.

[82] J. Sapirstein. Quantum Electrodynamics. In G. W. F. Drake, editor, *Atomic, Molecular, & Optical Physics Handbook*, chapter 27, pages 327 – 340. AIP Press, 1996.

[83] A. Petermann. Fourth order magnetic moment of the electron. *Helv. Phys. Acta*, 30:407–408, 1957.

[84] C. M. Sommerfield. Magnetic Dipole Moment of the Electron. *Phys. Rev.*, 107: 328–329, 1957.

[85] C. M. Sommerfield. The Magnetic Moment of the Electron. *Ann. Phys.*, 5(1):26 – 57, 1958.

[86] S. Laporta and E. Remiddi. The analytical value of the electron $g-2$ at order α^3 in QED. *Phys. Lett. B*, 379(1):283 – 291, 1996.

[87] T. Aoyama, M. Hayakawa, T. Kinoshita, and M. Nio. Revised Value of the Eighth-Order Contribution to the Electron $g-2$. *Phys. Rev. Lett.*, 99:110406, 2007.

[88] S. Laporta. High-precision calculation of the 4-loop contribution to the electron $g-2$ in QED. *Phys. Lett. B*, 772(Supplement C):232 – 238, 2017.

[89] D. Nomura and T. Teubner. Hadronic contributions to the anomalous magnetic moment of the electron and the hyperfine splitting of muonium. *Nucl. Phys. B*, 867(2):236, 2013.

[90] A. Kurz, T. Liu, P. Marquard, and M. Steinhauser. Hadronic contribution to the muon anomalous magnetic moment to next-to-next-to-leading order. *Phys. Lett. B*, 734:144, 2014.

[91] J. Prades, E. de Rafael, and A. Vainshtein. The hadronic light-by-light scattering contribution to the muon and electron anomalous magnetic moments. In *Lepton Dipole Moments*, volume 20 of *Advanced Series on Directions in High Energy Physics*, chapter 9, pages 303–317. World Scientific, Singapore, 2010.

[92] A. Czarnecki, B. Krause, and W. J. Marciano. Electroweak Corrections to the Muon Anomalous Magnetic Moment. *Phys. Rev. Lett.*, 76:3267–3270, 1996.

[93] V. W. Hughes and T. Kinoshita. Anomalous g values of the electron and muon. *Rev. Mod. Phys.*, 71:S133–S139, 1999.

[94] F. Jegerlehner and A. Nyffeler. The muon $g-2$. *Phys. Rep.*, 477(1):1 – 110, 2009.

[95] M. Lindner, M. Platscher, and F. S. Queiroz. A Call for New Physics : The Muon Anomalous Magnetic Moment and Lepton Flavor Violation. *ArXiv High Energy Physics*, 2017. arXiv:1610.06587v2 [hep-ph] .

[96] W.E. Caswell and G.P. Lepage. Effective lagrangians for bound state problems in QED, QCD, and other field theories. *Phys. Lett. B*, 167(4):437 – 442, 1986.

[97] K. Pachucki. Long-wavelength quantum electrodynamics. *Phys. Rev. A*, 69:052502, 2004.

[98] F. E. Close and H. Osborn. Relativistic extension of the electromagnetic current for composite systems. *Phys. Lett. B*, 34(5):400 – 404, 1971.

[99] S. G. Karshenboim. Non-relativistic calculations of the g-factor of a bound electron. *Phys. Lett. A*, 266(4):380 – 386, 2000.

[100] S. A. Zapryagaev. Zeeman effect of the fine structure levels of a hydrogenlike atom. *Opt. Spectrosc.*, 47:9–13, 1979.

[101] R. Bukowski, B. Jeziorski, R. Moszyński, and W. Kołos. Bethe Logarithm and Lamb Shift for the Hydrogen Molecular Ion. *Int. J. Quantum Chem.*, 42(2):287–319, 1992.

[102] K. Pachucki. Simple derivation of helium Lamb shift. *J. Phys. B*, 31(23):5123–5133, 1998.

[103] V. I. Korobov and S. V. Korobov. Bethe logarithm for the 1^1S and 2^1S states of helium. *Phys. Rev. A*, 59:3394–3396, 1999.

[104] K. Pachucki. Logarithmic two-loop corrections to the Lamb shift in hydrogen. *Phys. Rev. A*, 63:042503, 2001.

[105] K. Pachucki and U. D. Jentschura. Two-Loop Bethe-Logarithm Correction in Hydrogenlike Atoms. *Phys. Rev. Lett.*, 91:113005, 2003.

[106] A. Czarnecki, U. D. Jentschura, and K. Pachucki. Calculation of the One- and Two-Loop Lamb Shift for Arbitrary Excited Hydrogenic States. *Phys. Rev. Lett.*, 95:180404, 2005.

[107] U. D. Jentschura, A. Czarnecki, and K. Pachucki. Nonrelativistic QED approach to the Lamb shift. *Phys. Rev. A*, 72:062102, 2005.

[108] K. Pachucki. $\alpha^4\mathcal{R}$ corrections to singlet states of helium. *Phys. Rev. A*, 74:022512, 2006.

[109] M. Baranger, H. A. Bethe, and R. P. Feynman. Relativistic Correction to the Lamb Shift. *Phys. Rev.*, 92:482–501, 1953.

[110] K. Pachucki. Higher-Order Binding Corrections to the Lamb Shift. *Ann. Phys.*, 226(1):1 – 87, 1993.

[111] M. I. Eides. Weak-interaction contributions to hyperfine splitting and Lamb shift. *Phys. Rev. A*, 53:2953–2957, 1996.

[112] N. S. Oreshkina, D. A. Glazov, A. V. Volotka, V. M. Shabaev, I. I. Tupitsyn, and G. Plunien. Radiative and interelectronic-interaction corrections to the hyperfine splitting in highly charged B-like ions. *Phys. Lett. A*, 372(5):675 – 680, 2008.

[113] M. Puchalski and K. Pachucki. Ground State Hyperfine Splitting in ^{6,7}Li Atoms and the Nuclear Structure. *Phys. Rev. Lett.*, 111:243001, 2013.

[114] A. Czarnecki, K. Melnikov, and A. Yelkhovsky. Anomalous magnetic moment of a bound electron. *Phys. Rev. A*, 63:012509, 2000.

[115] M. I. Eides and H. Grotch. Gyromagnetic Ratios of Bound Particles. *Ann. Phys.*, 260(1):191 – 200, 1997.

[116] K. Pachucki, U. D. Jentschura, and V. A. Yerokhin. Nonrelativistic QED Approach to the Bound-Electron g Factor. *Phys. Rev. Lett.*, 93:150401, 2004.

[117] S. G. Karshenboim and A. I. Milstein. Delbrück scattering and the g-factor of a bound electron. *Phys. Lett. B*, 549(3-4):321 – 324, 2002.

[118] W. Greiner. *Theoretische Physik Band 6: Relativistische Quantenmechanik – Wellengleichungen*. Verlag Harri Deutsch, Thun und Frankfurt am Main, 1987.

[119] R. P. Feynman. Space-Time Approach to Quantum Electrodynamics. *Phys. Rev.*, 76:769–789, 1949.

[120] S. Tashenov and Z. Harman. Fundamental physics in strong Coulomb fields, 2014. https://www.physi.uni-heidelberg.de/Forschung/apix/APS/lectures/index.html.

[121] P. Hoyer. Bound states – from QED to QCD. *ArXiv High Energy Physics*, 2014. arXiv:1402.5005v1 [hep-ph].

[122] W. H. Furry. On Bound States and Scattering in Positron Theory. *Phys. Rev.*, 81:115–124, 1951.

[123] R. N. Hill. Hydrogenic Wave Functions. In G. W. F. Drake, editor, *Atomic, Molecular, & Optical Physics Handbook*, chapter 9, pages 120 – 134. AIP Press, 1996.

[124] R. Szmytkowski. Some summation formulae for spherical spinors. *J. Phys. A*, 38 (41):8993, 2005.

[125] R. A. Swainson and G. W. F. Drake. A unified treatment of the non-relativistic and relativistic hydrogen atom: I. The wavefunctions. *J. Phys. A*, 24(1):79, 1991.

[126] E. M. Rose. *Relativistische Elektronen-Theorie*, volume I. Hochschultaschebücher-Verlag, Mannheim Wien Zürich, 1971.

[127] P. J. Mohr, G. Plunien, and G. Soff. QED corrections in heavy atoms. *Phys. Rep.*, 293(5):227 – 369, 1998.

[128] V. M. Shabaev. Virial Relations for the Dirac Equation and Their Applications to Calculations of Hydrogen-Like Atoms. In S. G. Karshenboim and V. B. Smirnov, editors, *Precision Physics of Simple Atomic Systems*, pages 97–113. Springer-Verlag, Berlin Heidelberg, 2003.

[129] Q. Wang, O. Ronneberger, and H. Burkhardt. Fourier Analysis in Polar and Spherical Coordinates. Technical report, Albert-Ludwigs-Universität Freiburg, Institut für Informatik, Lehrstuhl für Mustererkennung und Bildverarbeitung, 2008. https://lmb.informatik.uni-freiburg.de/Publications/2008/WRB08/wa_report01_08.pdf.

[130] I. N. Bronstein, K. A. Semendjajew, G. Musiol, and H. Mühlig. *Taschenbuch der Mathematik*. Wissenschaftlicher Verlag Harri Deutsch GmbH, Frankfurt am Main, 2006.

[131] V. A. Yerokhin, K. Pachucki, and V. M. Shabaev. One-loop self-energy correction in a strong binding field. *Phys. Rev. A*, 72:042502, 2005.

[132] Ya. I. Granovskii and V. I. Nechet. Different forms of the electron propagator in the Coulomb field. *Theor. Math. Phys.*, 18(2):185–188, 1974.

[133] R. A. Swainson and G. W. F. Drake. A unified treatment of the non-relativistic and relativistic hydrogen atom: II. The Green functions. *J. Phys. A*, 24(1):95, 1991.

[134] R. A. Swainson and G. W. F. Drake. A unified treatment of the non-relativistic and relativistic hydrogen atom: III. The reduced Green functions. *J. Phys. A*, 24 (8):1801, 1991.

[135] D. J. Hylton and N. J. Snyderman. Analytic basis set for high-Z atomic QED calculations: Heavy He-like ions. *Phys. Rev. A*, 55:2651–2661, 1997.

[136] M. Gell-Mann and F. Low. Bound States in Quantum Field Theory. *Phys. Rev.*, 84:350–354, 1951.

[137] J. Sucher. *S*-Matrix Formalism for Level-Shift Calculations. *Phys. Rev.*, 107: 1448–1449, 1957.

[138] P. J. Mohr. Quantum electrodynamics of high-Z few-electron atoms. *Phys. Rev. A*, 32:1949–1957, 1985.

[139] S. A. Blundell, K. T. Cheng, and J. Sapirstein. Radiative corrections in atomic physics in the presence of perturbing potentials. *Phys. Rev. A*, 55:1857–1865, 1997.

[140] H. Persson, S. Salomonson, P. Sunnergren, and I. Lindgren. Radiative corrections to the electron g-factor in H-like ions. *Phys. Rev. A*, 56:R2499–R2502, 1997.

[141] T. Beier, I. Lindgren, H. Persson, S. Salomonson, P. Sunnergren, H. Häffner, and N. Hermanspahn. g_j factor of an electron bound in a hydrogenlike ion. *Phys. Rev. A*, 62:032510, 2000.

[142] W. Greiner and J. Reinhardt. *Theoretische Physik Band 7A: Feldquantisierung.* Verlag Harri Deutsch, Thun und Frankfurt am Main, 1993.

[143] G. C. Wick. The Evaluation of the Collision Matrix. *Phys. Rev.*, 80:268–272, 1950.

[144] G. Breit. The Magnetic Moment of the Electron. *Nature*, 122:649–649, 1928.

[145] H. Margenau. Relativistic Magnetic Moment of a Charged Particle. *Phys. Rev.*, 57:383–386, 1940.

[146] F. A. Parpia and A. K. Mohanty. Relativistic basis-set calculations for atoms with Fermi nuclei. *Phys. Rev. A*, 46:3735–3745, 1992.

[147] D. A. Glazov and V. M. Shabaev. Finite nuclear size correction to the bound-electron g factor in a hydrogenlike atom. *Phys. Lett. A*, 297(5):408 – 411, 2002.

[148] J. Zatorski, N. S. Oreshkina, C. H. Keitel, and Z. Harman. Nuclear Shape Effect on the g Factor of Hydrogenlike Ions. *Phys. Rev. Lett.*, 108:063005, 2012.

[149] V. M. Shabaev. Finite nuclear size corrections to the energy levels of the multicharged ions. *J. Phys. B*, 26(6):1103–1108, 1993.

[150] S. G. Karshenboim, R. N. Lee, and A. I. Milstein. g factor of an electron or muon bound by an arbitrary central potential. *Phys. Rev. A*, 72:042101, 2005.

[151] F. Salvat, J. M. Fernández-Varea, and W. Williamson, Jr. RADIAL: a FORTRAN subroutine package for the solution of the radial Schrödinger and Dirac wave equations, 2016. URL `http://users.df.uba.ar/dmitnik/estructura3/programas/salvat/radial.pdf`.

[152] R. F. Frosch, J. S. McCarthy, R. E. Rand, and M. R. Yearian. Structure of the He^4 Nucleus from Elastic Electron Scattering. *Phys. Rev.*, 160:874–879, 1967.

[153] H. De Vries, C. W. De Jager, and C. De Vries. Nuclear charge-density-distribution parameters from elastic electron scattering. *At. Data Nucl. Data Tables*, 36(3):495 – 536, 1987.

[154] G. Fricke, C. Bernhardt, K. Heilig, L. A. Schaller, L. Schellenberg, E. B. Shera, and C. W. De Jager. Nuclear Ground State Charge Radii from Electromagnetic Interactions. *At. Data Nucl. Data Tables*, 60(2):177 – 285, 1995.

[155] I. Angeli. A consistent set of nuclear rms charge radii: properties of the radius surface $R(N, Z)$. *At. Data Nucl. Data Tables*, 87(2):185 – 206, 2004.

[156] I. Angeli and K. P. Marinova. Table of experimental nuclear ground state charge radii: An update. *At. Data Nucl. Data Tables*, 99(1):69 – 95, 2013.

[157] I. Sick. Form Factors and Radii of Light Nuclei. *J. Phys. Chem. Ref. Data*, 44(3): 031213, 2015.

[158] R. F. Garcia Ruiz, M. L. Bissell, K. Blaum, A. Ekström, N. Frömmgen, G. Hagen, M. Hammen, K. Hebeler, J. D. Holt, G. R. Jansen, M. Kowalska, K. Kreim, W. Nazarewicz, R. Neugart, G. Neyens, W. Nörtershäuser, T. Papenbrock, J. Papuga, A. Schwenk, J. Simonis, K. A. Wendt, and D. T. Yordanov. Unexpectedly large charge radii of neutron-rich calcium isotopes. *Nat. Phys.*, 12:594, 2016.

[159] C. Brandau, C. Kozhuharov, Z. Harman, A. Müller, S. Schippers, Y. S. Kozhedub, D. Bernhardt, S. Böhm, J. Jacobi, E. W. Schmidt, P. H. Mokler, F. Bosch, H.-J. Kluge, Th. Stöhlker, K. Beckert, P. Beller, F. Nolden, M. Steck, A. Gumberidze, R. Reuschl, U. Spillmann, F. J. Currell, I. I. Tupitsyn, V. M. Shabaev, U. D. Jentschura, C. H. Keitel, A. Wolf, and Z. Stachura. Isotope Shift in the Dielectronic Recombination of Three-Electron $^A Nd^{57+}$. *Phys. Rev. Lett.*, 100:073201, 2008.

[160] H. Grotch. Electron g Factor in Hydrogenic Atoms. *Phys. Rev. Lett.*, 24(2):39–42, 1970.

[161] H. Grotch. Nuclear Mass Corrections to the Electron g Factor. *Phys. Rev. A*, 2: 1605–1607, 1970.

[162] R. Faustov. Magnetic moment of the hydrogen atom. *Phys. Lett. B*, 33(6):422 – 424, 1970.

[163] H. Grotch and R. A. Hegstrom. Hydrogenic Atoms in a Magnetic Field. *Phys. Rev. A*, 4:59–69, 1971.

[164] V. M. Shabaev. Mass corrections in a strong nuclear field. *Theor. Math. Phys.*, 63 (3):588–596, 1985.

[165] V. M. Shabaev. QED theory of the nuclear recoil effect in atoms. *Phys. Rev. A*, 57:59–67, 1998.

[166] V. M. Shabaev. QED theory of the nuclear recoil effect on the atomic g factor. *Phys. Rev. A*, 64:052104, 2001.

[167] V. M. Shabaev and V. A. Yerokhin. Recoil Correction to the Bound-Electron g Factor in H-Like Atoms to All Orders in αZ. *Phys. Rev. Lett.*, 88(9):091801, 2002.

[168] K. Pachucki. Nuclear mass correction to the magnetic interaction of atomic systems. *Phys. Rev. A*, 78(1):012504, 2008.

[169] W. C. Martin and R. Zalubas. Energy Levels of Silicon, Si I through Si XIV. *J. Phys. Chem. Ref. Data*, 12(2):323, 1983.

[170] G. Audi, A. H. Wapstra, and C. Thibault. The AME2003 atomic mass evaluation: (II). Tables, graphs and references. *Nucl. Phys. A*, 729(1):337 – 676, 2003.

[171] G. Audi, M. Wang, A. H. Wapstra, F.G. Kondev, M. MacCormick, X. Xu, and B. Pfeiffer. The AME2012 atomic mass evaluation. *Chin. Phys. C*, 36(12):1287, 2012.

[172] M. Wang, G. Audi, A.H. Wapstra, F.G. Kondev, M. MacCormick, X. Xu, and B. Pfeiffer. The AME2012 atomic mass evaluation (II). Tables, graphs and references. *Chin. Phys. C*, 36(12):1603, 2012.

[173] A. Kramida, Y. Ralchenko, J. Reader, and the NIST ASD Team. NIST Atomic Spectra Database (ver. 5.2), [Online]. National Institute of Standards and Technology, Gaithersburg, MD, 2014. URL `http://physics.nist.gov/asd`.

[174] J. Zatorski. Nuclear deformation correction to the g-factor of hydrogen-like ions in S-state. Working notes, 2013.

[175] G. Plunien, B. Müller, W. Greiner, and G. Soff. Nuclear polarization contribution to the Lamb shift in heavy atoms. *Phys. Rev. A*, 39:5428–5431, 1989.

[176] G. Plunien, B. Müller, W. Greiner, and G. Soff. Nuclear polarization in heavy atoms and superheavy quasiatoms. *Phys. Rev. A*, 43:5853–5866, 1991.

[177] A. V. Nefiodov, G. Plunien, and G. Soff. Nuclear-Polarization Correction to the Bound-Electron g Factor in Heavy Hydrogenlike Ions. *Phys. Rev. Lett.*, 89(8): 081802, 2002.

[178] A. V. Volotka and G. Plunien. Nuclear Polarization Study: New Frontiers for Tests of QED in Heavy Highly Charged Ions. *Phys. Rev. Lett.*, 113:023002, 2014.

[179] E. V. Stefanovich. Renormalization and dressing in quantum field theory. *ArXiv High Energy Physics*, 2005. arXiv:hep-th/0503076v4.

[180] P. J. Mohr. Self-Energy Radiative Corrections in Hydrogen-Like Systems. *Ann. Phys.*, 88(1):26 – 51, 1974.

[181] P. J. Mohr. Numerical Evaluation of the $1S_{1/2}$-State Radiative Levelshift. *Ann. Phys.*, 88(1):52 – 87, 1974.

[182] W. R. Johnson and G. Soff. The Lamb shift in hydrogen-like atoms, $1 \leq Z \leq 110$. *At. Data Nucl. Data Tables*, 33(3):405 – 446, 1985.

[183] Steven A. Blundell and Neal J. Snyderman. Basis-set approach to calculating the radiative self-energy in highly ionized atoms. *Phys. Rev. A*, 44:R1427–R1430, 1991.

[184] N. J. Snyderman. Electron Radiative Self-Energy of Highly Stripped Heavy Atoms. *Ann. Phys.*, 211(1):43 – 86, 1991.

[185] H. Persson, I. Lindgren, and S. Salomonson. A New Approach to the Electron Self Energy Calculation. *Phys. Scr.*, 1993(T46):125–131, 1993.

[186] V. A. Yerokhin, P. Indelicato, and V. M. Shabaev. Self-Energy Correction to the Bound-Electron g Factor in H-like Ions. *Phys. Rev. Lett.*, 89:143001, 2002.

[187] V. A. Yerokhin and U. D. Jentschura. Electron Self-Energy in the Presence of a Magnetic Field: Hyperfine Splitting and g Factor. *Phys. Rev. Lett.*, 100:163001, 2008.

[188] V. A. Yerokhin and U. D. Jentschura. Self-energy correction to the hyperfine splitting and the electron g factor in hydrogenlike ions. *Phys. Rev. A*, 81:012502, 2010.

[189] V. A. Yerokhin, C. H. Keitel, and Z. Harman. Nuclear-size self-energy and vacuum-polarization corrections to the bound-electron g factor. *J. Phys. B*, 46(24):245002, 2013.

[190] J. Holmberg. *QED corrections to Atomic Wavefunctions in Highly Charged Ions.* PhD thesis, University of Heidelberg, 2015.

[191] J. M. Jauch and F. Rohrlich. *The Theory of Photons and Electrons.* Springer-Verlag, New York Heidelberg Berlin, 1976.

[192] W. R. Johnson, S. A. Blundell, and J. Sapirstein. Many-body perturbation-theory calculations of energy levels along the lithium isoelectronic sequence. *Phys. Rev. A*, 37:2764–2777, 1988.

[193] W. R. Johnson. Lectures on Atomic Physics, 2006. URL `https://www3.nd.edu/~johnson/Publications/book.pdf`.

[194] W. R. Johnson. *Atomic Structure Theory: Lectures on Atomic Physics*. Springer-Verlag, Berlin Heidelberg New York, 2007.

[195] L. F. Richardson. The Approximate Arithmetical Solution by Finite Differences of Physical Problems Involving Differential Equations, with an Application to the Stresses in a Masonry Dam. *Philos. Trans. Royal Soc. A*, 210(459-470):307–357, 1911.

[196] D. A. Varshalovich, A. N. Moskalev, and V. K. Khersonskii. *Quantum Theory of Angular Momentum*. World Scientific, 1988.

[197] I. Lindgren, H. Persson, S. Salomonson, and P. Sunnergren. Analysis of the electron self-energy for tightly bound electrons. *Phys. Rev. A*, 58:1001–1015, 1998.

[198] J. Blomqvist. Vacuum polarization in exotic atoms. *Nucl. Phys. B*, 48(1):95 – 103, 1972.

[199] D. J. Hylton. Finite-nuclear-size corrections to the Uehling potential. *Phys. Rev. A*, 32:1303–1309, 1985.

[200] G. Soff and P. J. Mohr. Vacuum polarization in a strong external field. *Phys. Rev. A*, 38:5066–5075, 1988.

[201] S. A. Blundell. Accurate screened QED calculations in high-Z many-electron ions. *Phys. Rev. A*, 46:3762–3775, 1992.

[202] H. Persson, I. Lindgren, S. Salomonson, and P. Sunnergren. Accurate vacuum-polarization calculations. *Phys. Rev. A*, 48:2772–2778, 1993.

[203] A. N. Artemyev, V. M. Shabaev, and V. A. Yerokhin. Vacuum polarization screening corrections to the ground-state energy of two-electron ions. *Phys. Rev. A*, 56: 3529–3534, 1997.

[204] A. N. Artemyev, T. Beier, G. Plunien, V. M. Shabaev, G. Soff, and V. A. Yerokhin. Vacuum-polarization screening corrections to the energy levels of lithiumlike ions. *Phys. Rev. A*, 60:45–49, 1999.

[205] A. N. Artemyev, T. Beier, G. Plunien, V. M. Shabaev, G. Soff, and V. A. Yerokhin. Vacuum-polarization screening corrections to the energy levels of heliumlike ions. *Phys. Rev. A*, 62:022116, 2000.

[206] A. N. Artemyev, V. M. Shabaev, G. Plunien, G. Soff, and V. A. Yerokhin. Vacuum-polarization corrections to the hyperfine splitting in heavy ions and to the nuclear magnetic moments. *Phys. Rev. A*, 63:062504, 2001.

[207] W. H. Furry. A Symmetry Theorem in the Positron Theory. *Phys. Rev.*, 51: 125–129, 1937.

[208] E. A. Uehling. Polarization Effects in the Positron Theory. *Phys. Rev.*, 48:55–63, 1935.

[209] E. H. Wichmann and N. M. Kroll. Vacuum Polarization in a Strong Coulomb Field. *Phys. Rev.*, 101:843–859, 1956.

[210] Q. Lyu. Private communication, 2015.

[211] K. Momberger, N. Grün, W. Scheid, U. Becker, and G. Soff. Muon pair production with inner-shell capture in relativistic U^{92+}–U^{92+} collisions. *J. Phys. B*, 20(9): L281, 1987.

[212] C. Müller, C. Deneke, and C. H. Keitel. Muon-Pair Creation by Two X-Ray Laser Photons in the Field of an Atomic Nucleus. *Phys. Rev. Lett.*, 101:060402, 2008.

[213] T Franosch and G. Soff. The influence of the nuclear shape and of the muonic vacuum polarization on strongly bound electrons. *Z. Phys. D*, 18(3):219–222, 1991.

[214] R. Weis. Myonische Vakuumpolarisationskorrekturen zum g-Faktor eines gebundenen Elektrons. Bachelor's thesis, University of Heidelberg, 2014.

[215] R. N. Lee, A. I. Milstein, I. S. Terekhov, and S. G. Karshenboim. Virtual light-by-light scattering and the g factor of a bound electron. *Phys. Rev. A*, 71:052501, 2005.

[216] K. W. Ford, V. W. Hughes, and J. G. Wills. Theoretical Values for Magnetic Moments of Mu-Mesonic Atoms. *Phys. Rev.*, 129:194–201, 1963.

[217] E. Borie and G. A. Rinker. The energy levels of muonic atoms. *Rev. Mod. Phys.*, 54:67–118, 1982.

[218] T. N. Mamedov, K. I. Gritsay, A. V. Stoykov, D. Herlach, R. Scheuermann, and U. Zimmermann. Measurement of the magnetic moment of the negative muon bound in heavy atoms. *Phys. Rev. A*, 75:054501, 2007.

[219] K. P. Jungmann. Muonium spectroscopy. *Hyperfine Interact.*, 127(1-4):189–196, 2000.

[220] A. G. Fainshtein, N. L. Manakov, and A. A. Nekipelov. Vacuum polarization by a Coulomb field. Analytical approximation of the polarization potential. *J. Phys. B*, 24(3):559, 1991.

[221] R. N. Lee, A. I. Milstein, I. S. Terekhov, and S. G. Karshenboim. g factor of the bound electron and muon. *Can. J. Phys.*, 85(5):541–549, 2007.

[222] V. M. Shabaev, I. I. Tupitsyn, V. A. Yerokhin, G. Plunien, and G. Soff. Dual Kinetic Balance Approach to Basis-Set Expansions for the Dirac Equation. *Phys. Rev. Lett.*, 93:130405, 2004.

[223] N. Michel, N. S. Oreshkina, and C. H. Keitel. Theoretical prediction of the fine and hyperfine structure of heavy muonic atoms. *Phys. Rev. A*, 96:032510, 2017.

[224] T. Beier, G. Plunien, M. Greiner, and G. Soff. Two-loop ladder diagram for the vacuum polarization contribution in hydrogen-like ions. *J. Phys. B*, 30(12):2761–2772, 1997.

[225] G. Källén and A. Sabry. Fourth order vacuum polarization. *K. Dan. Vidensk. Selsk. Mat. Fys. Medd.*, 29(17), 1955.

[226] L. W. Fullerton and G. A. Rinker. Accurate and efficient methods for the evaluation of vacuum-polarization potentials of order $Z\alpha$ and $Z\alpha^2$. *Phys. Rev. A*, 13:1283–1287, 1976.

[227] P. Indelicato. Nonperturbative evaluation of some QED contributions to the muonic hydrogen $n = 2$ Lamb shift and hyperfine structure. *Phys. Rev. A*, 87: 022501, 2013.

[228] J. L. Friar, J. Martorell, and D. W. L. Sprung. Hadronic vacuum polarization and the Lamb shift. *Phys. Rev. A*, 59:4061–4063, 1999.

[229] S. Eidelman and F. Jegerlehner. Hadronic contributions to $(g-2)$ of the leptons and to the effective fine structure constant $\alpha(M_Z^2)$. *Z. Phys. C*, 67(4):585–601, 1995.

[230] E. Borie. Hadronic vacuum polarization correction in muonic atoms. *Z. Phys. A*, 302(3):187–189, 1981.

[231] R. N. Faustov, A. Karimkhodzhaev, and A. P. Martynenko. Evaluation of hadronic vacuum polarization contribution to muonium hyperfine splitting. *Phys. Atom. Nucl.*, 62:2103–2105, 1999.

[232] J. A. Fox and D. R. Yennie. Some Formal Aspects of the Lamb Shift Problem. *Ann. Phys.*, 81(2):438 – 480, 1973.

[233] A. Mitrushenkov, L. Labzowsky, I. Lindgren, H. Persson, and S. Salomonson. Second order loop after loop self-energy correction for few-electron multicharged ions. *Phys. Lett. A*, 200(1):51 – 55, 1995.

[234] V. A. Yerokhin. Loop-after-loop contribution to the second-order Lamb shift in hydrogenlike low-Z atoms. *Phys. Rev. A*, 62:012508, 2000.

[235] V. A. Yerokhin. Leading Logarithmic Contribution to the Second-Order Lamb Shift Induced by the Loop-After-Loop Diagram. *Phys. Rev. Lett.*, 86:1990–1993, 2001.

[236] V. A. Yerokhin, P. Indelicato, and V. M. Shabaev. Two-Loop Self-Energy Correction in High-Z Hydrogenlike Ions. *Phys. Rev. Lett.*, 91:073001, 2003.

[237] V. A. Yerokhin, P. Indelicato, and V. M. Shabaev. Two-loop self-energy correction to the ground-state Lamb shift in H-like ions. *Nucl. Instr. Meth. Phys. Res. B*, 235(1):36 – 39, 2005.

[238] V. A. Yerokhin, P. Indelicato, and V. M. Shabaev. Two-loop self-energy contribution to the Lamb shift in H-like ions. *Phys. Rev. A*, 71:040101, 2005.

[239] V. A. Yerokhin, P. Indelicato, and V. M. Shabaev. Two-loop Self-Energy Correction in a Strong Coulomb Nuclear Field. *J. Exp. Theor. Phys.*, 101(2):280–293, 2005.

[240] I. Goidenko, L. Labzowsky, G. Plunien, and G. Soff. Second-order electron self-energy loop-after-loop correction for low-Z hydrogen-like ions. *Nucl. Instr. Meth. Phys. Res. B*, 235(1):40 – 45, 2005.

[241] V. A. Yerokhin, P. Indelicato, and V. M. Shabaev. Nonperturbative Calculation of the Two-Loop Lamb Shift in Li-Like Ions. *Phys. Rev. Lett.*, 97:253004, 2006.

[242] V. A. Yerokhin, P. Indelicato, and V. M. Shabaev. Two-loop QED corrections with closed fermion loops. *Phys. Rev. A*, 77:062510, 2008.

[243] V. A. Yerokhin. Two-loop self-energy for the ground state of medium-Z hydrogenlike ions. *Phys. Rev. A*, 80:040501, 2009.

[244] V. A. Yerokhin. The two-loop self-energy: diagrams in the coordinate-momentum representation. *Eur. Phys. J. D*, 58(1):57–68, 2010.

[245] V. A. Yerokhin and V. M. Shabaev. Lamb Shift of $n = 1$ and $n = 2$ States of Hydrogen-like Atoms, $1 \leq Z \leq 110$. *J. Phys. Chem. Ref. Data*, 44(3):033103, 2015.

[246] V. A. Yerokhin. Two-loop self-energy in the Lamb shift of the ground and excited states of hydrogen-like ions. Submitted, 2017.

[247] C. Brandau, C. Kozhuharov, A. Müller, W. Shi, S. Schippers, T. Bartsch, S. Böhm, C. Böhme, A. Hoffknecht, H. Knopp, N. Grün, W. Scheid, T. Steih, F. Bosch, B. Franzke, P. H. Mokler, F. Nolden, M. Steck, T. Stöhlker, and Z. Stachura. Precise Determination of the $2s_{1/2}-2p_{1/2}$ Splitting in Very Heavy Lithiumlike Ions Utilizing Dielectronic Recombination. *Phys. Rev. Lett.*, 91:073202, 2003.

[248] M. Fischer, N. Kolachevsky, M. Zimmermann, R. Holzwarth, Th. Udem, T. W. Hänsch, M. Abgrall, J. Grünert, I. Maksimovic, S. Bize, H. Marion, F. Pereira Dos Santos, P. Lemonde, G. Santarelli, P. Laurent, A. Clairon, C. Salomon, M. Haas, U. D. Jentschura, and C. H. Keitel. New Limits on the Drift of Fundamental Constants from Laboratory Measurements. *Phys. Rev. Lett.*, 92:230802, 2004.

[249] P. Beiersdorfer, H. Chen, D. B. Thorn, and E. Träbert. Measurement of the Two-Loop Lamb Shift in Lithiumlike U^{89+}. *Phys. Rev. Lett.*, 95:233003, 2005.

[250] P. Indelicato and P. J. Mohr. Coordinate-space approach to the bound-electron self-energy. *Phys. Rev. A*, 46:172–185, 1992.

[251] P. Indelicato and P. J. Mohr. Coordinate-space approach to the bound-electron self-energy: Coulomb field calculation. *Phys. Rev. A*, 58:165–179, 1998.

[252] P. Indelicato and P. J. Mohr. Coordinate-space approach to the bound-electron self-energy: Self-energy screening calculation. *Phys. Rev. A*, 63:052507, 2001.

[253] P. Indelicato, P. J. Mohr, and J. Sapirstein. Coordinate-space approach to vacuum polarization. *Phys. Rev. A*, 89:042121, 2014.

[254] J. Holmberg, A. N. Artemyev, A. Surzhykov, V. A. Yerokhin, and Th. Stöhlker. QED corrections to radiative recombination and radiative decay of heavy hydrogenlike ions. *Phys. Rev. A*, 92:042510, 2015.

[255] W. R. Johnson, S. A. Blundell, and J. Sapirstein. Finite basis sets for the Dirac equation constructed from B splines. *Phys. Rev. A*, 37:307–315, 1988.

[256] G. S. Adkins and Y. Zhang. Infrared behavior of Yennie gauge QED at two-loop order. *Can. J. Phys.*, 76(5):333–349, 1998.

[257] S. Wolfram. *Mathematica – A System for Doing Mathematics by Computer.* AW, Reading, MA, 1988.

[258] K. Pachucki, M. Puchalski, and V. A. Yerokhin. Extended Gaussian quadratures for functions with an end-point singularity of logarithmic type. *Comput. Phys. Commun.*, 185(11):2913 – 2919, 2014.

[259] M. Serone. Anomalies in Quantum Field Theory, 2016. URL `http://gsfp.physi.uni-heidelberg.de/graddays/content/en/zubehoer/anhaenge/serone/Anomalies_Review_9.10.2016.pdf`. Lectures given at the "37th Heidelberg Physics Graduate Days", 10-14 October 2016.

[260] J. Gluza and T. Riemann. Evaluation of Feynman Integrals: Advanced Methods, 2009. https://www-zeuthen.desy.de/ riemann/Talks/riemann-recapp-09.pdf.

[261] I. Lindgren. *Relativistic Many-Body Theory: A New Field-Theoretical Approach*, volume 63 of *Springer Series on Atomic, Optical, and Plasma Physics.* Springer-Verlag, 2011.

[262] V. M. Shabaev. Generalizations of the virial relations for the Dirac equation in a central field and their applications to the Coulomb field. *J. Phys. B*, 24(21): 4479–4488, 1991.

[263] Wolfram mathworld. http://mathworld.wolfram.com/.

[264] R. C. Tautz. Instability conditions and maximum growth rate of aperiodic instabilities. *Phys. Plasmas*, 18(1):012101, 2011.

[265] S. Räsänen. Backreaction: directions of progress. *Class. Quantum Grav.*, 28(16): 164008, 2011.

[266] I. Feranchuk, A. Ivanov, V.-H. Le, and A. Ulyanenkov. *Non-perturbative Description of Quantum Systems*, volume 894 of *Lecture Notes in Physics*. Springer-Verlag, Heidelberg, 2015.

Acknowledgments

I would like to thank my advisor Honorarprof. Dr. Christoph H. Keitel for showing faith in me and giving me the opportunity to carry out my PhD research in the Theory Division at the Max Planck Institute for Nuclear Physics, and for his constant interest and support of my work.

I would also like to express my gratitude to PD Dr. Zoltán Harman who always had time for me. His constant support, guidance, advice, help and patience contributed immensely to this work.

Useful discussions on experimental aspects with Dr. Sven Sturm are gratefully acknowledged.

I would also like to thank Prof. Maurits Haverkort for agreeing to by a referee of my thesis, as well as Prof. Dr. Kurt Roth and PD Dr. Wolfgang Quint for agreeing to be members of my exam comittee.

I am very grateful to Prof. Dr. Vladimir Yerokhin for many enlightening discussions and plenty of help.

Fortran Codes which were essential for this work were provided by Prof. Dr. Vladimir Yerokhin, PD Dr. Zoltán Harman and Dr. Natalia Oreshkina.

I would like to thank also Dr. Natalia Oreshkina, Dr. Jacek Zatorski, Dr. Nikolay Belov and Dr. Vincent Debierre, Halil Cakir, Niklas Michel and Robin Weis for fruitful collaborations.

Special thanks to everyone who proof-read and in the process improved my thesis: Chunhai Lyu, Dr. Natalia Oreshkina, Dr. Vincent Debierre, Niklas Michel, Halil Cakir and, of course, my above mentioned thesis supervisors.

I would like to thank all colleagues in the Theory Division, past and present, for the excellent working environment.

Special thanks for love and support to my family and my girlfriend.